UNIVERSITY OF SOUTHAMPTON

FACULTY OF ENGINEERING, SCIENCE AND MATHEMATICS

School of Chemistry

Preparation and Characterisation of Pt/C and Ni/C Modified Electrocatalysts for Use Towards the Oxygen Reduction Reaction for Proton Exchange Membrane Fuel Cells

by

Gael Henri Chouchelamane

Thesis for the degree of Doctor of Philosophy

February 2010

ABSTRACT

FACULTY OF ENGINEERING, SCIENCE & MATHEMATICS

SCHOOL OF CHEMISTRY
Doctor of Philosophy

PREPARATION AND CHARACTERISATION OF Pt/C AND Ni/C MODIFIED ELECTROCATALYSTS FOR USE TOWARDS THE OXYGEN REDUCTION REACTION FOR PROTON EXCHANGE MEMBRANE FUEL CELLS

by Gael Henri Chouchelamane

The aim of this thesis is to develop more active catalysts for the oxygen reduction reaction whilst decreasing the metal content to drive forward the emergence of the fuel cell technology on the market.

Chapter 3 presents the preparation of Ni modified Pt/C catalysts ($Ni(acac)_2$ and $Ni(Cp)_2$) using the controlled surface modification technique. The resulting catalysts were heat treated at 200, 500, 750 and 900 °C and the catalysts were characterised by ICP-OES, TEM, EDX, CV, RDE, EXAFS and XPS. The catalysts exhibited up to 8-fold increase in specific activity and up to 9-fold increase in mass activity. The increase in activity was assigned to (a) the synergistic effect of Ni on Pt and (b) the degree of alloying which has two consequences: (a) decrease of the Pt *d*-band centre and (b) change of the arrangement of the Pt and Ni atoms at the surface of the particles. The decrease in the Pt *d*-band centre resulted in the lowering of the adsorption strength of the oxide species which in turn led to a lower Pt-O coverage. This was supported by the decrease of the reduction potential of the oxide reduction peak as the heat treatment temperature increased. In addition, as the heat treatment temperature increased, the Pt surface concentration increased due to the diffusion of the Ni atoms inwards and the diffusion of the Pt atoms towards the outside of the particle. This led to larger and more well-defined Pt crystal planes. The presence of more well-defined Pt crystal planes seemed to provide more suitable adsorption site for the dual-site adsorption of the oxygen, thus increasing the activity. Last but not least, the highest increase in catalytic activity was exhibited by the catalysts heat treated at 500 °C. This demonstrated the importance of the choice of the secondary metal and the importance of the arrangement of the atoms at the surface of the particles.

Chapter 4 presents what is believed to be the first attempt to prepare Pt modified Ni/C catalysts ($Pt(acac)_2$) using the controlled surface modification technique. The catalysts were characterised by TEM, CV and RDE. The deposition of the Pt precursor was shown to be incomplete; however, the catalysts still had a Pt content of ~ 4 wt%. Despite the low Pt content, the catalysts exhibited up to 8-fold increase in specific activity. The increase in activity was assigned to the synergistic effect between Ni and Pt which was shown by the decrease in the lattice parameter and the decrease of the overpotential of the oxide reduction peak.

Chapter 5 offers a summary of the thesis as well as a list of the strategies employed to date to increase the catalytic activity of the cathode catalysts. It also includes some suggestion for future work including underpotential deposition (UPD), MEA testing and stability testing.

DECLARATION OF AUTHORSHIP

I, **Gael Henri Chouchelamane**, declare that the thesis entitled

Preparation and Characterisation of Pt/C and Ni/C Modified Electrocatalysts for Use Towards the Oxygen Reduction Reaction for Proton Exchange Membrane Fuel Cells

and the work presented in the thesis are both my own, and have been generated by me as the result of my own original research. I confirm that:

- This work was done wholly or mainly while in candidature for a research degree at this University;
- Where any part of this thesis has previously been submitted for a degree or any other qualification at this University or any other institution, this has been clearly stated;
- Where I have consulted the published work of others, this is always clearly attributed;
- Where I have quoted from the work of others, the source is always given. With the exception of such quotations, this thesis is entirely my own work;
- I have acknowledged all main sources of help;
- Where the thesis is based on work done by myself jointly with others, I have made clear exactly what was done by others and what I have contributed myself;

Signed: ……..

Date:…….

ACKNOWLEDGMENTS

Firstly, I would like to thank my boss, Prof. A.E. Russell for all her advice and guidance during my PhD. She has been very knowledgeable and enthusiastic throughout this research project. She is also to be mentioned for going for a nap on a table at the ESRF whilst EXAFS scans were being collected.

I would like to thank all those who helped me at *Johnson Matthey*: Dave Thompsett, Sarah Ball, and the whole analytical team especially Hoi Johnson and James McNaught for performing the XRD analysis, Jingshan Dong and D. Ozkaya for most of the TEM results, Paul Fisher, Godson Nnorom-Junior, Stephen Thompson and Matt Gregory for the metal assay data, and Richard A.P. Smithand and Sarennah J. P. Longworth for the XPS analysis. Thank you all for your hard work and efforts.

I would like to show my gratitude to Brian Theobald. He has been my contact at JM for the duration of my PhD, answering questions and preparing the Ni/C support used in this work. He has also spent a great amount of time and effort chasing after the analysis of my samples. His knowledge and input into this work were very valuable. Once again thank you.

For all their help at the SLS and BNL, I would like to thank Maarten Nachtegaal and Kaumudi Pandya without whom I could not have been able to collect the EXAFS data recorded in this work.

There are a lot of people that are working behind-the-scene to ensure that all the research in the chemistry department is carried out in the best possible manner. A huge vat of thanks should therefore be addressed to Sally, Jane, Bevy and Mary for their help with the administration work. I am also grateful to the glassblowers, Pzemyslaw, Lee and Clive, for their hard work and for making and fixing a number of cells that I have used in my research. I enjoyed every debate we had regarding those cells and learnt a lot from you. I would like to show my appreciation to the technical workshop and especially to Allan and John for working on the different EXAFS cells. And finally, what would a researcher be without people dedicating to the receiving and delivering of the goods? A BIG thank must therefore go to the Karl, Clive, Tony and Graham for their exceptional service and hard work. I enjoyed coming around for a chat and a good laugh.

Now, I'd like to thank every member of the Russell group as they have made my time here very enjoyable and have also been good friends. Fabrice is to be remembered for our French Scrabble games and especially for bursting out of his chair and arguing with me for playing "NEZ" as he forgot that it was the French for "nose". Suzanne was an exceptional English Scrabble partner. I loved trying to beat you every day and thanks to you, I learnt lots of useless but quite interesting words. For passing on

his electrochemistry and EXAFS knowledge, I have to thank Peter. For witnessing the "flaming" pizza and for the hours of football played together, Dave should also be mentionned. For allowing me to have my first escapade in NYC and for laughing to tears whilst trying to clarify that "supersize" is NOT what a waiter/waitress says when you sit down in a diner rather she/he says "soup or salad" (and that's before serving the starter, the main and the dessert…god bless America!!), Katie is to be acknowledged here. For her EXAFS experiment at the ESRF which allowed me to go back and eat lots of French pastries and food (yummyyyyyyy), I am grateful to Sarah. Beatrice is also to be named (and Andrea as well) for the knitting lessons and for the "night shift" song. For our endless conversations in the office (before she got pregnant) and for her theoretical knowledge of chemistry, a big thank you to Prabalini. For being a fun football team-mate and for remaining on the pitch despite a broken toe, Piotr has to be named. For his helping attitude and because I don't think I have ever heard him say "no" to anyone, Steve should also be mentionned. Also, after going to America with him, I do know what jet lag is and how it affects people. For his enthusiasm and for trying to find the perfect recipe and procedure for mint/spicy hot chocolate and omelette (which he never passed on, meanie!), Jon has to be acknowledged. For teaching me that trying to take down a tree with your body may result in the victory of the tree and broken ribs, Anna should be mentioned.

Another thank you has to go to all the athletes I have encountered during my PhD, and especially to the Commoners, none of you shall be forgotten.

I also have to mention and thank Miss Ashford (and Nessie) for reading my introduction and for making it the best introduction ever read by Andrea. The praises I received are also hers to share. I think finding your name in my thesis will be considered as an achievement and as your contribution to the scientific community.

Jasmine has to be thanked for putting up with me for most of my PhD, for helping me improve my writing skills, for her constant support and for being my unforgettable XRD team-mate. She did get up at 2 and 5 am on Saturdays to provide me support to change sample (that is dedication to try and save the world) and she also tried to understand the technique but without success unfortunately. I could not convert you but at least you learnt and will never forget what XRD stands for.

Finally, I can't thank Jennifer enough for her support and understanding during the writing up of this piece of work. She put up with my frustration and my determination. She never got mad for all the phone conversations she had with herself whilst I was thinking about the thesis. However, she did get me back when I was seeing her as she never allowed me to think about writing up during this time. I did love all the efforts you put in to realise this daunting task. You do deserve the last "Thank you" and I hope I will be able to return the favour in the future.

CHAPTER ONE: INTRODUCTION

This chapter briefly reviews the current stage of the fuel cell technology with a particular emphasis on the proton exchange membrane fuel cell (PEMFC). It begins with an overview of these power supplies including their historical developments, their applications and the motivations behind their advancements. Subsequently, their principles of operation followed by a comprehensive description of PEMFC are detailed. This chapter concludes by clearly stating the aims of this research project.

1 General introduction

1.1 Environmental driving force

Earth is the only planet known to mankind capable of sustaining life. Since the beginning of time, man's desire to continually broaden their knowledge led to major scientific breakthroughs (e.g. canon powder, vaccination, theory of relativity and radioactivity). Also, their drive to live a more comfortable life initiated industrial revolutions and the last one resulted with the birth of the internal combustion engine (ICE).

Nowadays millions of ICE cars are driven worldwide, emitting a mixture of gases which are poisonous to our environment and to human beings. This mixture contains sulphur oxides (SO_x), nitrous oxides (NO_x) and carbon dioxide (CO_2). SO_x are the major source of acid rains which have adverse effects on forests, freshwaters and soils. NO_x reacts with volatile organic compounds in the presence of sunlight to form photochemical smog that surrounds cities with dense traffic on hot and dry days. People inhale these particles which travel deep into the lungs and potentially cause diseases such as asthma or cancer. Finally, CO_2 is thought to be directly responsible for the greenhouse effect since it thickens the troposphere trapping more infrared radiation. As a consequence, the overall temperature of the Earth has increased resulting in greater proportion of ice melting and hotter summers (e.g. heat wave of summer 2003).

Governments across the world are taking important measures to tackle the greenhouse effect. In 1997 more than 100 developing countries ratified the Kyoto

protocol[1], hence showing their commitment to reducing their emissions of greenhouse gases. In addition, Governments are implementing more stringent automotive gas emission directives (e.g. European emission standard EURO 5). As a result, car manufacturers are developing more efficient engines and exhaust systems.[2, 3] In certain American states, the latter developments are not sufficient to improve the air-quality and car manufacturers are being forced to sell zero-emission vehicles. For example, the state of California requires car manufacturers to sell about 10 % of zero-emission vehicles by 2010.[4]

Despite all the actions undertaken, the emission of greenhouse gases is still rising. In addition, the rise in oil prices (which is directly related to the depletion of natural oil resources) has led to the development of more environmentally friendly power generation sources. One class of these developed power generation sources being developed are the fuel cells (FC). FCs are very attractive as they could be used as a replacement of the ICE. FCs have several advantages over the ICE such as minimisation of noise and vibration, high efficiency and cleanliness as water is the only product rejected from the exhaust if hydrogen is used as the fuel.

1.2 History

In January 1839, Professor C. F. Schoenbein (1799-1868) first reported the fuel cell effect as he concluded that a current was caused by the combination of hydrogen (H_2) with oxygen (O_2).[5] However, in February 1839, Sir W. R. Grove (1811-1896) first reported the use of this effect as an electricity generator[6], hence earning him the honour of being remembered as the discoverer of fuel cell technology . In 1842, Grove published a detailed record of his research on the new electricity power supply. His experimental set-up involved two strips of platinum (Pt) surrounded by tubes containing O_2 and H_2 immersed into dilute sulphuric acid. He observed a current and water formation on the side of the tubes. He linked several of cells in series and described the system as a *gaseous voltaic battery*.[7]

In 1889, L. Mond and C. Langer revised and improved Grove's cell design by using porous electrodes coated with a hydrophobic layer and by operating the cell at 0.7 V vs. RHE. Mond and Langer are also to be mentioned because they were the first to introduce the term "*Fuel cell*".[8, 9]

In 1932, Dr F. T. Bacon resurrected and upgraded the device developed by Mond and Langer. After more than 20 years of research, he produced an alkaline fuel cell (AFC) which was able to deliver a power corresponding to *ca.* 700 mA cm^{-2}. The AFC used a caustic potash (KOH) electrolyte with nickel electrodes and operated at 200 °C and 41 bar.[10]

In 1959, W. T. Grubb studied the conductivity of protons in an ion-exchange membrane[11]; the proton exchange membrane fuel cell (PEMFC) was born. The PEMFC was first used by the *National Aeronautics and Space Administration* (*NASA*) as a power supply for the Gemini project.[12, 13] However, at the time, low efficiency and issues with the membrane degradation made the PEMFCs not suitable candidates for manned flights of extended period of time. Consequently, *NASA* considered other fuel cells possibilities and placed an order for an AFC from *Pratt & Whitney* (East Hartford, Connecticut, USA). The AFC was preferred since it had 70 % efficiency and it could provide drinking water to the astronauts. *Pratt & Whitney* improved Bacon's fuel cell by increasing the KOH electrolyte concentration to 75 % and by decreasing the total pressure to 4 bar, leading to a lighter fuel cell. This developed AFC was then used in the Apollo space project.[9, 14]

However, this major achievement did not result in any commercial application because of the large amount of precious metal used to make the catalysts, which rendered the device too expensive. Furthermore, the carbon monoxide (CO) tolerance of the AFC was very low which meant that highly purified H_2 and O_2 had to be used at the anode and cathode, respectively.

To overcome these difficulties several types of FC have been developed since. Several studies were carried out to decrease the noble metal content and to select the optimum materials. PEMFCs have recently received particular attention, especially because of their potential use as a substitute for the ICE. Major improvements were achieved over the years to decrease the Pt-loading from *ca.* 4 mg cm^{-2} to *ca.* 0.4 mg cm^{-2}.[15] However, further advances are required before this technology emerges on the market.

1.3 Applications

FC are a rapid developing power supply technology and their potential applications are enormous. Each type of FC has its own characteristics and advantages. As a

consequence, FC can be seen as a potential replacement for certain current technologies especially in stationary or portable power supply as well as transportation.

The automotive market is the most promising market available to PEMFC technology. Several car companies have developed H_2-powered cars.[16, 17] However, a few challenges are still to be overcome. Firstly, it is important to develop a more competitive, more efficient and cheaper H_2-powered vehicle. The ultimate aim would be that FC cars reach a similar mileage and price to that of ICE cars. Secondly, the use of pure H_2 raises health and safety concerns as it is highly flammable. Lastly and more importantly, substituting petrol by H_2 would mean that new supply infrastructures would need to be implemented and Governments seem to be reluctant to this idea as PEMFC are still at an early stage of their development. However, the last few years have seen the development of a few H_2 filling stations mainly across the United States but also worldwide.[18]

Phosphoric acid fuel cells (PAFC) are of great interest as a stationary power supply unit. Their relatively mild working temperature allows for the conversion of natural gas into H_2 with no prior treatment of the feeding stock material. In Germany, a PAFC cell is employed in combination with two existing gas engine cogeneration units to provide a power output of 600 kW. This device is currently used in a hospital to provide electricity and to drive adsorption chillers in the air conditioning system during the summer.[19] Some of these power plants have run for more than 40000 h.[20]

At present, direct methanol fuel cells (DMFC) are being developed as a substitute for lithium batteries for portable applications. The DMFC has the potential to increase battery run-time for laptops and mobile phones by a factor of 3.[19]

2 Fuel cells principles

Fuel Cells (FC) are electrochemical devices that convert chemical energy into electricity and heat. Unlike batteries, FC can work continuously as long as the fuel is externally provided. Using the PEMFC as an example (**Figure 1- 1**), H_2 is oxidised into protons and electrons at the anode (**Equation 1-1**) whilst air (or pure O_2) is reduced at the cathode (**Equation 1-2**). The two electrodes are separated by a proton conducting membrane electrolyte which enables the transfer of protons from the

anode to the cathode and acts as an electron insulator forcing the electrons to go through an electrical load. This process results in the production of an electric current and emission of water as a by-product (**Equation 1-3**).

When hydrogen is the fuel, the anode reaction is:

$H_2 \rightarrow 2\,H^+ + 2\,e^-$ $\quad E^0 = 0.00$ V vs. RHE **Equation 1-1**

After the electrons pass through the external circuit they reach the cathode where oxygen is reduced to produce water:

$O_2 + 4\,H^+ + 4\,e^- \rightarrow 2\,H_2O$ $\quad E^0 = 1.23$ V vs. RHE **Equation 1-2**

The overall equation for the reaction is as follows:

$2\,H_2 + O_2 \rightarrow 2\,H_2O$ $\quad E^0 = 1.23$ V vs. RHE **Equation 1-3**

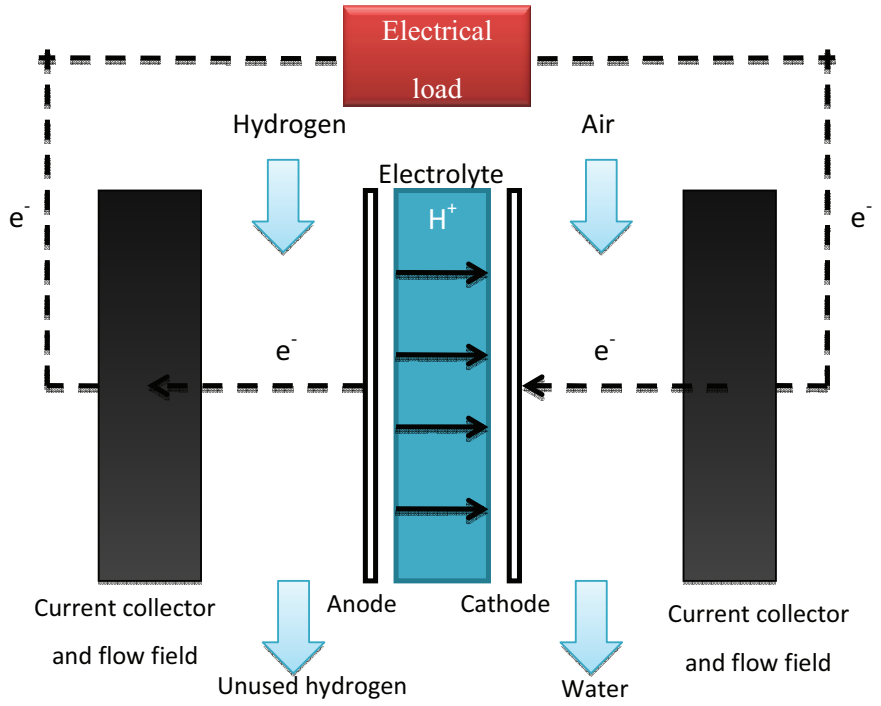

Figure 1- 1 Schematic of a PEMFC

The maximum electric work obtainable from a chemical reaction is given by the Gibbs equation (**Equation 1-4**):

$$\Delta G = -nFE \qquad \textbf{Equation 1-4}$$

Where ΔG is the change in the Gibbs free energy, n is the number of electrons, F is the Faraday constant and E is the thermodynamic cell voltage.

The ideal efficiency of energy conversion, ξ_{th}, is related to reaction enthalpy (ΔH) and Gibbs free energy according to **Equation 1-5**:

$$\xi_{th} = \frac{\Delta G}{\Delta H} \qquad \textbf{Equation 1-5}$$

For the above fuel cell reaction, ΔG = - 237.3 kJ mol^{-1} and ΔH = - 286.0 kJ mol^{-1} and thus a theoretical ζ_{th} = 0.83 is achievable.[21]

3 Proton Exchange Membrane Fuel Cells (PEMFC)

There are several types of fuel cells which have similar principles to that described in *section 2*, but differ by the electrolyte, the species transported through the electrolyte, the cathode/anode materials and the working temperature. These fuel cells can be categorised into two groups; the low temperature fuel cells and high temperature fuel cells. The high temperature fuel cells include the solid oxide fuel cell (SOFC)[22-24] and the molten carbonate fuel cell (MCFC).[25] The low temperature fuel cells are the AFC[26, 27], DMFC, PEMFC and PAFC.[20]

The description of each FC is not in the scope of this thesis. However, as this work focuses on the PEMFC, a detailed account of this fuel cell will be given in the following sections.

PEMFC have been the centre of attention in the last few decades due to their possible automotive application. They operate at temperatures between 60 °C and 90 °C using H_2 and air as anode and cathode gas feed, respectively. The H_2 can be supplied in its pure form or through the reforming of hydrocarbons. The anode fuel stream can also be methanol and this type of fuel cells is termed the direct methanol fuel cell (DMFC).

3.1 Structure

The core component of the PEMFC is the membrane electrode assembly (MEA). The MEA consists of a proton exchange membrane inserted between the anode and the cathode catalysts. To complete the PEMFC unit, two current collectors (which also allow the different fuels to be evenly distributed on the catalyst surface) are located

on either side of the MEA (Error! Reference source not found.). One PEMFC unit cannot provide the required voltage for most applications and as a consequence several PEMFC units are linked together in series to form a fuel cell stack.

3.2 Anode fuel

3.2.1 Hydrogen production

Hydrogen is the most prevalent element in the universe; however its abundance on Earth (in its gaseous form) is small because of its low density. Consequently, H_2 has to be extracted from naturally occurring substances such as water and hydrocarbons. Electrolysis of water and reformation of hydrocarbons are the preferred processes to produce H_2. Other methods to produce H_2 can be found in the literature but will not be discussed in this thesis.[28-31]

Reforming of hydrocarbons is the most economic way to produce H_2. Methane (or natural gas) is the most suitable hydrocarbon to produce H_2 from because it is widely available, easy to handle, cheap and above all, it has the highest hydrogen-to-carbon ratio amongst all the hydrocarbons. Several industrial processes were developed to produce H_2 such as *steam reforming* (SR), *partial oxidation* (POX) and *autothermal reforming* (ATR) which is a combination of SR and POX.

The *SR* of natural gas involves the reaction of methane with steam over a nickel-based catalyst at around 900 °C and 3 to 25 bar (**Equation 1-6**):

$$CH_4 + H_2O \rightarrow CO + 3\ H_2 \qquad \textbf{Equation 1-6}$$

The presence of CO is major issue for the use of reformate as fuel because even traces of CO would be enough to lower the activity of the Pt-catalysts.[32] CO acts as a poison, binding strongly to Pt sites, hence reducing the number of Pt sites available for H_2 oxidation. Therefore, CO has to be removed from the reformate. As a result, the syngas (mixture of CO and H_2 gases) is subjected to a clean-up process called the *water-gas shift reaction*. This process involves the reaction of CO with steam to produce CO_2 and H_2 (**Equation 1-7**):

$$CO + H_2O \rightarrow CO_2 + H_2 \qquad \textbf{Equation 1-7}$$

Several clean-up steps are needed in order to achieve the purity of H_2 required for fuel cell applications. Several other processes have been developed in order to reduce the CO level to few ppm (e.g. preferential oxidation (PROX) [33]).

The overall reaction for the SR of methane is given by **Equation 1-8**:

$$CH_4 + 2\ H_2O \rightarrow CO_2 + 4\ H_2 \qquad \textbf{Equation 1-8}$$

The H_2 is eventually extracted from the final gas mixture by a process called *process swing adsorption* (PSA). PSA involves the adsorption of all gases and impurities except H_2 onto a suitable absorbent (e.g. molecular sieve) in a packed bed at high pressure.

POX of natural gas is the process whereby H_2 is produced through the partial combustion of methane with O_2 yielding carbon monoxide and hydrogen (**Equation 1-9)**.

$$CH_4 + ½\ O_2 \rightarrow CO + 2\ H_2 \qquad \textbf{Equation 1-9}$$

The further oxidation of CO into CO_2 as well as the removal of CO_2 are performed similar to that described for the SR of methane.

The reforming of hydrocarbons still produces CO_2 and therefore this process still contributes to the greenhouse effect. To reduce the emission of greenhouse gases to zero, CO_2 could be captured and stored underground.[34] However, the feasibility and proof of permanent CO_2 storage in geological formations have yet to be determined. Consequently, the ideal solution would be to produce H_2 through the electrolysis of water using renewable energy sources (sunlight, wind or wave).

At the end of March 2008, the HYDROSOL 2 plant (Almeria, Spain) started its production of H_2 via electrolysis of water using solar energy.[35] It generates 3 kg of H_2 per hour, which represents about 300,000 m^3 of H_2 a year. This is a small amount in comparison to the production of H_2 obtained via reforming of hydrocarbons (~ 100 millions m^3 of H_2 in the United States only [36]). More work needs to be undertaken in order to increase the production of H_2 using renewable power sources through the electrolysis of water so that it becomes a more viable and cheaper process.

3.2.2 Hydrogen storage

H_2 has a wide range of flammability (from 4 % up to 70 % by volume) at standard pressure and temperature and as a consequence health and safety issues are raised with regard to its storage for automotive applications. Several solutions are being put forward such as high hydride storage, cryogenic and pressure cylinders.

High pressure gas cylinders made of steel or composites have been developed and can now withstand pressures up to 700 bar. However, there are still concerns about letting the general public have access to these cylinders.[37, 38]

Cryogenic storage of H_2 is a solution to decrease the size and weight of the storage system. However, its development is hindered by the required amount of energy necessary to maintain the low temperature (20 K). In addition, other hurdles have to be overcome such as finding a suitable energy efficient cryogenic process as well as improving the thermal insulation of the cryogenic device in order to decrease the boil off of H_2.[37, 38]

Metal hydrides are also receiving high interest due to their potential to become a safe and efficient way to store H_2. They are formed by reacting H_2 with a transition metal or their alloys at elevated temperature. This forces the hydrogen atoms into the interstitial sites of the metal (octahedral, tetrahedral sites or a combination of both). The main advantage of metal hydrides is their high-volumetric storage density.[37-39]

3.2.3 Methanol (DMFC)

So far, all the anode fuel feeds have been gases and therefore new ways to store and produce hydrogen needed to be developed. Using methanol would prove to have several advantages such as removal of the reforming step and removal of the CO clean-up process. In addition, no drastic changes to the actual storage system would be required. The reaction occurring at the anode and cathode are defined by **Equation 1-10** and **Equation 1-11**, respectively.

$CH_3OH + H_2O \rightarrow CO_2 + 6\ H^+ + 6\ e^-$ $\quad E^0 = 0.05$ V vs. RHE **Equation 1-10**

$3/2\ O_2 + 6\ H^+ \rightarrow 3\ H_2O$ $\quad E^0 = 1.23$ V vs. RHE **Equation 1-11**

The overall reaction is:

$CH_3OH + H_2O + 3/2\ O_2 \rightarrow CO_2 + 3\ H_2O$ $\quad E^0 = 1.18$ V vs. RHE **Equation 1-12**

The reaction mechanism is still not completely understood. However, it is thought to initially involve 3 adjacent Pt sites to dissociate one methanol molecule.[40] The methanol oxidation reaction scheme is described in **Figure 1- 2**. It involves the adsorption of a methanol molecule onto Pt and each step involves the removal of a proton and an electron. All the intermediates have been confirmed by IR measurements.[41]

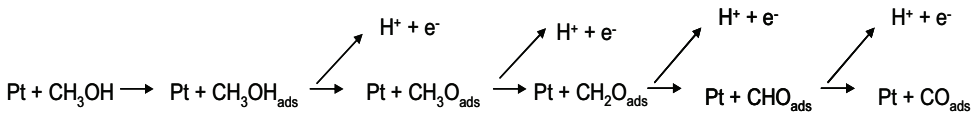

Figure 1- 2 Scheme of the consecutive intermediate formed during the methanol oxidation on Pt surface.

The mechanism of CO removal has been suggested to follow the Langmuir-Hinshelwood mechanism as shown in **Equation 1-13** and **Equation 1-14.** [42]

$$Pt + H_2O \rightarrow Pt\text{-}OH_{ads} + H^+ + e^- \qquad \textbf{Equation 1-13}$$

$$Pt\text{-}OH_{ads} + Pt\text{-}CO_{ads} \rightarrow CO_2 + H^+ + e^- + 2\ Pt \qquad \textbf{Equation 1-14}$$

However, this process does not occur before 0.75 V vs. RHE on a Pt surface[43] hence, resulting in a polarisation loss at the anode.

Methanol crossover is also a concern associated with DMFC. It occurs because of the relatively small thickness of the membranes. In spite of limiting the *iR* drop across the membrane, the small thickness of the membrane results in a thinner barrier for the methanol molecules to overcome. Several studies on membrane development led to a membrane capable of decreasing the methanol crossover by a factor of 10. Such a membrane consists of polybenzimidazole doped with inorganic acids.[40]

The main challenges related to the emergence of the DMFC technology are: to decrease the working temperature below 100 °C; to decrease the noble metal loading; and to develop membranes with higher thermal stability and a low or zero methanol crossover.[40]

3.3 Anode catalyst

H_2 oxidation occurs with a small overpotential at a Pt electrode. However, as discussed in section 3.2.1, the production of H_2 also involves traces of CO. As a consequence, CO poisoning of the Pt surfaces is likely to occur hence reducing the PEMFC performance.[44, 45] As a result, it was critical to improve the CO tolerance of the anode catalyst whilst increasing or maintaining the cell performance. Pt was alloyed with several transition metals[46, 47] to improve its tolerance towards CO poisoning. A Pt-Ru alloy catalyst has been found to exhibit the best CO tolerance as

well as a higher cell performance than Pt when the anode feed was contaminated by CO.[48]

The improvement exhibited by a Pt-Ru catalyst towards CO tolerance can be described by an intrinsic mechanism. The Pt-Ru alloy anode catalyst has to be considered not as one catalyst but as two separate catalysts, Pt and Ru, working closely together. The effect is based on the high mobility of CO molecules on Pt surfaces and the ability of Ru metal to form hydroxide/oxide species at low potential. As a consequence, a bifunctional mechanism can be presented to illustrate the enhancement. The process involves the oxidation of the CO adsorbed on the Pt site with the OH adsorbed species on the adjacent Ru (**Equation 1-15** to **Equation 1-17**).[49]

$$Pt + CO \rightarrow Pt\text{-}CO_{ads} \qquad \textbf{Equation 1-15}$$

$$Ru + H_2O \rightarrow Ru\text{-}OH_{ads} + H^+ + e^- \qquad \textbf{Equation 1-16}$$

$$Pt\text{-}CO_{ads} + Ru\text{-}OH_{ads} \rightarrow CO_2 + Pt + Ru + H^+ + e^- \qquad \textbf{Equation 1-17}$$

The bifunctional mechanism allows the CO oxidation to take place at 0.4 V vs. RHE[50], which is a tremendous improvement.

3.4 Proton exchange membrane

The membrane used in PEMFC has several roles. Firstly, it acts as an insulator, forcing the electrons to go through a load before reaching the cathode. Secondly, it allows the transport of protons from the anode to the cathode only. Finally, it prevents any mixing of gas feeds.

Nowadays, a solid polymer membrane such as Nafion® is used. Nafion® was developed in the 1960s by *DuPont* (Wilmington, Delaware, USA) [51] and consists of a polytetrafluoroethylene backbone with sulfonated side chains, as shown in **Figure 1- 3**.

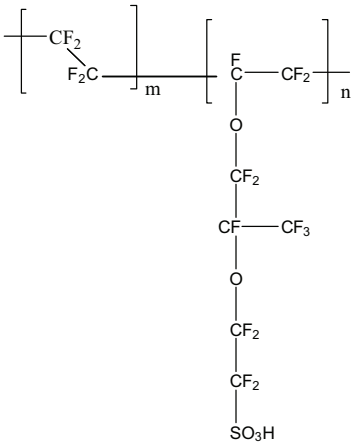

Figure 1- 3 Chemical structure of Nafion® (the ratio n to m determines the acidity of the membrane electrolyte)

The CF_2 groups give the membrane a strong stability in both the reducing and oxidising environment. In addition, the presence of fluorine atoms bonded to the same carbon as the SO_3H groups make the sulfonic acid a superacid, hence increasing its conductivity.[52]

The major drawback with the membrane resides with its hydration level. In other words, to be highly proton conductive, it has to be fully hydrated.[53] However, under the working temperature and high current density that fuel cells are subjected to, dehydration is a common phenomenon. At high current density (or at high gas flow rate), the proton migration drags the water molecule to the cathode side. Consequently, the anode dries out and the cathode floods leading to ohmic losses. To overcome the dehydration of the anode and flooding of the cathode, SiO_2 was introduced in the catalyst ink of the anode and air can be blown on the cathode side. The hydrophilic nature of SiO_2 allows the full hydration of the anode due to the back diffusion of water, whilst blowing air at the cathode prevents the cathode from flooding.[54] To maintain a suitable membrane hydration level of small FC stacks, the more common technique remains the humidification of the feeding gases.

3.5 Gas diffusion electrode (GDE)

The GDE is composed of a gas diffusion layer (GDL) onto which a catalyst layer is deposited. The GDL is usually a mixture of porous carbon and polytetrafluoroethylene (PTFE). Carbon is the material of choice because it acts as an electron conductor and a current collector. PTFE prevents the water from flooding the pores hence allowing the diffusion of the gases.

GDEs can be easily prepared. Firstly, the Pt or Pt-alloy supported on carbon catalyst is mixed with some Nafion® and water to form an ink. This ink is then applied onto the GDL until the desired loading of metal has been achieved. Several techniques can be used to disperse the ink onto the GDL such as spraying or manual painting. Eventually, the GDE is pressed onto the membrane in order to obtain a good three-point contact between the catalyst particles and the membrane via the ionomer.

3.6 Cathode

3.6.1 Cathode reactions

The reduction of O_2 can occur via 2 different routes: a simple 4 electron process or a 2 step reaction involving 2 electrons each (the hydrogen peroxide (H_2O_2) route).

The 4 electron process involves the direct electrochemical reduction of O_2 to water without creating any intermediate as shown by **Equation 1-18**.

$$O_{2\,(g)} + 4\,e^- + 4\,H^+_{(aq)} \rightarrow 2\,H_2O_{(l)} \qquad E^0 = 1.23 \text{ V vs. RHE} \qquad \textbf{Equation 1-18}$$

The hydrogen peroxide route, involves the formation of an intermediate (**Equation 1-19**), H_2O_2, which can further be electrochemically or non-electrochemically reduced to water as shown by **Equation 1-20** and **Equation 1-21**, respectively. If H_2O_2 were to be produced, it would cause an additional decrease in cell performance due to membrane and catalyst degradation as well as a decrease in cell voltage.

$$O_{2\,(g)} + 2\,e^- + 2\,H^+_{(aq)} \rightarrow H_2O_{2\,(l)} \qquad E^0 = 0.68 \text{ V vs. RHE} \qquad \textbf{Equation 1-19}$$

Followed by:

$$H_2O_{2\,(aq)} + 2\,e^- + 2\,H^+_{(aq)} \rightarrow 2\,H_2O_{(l)} \qquad E^0 = 1.78 \text{ V vs. RHE} \qquad \textbf{Equation 1-20}$$

$$\text{or} \qquad 2\,H_2O_{2\,(l)} \rightarrow 2\,H_2O_{(l)} + O_{2\,(g)} \qquad \textbf{Equation 1-21}$$

The four electron route is preferable for improved fuel cell efficiency because it has the highest electrode potential. It also does not involve the production of an intermediate species.

3.7 Cathode catalyst

The O_2 reduction process is limited by its slow kinetics which are 10^7 to 10^9 times slower than that of H_2 oxidation at the anode.[55] As a result, the development of more active catalysts than Pt became a priority in the development of PEMFC technology.

Pt was alloyed with several transition metals (e.g. iridium[56], iron[57], nickel[58]) and a significant improvement in catalytic activity towards the oxygen reduction reaction (ORR) was observed. The reasons associated with the increase in activity of Pt-alloys towards the ORR has been thoroughly discussed.

Alloying Pt with another metal result in different degree of overlap of their respective *d*-bands. A greater downshift of the Pt *d*-band centre will be observed if the overlap is high which will only occur if a high synergistic interaction exists between the two metals. The reduction in the Pt *d*-band centre will decrease the adsorption energy and adsorption strength of the oxygenated species. This will in turn enable a lower Pt-O coverage and faster Pt-O^- electro-reduction.[59]

For Pt-Alloys, it was concluded that the shorter the Pt-Pt bond distance, the higher the ORR activity because it is thought that the oxygen molecules adsorb by a dual site mode. As a result, being able to change/shorten the Pt-Pt bond distance would influence the adsorption property of oxygenated molecules on the Pt surface. [60-62]

Under PEMFC conditions, Pt-alloys exhibit a slower rate of decay than Pt/C hence retaining a higher active area than Pt/C over time. This results in Pt-alloys exhibiting a more stable cell performance over time. The main loss in active area for Pt/C is caused by the sintering of the Pt particles. This process involves the formation of larger Pt particles which inevitably decreases the Pt active area. However, the leaching out of the secondary metal in Pt-alloys remains the major issue related to the use of Pt-alloys in fuel cell. The dissolution of the secondary metal has nasty effects on the cell performance e.g. it lowers the conductivity of the membrane leading to higher membrane resistance, increases the resistance of the cathode catalyst layer due to higher ionomer resistance, lowers the diffusion of oxygen in the ionomer in the catalyst layer, and causes degradation of the membrane.[63]

Non Pt-catalysts such as ruthenium-based[64], palladium-cobalt[65], tungsten nitride[66] or Zirconium oxynitride[67] were developed in the last few years with the intention of lowering the cost of the catalyst whilst trying to improve the catalytic activity.

Despite the greater activity of Pt-alloys and the lower cost of non-Pt catalysts, Pt dispersed on carbon is still the preferred cathode catalyst for PEMFC.

4 Aims and objectives

This thesis involves the preparation and characterisation of various electrocatalysts with the aim to enhance their catalytic activity towards the oxygen reduction reaction. A surface organometallic chemistry technique will be used to modify the surface of both precursors, platinum on carbon (Pt/C) and nickel on carbon (Ni/C). This technique allows for the specific targeting of the reduced metal by the organometallic precursor hence ensuring the preparation of binary metal electrocatalysts.

Chapter 3 focuses on the preparation and characterisation of Pt/C catalysts surface modified with 2 nickel precursors, nickelocene and nickel (II) acetylacetonate. However a reduction of the Pt amount used to prepare active electrocatalysts is also a very important subject if FC are to replace the ICE. **Chapter 4** addresses this issue directly by dealing with the preparation of Ni/C catalysts surface modified with platinum acetylacetonate.

The electrocatalysts were characterised by Cyclic Voltammetry, Rotating Disk Electrode, Extended X-ray Absorption Fine Structure, X-ray Diffraction, X-ray Photoelectron Spectroscopy, Transmission Electron Microscopy, Energy Dispersive X-ray and Inductively Coupled Plasma - Optical Emission Spectroscopy. All these techniques are described in details in **Chapter 2**.

5 References

1. Kyoto Protocol for the United Nations Framework on Climate Change, in *Third Conference of the Parties*, Kyoto (Japan) (1997).
2. M. V. Twigg, *Catalysis Today*, **117**, 407 (2006).
3. J. C. Summers, S. VanHoutte and D. Psaras, *Applied Catalysis B-Environmental*, **10**, 139 (1996).
4. A. C. Lloyd, *Journal of Power Sources*, **86**, 57 (2000).
5. C. F. Schoenbein, *Philosophical Magazine*, **14**, 43 (1839).
6. W. R. Grove, *Philosophical Magazine*, **14**, 127 (1839).
7. W. R. Grove, *Philosophical Magazine*, **21**, 417 (1842).
8. L. Mond and C. Langer, *Proceedings - Royal Society*, **45**, 296 (1889).
9. W. Vielstich, A. Lamm and H. A. Gasteiger, *Handbook of Fuel Cells: Fundamentals, Technology and Applications. Volume 1, Chapter 12: History of Low Temperature Fuel Cells*, John Wiley & Sons ltd, New york (2003).
10. F. T. Bacon and J. S. Forrest, in *the 5th World Power Conference*, p. 5397, Vienna (Austria) (1956).
11. W. T. Grubb, *Journal of Physical Chemistry*, **63**, 55 (1959).
12. T. K. Johnson, *Proceedings of the 18th Annual Power Sources Conference*, 25 (1964).
13. J. H. Russell, in *Proceedings of the 19th Annual Power Sources Conference*, p. 35, Red Bank, NJ (1965).
14. C. C. Morrill, in *19th Annual Power Sources Conference*, p. 38, Red Bank, NJ (1965).
15. E. Antolini, *Journal of Applied Electrochemistry*, **34**, 563 (2004).
16. http://world.honda.com/FuelCell/FCX/ (Accessed on the 05th February 2009).
17. http://www.hydrogencarsnow.com/audi-a2h2-hydrogen-car.htm (Accessed on the 05th February 2009).
18. http://www.fuelcells.org/info/charts/h2fuelingstations.pdf (Accessed on the 23rd of September 2009).
19. A. A. Evers, *International Journal of Hydrogen Energy*, **28**, 725 (2003).
20. N. Sammes, R. Bove and K. Stahl, *Current Opinion in Solid State and Materials Science*, **8**, 372 (2004).

21. W. Vielstich, A. Lamm and H. A. Gasteiger, *Handbook of Fuel Cells: Fundamentals, Technology and Applications. Volume 1, Part 1: Thermodynamics and kinetics of fuel cell reactions.*, John Wiley & Sons ltd, New york (2003).
22. L. S. E. Moore, *Solid State Chemistry, An Introduction*, Chapman & Hall (1992).
23. M. C. Williams, *Fuel Cells*, **7**, 78 (2007).
24. E. Ivers-Tiffée, A. Weber and D. Herbstritt, *Journal of The European Ceramic Society*, **21**, 1805 (2001).
25. P. Tomczyk, *Journal of Power Sources*, **160**, 858 (2006).
26. L. Carrette, K. A. Friedrich and U. Stimming, *ChemPhysChem*, **1**, 162 (2000).
27. T. N. G.F. McLean, S. Prince-Richard, N. Djilali, *International Journal of Hydrogen Energy*, **27**, 507 (2002).
28. C. Huang and A. T-Raissi, *Journal of Power Sources*, **175**, 464 (2008).
29. M. G. Poirier and C. Sapundzhiev, *International Journal of Hydrogen Energy*, **22**, 429 (1997).
30. B. Lindstrom and L. J. Pettersson, *Journal of Power Sources*, **118**, 71 (2003).
31. R. M. Navarro, M. A. Pena and J. L. G. Fierro, *Chemical Reviews*, **107**, 3952 (2007).
32. M. Götz and H. Wendt, *Electrochimica Acta*, **43**, 3637 (1998).
33. C.-Y. Huang, Y.-Y. Chen, C.-C. Su and C.-F. Hsu, *Journal of Power Sources*, **174**, 294 (2007).
34. D. A. J. Rand and R. M. Dell, *Hydrogen Energy: Challenges and Prospects*, Royal Society Of Chemistry (2007).
35. R. V. Noorden, *Cracking water with sunlight,* http://www.rsc.org/chemistryworld/Issues/2008/April/CrackingWaterWithSunlight.asp (accessed on the 6th January 2009).
36. The Impact of Increased Use of Hydrogen on Petroleum Consumption and Carbon Dioxide Emissions (report number: SR-OIAF-CNEAF/2008-04), in, p. 53, Energy Information Administration (U.S. Department of Energy) (August 2008).
37. A. Zuttel, *Naturwissenschaften*, **91**, 157 (2004).
38. D. K. Ross, *Vacuum*, **80**, 1084 (2006).

39. U. Eberle, G. Arnold and R. von Helmolt, *Journal of Power Sources*, **154**, 456 (2006).
40. S. Wasmus and A. Kuver, *Journal of Electroanalytical Chemistry*, **461**, 14 (1999).
41. T. Iwasita, *Electrochimica Acta*, **47**, 3663 (2002).
42. F. Maillard, E. R. Savinova and U. Stimming, *Journal of Electroanalytical Chemistry*, **599**, 221 (2007).
43. T. Vidakovic, M. Christov and K. Sundmacher, *Electrochimica Acta*, **52**, 5606 (2007).
44. S. Jimenez, J. Soler, R. X. Valenzuela and L. Daza, *Journal of Power Sources*, **151**, 69 (2005).
45. G. J. K. Acres, J. C. Frost, G. A. Hards, R. J. Potter, T. R. Ralph, D. Thompsett, G. T. Burstein and G. J. Hutchings, *Catalysis Today*, **38**, 393 (1997).
46. T. F. Hiroshi Igarashi, Yimin Zhu, Hiroyuki Uchida and Masahiro Watanabe, *Physical Chemistry Chemical Physics* 306 (2001).
47. Y. Morimoto and E. B. Yeager, *Journal of Electroanalytical Chemistry*, **441**, 77 (1998).
48. J. H. Wee and K. Y. Lee, *Journal of Power Sources*, **157**, 128 (2006).
49. D. Chu and S. Gilman, *Journal of The Electrochemical Society*, **143**, 1685 (1996).
50. H. A. Gasteiger, N. Markovic, P. N. Ross and E. J. Cairns, *The Journal of Physical Chemistry*, **98**, 617 (1994).
51. S. Banerjee and D. E. Curtin, *Journal of Fluorine Chemistry*, **125**, 1211 (2004).
52. P. Costamagna and S. Srinivasan, *Journal of Power Sources*, **102**, 242 (2001).
53. P. P. Kundu and A. Pal, *Reviews in Chemical Engineering*, **22**, 125 (2006).
54. U. H. Jung, S. U. Jeong, K. T. Park, H. M. Lee, K. Chun, D. W. Choi and S. H. Kim, *Journal of Hydrogen Energy*, **32**, 4459 (2007).
55. M. P. Hogarth and T. R. Ralph, *Platinum Metals Review*, **46**, 146 (2002).
56. T. Ioroi and K. Yasuda, *Journal of The Electrochemical Society*, **152**, A1917 (2005).

57. H. I. Takako Toda, Hiroyuki Uchida, and Masahiro Watanabe, *Journal of The Electrochemical Society*, **146**, 3750 (1999).

58. V. R. Stamenkovic, B. Fowler, B. S. Mun, G. F. Wang, P. N. Ross, C. A. Lucas and N. M. Markovic, *Science*, **315**, 493 (2007).

59. L. Santos, C. H. F. Oliveira, I. R. Moraes and E. A. Ticianelli, *Journal of Electroanalytical Chemistry*, **596**, 141 (2006).

60. V. Jalan and E. J. Taylor, *Journal of The Electrochemical Society*, **130**, 2299 (1983).

61. M.-K. Min, J. Cho, K. Cho and H. Kim, *Electrochimica Acta*, **45**, 4211 (2000).

62. E. Antolini, J. R. C. Salgado, M. J. Giz and E. R. Gonzalez, *International Journal of Hydrogen Energy*, **30**, 1213 (2005).

63. E. Antolini, J. R. C. Salgado and E. R. Gonzalez, *Journal of Power Sources*, **160**, 957 (2006).

64. L. Liu, J.-W. Lee and B. N. Popov, *Journal of Power Sources*, **162**, 1099 (2006).

65. W. Wang, D. Zheng, C. Du, Z. Zou, X. Zhang, B. Xia, H. Yang and D. L. Akins, *Journal of Power Sources*, **167**, 243 (2007).

66. H. Zhong, H. Zhang, Y. Liang, J. Zhang, M. Wang and X. Wang, *Journal of Power Sources*, **164**, 572 (2007).

67. G. Liu, H. M. Zhang, M. R. Wang, H. X. Zhong and J. Chen, *Journal of Power Sources*, **172**, 503 (2007).

CHAPTER TWO: EXPERIMENTAL METHODS AND TECHNIQUES

Theoretical and practical aspects of the experimental work carried out in this project are presented in this chapter. This includes descriptions of the electrochemical studies (Cyclic Voltammetry and Rotating Disk Electrode) as well as the physical characterisation (X-ray diffraction, X-ray photoemission spectroscopy, Extended X-ray Absorption Fine Structure, Transmission Electron Microscopy and Energy Dispersive X-ray). The procedure of preparation of the electrocatalysts will be described in detail in **Chapters 3 and 4**.

1 Reagents and Materials

The materials and reagents used within this study, along with their suppliers, are detailed below in **Table 1**.

Table 1 List of the reagents & materials used and their suppliers

Reagent / Material	Supplier
Chloroform ($CHCl_3$)	Fisher scientific
Concentrated sulphuric acid 98% (H_2SO_4)	Fisher scientific
Toluene-low sulfur	Fisher scientific
Platinum(II) acetonylacetonate 97% ($Pt(acac)_2$)	Sigma-Aldrich
Nickelocene ($Ni(Cp)_2$)	Sigma-Aldrich
Nickel(II) acetonylacetonate 95% ($Ni(acac)_2$)	Sigma-Aldrich
19.6 wt% platinum supported on carbon (Pt/C)	Johnson Matthey
9.57 wt% Nickel supported on carbon (Ni/C)	Johnson Matthey
Nafion® 5wt% solution in alcohol	Sigma-Aldrich
4% H_2/N_2	BOC gases
Carbon monoxide 99.9 % (CO)	BOC gases
Hydrogen 99.995 % (H_2)	BOC gases
Nitrogen (Oxygen free) (N_2)	BOC gases
Oxygen (O_2)	BOC gases
Water purification system (18 MΩ-cm)	Pure1te SELECT FUSION

2 Electrochemical methods

Electrochemical techniques are essential methods in the study of fuel cell electrocatalysts. These techniques are employed to characterise the materials and to assess their catalytic activity. Firstly, the characterisation of the materials is performed by cyclic voltammetry experiments. This sensitive technique allows the determination of the electrochemical surface area and the determination of the adsorption processes. Secondly, the catalytic activity is assessed by rotating disk electrode (RDE) experiments. The polarisation curves give a measure of the activity of the electrocatalysts.

The different methodologies used as part of this project are presented within this section. The voltammetry of a polycrystalline Pt electrode is also described. In addition, the details of the electrochemical cells and procedures used for the electrochemical characterisation of the carbon-supported catalysts are discussed.

2.1 Cyclic voltammetry

Cyclic voltammetry is one of the potential sweep techniques widely used to determine the variety of mechanisms taking place at the electrode surface. In a cyclic voltammetry experiment, the potential is swept from an initial potential, E_1, to a final potential, E_2, and back to E_1, at a known sweep rate, ν (**Figure 2- 1 left**). The current is recorded as a function of potential (**Figure 2- 1 right**). The cathodic limit was set so that it corresponds to the H_2 evolution whereas the anodic limit was set to a potential lower than that of O_2 evolution.

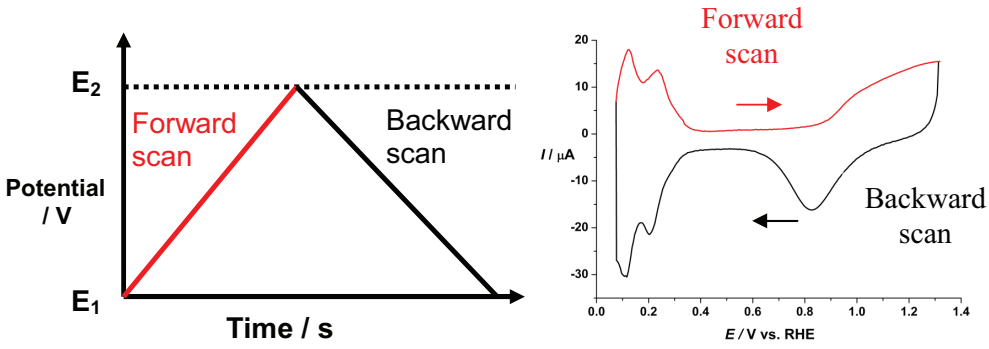

Figure 2- 1 **Applied potential (left) and current response (right) for a cyclic voltammogram of a Pt electrode (geometrical area = 0.196 cm^2) in 1 M H_2SO_4 at ν = 50 mV s^{-1}.**

One of the main uses of cyclic voltammetry for Pt-based catalysts is to evaluate the electrochemical surface area of the catalysts. This will be described in more detail in the following section.

2.1.1 Cyclic voltammogram of polycrystalline platinum

The cyclic voltammogram (CV) of platinum (Pt) electrode, shown in **Figure 2- 2**, exhibits characteristic features, which can be divided into 3 separate regions, a, b and c.

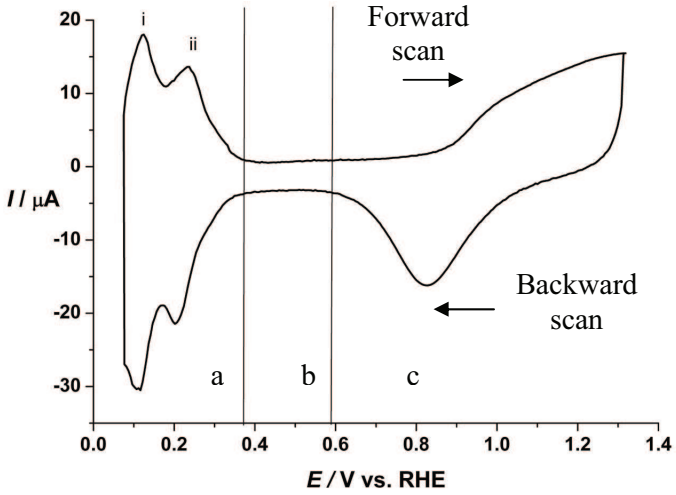

Figure 2- 2 Cyclic voltammogram of a Pt electrode (geometrical area = 0.196 cm^2) in 1 M H_2SO_4 at ν = 50 mV s^{-1}.

Region a is the hydrogen region. The peaks observed in the forward scan correspond to the desorption of hydrogen from the Pt surface.[1] The peaks observed on the reverse scan represent the adsorption of hydrogen onto the Pt surface (**Equation 2-1**).

$$Pt + H^+ + e^- \rightarrow Pt\text{-}H_{ads} \qquad \textbf{Equation 2-1}$$

The peak position is indicative of the strength with which the hydrogen atoms are adsorbed onto the surface. Peak i represents the hydrogen atoms bound to the Pt(100) crystal planes and a low overpotential is required to desorb the hydrogen atoms in the forward scan. Peaks ii represents the hydrogen atoms adsorbed on the Pt(111) crystal plane and a higher overpotential is required to desorb the hydrogen atoms in the forward scan. A third peak can also be observed between the Pt(100) and Pt(111) peaks and it is assigned to the Pt(110) planes. The hydrogen adsorption region can be used to determine the Pt surface area as they will adsorb onto Pt

surface until a full monolayer coverage is achieved. The Pt surface area is the ratio between the measured hydrogen adsorbed (H_{ads}) charge and the theoretical charge associated with hydrogen adsorption/desorption on a polycrystalline Pt surface (210 μC cm^{-2} Pt)[2] (**Equation 2-2**).

$$Pt_{area}\left(cm^2\right) = \frac{\text{Measured } H_{ads} \text{ charge } (\mu C)}{210\ \mu C\ cm^{-2}\ Pt} \qquad \textbf{Equation 2-2}$$

It is important not to use the hydrogen desorption peaks to calculate the Pt surface area for the carbon-supported catalysts as H_2 could be trapped in the catalyst pores and be re-oxidised in the following forward scan. The oxidation of H_2 occurs at similar potential to that of H_{des} and it is not possible to distinguish between the two. As a consequence, the integration of the H_{des} region would include both the H_{des} on polycrystalline Pt and the H_2 oxidation. As a result, the calculated Pt surface area would be higher than the real Pt surface area.

Region b is the double layer region. The double layer arises from the accumulation of charges at the interface between the working electrode and the electrolyte. The measured current (I_m) can be separated into 2 components, the Faradaic current (I_f) and the charging current (I_c) as described by **Equation 2-3**.

$$I_m = I_f + I_c \qquad \textbf{Equation 2-3}$$

The duration of I_c is typically few microseconds and therefore if a high scan rate were to be used, I_c would no longer be negligible. As a consequence, most potential sweep experiments were carried out at slow scan rate, typically 10 mV s^{-1}.

Region c is the oxide region[3, 4]. In the forward scan, the peak occurring at 0.85 V vs. RHE corresponds to the adsorption of oxide species onto the Pt surface (**Equation 2-4**).

$$Pt + H_2O \rightarrow Pt\text{-}O_{ads} + 2\ H^+ + 2\ e^- \qquad \textbf{Equation 2-4}$$

Once the Pt surface has been saturated with oxide, a *place-change mechanism* occurs where the oxygen adsorbed on the surface of Pt is flipped over and dermasorbed into the bulk (**Equation 2-5**).

$$Pt\text{-}Pt\text{-}O \rightarrow Pt\text{-}O\text{-}Pt \qquad \textbf{Equation 2-5}$$

The oxide layer then reforms on the Pt surface. On the reverse scan, the peak at *ca.* 0.8 V vs. RHE corresponds to the stripping of the oxide layer. The peak position

and area of this peak is dependent upon the length of time spent in the oxide region and the upper potential limit (**Figure 2- 3**).

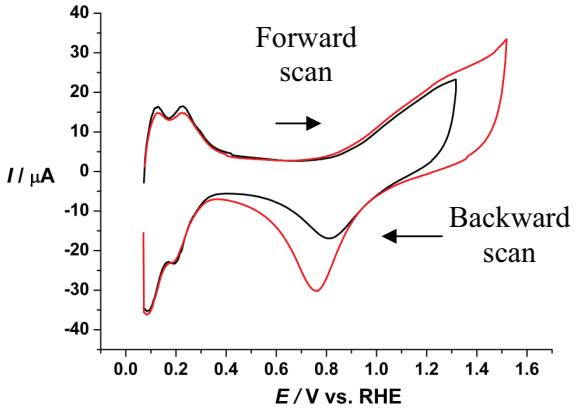

Figure 2- 3 Cyclic voltammogram of a Pt electrode (0.196 cm^2) in 1 M H_2SO_4 recorded with different upper limits at v = 50 mV s^{-1}.

2.1.2 CO stripping on polycrystalline Pt

CO has a strong affinity with Pt and changes its voltammetric response. This can be seen by the absence of the hydrogen desorption peak in the forward scan after CO adsorption has occurred (**Figure 2- 4**). This also draws attention to the problem with PEMFCs, where CO in the anode gas feed acts as a poison, hindering the oxidation of hydrogen. Once the CO has been removed, the normal Pt features can be observed (hydrogen absorption and oxide reduction peaks, shown in the red second cycle curve in **Figure 2- 4**).

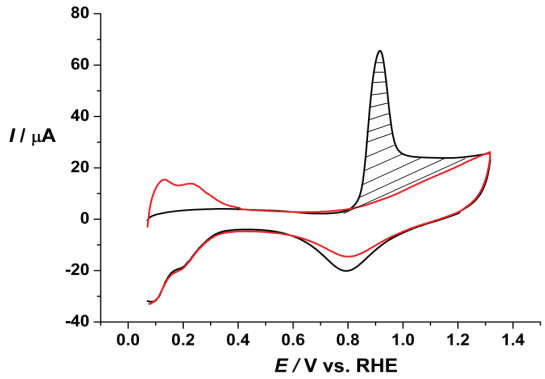

Figure 2- 4 Cyclic voltammogram of a Pt electrode (geometrical area = 0.196 cm^2) in 1 M H_2SO_4 at v = 50 mV s^{-1} showing CO stripping (black curve) and subsequent scan of electrode after CO stripping (red curve).

The peak occurring at 0.8 V vs. RHE is the oxidation of CO to carbon dioxide (CO_2). The mechanism of oxidation of CO on Pt sites has been extensively discussed [5, 6]. It is believed to proceed according to the *Langmuir-Hinshelwood* mechanism which involves two steps[6]:

$$Pt + H_2O \leftrightarrows Pt\text{-}OH_{ads} + H^+ + e^- \qquad \textbf{Equation 2-6}$$

$$Pt\text{-}OH_{ads} + Pt\text{-}CO_{ads} \rightarrow CO_2 + H^+ + e^- + 2\,Pt \qquad \textbf{Equation 2-7}$$

It is also assumed that CO adsorption is restrained to a monolayer coverage on Pt surface and that 1 CO molecule binds to 1 Pt atom. Therefore, the active Pt surface area can be determined using **Equation 2-8**.

$$Pt_{area}\left(cm^2\right) = \frac{\text{Measured CO charge } (\mu C)}{420\ \mu C\ cm^{-2}\ Pt} \qquad \textbf{Equation 2-8}$$

This can then be normalised to express the amount of Pt surface area present as a function of mass Pt present (**Equation 2-9**)

$$Pt_{area}\ (m^2_{Pt}\ g^{-1}_{Pt}) = \frac{Pt_{area}\left(m^2_{Pt}\right)}{\text{Pt loading } (g_{Pt}\ cm^{-2}) \text{ x Electrode area } (cm^2)} \qquad \textbf{Equation 2-9}$$

2.2 Half-cell studies

2.2.1 Preparation of painted electrodes

The required amount of catalyst (~ 60 mg) was dispersed in a small amount of purified water (millipore 18 mΩ.cm) (~ 0.5 ml). The required amount of 5 wt% Nafion® in alcohol suspension, to prepare a dry catalyst containing 15 wt% Nafion® solids was added to the solution. The resulting mixture was mixed using a Fisher PowerGen 125 homogeniser and subsequently painted onto a circular piece of carbon paper (TGHP 090) with an area of 5.31 cm^2. The carbon paper was painted, dried on a hot plate, and then weighed. This process was repeated until a total metal loading of *ca.* 0.20 mg cm^{-2} was obtained. The electrodes were hot pressed at 10 bar and 100 °C for 3 min. Electrodes of the appropriate size (1.32 cm^2) were cut out of the larger sheet and boiled in purified water to ensure a fully hydrated state.

2.2.2 Equipment and apparatus

A detailed drawing of the electrochemical cell used in these studies is shown below in **Figure 2- 5**.

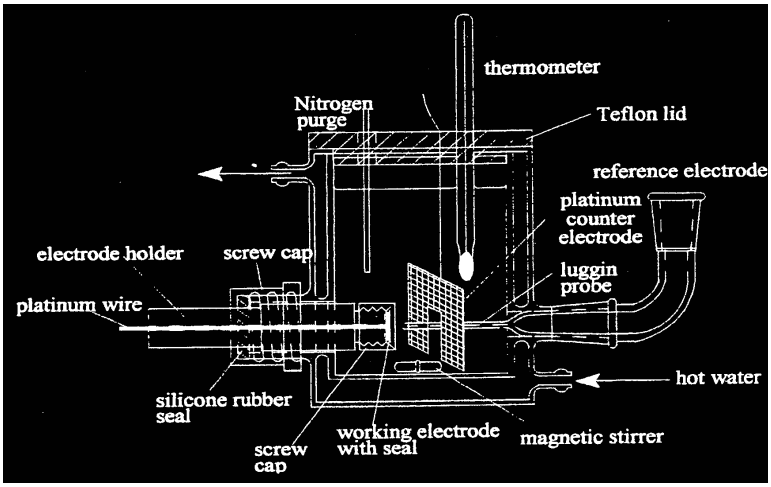

Figure 2- 5 Example of the three electrode electrochemical cell used to test fuel cell catalysts.[7]

The cell used is a 3 electrode electrochemical cell; all the electrodes are connected to an Autolab PGSTAT30 potentiostat. The painted electrode was held in position at the working electrode (WE) by a screw-on cap. A Pt wire was used as an electrical contact to the back of the WE. The WE holder was mounted in a glass cell with a capacity of 150 cm^3, which had an integrated water jacket for temperature control. A mercury mercurous sulphate (MMS), Hg / Hg_2SO_4, reference electrode (RE) was used and Pt gauze acted as the counter electrode (CE). The RE was calibrated prior to use by comparison to a dynamic hydrogen/Pt electrode in the same electrolyte used for the measurement (RHE). All potentials reported in this thesis are corrected to the RHE scale. A Luggin capillary was used with the MMS reference electrode to reduce potential errors due to solution resistance.

2.2.3 Procedures

2.2.3.1 Cyclic voltammetry

The cell was set-up as detailed in **section 2.2.2** and filled with 1 M H_2SO_4. The electrolyte was purged with $N_2(g)$ for 15 min whilst stirring the electrolyte to remove any dissolved oxygen. Stirring was then stopped and any trapped bubbles on the electrode surface were removed by slowly removing the purging tube close to the electrode. Cyclic voltammograms (CVs) were acquired between 0.00 V and

1.10 V vs. RHE with a scan rate of 10 mV s^{-1} whilst flowing N_2(g) over the surface of the electrolyte until reproducible CVs were collected.

2.3 Rotating disk electrode (RDE)

2.3.1 Principle

As the RDE rotates, it pulls the solution towards the disc and then expels it towards the sides as it approaches the electrode surface. The concentration of all species is equal to their bulk value throughout the whole of the solution except at the electrode surface. At the electrode surface a boundary layer exists in which the flux of species occurs via diffusion only. The rate of diffusion is dependent upon the rotation speed of the disk; this can be attributed to a decrease in the diffusion layer thickness as the rotation speed increases. The Levich equation (**Equation 2-10**) describes the relationship between the observed limiting current density (for an oxidation), I_L, and the rotation rate, ω, when the surface concentration of the electroactive species is equal to zero.

$$I_L = 0.201 \times n \times F \times D^{2/3} \times \upsilon^{-1/6} \times c^{\infty} \times \omega^{1/2} \qquad \textbf{Equation 2-10}$$

Where I_L is the limiting current density (A cm^{-2}), n is the number of electrons involved in the process, F is the Faraday constant (96485 C mol^{-1}) , D is the diffusion coefficient of the species (cm^2 s^{-1}), υ is the kinematic viscosity (cm^2 s^{-1}) , c^{∞} is the concentration of electroactive species in the bulk solution (mol cm^{-3}), ω is the angular rotation rate of the disc (*RPM*), and 0.201 is a constant, the value of this constant depends on the units of the other variables in the equation.

A plot of I_L against $\omega^{1/2}$ should therefore be linear and pass through the origin and is used to confirm that the RDE experiment is operating under good mass transport control.

The polarisation curves obtained from running RDE experiments can be divided into 3 regions, a, b and c as described in **Figure 2- 6**.

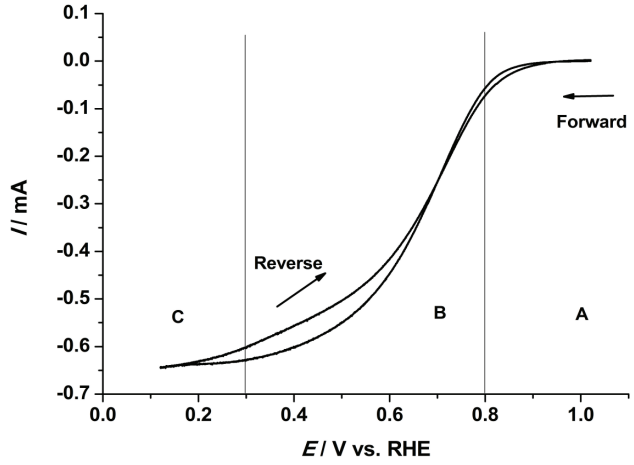

Figure 2- 6 Typical polarisation curves of 20 wt% Pt/C in O_2 saturated 1 M H_2SO_4. Scan rate of 2 mV s^{-1}, rotation rate: 2500 RPM.

Region A is *the kinetically controlled region*. The current is low and therefore indicates that there is only a little or no existing chemical change occurring. In this region, the mass transport conditions have a negligible effect on the surface concentration and the concentration of the species will be similar to that of their bulk value (greater than 95 % of the bulk value). The measured current is determined by the rate of electron transfer.

Region B is *the mixed region*. There is a mixed control of current by the mass transport and the electron transfer. In this region the concentration of the species at the surface of the electrode will fall in the range 5 % to 95 % of the bulk concentration of the species. Mass transport plays a major role in maintaining the concentration of the species constant throughout the cell up to the diffusion layer.

Region C is *the mass transport controlled region*. In this region, the kinetics of the reaction are fast but the mass transport of the species is the rate determining step. The surface concentration of the species will be 0. The measured current will be susceptible to any change in rotation rate

In the mixed region, the current at any potential is given by both the kinetic equation (**Equation 2-11**) and the Nernst diffusion layer model (**Equation 2-12**).

$$-I = n \times F \times \vec{k} \times c_0^{\sigma} \qquad \textbf{Equation 2-11}$$

$$-I = n \times F \times k_m \times (c_0^{\infty} - c_0^{\sigma}) \qquad \textbf{Equation 2-12}$$

Where where k_m is the mass transport coefficient, and c_o^{σ} is the concentration of the electroactive species at the electrode surface, $\vec{k}$ is the rate constant for the electron transfer reaction and c_O^{∞} is the concentration of electroactive species in the bulk solution.

Combining **Equation 2-11** and **Equation 2-12** gives:

$$-\frac{1}{I} = \frac{1}{nF\vec{k}c_O^{\infty}} + \frac{1}{nFk_m c_O^{\infty}} \qquad \textbf{Equation 2-13}$$

Equation 2-13 can be simplified to:

$$\frac{1}{I} = \frac{1}{I_k} + \frac{1}{I_L} \qquad \textbf{Equation 2-14}$$

Where I_L is the diffusion limited current density and I_k is the true kinetic current density [8]. Hence, the kinetic current can be separated out from any mass transport effects.

2.3.2 Electrode preparation

Prior to applying the catalyst suspension the glassy carbon electrode was polished to a 0.05 μm mirror finish alumina and sonicated in distilled water for 1 min to remove any particulates affixed to the disk. 10 mg catalyst and 10 ml chloroform was mixed using an ultrasonic bath for 20 min to form a suspension of well dispersed catalyst. A 5 μL aliquot of this suspension was deposited onto the surface of a glassy carbon rotating disk electrode (area = 0.196 cm^2) and allowed to dry in air. 5 μL of a solution of 5 wt% Nafion® in low weight alcohol (50 μL) and isopropyl alcohol (4950 μL) was subsequently deposited onto the catalyst layer and allowed to dry in air.

2.3.3 Equipment and apparatus

The RDE was attached to a PINE AFMSRX modulated speed rotator and mounted into the RDE cell (**Figure 2- 7**). As with the half-cell studies, all electrodes were connected to a Autolab PGSTAT12 potentiostat and a MMS and a Pt gauze were used as RE and CE, respectively.

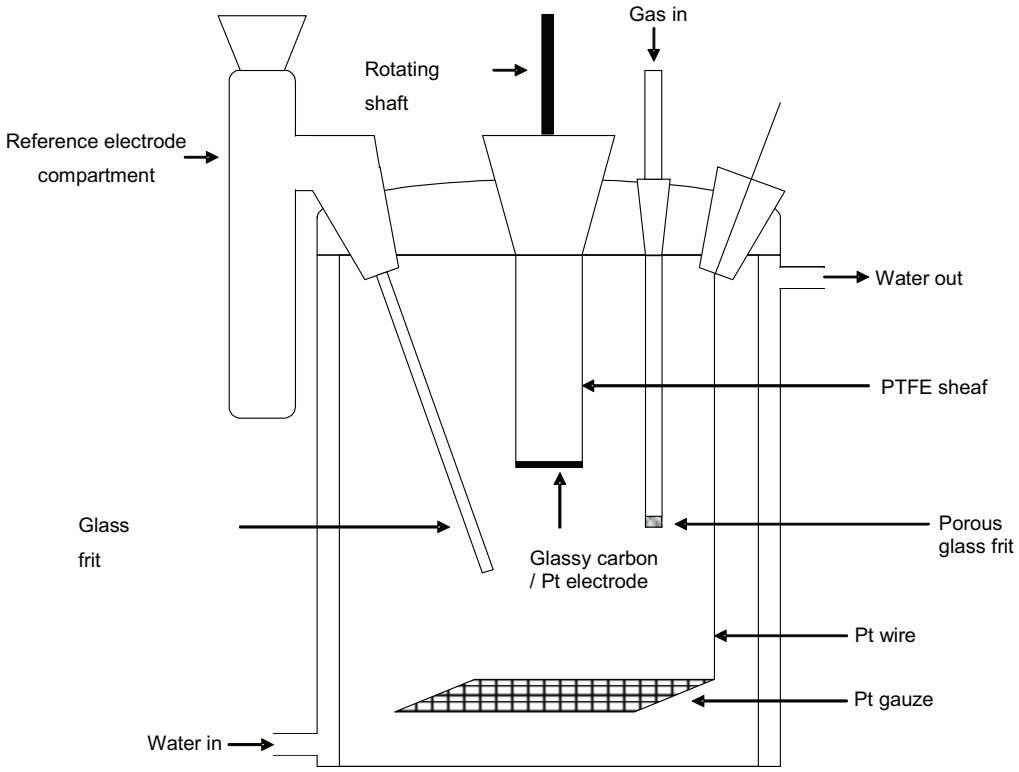

Figure 2- 7 Electrochemical cell for RDE measurements [9].

2.4 RDE experimental procedure

2.4.1 Cyclic voltammetry

The electrolyte was purged with $N_2(g)$ whilst rotating the electrode at 1000 RPM for 10 min. Prior to acquiring any CVs, any trapped bubbles on the electrode surface were removed by slowly removing the purging tube close to the electrode and the rotation rate of the electrode was set to 0 RPM. Cyclic voltammograms were acquired from 0.05 V and 1.10 V vs. RHE with a scan rate of 20 mV s^{-1} until reproducible CVs were collected.

2.4.2 CO stripping

After reproducible CVs were collected, a CO stripping experiment was performed to determine the active Pt surface area. The potential of the WE was held constant at 0.05 V vs. RHE for 30 min. For the first 15 min, CO(g) was purged through the solution whilst rotating the electrode at 1000 RPM. For the remaining 15 min, N_2(g) was purged through the solution whilst rotating the electrode at 1000 RPM. The N_2(g) purge ensures that any CO oxidation observed in the voltammetric response is from CO adsorbed on the Pt surface only. Prior to acquiring the CVs, any trapped bubbles on the electrode surface were removed by slowly removing the purging tube close to the electrode and the rotation rate of the electrode was set to 0 RPM. Cyclic voltammograms were acquired from 0.05 V and 1.10 V vs. RHE with a scan rate of 20 mV s^{-1}.

2.4.3 Oxygen reduction

Following the CO stripping experiment, the oxygen reduction experiment was carried out. The electrolyte was purged with O_2(g) for 15 min whilst rotating the electrode at 1000 RPM. Prior to acquiring any CVs, any trapped bubbles on the electrode surface were removed by slowly removing the purging tube close to the electrode. CVs were acquired between 1.10 V and 0.05 V vs. RHE with a scan rate of 10 mV s^{-1}, whilst flowing O_2(g) over the surface of the electrolyte using rotation rates of 900, 1600 and 2500 RPM. In between measurements, the electrolyte was purged with O_2(g) for 2 min whilst rotating the electrode at 1000 RPM.

3 XRD

XRD is a versatile, non-destructive and one of the most frequently applied techniques in catalyst characterisation. It can provide information regarding the identification of the bulk phase and the crystallites particle size. However, XRD analysis requires long-range order of material because it depends on the constructive interference of radiation that is scattered by the sample.

3.1 Theory of XRD

X-rays radiation was discovered in 1895 by a German physicist W.C. Röntgen.[10] X-rays have wavelengths on the order of a few angstroms making them a suitable radiation source to be used for diffraction of atoms of crystalline material.

Consider a long-range order material which has the simple structure composed of only one kind of atoms. These periodically arranged atoms are disposed in parallel rows regularly spaced by a value, *d* (*intermolecular spacing*). Now consider 2 incident coherent X-ray beams, beam α and β, respectively targeting at atom 1 and 2, at an angle *θ*. Under the influence of the beams, these atoms will act as scattering atoms. However, the distance (or *path length*) travelled by beam 2 is greater than that of beam 1. In fact, if centre of atom 1 is perpendicularly projected onto the path of beam 2, the extra path would be equal to the distance AB plus BC, with B being the centre of atom 2 (**Figure 2- 8**).

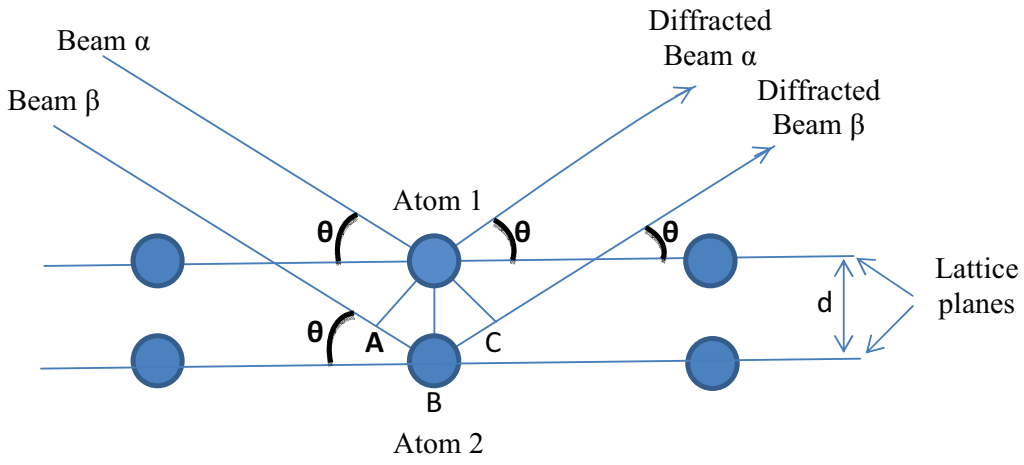

Figure 2- 8 Schematic diagram for determining Bragg's law.

Bragg discovered that if the *path length* was an integer of the wavelengths of the source used, maximum constructive interference occurred. Bragg derived a mathematical equation know as Bragg's law (**Equation 2-15**).

$$n\lambda = 2d\sin\theta \qquad \textbf{Equation 2-15}$$

where λ is the wavelength, θ is the diffraction angle, d_{hkl} is the spacing of the planes (hkl) and n is an integer.

Equation 2-15 shows that for a given λ, diffraction is only possible at certain angles determined by *d*. Carbon supported Pt or Ni catalysts are composed of crystallites that have random orientations. Therefore, every set of crystal planes in the correct orientation will give rise to a Bragg angle satisfying Bragg's law.

Assuming a fcc (*face centred cubic)* structure (because Pt and Ni exhibits fcc structure), the intermolecular spacing, d_{hkl}, and the lattice parameter, a, can then be determined using **Equation 2-16** and **Equation 2-17**.

$$d_{hkl} = \frac{a}{\sqrt{h^2 + k^2 + l^2}} \qquad \textbf{Equation 2-16}$$

$$\sin^2 \theta_{hkl} = \frac{\lambda^2}{4a^2}\left(h^2 + k^2 + l^2\right) \qquad \textbf{Equation 2-17}$$

where λ is the wavelength of the X-ray source, a is the lattice parameter, d_{hkl} is the intermolecular spacing, θ_{hkl} is the peak position and h,k,l are the Miller indices of the crystal plane.

3.2 Data analysis

Using an algorithm, each reflection peak was deconvoluted into peaks representing the different phases responsible for the observed XRD peak (**Figure 2- 9** and **Figure 2- 10)**. This deconvolution was performed by using the Rietveld analysis which is peak profile analysis tool. The peak deconvolution was obtained by least square fitting in which the algorithm calculates the difference between the calculated and the measured pattern (by varying peak shape and lattice constant) until a good agreement between the calculated and theoretical pattern is obtained. These deconvoluted peaks are Gaussian-like shape (**Figure 2-10**) and can therefore be used to calculate the lattice parameter and particle size using the Scherrer equation. However, in this work, the particle size was determined by TEM analysis. The composition of the phase can also be determined by the peak position of the deconvoluted peak as it has been tabulated.

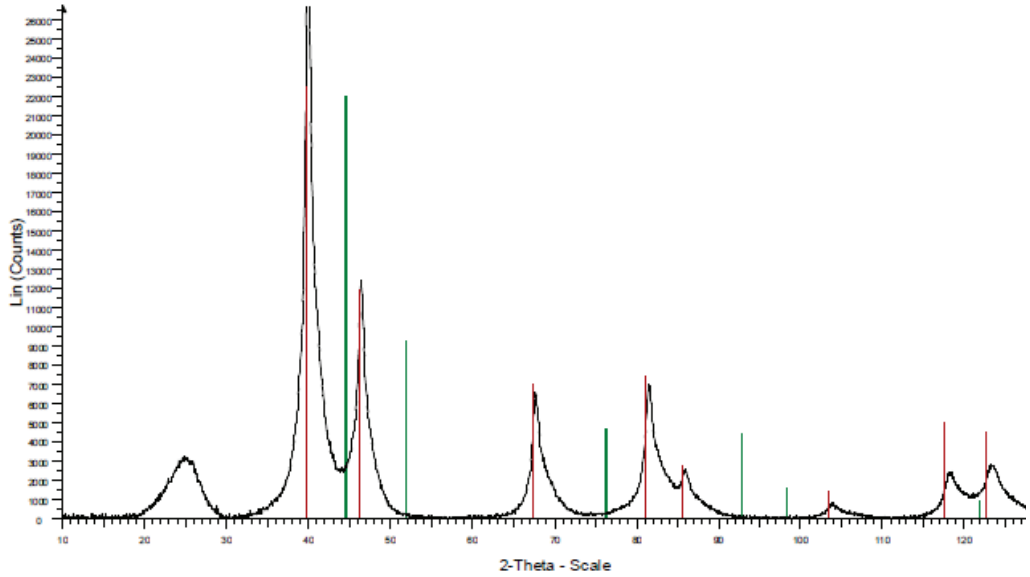

Figure 2- 9 Typical XRD pattern showing the reflection peaks for Pt fcc (red) and Ni fcc (green) (x-axis is 2 theta angle ranging from 10 to 113 º and they-axis is the lin counts ranging from 0 to 26000)

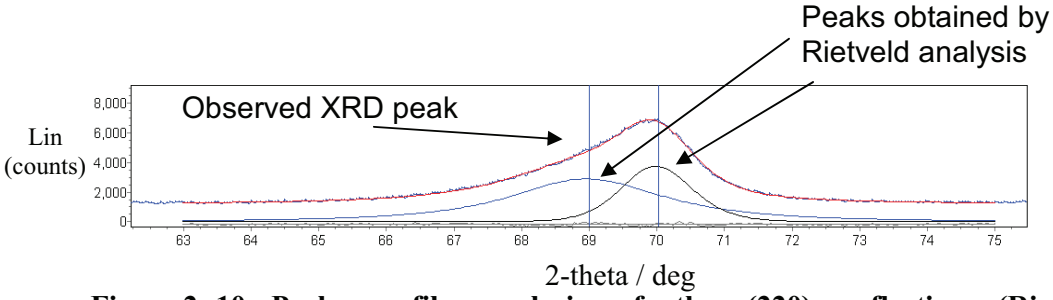

Figure 2- 10 Peak profile analysis of the (220) reflection (Rietveld deconvolution)

3.3 Experimental aspects of XRD

The X-ray diffractometer used to perform the analysis was a Bruker AXS D-500 with Cu K_α (Ni filtered) radiation source. It was operated at 0.25º 2θ per minute with a 0.02º step size. The tube voltage and current were 40kV and 30 mA, respectively.

All XRD data reported as part of this work were carried out by Hoi Johnson and James McNaught at the *Johnson Matthey Technology Centre*.

4 Transmission Electron Microscopy (TEM) and Energy Dispersive X-Ray Analysis (EDX)

TEM analysis was used to provide information regarding the particle size distribution. Its EDX function was used to support the effective preparation of a binary metal electrocatalyst.

4.1 TEM

4.1.1 Principle of TEM

Goodhew *et al.* [11] have described the principle of operation of TEM. Briefly, an image of the sample with a magnification of up to 10^6 times can be obtained by detection of electrons focused on and transmitted by the sample. The transmitted electrons hit a fluorescent screen and an image of the sample can be viewed. As the image is obtained from the transmitted electrons, the sample must be very thin. Then, a camera is used to capture shots of the area under study. The TEM microscope operates under very high vacuum.

4.1.2 TEM data analysis

For the 1 ML Ni/Pt/C prepared via the $Ni(acac)_2$ route, one of the snapshots captured for each TEM experiment was used to determine the particle size distribution as shown by **Figure 2- 11a**. the particle distribution was determined by randomly selecting about 250 particles (**Figure 2- 11b**). Following this, a histogram representing the number of counts versus particle size is obtained and the average particle size and its associated standard deviation are given (**Figure 2-** 12).

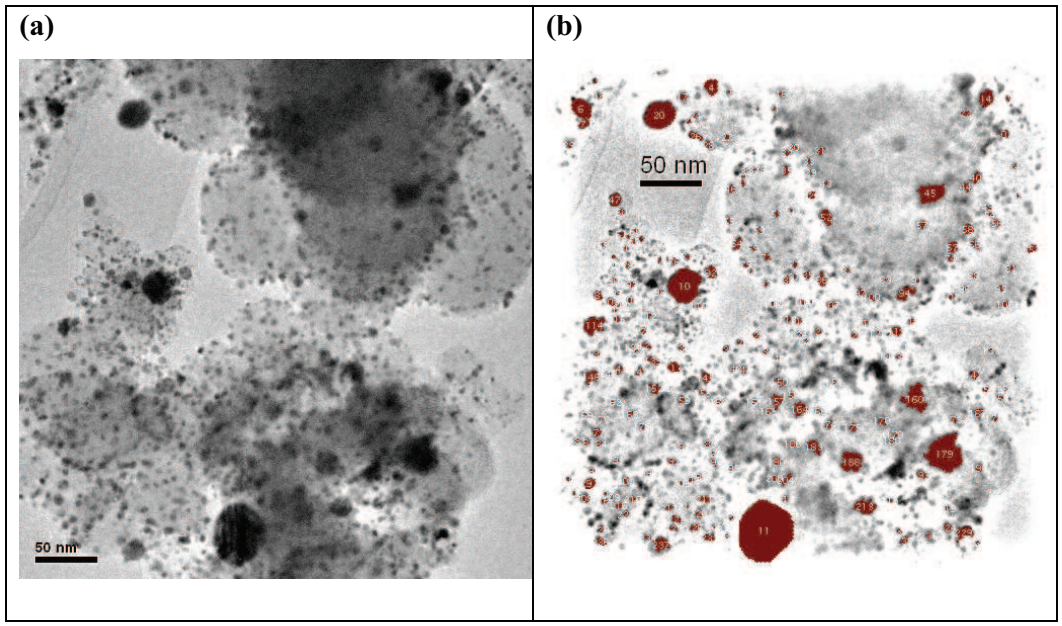

Figure 2- 11 Typical TEM micrograph used to calculate particle size (a) and the randomly chosen particle used to calculate the particle size distribution (b).

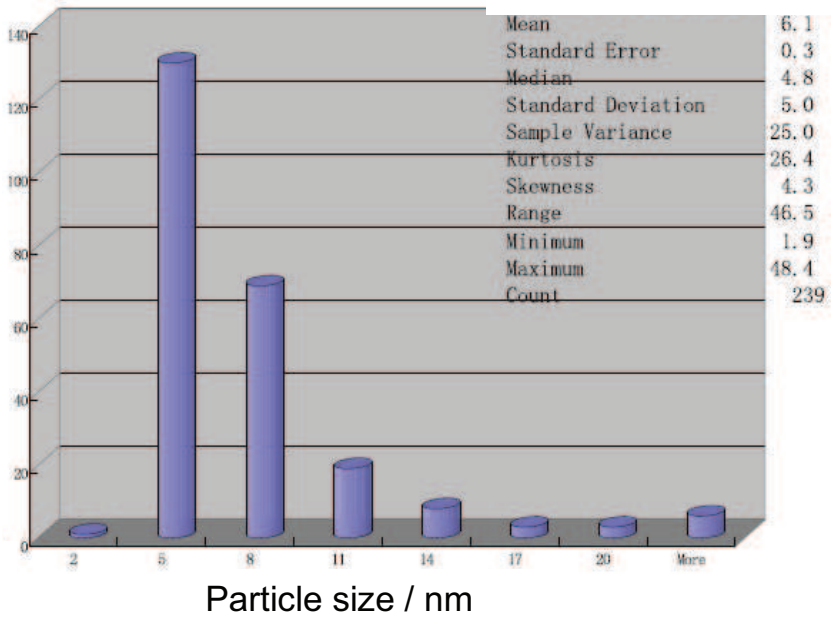

Figure 2- 12 Typical particle size distribution

For the other catalysts, again, the average particle size was determined from a sample of 45 particles randomly chosen and the average particle size and its associated error was determined manually.

4.2 EDX

4.2.1 Principle of EDX

EDX can be coupled to TEM to determine the identity of the materials present and their respective proportion. The basic principle of operation is that when a material is bombarded with high energy electrons, it results in X-rays characteristic of the material being emitted. These emitted X-rays are detected by the detector. The detector consists of small pieces of Si or Ge, held in a position so that most of the X-rays emitted from the specimen falls upon it. Since X-rays are not deflected, the detector must be in line of sight with the specimen. The emitted X-rays excite electrons in the conduction band of Si leaving an identical number of positively charged holes in the outer electron shells. The number of electron-hole pairs generated is proportional to the energy of the X-ray photon being detected and can therefore be used to determined the atomic species present.[11]

4.2.2 EDX data analysis

A typical set of EDX data is shown in **Figure 13**. EDX data was collected by narrowing the size of the beam and focusing on different areas of the catalysts. The picture in the top left corner represents the area under investigation. The bright white spots represent the catalyst particles whilst the grey area represents the carbon support. The line running across the particles represents the line along which the EDX analysis was performed. An example of the EDX response is given in the bottom left corner. This EDX response was collected on the area of the particle denoted by a red square. The number of counts for Pt and Ni was plotted against the distance covered by the EDX spot and the resulting graph is given in the bottom right corner. The graph, plotted in the top right corner, represents the total number of count as a function of distance covered by the EDX spot.

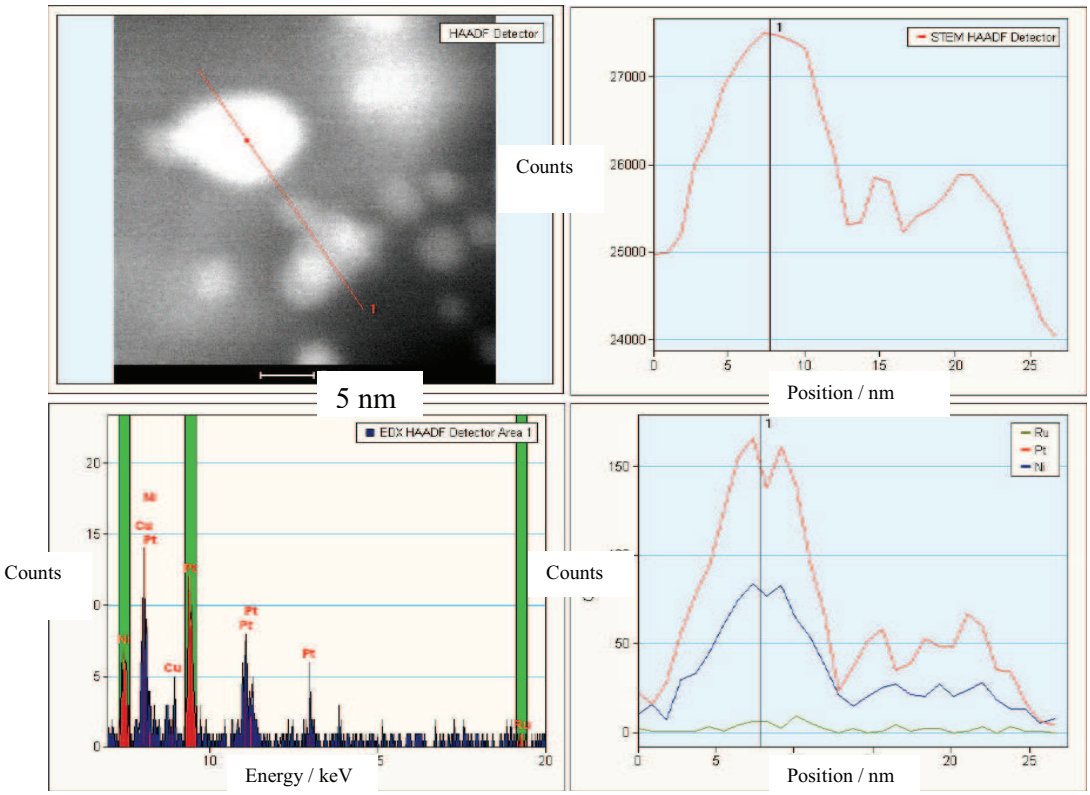

Figure 2- 13 Typical TEM EDX line profile analysis. (a) shows the TEM image of the area under investigation (scale is 5 nm), (b) shows the EDX response for the red box in the TEM image, (c) shows the total number of counts from both Pt and Ni across the red line labelled 1 and (d) shows the EDX responses across the red line labelled 1, in descending order show total counts, counts from Pt (red), Ni (blue) and Ru (green).

4.3 Experimental of TEM and EDX

The 1 ML Ni/Pt/C powders prepared via the $Ni(acac)_2$ route were crushed and dusted on a holey carbon films as TEM specimen. Subsequently, they were examined using a Tecnai F20 Transmission Electron Microscope using the following instrumental conditions:

- Voltage : 200 kV
- C2 aperture (m): 30 & 50
- Mode: Bright Field (BF), High resolution electron microscopy (HREM) and high angle annular dark field (HAADF) method.

This work was carried out at the *Johnson Matthey Technology Centre* by Jingshan Dong and D. Ozkaya.

For all other catalysts, a solution of 1 mg of catalyst in 3 ml of chloroform was sonicated for 1 h prior to depositing 2 μl onto the TEM copper grid. The grid was allowed to dry at air and was analysed using a Hitachi H 7000 Transmission Electron Microscope with a voltage of 70 kV. This work was conducted at the Biomedical Imaging Unit at Southampton General Hospital by myself.

5 X-ray Absorption Spectroscopy

X-ray Absorption Spectroscopy (XAS) is a powerful technique to obtain structural information on the atomic scale. The main advantages of XAS over the other techniques are that (a) no long range order of material is needed (e.g. as opposed to XRD) and (b) the environmental requirements for the sample are not as strict as when using other analytical methods (e.g. use of high vacuum for TEM). The XAS spectrum can be divided into two parts, the X-ray Absorption Near Edge Structure (XANES) and Extended X-ray Absorption Fine Structure (EXAFS) both of which provide information on the structural properties of the electrocatalysts.

5.1 Theory of XAS

5.1.1 General principles

When X-rays photons pass through a material, a reduction in the incident intensity (I_o) of the X-rays is observed. For a path length dx of the radiation through the material, the loss dI is given as follow (**Equation 2-18**):

$$dI = -\mu I.dx \qquad \textbf{Equation 2-18}$$

where μ is the linear absorption coefficient which is a function of the energy of the photons. μ is proportional to the probability for absorption of a photon according to the Fermi's Golden Rule as given by **Equation 2-19.**[12]

$$\mu(E) = \frac{8\pi\ e^2\omega^3 n}{hc^3}.\left|\left\langle \Psi_f \left| \hat{e}.r \right| \Psi_i \right\rangle\right|^2.\delta\left(E_f - E_i - h\upsilon\right) \qquad \textbf{Equation 2-19}$$

where ψ_i and ψ_f are the initial and final wave functions, respectively, $\hat{e}$ represents the electric field polarisation vector of the photon and r is the coordinate vector of the photon.

Integrating **Equation 2-19** over the whole thickness of the sample leads to the Beer-Lambert law (**Equation 2-20**)

$$I_t = I_0 e^{-\mu x} \qquad \textbf{Equation 2-20}$$

where I_t is the transmitted intensity, I_0 is the incident intensity, μ is the linear absorption coefficient and x is the thickness of the material.

The absorption of the X-rays by the material will decrease as the energy increases until a specific energy. At this energy, a sudden rise in absorption will occur. This discontinuity is called the absorption edge and it refers to a core–electron being excited to a valence state or to the continuum.[13] The ejected electron possesses an energy (E_k) which is defined by **Equation 2-21**.

$$E_k = h\upsilon - E_{binding} \qquad \textbf{Equation 2-21}$$

where E_k is the kinetic energy of the ejected electron, $h\upsilon$ is the energy of the incident X-rays and $E_{binding}$ is the binding energy.

A further increase in energy causes the absorption to drop again but at a different rate until another absorption edge is reached. The overall process is termed the photoelectric effect.

The absorption edges are labelled in order of increasing energy K, L_I, L_{II}, L_{III} etc., according to the principle quantum number of the orbital from which the core electron was ejected. For example, K, L_I, L_{II}, L_{III} correspond to the excitation of an electron from the $1s(^2S_{1/2})$, $2s(^2S_{1/2})$, $2p(^2P_{1/2})$, $2p(^2P_{3/2})$ orbitals respectively (**Figure 2-14**).

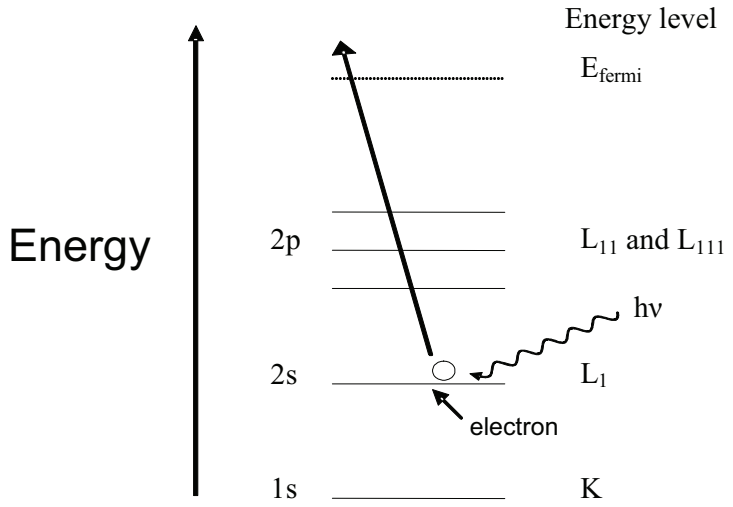

Figure 2- 14 Schematic diagram of the photoelectric effect - excitation of a 2s electron giving rise to the L_I edge

The outgoing electron can be viewed as a spherical wave vector, *k*, related to the photon energy. This is shown by **Equation 2-22** where E_o is the zero point energy, usually taken as the inflection point of the absorption edge or the maximum of the first derivative, and m_e is the mass of the electron.

$$k = \sqrt{\left(\frac{8\pi^2 m_e}{h^2}\right)\left(h\nu - E_0\right)} \qquad \textbf{Equation 2-22}$$

The outgoing photoelectron wave is scattered from the neighbouring atoms producing a backscattered wave which then interferes either constructively or destructively with the outgoing wave (**Figure 2- 15**). The interference between these two wave functions results in the oscillatory behaviour of the absorption observed above the absorption edge.

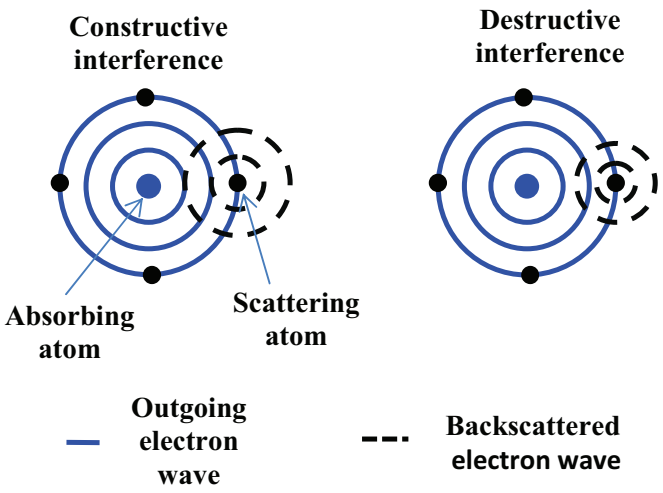

Figure 2- 15 Schematic of the interference patterns in the final state wave-functions (The rings represent the maxima of the forward scattered and back scattered waves).

The absorption coefficient above the absorption edge is defined as follow:

$$\mu_{tot} = \mu_0 \cdot (1 + \chi) \qquad \textbf{Equation 2-23}$$

where μ_o is the background absorption of a single atom as a result of elastic and inelastic scattering. χ refers to the EXAFS which can be extracted from the experimental data using the following equation, where the oscillatory behaviour is given as a function of the wavevector, *k*.

$$\chi(k) = \frac{\mu_{tot}(k) - \mu_0(k)}{\mu_0(k)} \qquad \textbf{Equation 2-24}$$

with $\mu_{tot}(k)$ is the total absorption and $\mu_0(k)$ is the background absorption.

A typical XAS spectrum is shown in **Figure 2- 16** and is generally divided into three regions: the pre-edge, X-ray Absorption Near Edge Structure (XANES) and EXAFS.

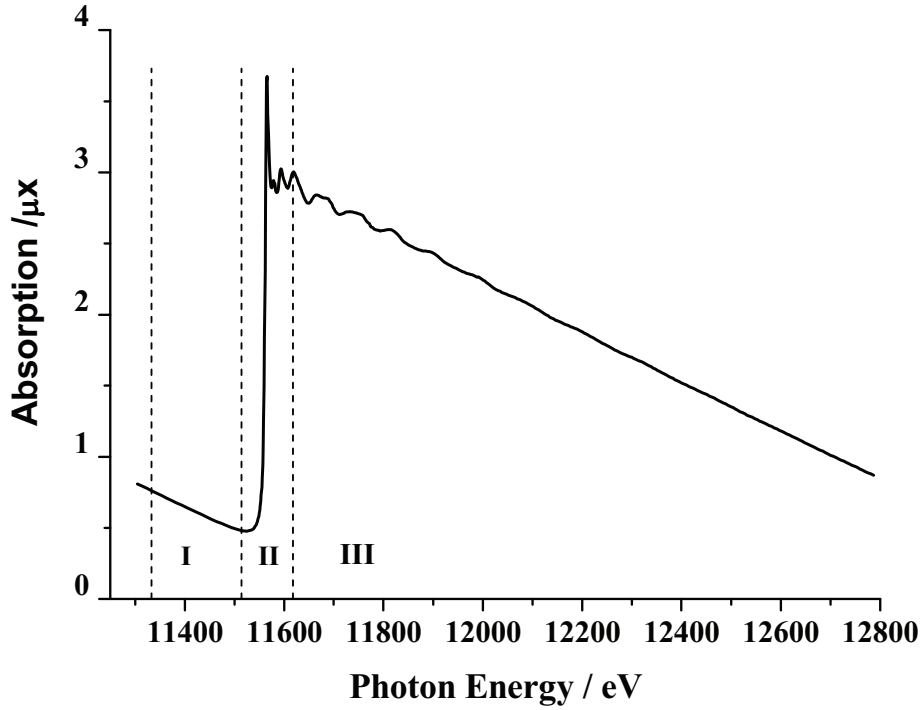

Figure 2- 16 XAS spectrum of a Pt foil at the Pt L_{III} edge showing: I – pre-edge region, II - edge and XANES region, III – EXAFS region.

The first part, known as the pre-edge region, is where the energy of the incident X-rays is not sufficient enough to excite the electron of the studied element.

The second region includes the absorption edge and the XANES which extends up to about 40 eV after the edge. The absorption edge occurs at an energy which is specific to the element being studied. The absorption edge can also be used to determine the electron occupancy of metal in alloys[14] and therefore enables the determination of any change in electronic configuration of the metal due to the alloying process. The edge position also provides the oxidation state of the absorber. The features observed in the XANES region arise due to electron transitions from the core level to higher unfilled or partially filled orbitals. However, multiple scattering and multi-photon absorptions render the analysis of the XANES region more difficult than the EXAFS region.

The third section is the EXAFS. In this region, the ejected photoelectrons have high kinetic energy and single scattering by the nearest neighbour dominates. This region may extend up to 1000 eV.

5.1.2 EXAFS equation

The structural content of the EXAFS was only recognised in the early 70s after a study by Sayers *et al*[15] involving quantitative determination of crystalline and amorphous germanium was published. This work is still used as a standard for the current analyses. The EXAFS function (**Equation 2-25**), $\chi(k)$, is a sum of sine waves produced from the outgoing photoelectron wavefunction and the backscattered wavefunction from each coordination shell, *j*.

$$\chi(k) = \sum_{j=1}^{shells} A_j(k) \sin \delta_j(k) \qquad \textbf{Equation 2-25}$$

The formula contains an amplitude term, A_j, which can be described as follows:

$$A_j(k) = \frac{N_j}{kR_j^2} S_i^2 F_j(k) e^{-2k^2\sigma_j^2} e^{\frac{-2R_j}{\lambda(k)}} \qquad \textbf{Equation 2-26}$$

where N_j is the number of atoms of type *j* at distance R_j from the absorber atom.

S_i is the amplitude reduction factor reflecting multi-electron effects and central atom shake-up and shake-off due to relaxation processes after photo-ionisation.

F_j is the backscattering amplitude from the *j*th atom and can be extracted from reference compounds or calculated theoretically.[16, 17]

$e^{-2k^2\sigma_j^2}$ is the Debye-Waller term. This factor accounts for thermal vibration and static disorder which cause movement of the atoms from their equilibrium positions. It is an exponential term and, therefore, reduces the amplitude of χ at high *k* regions more than at low *k* values.

$e^{\frac{-2R_j}{\lambda(k)}}$ accounts for inelastic losses in the scattering process by the neighbouring environment. The decay arises from the mean free path, λ or finite lifetime of the photoelectron and is responsible for the relatively short photoelectron range (few tens of Å) in a material analysed by EXAFS.

The second part of the term (**Equation 2-27**) is a sine function that reflects the dependence of the oscillatory structure on interatomic distances and energy.

$$\sin\delta(k) = \sin\left(2kR_j + \varphi_{ij}(k)\right) \qquad \textbf{Equation 2-27}$$

The sine function consists of the interatomic distance R_j between the absorber atom and the scatterer as well as a phase factor $\varphi_{ij}(k)$ which can be expressed as follows:

$$\varphi_{ij}(k) = 2\varphi_{absorber}(k) + \varphi_{backscatter}(k) \qquad \textbf{Equation 2-28}$$

The larger contribution from the absorber arises because the photoelectron sees the potential created by this atom twice. The phase factor must be extracted from reference compounds or calculated theoretically as in the case of F_j.

These equations were derived from the plane wave theory.

5.1.3 Data analysis

The extraction of the EXAFS and corresponding fitting to obtain the structural parameters were performed using 5 software packages: EXCALIB, ATHENA, XMULT, EXBROOK and EXCURV98.

The EXCALIB and ATHENA programs were used to read the raw data and to add the recorded scans together to improve the signal to noise ratio. EXCALIB and ATHENA also allowed the data to be deglitched or truncated accordingly.

The EXBROOK and XMULT programs were used to perform the energy identification along with the pre-edge and post edge background subtraction (normalisation) providing the EXAFS data in the form of a chi plot. The first step involved the pre-edge substraction and the identification of the edge position, E_0. To proceed with the background substraction, two quadratics are used; one is fitted to the pre-edge slope and the other to the post-edge slope. This was then substracted from the whole spectrum (**Figure 2-17 a**). Next, the data were also normalised giving an edge step of one, placing the measured spectrum on a per absorber atom basis (**Figure 2-17 b**).

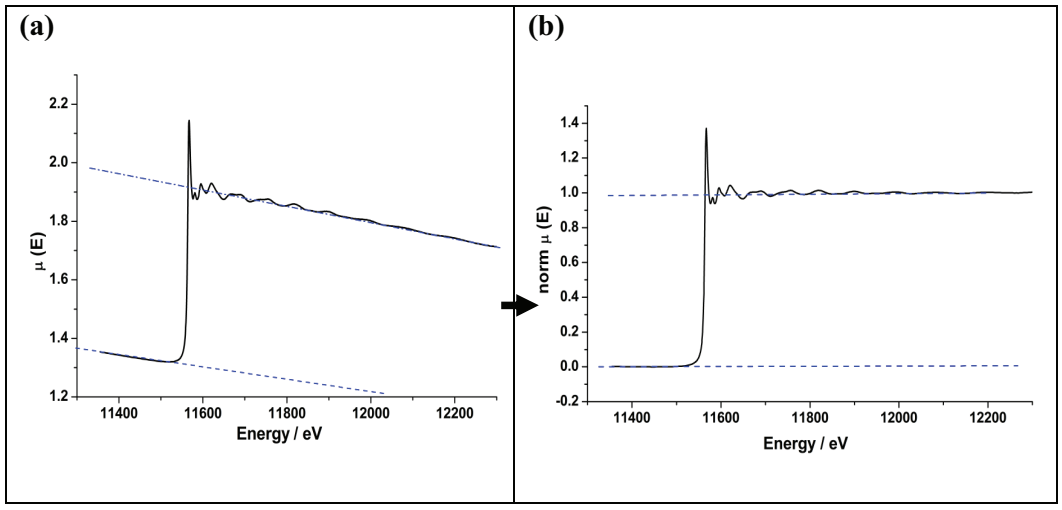

Figure 2- 17 Raw XAS data (a) before and (b) after pre-edge background subtraction and normalisation

The energy range was then rescaled so that the inflection point at the edge was set equal to 0 eV. The position of the inflection point (or edge position) was determined by the peak position of the maximum in the first derivative (**Figure 2- 18**)

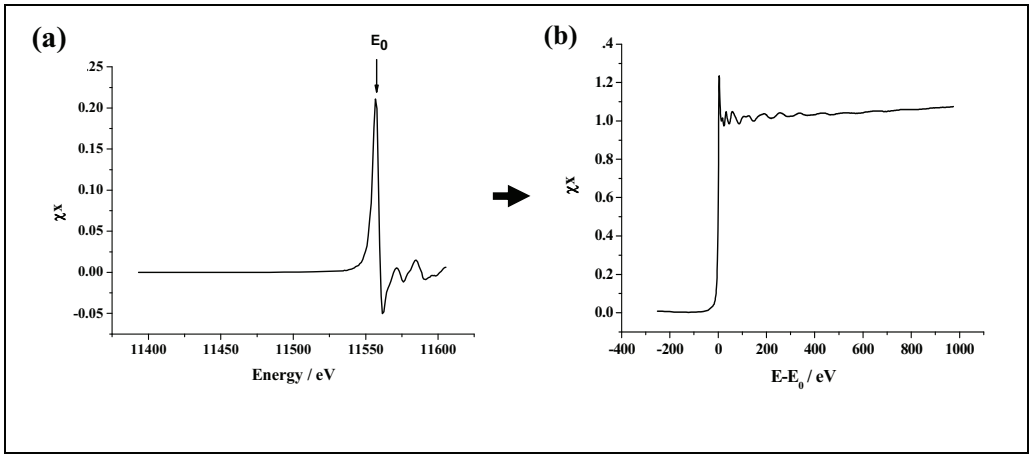

Figure 2- 18 (a) E_0 identification using the first derivative and (b) the rescaled XAS spectrum

The last stage consisted of post edge background subtraction and extraction of the chi data of the EXAFS. The post-edge background was removed using a cubic spline smoothing algorithm. To ensure no loss of information, the spline was not allowed to follow the EXAFS oscillations, but chosen so as to pass through the centre of the oscillations without oscillating itself. A smoothing factor, *SM* (**Equation 2-29**), was entered to adjust the spline function of the background, *BCK*, while the weight factor, *WE*, can be used to enhance the high *k* part of the spectrum.

$$\sum_{i=1}^{NPTS} \frac{(\mu_i - BCK_i)^2}{e^{-WEk_i^2}} \leq SM \qquad \textbf{Equation 2-29}$$

The aim was to reduce the low-frequency oscillations that distort low R (Å) information in the Fourier Transform (FT). The *SM* value was adjusted and the effects were monitored by observing the $\chi(\underline{k})$, derivative of $\chi(\underline{k})$ and the FT plots. The objective was to obtain chi data where the amplitude was evenly distributed above and below the axis (**Figure 2- 19)** and where the first peak of the FT was maximised whilst minimising the contributions below 1 Å.

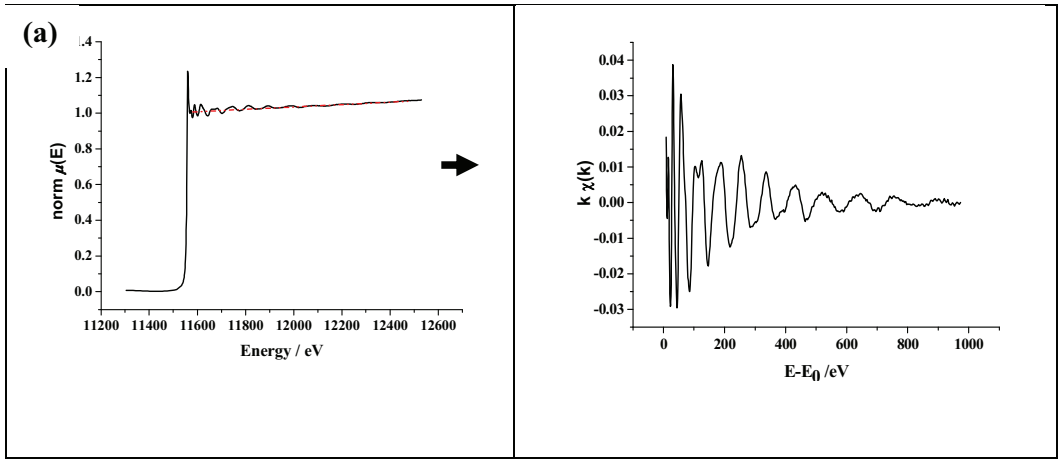

Figure 2- 19 (a) Selection of cubic spline for post-edge background removal (b) and the resulting chi plot (y-axis in Å^{-1}).

The EXAFS data were then read into the EXCURV98 program which was used to fit the data and extract the structural parameters. The EXCURV98 program simulates EXAFS spectra using rapid curved wave theory[18] and Rehr Albers theory[19-21] from the parameters of the radial shells of atoms surrounding the central atom. When the data is read into EXCURV98, the energy range is converted from *E* (eV) into *k*-space (Å^{-1}) (**Equation 2-30)**. This results in the levelling out of the amplitude across the width of the spectrum. The resulting chi plot along with the FT are then displayed (**Figure 2-20)**.

$$k = \left(\frac{2m_e}{\hbar} \left(E_{hv} - E_0 \right) \right)^{1/2} \qquad \textbf{Equation 2-30}$$

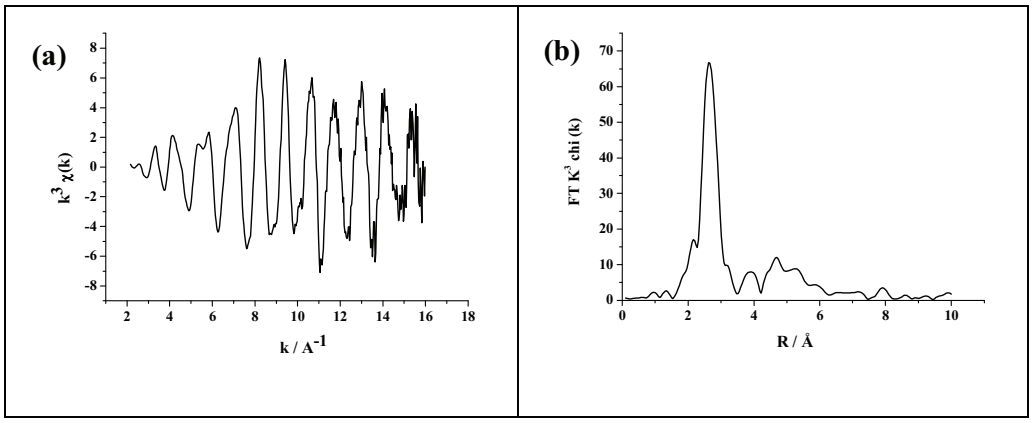

Figure 2- 20 (a) Chi data (b) and its corresponding Fourier transform (y-axis of (a) in Å^{-3})..

The EXCURV98 program produces a theoretical EXAFS spectrum by using probable values for coordination number (*N*), distance to the nearest neighbour (*R*), the Debye-Waller term ($2\sigma^2$) and the shift in Fermi energy (E_f). These values are then refined using a least-squares minimum of the fit index. The goodness of the fit is represented by the R_{EXAFS} value (**Equation 2-31**).

$$R_{EXAFS} = \sum_i^N \frac{1}{\sigma_i}\left(\left|\chi_i^{\exp}(k) - \chi_i^{fit}(k)\right|\right)\times 100\% \qquad \textbf{Equation 2-31}$$

where *N* is the number of data points, σ_i the standard deviation for each data point, *i*, and $\chi_i^{exp}(k)$ and $\chi_i^{th}(k)$, the experimental and theoretical EXAFS, respectively. A R_{EXAFS} value between 20 – 30 % is considered to be a reasonable fit, although if the data were noisy, a larger R_{EXAFS} would be acceptable. Errors in the parameters are estimated from their standard deviations. The number of statistically justified free parameters, *n*, that may be fitted should also be taken into account when fitting the data. This is estimated using the Nyqvist theorem (**Equation 2-32**):

$$n = \frac{2\Delta k \Delta r}{\pi} + 1 \qquad \textbf{Equation 2-32}$$

where Δk and Δr are the ranges in *k*- and *r*-space over which there is useful data.

There is a variation in the amplitude of the EXAFS oscillations with respect to *k*, with the amplitude being less at high *k* space. The EXAFS function can be multiplied by k^i, where i = 1, 2, or 3. This allows the emphasis of the chi plot to be tilted in favour of high or low *Z* (where Z is the atomic number) neighbours. A

weighting of 1 is used for low *Z* neighbours, 3 for high *Z* neighbours, and 2 being used as a compromise between low and high *Z* neighbours.

5.2 Experimental aspect of XAS

5.2.1 Synchrotron

Two synchrotrons were used in this study, the National Synchrotron Light Source (NSLS), Brookhaven, USA and the Swiss Light Source (SLS), Villegen, Switzerland. Synchrotron radiation is emitted by charged particles (travelling close to the speed of light) contained within a storage ring defined by bending magnets. The advantages of using synchrotron radiation are its high intensity, wide energy range, high collimation and plane polarisation.[17]

Synchrotron radiation requires high-energy electrons which are produced in a similar fashion at both synchrotrons. The main components of a synchrotron are the LINAC (Linear Accelerator), the Booster Ring and the Storage Ring.

The LINAC pre-accelerates electrons from an electron source to an intermediate energy. Pulses of these electrons are then injected into the Booster Ring where they are further accelerated by the application of radio frequencies. The acceleration causes the electrons to increase their energy to their final value (2.4 GeV for the SLS and 2.8 GeV for the NSLS). The beam is contained within the Booster ring by a series of dipole bending magnets. Finally, electrons from the Booster ring are injected into the Storage ring. In the Storage ring, these high-energy electrons are kept in a curved path by bending magnet. When the electrons are bent, they lose speed and this loss of speed is accompanied by a loss of energy, this is the so-called "synchrotron radiation". The electromagnetic radiation is produced tangentially from the storage ring and directed onto a beamline. This loss in energy is compensated on a regular basis either by injected fresh electrons once per day (NSLS) or by top-up injection (SLS). The top-up injection means that electrons are periodically injected into the storage ring to keep the intensity of the circulating beam constant. The Storage Ring must be kept under ultra-high vacuum to guarantee a long lifetime of the circulating beam, ensuring small beam loss.

5.2.2 Experimental station X11B

Work carried out at the NSLS was on station X11B which is sourced by a bending magnet. Station X11B has channel-cut sinearm-driven double-crystal monochromator containing Si(111) crystals and can measure an energy range of 4.5-22 keV. The NSLS operates with a ring energy of 2.8 GeV and a maximum current of 300 mA.

The experiments on X11B were conducted by Steve Price, Andrea Russell and myself.

5.2.3 Experimental station at X10DA

Work carried out at the SLS was on station X10DA which is sourced by a bending magnet. Station X10DA has a double crystal monochromator containing Si(111) and Si(311) crystals allowing measurement between 4.5 and 35 keV. The SLS operates at a ring energy of 2.4 GeV and a current of 400 mA.

The experiments on X10DA were conducted by Peter Wells, Anna Wise, Béatrice Tessier, and myself.

5.2.4 XAS transmission experiments

The simplest acquisition mode for XAS is the transmission mode (the other being fluorescence mode but it is not described herein as it was not used in this work). A transmission experiment measure the change in absorption of X-rays as the energy of the incident beam is increased. A basic set-up is shown in **Figure 2-21**.

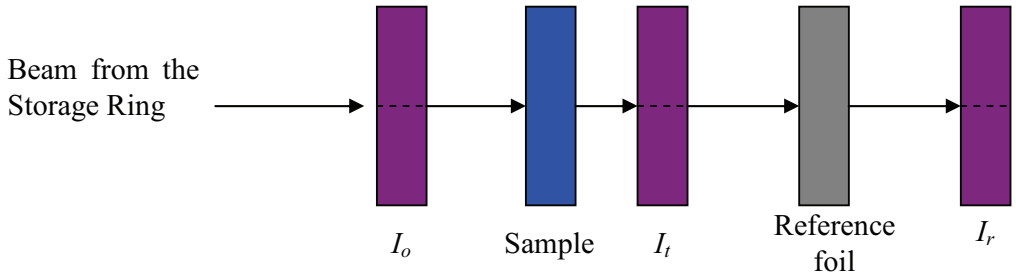

Figure 2- 21 Set-up of an experiment in transmission mode where I_o, It and Ir are the currents detected in the ion chamber for the incident, the transmitted and the reference beams, respectively.

The role of the ion chambers is to measure the intensity of the X-rays beam before it passes through the sample (I_o), after it passed through the sample (I_t) and after it passes through the foil (I_r). Each ion chambers is filled with a mixture of gases set to

absorb a specific amount of the X-ray flux. I_o is set to absorb around 20% of the flux whilst I_t and I_r are set to absorb 80% of the flux. The ion chambers contain two metal plates, with a constant potential applied between them, so that ions are attracted to the negative side and the electrons to the positive. The size of the resultant current that flows is therefore directly related to the number of photons entering the chamber. The absorption of the X-rays by the sample is given by $\ln(I_o/I_t)$.

Transmission experiments are typically used for concentrated samples. If the sample is too dilute, the resulting absorption of X-rays will be low, resulting in a poor signal to noise ratio. However, if the prepared sample contains too much of the element under study then all the X-rays will be absorbed. It is also very important to consider all the elements present in the sample, their relative proportions, and their absorption coefficients as they will affect the absorption edge. The ideal absorption edge (μx) of the probed element is within a value of 0.3 to 1, with the total absorption of the sample being below 2.5. This gives rise to errors in the determination of coordination numbers from EXAFS spectra. The mass of sample needed to obtain the desired edge step can be calculated using the equation below (**Equation 2-33**)

$$mass = \frac{(\mu x)(area)}{(\mu/\rho)} \qquad \textbf{Equation 2-33}$$

where (μ/ρ) is the mass absorption coefficient of the element of interest, with ρ being the density. Values for mass absorption coefficient have been calculated by McMaster *et al.*[22] and have been used in this study to calculate the absorbance of the samples used.

Transmission is the desired mode of data acquisition due to its simplicity and high signal to noise ratio. However, the samples must be homogeneous as any pinholes would result in the leaking of the X-rays which would result in noise.

5.2.5 Gas treatment cell

For the XAS experiments, the electrocatalysts to be studied were prepared as boron nitride pellets. The pellets were prepared by grinding a set amount of catalyst and boron nitride to form a homogenous mixture. The resulting mixture was then compacting in a pellet holder using a purpose built press. Boron nitride was used because it allows gas to flow through the pellet and because it has a low absorbance at the Pt L_3 edge. The pellet holder was mounted onto the removable arm of the gas cell treatment cell (**Figure 2- 22**).

The gas cell consists of a gas inlet and a gas outlet taps so that gases can be purged through the cell. The purged gas can be contained in the cell by closing the inlet and outlet taps. The cell is made of steel with Kapton windows for the entry and exit of the X-ray beam. The angle of the removable cell arm can be orientated for fluorescence or transmission experiments.

To collect EXAFS spectra in hydrogen, the cell was purged with hydrogen for 30 minutes before closing the gas taps. At the end of an experiment the cell was purged with $N_2(g)$ for 5 min before opening to air.

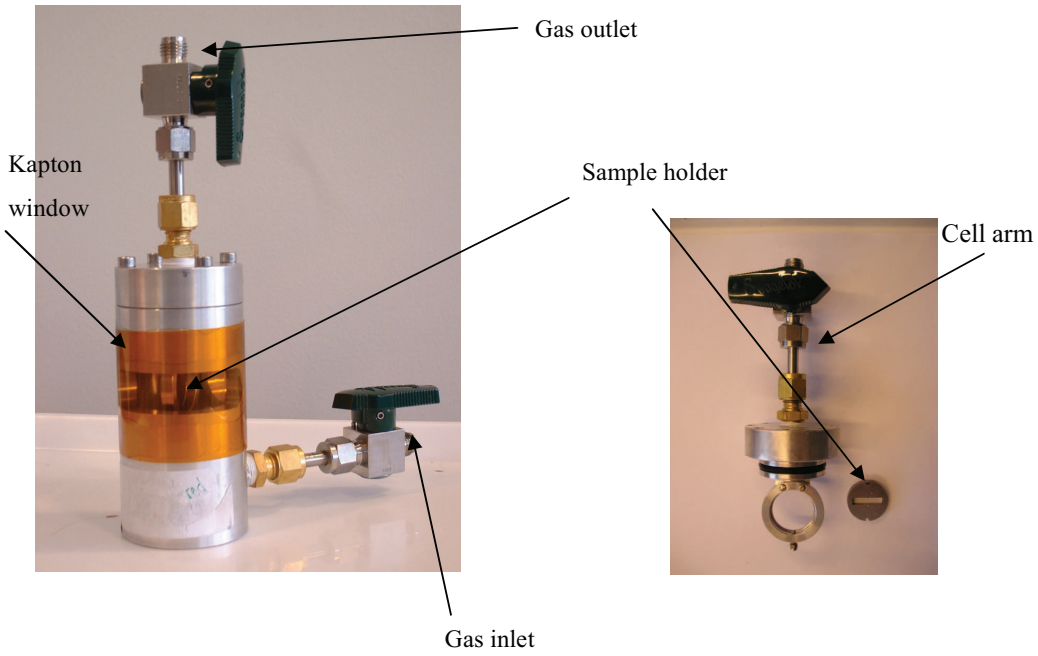

Figure 2- 22 Gas treatment cell, highlighting gas inlet and outlet, Kapton windows, and the sample holder.

6 X-ray photoelectron spectroscopy

6.1 Principle of XPS

X-ray photoelectron spectroscopy (XPS) was first discovered in 1887 by Heinrich Rudolf Hertz. However, he could not fully understand what was happening as the electron had yet to be discovered. It was only in 1899 when J. J. Thompson discovered the electron, that real breakthroughs in explaining this phenomena took place.[23]

XPS is based on the photoelectric effect. An X-ray (of energy *hv*) is absorbed by a sample which causes a core or valence electron to be ejected with a kinetic energy, E_k, if the photon has an energy greater than the and a binding energy, E_b, as shown in **Figure 2- 23.** E_k and E_b are related according to **Equation 2-34.**

$$E_k = h\upsilon - E_b - \varphi_{spectrometer} \qquad \textbf{Equation 2-34}$$

Where E_k is the kinetic energy of the photoelectron, E_b is the binding energy of the photoelectron with respect to the Fermi level of the sample, h is Planck's constant, υ is the frequency of the exciting radiation and $\varphi_{spectrometer}$ is the work function of the spectrometer.

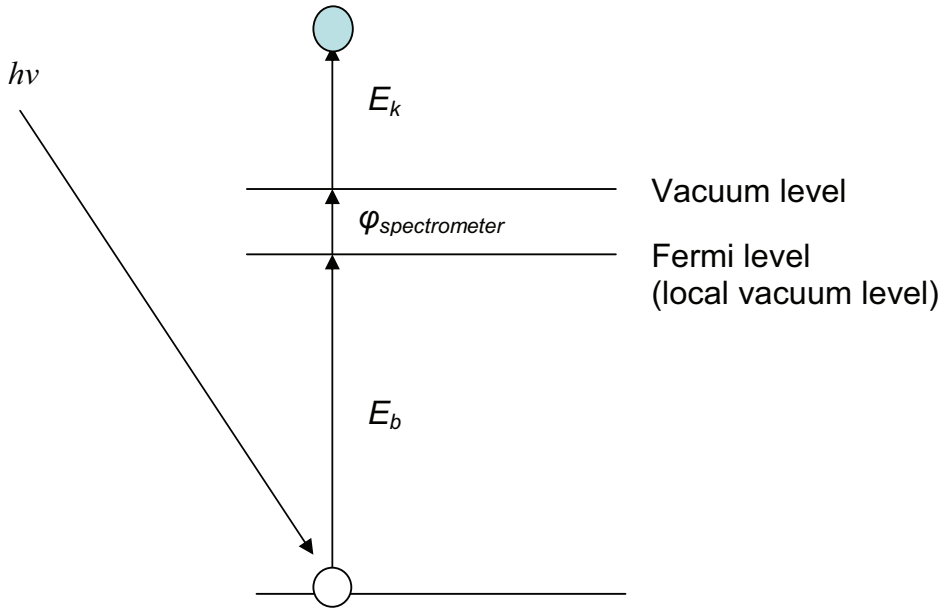

Figure 2- 23 Schematic of the photoemission process

$\varphi_{spectrometer}$ has to be included in **Equation 2-34** and **Figure 2- 23** because even though the sample and the XPS spectrometer are in electrical contact which causes their Fermi levels to line-up, they still possess different work functions. To remove an electron from the Fermi level of the sample costs an amount of energy equal to the work function of the sample (E_b). This causes the electron to be just outside the sample (local vacuum level). However, the electron has not yet reached the analyser of the spectrometer (or vacuum level). This will cost another amount of energy to the photoelectron which is known as the work function of the spectrometer.

Typically, the intensity of the photoelectron vs. binding energy is plotted (**Figure 2- 24**).[24] The intensity of the peaks is given by **Equation 2-35**.

$$I = F_x S(E_k)\sigma(E_k)\int_0^\infty n(z)e^{(-z/\lambda(E_k)\cos\theta)}dz \qquad \textbf{Equation 2-35}$$

Where I is the intensity of the XPS peak, F_x is the X-ray flux on the sample, $S(E_k)$ is the spectrometer efficiency for detecting the electron at kinetic energy (E_k), $\sigma(E_k)$ is the cross section for photoemission, $n(z)$ is the concentration (number of atoms per unit volume, z is the depth below the surface. $\lambda(E_k, z)$ is the mean free path of the photoelectron at E_k through the material present at depth z and θ is the take off angle (angle between the direction in which the photoelectron is emitted and the normal of the surface). $\sigma(E_k)$ has been calculated and tabulated by Scotfield.[25] The mean free paths, $\lambda(E_k, z)$, are approximated from a general formula.[26, 27]

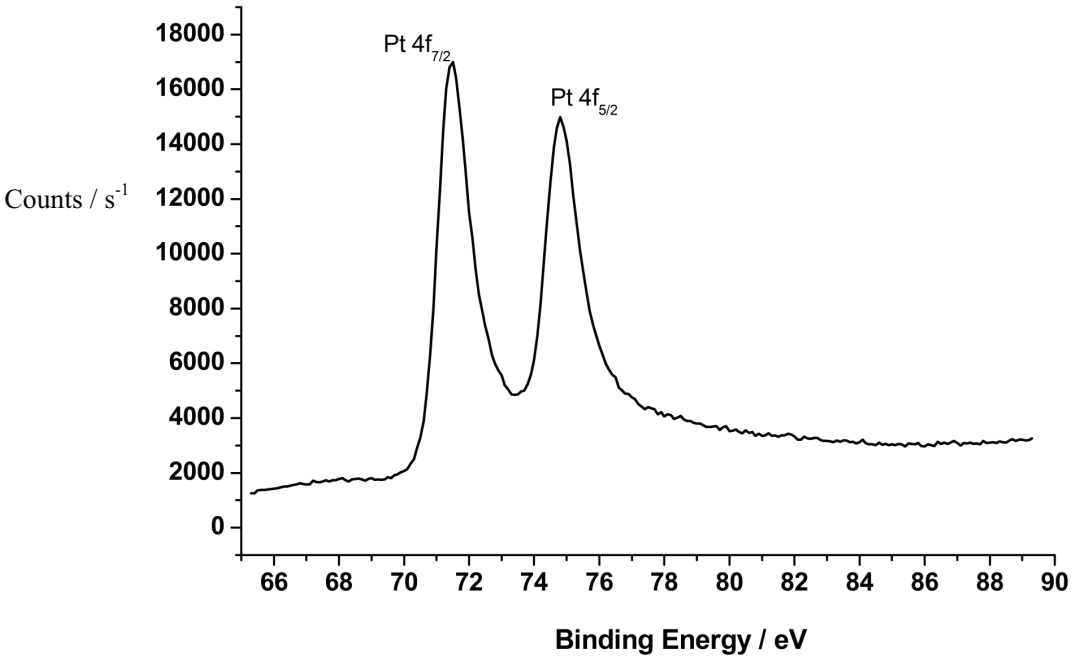

Figure 2- 24 Typical XPS of Pt(4f) core level region

Photoelectron peaks are usually labelled according to the quantum number (n) of the energy level from which they originate. An electron with an orbital momentum, l, and a spin momentum, s, will have a total momentum, j. (**Equation 2-36**)

$$j = l + s \qquad \textbf{Equation 2-36}$$

Split-orbit splitting occurs at $l>1$ because $s = \pm ½$. This causes the peaks to split into two according to both total momenta. (e.g. peaks for Pt 4f are Pt $4f_{7/2}$ and Pt $4f_{5//2}$) The intensity ratio of the peaks of spit orbit doublet is determined by the multiplicity of the level, and is equal to $2j + 1$. (e.g. for the Pt 4f peaks the intensity ratio would be 8:6)

XPS can be used to determine the chemical state of the elements present in the sample.[24] Also, the photoelectrons in XPS analysis have an energy within 0.2-1.5 keV. As a consequence, the mean free path of the electron ranges from 1-6 nm[24] making XPS technique a surface sensitive technique which can be used to analyse the composition of the samples.

6.2 Experimental aspect of XPS

The exciting radiation used in the studies was for that of a monochromatised aluminium K_α radiation in a 650 μm spot at 200 W power. Charge compensation was activated, provided by an in-lens flood gun at a 2 eV setting and the 401 argon ion flood source at a "zero energy" setting. Sensitivity factors from Scofield[25] were used in quantification. The energy scales were corrected such that the carbon 1*s* signals were set to 284.6 eV.

To calculate the atomic percentage (At%) of each element, the following procedure was followed. A boundary line which separates each peak from the background was defined. The area of this “new” peak is related to the number of photoelectrons detected by the XPS machine which is a function of the amount of the element present in the sample, the sensitivity of the band to photo-ionisation at the photon energy used (1487 eV) and the sampling volume (which varies with the kinetic energy of the photoelectron). The area of the peak is corrected to the sensitivity factor and the sampling volume and is then normalised to 100 %. The fraction of each contribution is the At% recorded in this work. The At% values have a small relevance by themselves. However, the ratio between elements of interest is a more useful information.

Spectra were collected and analysed by Richard A.P. Smithand and Sarennah J P Longworth at the *Johnson Matthey technology centre*.

7 REFERENCES

1. F. G. Will, *Journal of The Electrochemical Society*, **112**, 451 (1965).
2. S. B. Brummer and M. J. Turner, *The Journal of Physical Chemistry*, **71**, 2825 (1967).
3. J. P. Hoare., *Journal of The Electrochemical Society*, **132**, 301 (1985).
4. B. E. Conway and S. Gottesfeld, *Journal of the Chemical Society, Faraday Transactions 1: Physical Chemistry in Condensed Phases* **69**, 1090 (1973).
5. S. C. S. Lai, N. P. Lebedeva, T. H. M. Housmans and M. T. M. Koper, *Topics in Catalysis*, **46**, 320 (2007).
6. F. Maillard, E. R. Savinova and U. Stimming, *Journal of Electroanalytical Chemistry*, **599**, 221 (2007).
7. M. P. Hogarth, The Development of the Direct Methanol Fuel Cell, PhD in Chemistry, University of Newcastle upon Tyne, Newcastle (1995).
8. T. J. Schmidt and H. A. Gasteiger, *Handbook of Fuel Cells: Fundamentals, Technology and Applications. Volume 2, Chapter 22: rotating thin-film methods for supported catalysts*, John Wiley & Sons ltd, New york (2003).
9. P. Wells, Controlled surface modification of supported platinum group metal catalysts, Thesis (PhD in Chemistry), University of Southampton, Southampton (2007).
10. O. Glasser, *Dr. W. C. Röntgen*, p. 33, Charles C Thomas, Springfield (ill) (1945).
11. P. J. Goodhew, J. Humphreys and R. Beanland, *Electron microscopy and analysis*, Taylor & Francis, London (2001).
12. F. W. H. Kampers, EXAFS in catalysis: Instrumentation and Applications, in, Technische Universiteit Eindhoven, Eidhoven (1988).
13. M. Brown, R. E. Peierls and E. A. Stern, *Physical Review B*, **15**, 738 (1977).
14. S. S. Sanjeev Mukerjee, Manuel P. Soriaga, and James McBreen, *Journal of Physical Chemistry*, **99**, 4577 (1995).
15. D. E. Sayers, E. A. Stern and F. W. Lytle, *Physical Review Letters*, **27**, 1204 (1971).
16. A. E. Russell and A. Rose, *Journal of the American Chemical Society*, **104**, 4613 (2004).

17. B. K. Teo, *EXAFS: Basic principles and Data Analysis*, Springer-Verlag, Berlin (1986).
18. S. J. Gurman, N. Binsted and I. Ross, *Journal of Physics C-Solid State Physics*, **17**, 143 (1984).
19. J. J. Rehr and R. C. Albers, *Phys. Rev. B*, **41**, 8139 (1990).
20. J. J. Rehr and R. C. Albers, *Rev. Mod. Phys.*, **72**, 621 (2000).
21. J. J. Rehr, R. C. Albers and S. I. Zabinsky, *Phys. Rev. Lett.*, **69**, 3397 (1992).
22. W. H. McMaster, N.K. Del Grande, J.H. Mallet, J.H. Hubbell, *Compilation of X-ray Cross-Sections, National Bureau of Standards, for calculation of x-ray cross sections,* Lawrence Livermore radiation laboratory, Livermore (California) (1969).
23. H. P. Bonzel and C. Kleint, *Progress in Surface Science*, **49**, 107 (1995).
24. J. W. Niemantsverdriet, *Spectroscopy in Catalysis: An Introduction, Chapter 3: Photoemmission and Auger Spectroscopy*, p. 37, Wiley-VCH, Weinheim (2000).
25. J. H. Scofield, *Journal of Electron Spectroscopy and Related Phenomena*, **8**, 129 (1976).
26. S. Tanuma, C. J. Powell and D. R. Penn, *Surface and Interface Analysis*, **11**, 577 (1988).
27. M. P. Seah and W. A. Dench, *Surface and Interface Analysis*, **1**, 2 (1979).

CHAPTER THREE: Ni MODIFIED Pt/C ELECTROCATALYSTS FOR THE ORR FOR USE IN PEMFC

1 Introduction

Proton exchange membrane fuel cells are widely being developed as clean power sources for cars, electronic devices and power plants. However, the penetration of this technology into the market is hindered by the oxygen reduction reaction (ORR). The electrocatalytic reduction of oxygen has been the focus of attention for many years and its mechanism is still not fully understood. The ORR is a multi-electron reaction which consists of a number of elementary steps involving different intermediates as depicted in **Figure 3- 1**.

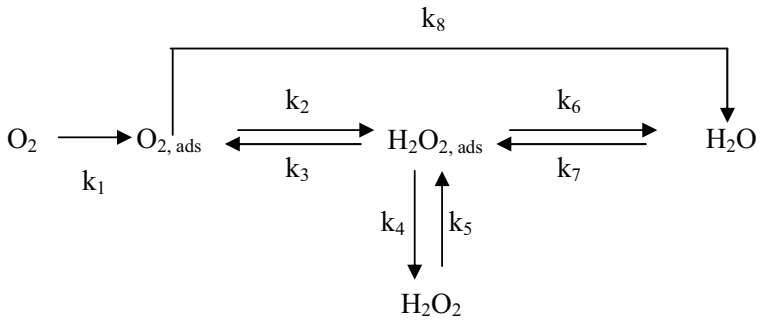

Figure 3- 1 Scheme of the ORR pathways in aqueous electrolyte

Yeager[1] discussed the different mechanisms for the ORR on Pt. By comparing the current densities of Pt in deuterated and undeuterated phosphoric acid, it was found that protons were not involved in the rate determining step (RDS) at potentials where the surface is free of the anodic film (oxide free surface). It was also explained that at potentials where the anodic film is not present, the RDS is the adsorption of oxygen on the Pt surface. However, when the anodic film is present, the RDS is the scission of the oxygen bond together with the formation of OH_{ads} on the Pt surface.

Similarly, Jacob[2] also studied the ORR using a 35 Pt-atom cluster and density functional theory (DFT) calculations. His model had 14 Pt-atom in the first layer, 13 Pt-atom in the second layer and 8 Pt-atoms in the third layer. This formation allowed a small planar cluster, containing 12 Pt-atom, to be created. This planar cluster was used to calculate the initial energy of the chemisorbed intermediates. Starting with hydrogen (H_2) and oxygen (O_2) in gas-phase, two different mechanisms were discussed, namely, the oxygen dissociation (OO) pathway and the peroxyl radical (OOH) formation pathway. Both mechanisms start with the adsorption of a hydrogen molecule ($H_{2,ads}$) onto the Pt surface which is then dissociated into two adsorbed protons (H_{ads}). For the OOH formation pathway, the oxygen, already adsorbed on the surface, reacts with H_{ads} to form OOH_{ads}. This intermediate is then dissociated into OH_{ads} and O_{ads}. The OH_{ads} further reacts with another H_{ads} to form water which is in turn desorbed from the Pt surface. The RDS was found to be the dissociation of OOH_{ads} to OH_{ads} which has a barrier of 71.72 kJ mol^{-1}. For the OO dissociation pathway, the adsorbed oxygen molecule ($O_{2,ads}$) is dissociated into two adsorbed oxygen atoms (O_{ads}). One of these O_{ads} further reacts with a H_{ads} to form an adsorbed hydroxyl intermediate (OH_{ads}). This OH_{ads} intermediate further reacts with another H_{ads} to form water which in turn is desorbed from the Pt surface. The RDS was found to be the formation of OH_{ads}, by combining O_{ads} and H_{ads}, which has a barrier of 132.55 kJ mol^{-1}. It was also found that the OOH formation pathway was the most likely mechanism as the heat of formation between $O_{2,ads}$ and H_{ads} to form OOH_{ads} is more favourable (-102.87 kJ mol^{-1}) than that of the breaking of the oxygen bond to form two O_{ads} (-44.55 kJ mol^{-1}).

The direct reduction of oxygen to water is preferred as it leads to the highest electrode potential and efficiency. However, no catalyst has shown a cell voltage equal to the thermodynamic potential for ORR (1.23 V vs. RHE). In fact, a lower potential has always been recorded.[3, 4] This potential loss is correlated to the amount of current drawn from the fuel cell - the higher the current density, the higher the potential loss as depicted by **Figure 3- 2**.

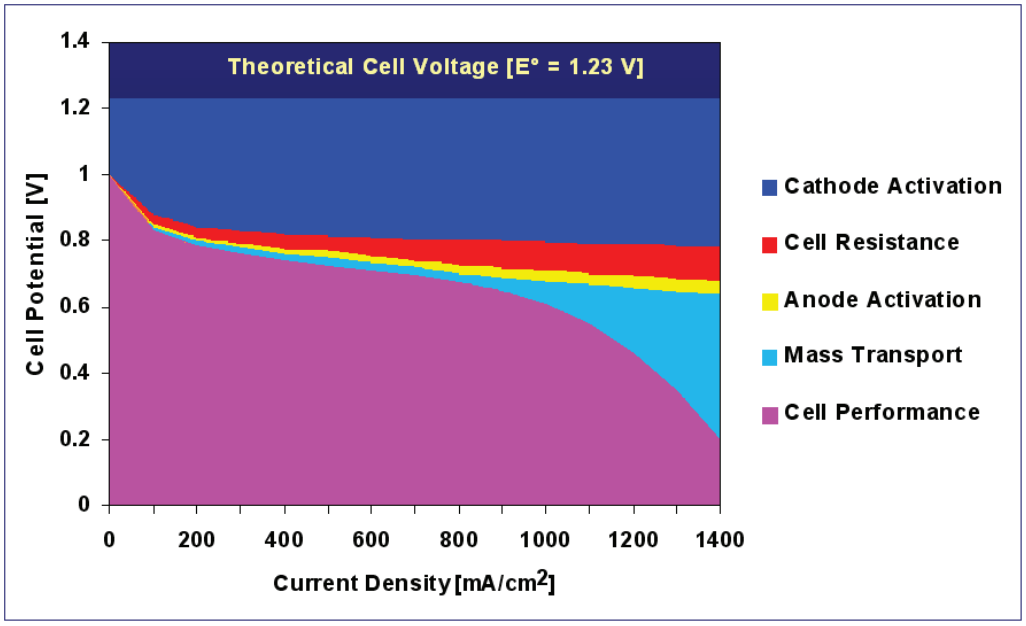

Figure 3- 2 Schematic showing the typical cell potential versus current density output from an MEA. The factors influencing the MEA performance along with their relative contribution to the cell potential loss are also shown. Adapted from Hogarth *et al.*.[5]

The cell voltage loss can be attributed to several factors: anode activation; cell resistance; mass transport; and cathode activation. The anode activation losses occur by either fuel leaking or electrons leaking through the electrode. Fuel leakage causes most of the problems but it can be significantly lowered by working at high temperature. Cell resistance losses arise from the internal resistance of the different components present in a fuel cell e.g. electrodes, membrane and connections. The mass transport losses result from the oxygen (or fuel) being used faster than it can be supplied and mainly occur at high current density. The cathode activation loss is due to the slow kinetics of the ORR (due to its complex mechanism and the many reaction pathways) and has a great effect at low current density. As shown in **Figure 2-2**, the major source of cell voltage loss is caused by cathode activation.

To improve the kinetics of the ORR, platinum (Pt) was alloyed with several transition metals (e.g. Ir[6], Fe[7], Ni[8]). Mukerjee *et al.*[9] reported the preparation of binary Pt-alloys with Mn, Cr, Fe, Co and Ni as the secondary metal. The performance of the catalysts was tested using a single cell MEA operating at 95 ^{o}C. Oxygen and hydrogen were humidified at 100 ^{o}C and 105 ^{o}C, respectively, and the

pressure of the reactant gases was set to 5 atm. An activity gain of 20-30 mV over Pt/C corresponding to a 1.2 to 5.0-fold enhancement of the specific activity was obtained, with PtCr/C exhibiting the highest performance. Binary Pt-alloys (Mn, Ni, Cr, Ti and Fe) were also studied by scientists at *Johnson Matthey* from 1995 to 1997.[10] The catalysts were tested as MEAs under H_2/O_2 at 75 ^oC at 308/377 kPa. PtTi, PtFe, PtMn and PtCr alloys were found to exhibit performance enhancements of 20- 40 mV.

The reason for the activity enhancement of the Pt-alloys towards the ORR is still the subject of many discussions but several theories have been published.

Nørskov *et al.*[11] studied the effect of 3*d* transition metals subsurface on the electronic and chemical properties of Pt(111) using a layered model structure in which a single layer of the secondary metal was situated in the second atomic layer. It was found in each case that the Pt *d*-band of the surface layer was lowered and broadened with respect to that of pure Pt(111). The Pt *d*-band broadening effect was attributed to the strong bonding between the Pt and the 3*d* metal; the stronger the bond, the higher the overlap of *d*-orbitals between the metals and the lower the *d*-band centre. The lowering of the Pt *d*-band centre was also found to be directly related to the dissociative adsorption energy of O_2 (adsorption and dissociation energy of the O_2 molecule) as well as the adsorption strength of the oxygenated species. They also showed that as the *d*-band centre move to more negative value, the dissociation of oxygen on the bimetallic surface became harder. Nørskov *et al.*[12] also showed that as the dissociative energy decreases (moving to more negative values), the strength of the bond with which the intermediates are bound to the catalyst surface also decreases. This is of particular interest for the ORR because a decrease in adsorption strength of the oxygenated species corresponds to a decrease in oxide coverage of the catalysts, which in turn induces a faster electroreduction of oxygenated species. As a result, an enhancement of activity of the catalysts towards the ORR should be observed.[7, 13]

Jalan and Taylor[14] prepared Pt-M/C alloys (M = Cr, V, Ti, W, Tl, Sl, Al, C and Ag) to study the effect of the Pt-Pt nearest neighbour distance on the ORR in phosphoric acid. They found that as the Pt-Pt nearest distance decreases, the activity of the

catalyst towards the ORR increases. As the oxygen can adsorb by a dual site mode,[1] it is thought that the Pt-Pt bond distance greatly influenced the adsorption property of oxygen on the Pt surface. A similar effect was found for PtNi[15] and PtCo[16] alloys.

Colón-Mercado and Popov[17] compared a PtCo/C alloy to Pt/C in a fuel cell. The loadings of the cathode (PtCo/C or 19.6 wt% Pt/C) and anode catalysts (30 wt% Pt/C) were 0.4 mg cm^{-2} and 0.5 mg cm^{-2}, respectively. The oxygen and hydrogen were humidified at 75 °C and 77 °C, respectively. Finally, the cell was run at a constant current density of 1 A cm^{-2}. It was found that the PtCo/C alloy exhibited a higher stability than that of Pt/C. The enhanced stability was explained by a slower rate of decay (decrease in active surface area) for the PtCo/C alloy catalyst than that of Pt/C. Similar results were found by Antolini *et al*..[4]

However, despite having greater activities than that of Pt/C, binary Pt-alloys are still not commonly used as the cathode catalysts in operating fuel cells. This is mainly due to the leaching of the secondary metal which can lower the conductivity of the membrane leading to higher membrane resistance, increase the resistance of the cathode catalyst layer due to higher ionomer resistance, lower the diffusion of oxygen in the ionomer in the catalyst layer, and cause degradation of the membrane.

For Pt-alloys to exhibit their best performance it is important for the second metal to be in intimate contact with Pt.[18] This can be difficult to achieve using conventional methods as the second metal could deposit onto the support. As a result, a number of different techniques have emerged to prepare multi-components catalysts known as core shell catalysts[19-23]. One technique, called surface organometallic chemistry (SOMC), has come forward over the last decade as it enables good control over the preparation of binary metal catalysts.

SOMC allows the specific deposition of a metal, M_2, using an organometallic compound of this metal, M_2R_n, over the reduced surface of a first metal M_1-H_{ads}. The metal-carbon bond of M_1-M_2-R_y is subsequently broken by hydrogenolysis to give M_2 deposited on the surface of M_1. The general mechanism is believed to occur via physisorption of M_2R_n on the surface, leading to the surface organometallic species as described by **Equations 3-1 to 3-3.** [24, 25]

$$2\ M_1 + H_2 \rightarrow 2\ M_1\text{-}H_{ads} \qquad \textbf{Equation 3-1}$$

$$M_1\text{-}H_{ads} + R_n\text{-}M_2 \rightarrow M_1\text{-}M_2\text{-}R_y + x\ R\text{-}H \qquad \textbf{Equation 3-2}$$

$$M_1\text{-}M_2\text{-}R_y \xrightarrow{\Delta \text{ and } H_2} M_1 - M_2 + y\ R - H \qquad \textbf{Equation 3-3}$$

The second metal is believed to exist as "ad-atoms", which are localised on specific crystallographic sites of M_1. A surface alloy can then be produced by heat treating the then formed core-shell particles.

SOMC was used by Wells *et al* [26] to specifically modify Pt particles by adding chromium (Cr) using 2 Cr precursors, namely, chromium (III) acetylacetonate and biscyclopentadienyl chromium to carbon supported Pt particles. The catalysts were further heat treated to study the effect of alloying with the temperature. The PtCr catalyst exhibited a 2 to 3.5 fold increase in specific activity. This enhancement in catalytic activity was attributed to an alloy phase formation, which in turn shortened the Pt-Pt nearest neighbour bond distance.

In this thesis the focus is on the preparation of Pt-Ni electrocatalysts, as they have shown an improvement in catalytic activity towards the ORR. Yang *et al.*[27] studied the activity of carbon-supported PtNi alloys. PtNi alloys with different atomic composition were prepared via the carbonyl complex route. Briefly, the Pt and Ni carbonyl complexes were prepared simultaneously by mixing Pt and Ni salt with CO at 55 °C for 24 h until the solution turned green. Sodium acetate was added to the mixture to reach a sodium acetate:Pt molar ratio of 6:1. Then, Vulcan XC-72 carbon was added to the mixture under N_2 and the solution was stirred at 55 °C for another 6 h. The resulting catalysts were further heat-treated under H_2 at temperature ranging from 200 to 500 °C. This led to well dispersed catalysts with a narrow particle size distribution and a similar average particle size (*ca.* 3 nm). The CV and XPS data showed the presence of a disordered PtNi phase with no surface enrichment of Pt and the RRDE measurements demonstrated the direct 4 electron conversion of oxygen into water with a small amount, <10 %, of hydrogen peroxide being produced in the process. All PtNi alloy catalysts exhibited a catalytic enhancement of a factor of 1.5 to 4 (specific activity) with respect to that of 20 wt% Pt/C catalyst. The activity enhancement of the PtNi catalysts was shown to be dependent upon the composition of the alloy. Moreover, their results suggested that a maximum activity

was obtained for a nickel atomic percentage of 40. The catalytic enhancement shown by this catalyst was ascribed to a favourable Pt-Pt mean interatomic distance caused by alloying, the presence of disordered surface structures, and the good dispersion of the catalyst particles on the carbon support.

Lima *et al.*[15] reported the electrocatalytic properties of PtNi alloys for the ORR in alkaline solution. The PtNi alloys exhibited a slight catalytic improvement towards the ORR with respect to Pt/C. The slight improvement was attributed to the electrolyte used during the study, potassium hydroxide (KOH). KOH provides more OH species and therefore increases the likelihood of having the non-metal atoms present in the form of oxide or hydroxide which would induce a screening effect on the neighbouring Pt atoms. As a consequence, a lower amount of Pt sites are available to carry out the ORR. Nevertheless, the catalytic enhancement was attributed to a reduced Pt-OH or Pt-O bond strength in the PtNi alloys due to a decrease in the *d*-band centre, which led to lower Pt-O coverage and faster $Pt\text{-}O^-$ electroreduction.

Stamenkovic *et al.*[8] studied the ORR on $Pt_3Ni(hkl)$ single crystal surfaces. LEIS measurements showed that the alloys exhibited a different degree of surface enrichment of Pt in the first layer resulting in a shift of the *d*-band centre. RDE experiments demonstrated that the $Pt_3Ni(111)$ exhibited a higher activity than that of Pt(111) as the polarisation curve is positively shifted by 100 mV. Also, the structure sensitivity of the ORR was illustrated by comparing $Pt_3Ni(111)$ to both $Pt_3Ni(110)$ and $Pt_3Ni(100)$. $Pt_3Ni(111)$ exhibited the highest catalytic activity and this was explained by the structure sensitivity of OH adsorption on the different crystal planes and its inhibiting effect on O_2 adsorption. The $Pt_3Ni(111)$ surface was reported to show a 90-fold catalytic enhancement in specific activity towards the ORR with respect to that of 20 wt% Pt/C.

Qian[28] also used the SOMC to prepare Ni deposited on Pt/C to study the ORR. The catalysts were prepared by first reducing the Pt/C under H_2 then adding a solution of $Ni(Cp)_2$ dissolved in n-heptane. For the first 12 h, the solution was stirred at room temperature before increasing the temperature to 90-95 °C for 8 to 12 h. The amount of Ni precursor added was equivalent to 0.25, 0.5, 0.75 and 1 monolayer coverage.

The catalysts were further heat-treated at different temperature between 450 and 950 °C under 10% H_2/N_2 atmosphere. It was found that the secondary metal did not fully deposit on the Pt/C precursor. Despite the lack of deposition of the secondary metal, the catalysts still exhibited a mass activity and specific activity enhancement by a factor of 1.3 and 2.3, respectively. The catalytic improvement was attributed to an alloy formation and to an increase in particle size.

In this chapter, the preparation of nickel on Pt/C electrocatalysts (Ni/Pt/C) using the SOMC methodology is reported. The Ni/Pt/C electrocatalysts were prepared by depositing Ni on 19.6 wt% Pt/C using 2 different Ni precursors, nickel acetonylacetonate and nickelocene in toluene. To study the effect of heat-treatment temperature on the catalytic activity of the catalysts, the catalysts were also heat-treated at 200, 500, 750 and 900 ^oC under 4% H_2/N_2. The catalysts were characterised using Cyclic Voltammetry (CV), Rotating Disk Electrode (RDE), X-ray diffraction (XRD), X-ray photoemission spectroscopy (XPS), Extended X-ray Absorption Fine Structure (EXAFS), Transmission Electron Microscopy (TEM) and Energy Dispersive X-ray (EDX) analysis.

2 Experimental

2.1 Catalyst preparation

5 g of 19.6 wt% Pt/C was introduced into a 2 neck round-bottomed flask fitted with a dropping funnel, a condenser and a thermocouple. N_2 was then flowed through (75 ml min^{-1}) the flask for 20 min to remove any traces of O_2. Next, to reduce the Pt surface, the temperature was increased to 200 °C for 3 h and H_2 was flowed (75 ml min^{-1}) through the flask. The Pt/C was subsequently allowed to cool down to room temperature (whilst still flowing H_2) before adding 100 ml of toluene previously deaerated with N_2 for 15 min. The mixture was stirred and heated at 90 °C using a water bath whilst bubbling H_2 through the mixture. A solution containing the required amount of Ni precursor (nickel acetonylacetonate or nickelocene) in toluene corresponding to either half, 1 or 2 monolayer(s) (previously deaerated with N_2 for 15 min) was added dropwise to keep the temperature constant at 90 °C. Once the addition was completed, the slurry was left under constant stirring and heating for 5.5 h at 90 °C whilst bubbling H_2 through the solution. The mixture was then allowed to cool to room temperature and the gas was switched to N_2 for another 15 min to remove any traces of H_2. The mixture was filtered off and the precipitate was thoroughly washed with toluene and then with water.

A portion of the catalyst underwent further heat treatment. 1 g of samples of the catalyst was loaded into a tube furnace (1 g per heat treatment temperature). The tube was purged with N_2 for 30 min prior to switching the gas to a 10% H_2 / N_2 mixture, at a flow rate of 60 cm^3 min^{-1}. The temperature was increased from room temperature to the desired temperature (200, 500, 750 or 900 ºC) at a heating rate of 5 ºC min^{-1} and held there for 1 hour and then allowed to cool back to room temperature. Finally the gas was switched back to N_2 and the tube was purged for another 30 min.

2.2 ICP-OES

All samples were submitted to *Johnson Matthey Technology Centre* where the analyses were performed.

2.3 Electrochemical characterisation

2.3.1 Cyclic voltammetry

All samples were analysed using the procedure detailed in **Chapter 2 section 2.2**.

2.3.2 Oxygen reduction testing

All samples were analysed using the procedure detailed in **Chapter 2 section 2.3**.

2.4 XRD

All samples were submitted to *Johnson Matthey Technology centre* where the analyses were performed. See **Chapter 2 section 3** for more information on the experimental procedure followed.

2.5 TEM-EDX

See **Chapter 2 section 4** for more information on the experimental procedure followed.

2.6 XAS studies

All samples were analysed using the procedure detailed in **Chapter 2 section 5**.

2.7 XPS

All samples were submitted to *Johnson Matthey Technology centre* where the analyses were performed. See **Chapter 2 section 6** for more information on the experimental procedure followed.

3 Results

3.1 Structure of the catalysts

3.1.1 Metal assay analysis

Elemental analysis of the prepared 0.5, 1 and 2 monolayer(s) (ML) Ni/Pt/C catalysts via the $Ni(acac)_2$ route and 1 ML and 2ML via the $Ni(Cp)_2$ route were carried out using ICP-OES. The experimental and theoretical values based on the amount of Ni and Pt/C introduced, are shown in **Table 3-1 and Table 3-2**.

Table 3-1 Elemental analysis for 0.5, 1 and 2 ML Ni/Pt/C prepared via the $Ni(acac)_2$ route.

Sample	Pt wt% theory	Pt wt% experimental	Ni wt% theory	Ni wt% experimental
0.5 ML, $Ni(acac)_2$	19.3	19.6 ± 0.3	1.5	1.4 ± 0.3
1 ML, $Ni(acac)_2$	19.0	19.3 ± 0.3	3.0	2.8 ± 0.3
2 ML, $Ni(acac)_2$	18.4	18.5 ± 0.3	6.0	5.6 ± 0.3

Table 3-2 Elemental analysis for 1 and 2 ML Ni/Pt/C prepared via the $Ni(Cp)_2$ route.

Sample	Pt wt% theory	Pt wt% experimental	Ni wt% theory	Ni wt% experimental
1 ML, $Ni(Cp)_2$	18.5	18.5 ± 0.3	4.5	4.2 ± 0.3
2 ML, $Ni(Cp)_2$	17.7	17.2 ± 0.3	8.7	7.9 ± 0.3

The assays of the prepared electrocatalysts show a good agreement with the theoretical values, indicating that the reaction between the Ni precursors and 20 wt% Pt/C appears to be complete.

3.1.2 XRD analysis

XRD patterns of 0.5, 1 and 2 ML Ni/Pt/C prepared via the $Ni(acac)_2$ route are presented in **Figure 3- 3, Figure 3- 4 and Figure 3- 5**, respectively. XRD patterns of 1 and 2 ML Ni/Pt/C catalysts prepared via the $Ni(Cp)_2$ route are presented in **Figure 3- 6** and **Figure 3- 7**. The black vertical dotted lines correspond to the peak positions of face-centred cubic (fcc) Pt. The orange vertical dotted lines (**Figure 3- 5, Figure 3- 6** and **Figure 3- 7**) correspond to the peak position of fcc Ni. (all the Bragg angles for both Pt and Ni can be calculated theoretically using **Equation 2-17**, in our case the Bragg angles were part of a database Bruker AXS Diffrac Plus, Eva 2005 (V13)).

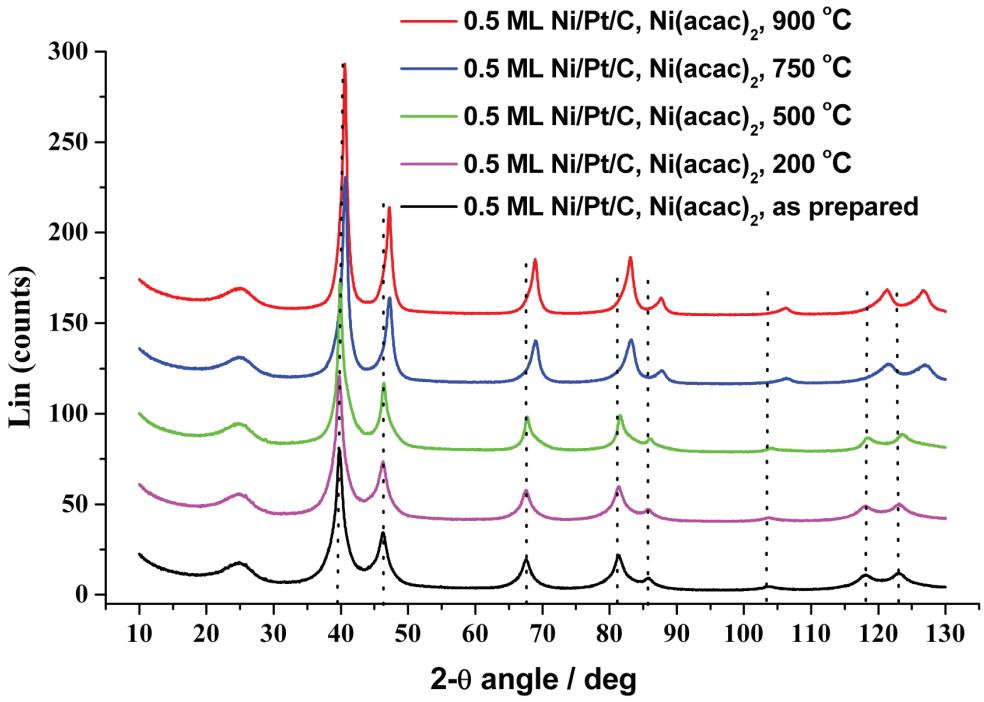

Figure 3- 3 XRD patterns of the 0.5 ML Ni/Pt/C catalysts prepared via the $Ni(acac)_2$ route. Peak position of fcc Pt is shown by the black vertical dotted lines.

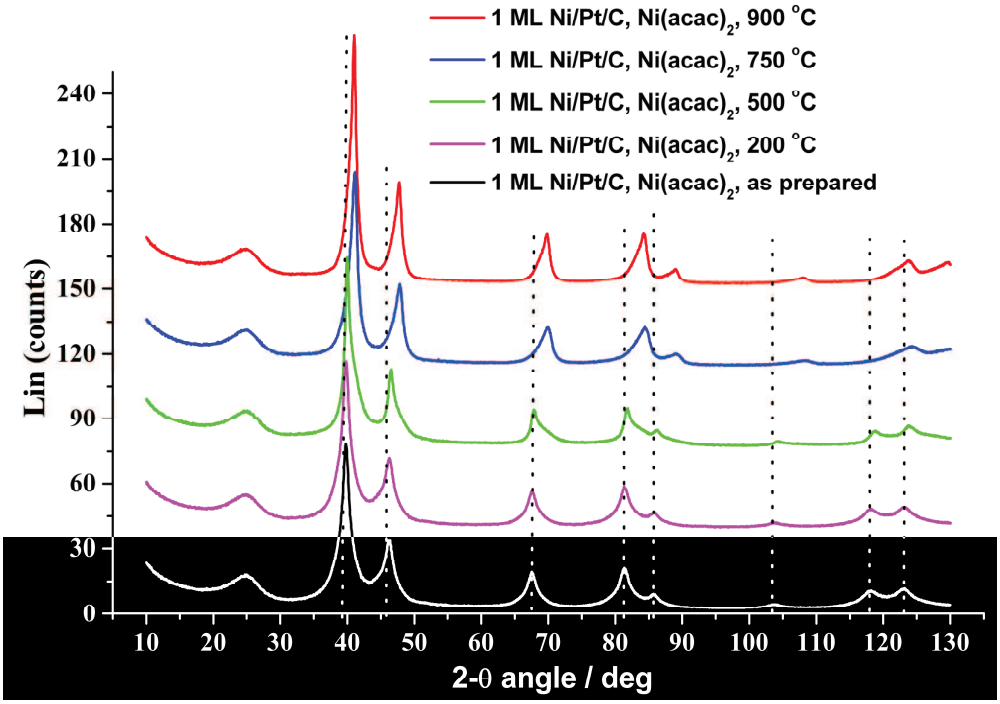

Figure 3- 4 XRD patterns of the 1 ML Ni/Pt/C catalysts prepared via the $Ni(acac)_2$ route. Peak position of fcc Pt is shown by the black vertical dotted lines.

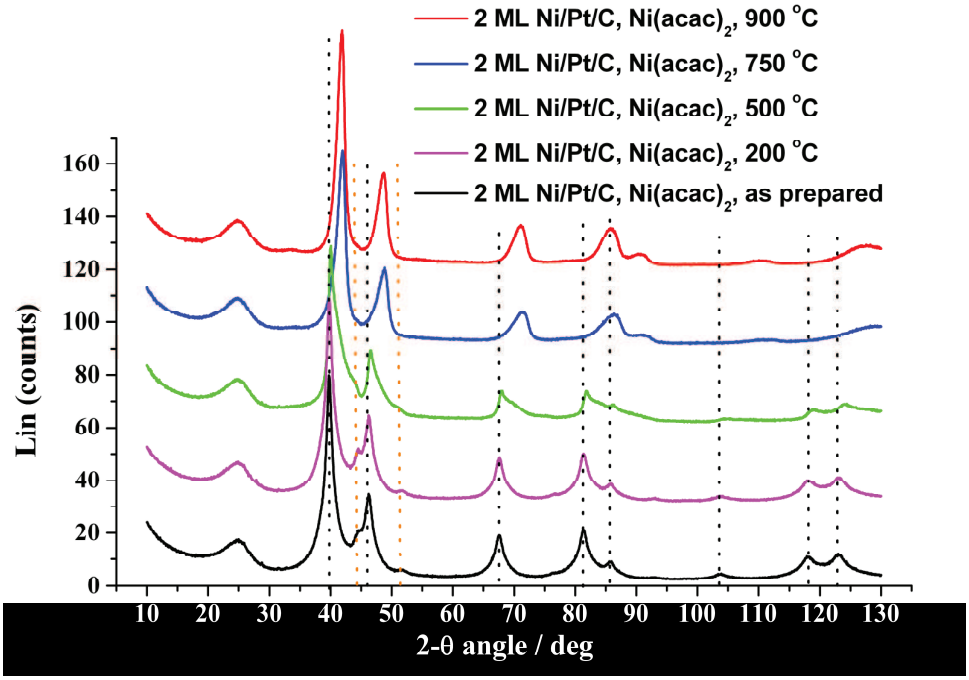

Figure 3- 5 XRD patterns of the 2 ML Ni/Pt/C catalysts prepared via the $Ni(acac)_2$ route. Peak position of fcc Pt is shown by the black vertical dotted lines.Peak position of fcc Ni is shown by the orange vertical dotted lines.

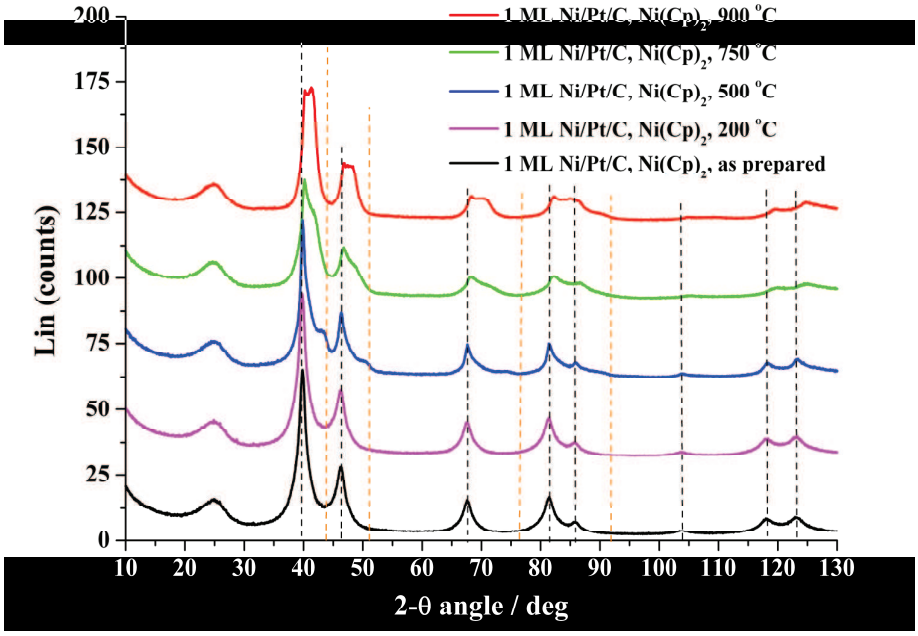

Figure 3- 6 **XRD patterns of the 1 ML Ni/Pt/C catalysts prepared via the $Ni(Cp)_2$ route. Peak position of fcc Pt is shown by the black vertical dotted lines.Peak position of fcc Ni is shown by the orange vertical dotted lines.**

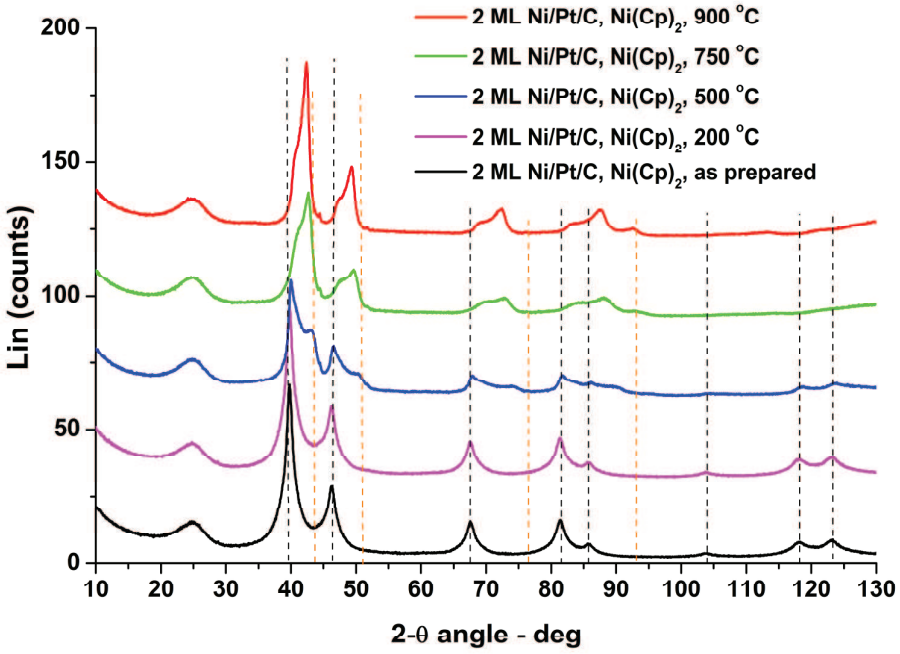

Figure 3- 7 **XRD patterns of the 2 ML Ni/Pt/C catalysts prepared via the $Ni(Cp)_2$ route. Peak position of fcc Pt is shown by the black vertical dotted lines.Peak position of fcc Ni is shown by the orange vertical dotted lines.**

The diffraction peak at $2\theta \sim 25^{o}$ observed in all the XRD patterns is due to the (002) plane of the hexagonal structure of Vulcan XC-72 carbon.[29] All XRD patterns show the main characteristics of the fcc crystalline Pt. In order of increasing diffraction angle, the Pt crystal planes are (111), (200), (220), (311), (222), (400), (331) and (420). No peaks are observed for the fcc crystalline Ni in the 0.5 and 1 ML Ni/Pt/C catalysts prepared via $Ni(acac)_2$ and the 1 ML Ni/Pt/C catalysts prepared via the $Ni(Cp)_2$ route. This indicates that Ni is present as a highly dispersed amorphous species assumed to be decorating the Pt particles. However, the (111) and (200) planes of the Ni fcc structure were detected in both 2 ML Ni/Pt/C sets of catalysts, indicating the presence of a poorly crystalline Ni phase. The presence of poorly crystalline Ni for these sets of catalysts can be explained by the high concentrations of Ni in the samples. The observed shift for the Pt diffraction angle to higher values as the heat treatment temperature increased indicates a lattice contraction and the formation a PtNi alloy phase.

As described in **Chapter 2 section 3.3**, Rietveld analysis was performed by fitting theoretical curves to the experimental XRD data. This technique enables the determination of the different alloy phases present in the sample (if not amorphous) to be determined. However, if more than 2 phases were present in the samples, it proved to be difficult to fit the data. As a consequence, the Rietveld analysis could not be performed on some of the samples because of their complexity. The results of the Rietveld analyses are summarised in **Table 3-3** and **Table 3-4**.

Table 3-3 and **Table 3-4** summarises the Pt lattice parameters for 0.5 ML, 1 ML, and 2 ML Ni/Pt/C prepared via the $Ni(acac)_2$ route and 1ML and 2 ML Ni/Pt/C prepared via the $Ni(Cp)_2$ route, respectively. The XRD data showed two PtNi alloy phases. For the catalysts prepared via the $Ni(acac)_2$ route, it can be seen that as the heat-treatment temperature increases, the lattice parameter of Pt decreases from 3.9121 to 3.8561 Å, 3.9073 to 3.8095 Å and 3.7791 to 3.7264 Å for 0.5 ML, 1ML and 2 ML Ni/Pt/C ($Ni(acac)_2$), respectively. The observed decrease in lattice parameter indicates that the degree of alloying increases as the heat-treatment temperature increases. This results from more Ni atoms being incorporated into the Pt structure.[30] No conclusion can be drawn from the lattice parameter of the catalysts

prepared via the $Ni(Cp)_2$ route as most of the catalysts exhibited several PtNi alloy phases and were very poorly crystalline and this complexity rendered the Rietveld analysis impossible.

Table 3-3 Lattice parameters for 0.5 ML, 1 ML, 2 ML Ni/Pt/C, $Ni(acac)_2$, as prepared, 200, 500, 750 and 900 ^oC catalysts

	0.5 ML Ni/Pt/C, $Ni(acac)_2$				
	As prepared	**200 ^oC**	**500 ^oC**	**750 ^oC**	**900 ^oC**
Lattice parameter / Å	*	*	3.9121 (2)	3.8915 (1)	3.8908 (6)
	*	*	3.8704 (8)	3.8519 (2)	3.8561 (1)
	1 ML Ni/Pt/C, $Ni(acac)_2$				
	As prepared	**200 ^oC**	**500 ^oC**	**750 ^oC**	**900 ^oC**
Lattice parameter / Å	*	*	3.9073 (2)	3.8466 (9)	3.8475 (7)
	*	*	3.8457 (8)	3.8005 (3)	3.8095 (2)
	2 ML Ni/Pt/C, $Ni(acac)_2$				
	As prepared	**200 ^oC**	**500 ^oC**	**750 ^oC**	**900 ^oC**
Lattice parameter / Å	*	*	**	3.7791 (9)	3.7752 (6)
	*	*	**	3.7182 (5)	3.7264 (4)

Table 3-4 Lattice parameters for 1 ML and 2 ML Ni/Pt/C, $Ni(Cp)_2$, as prepared, 200, 500, 750 and 900 ^oC catalysts

	1 ML Ni/Pt/C, $Ni(acac)_2$				
	As prepared	**200 ^oC**	**500 ^oC**	**750 ^oC**	**900 ^oC**
Lattice parameter / Å	*	*	**	3.8838(7)	**
	*	*	**	3.750(2)	**
	2 ML Ni/Pt/C, $Ni(acac)_2$				
	As prepared	**200 ^oC**	**500 ^oC**	**750 ^oC**	**900 ^oC**
Lattice parameter / Å	*	*	**	3.8106 (9)	**
	*	*	**	3.6837 (9)	**

* Peak profile analysis showed the presence of a bi-modal Platinum crystallite size distribution. Rietveld analysis to calculate Pt crystallite size could not therefore be accurately carried out.

** Several alloy phases were detected. Due to the complexity of this sample, it was not possible to determine the lattice parameter and crystalline size. The analysis of this sample by X-ray diffraction was therefore limited.

3.1.3 XPS analysis

XPS analysis was performed at the Pt(4f), Ni(2p) and O(1s) core level energies for all the series of electrocatalysts. The XPS signal of all three core level regions for 1 ML Ni/Pt/C are presented as an example of the data generated in **Figure 3- 8**, **Figure 3- 9** and **Figure 3- 10** respectively. The data for the 0.5 and 2 ML Ni/Pt/C prepared via the $Ni(acac)_2$ route can be found in **Appendix 1a** and those of 1 and 2 ML Ni/Pt/C prepared via $Ni(Cp)_2$ can be found in **Appendix 1b**.

Table 3-5 to **Table 3-9** summarise the binding energies of the $Pt(4f_{7/2})$, $Ni(2p_{3/2})$ and O(1s) signals for all the electrocatalysts as observed in the respective XPS spectra. At this moment of the thesis it is worth pointing out a few points of caution regarding the analysis of the XPS data: the %At of each element is relative to other elements detected and the technique is semi-quantitative. Errors on the At% were not calculated as it is difficult to calculate them without making a reference to an expected, known or proposed surface morphology. In addition, the lack of knowledge regarding the exact morphology of the catalysts renders these calculations even more complicated.

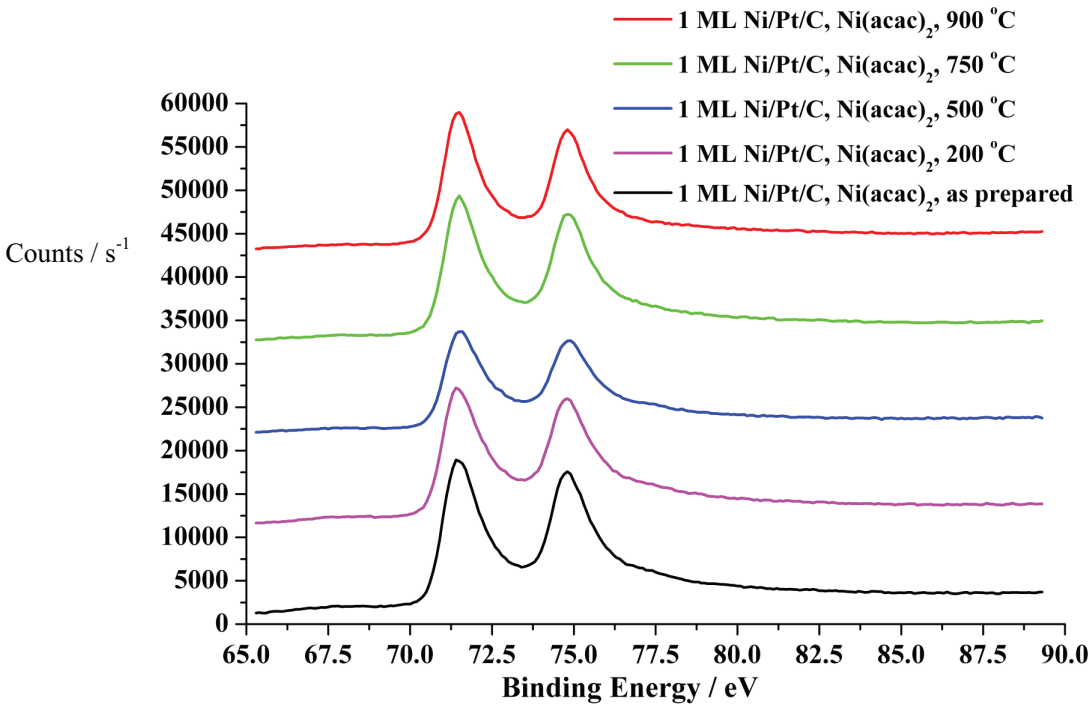

Figure 3- 8 XPS of Pt(4f) core level region of 1 ML Ni/Pt/C electrocatalysts prepared via the $Ni(acac)_2$ route

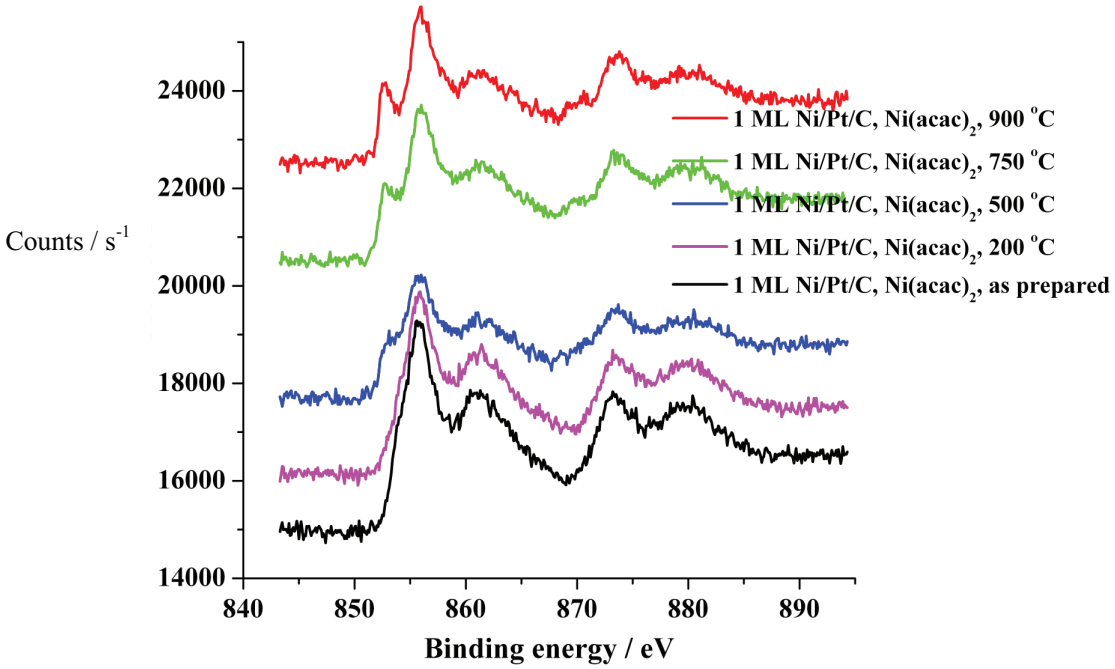

Figure 3- 9 XPS of Ni(2p) core level region of 1 ML Ni/Pt/C electrocatalysts prepared via the $Ni(acac)_2$ route

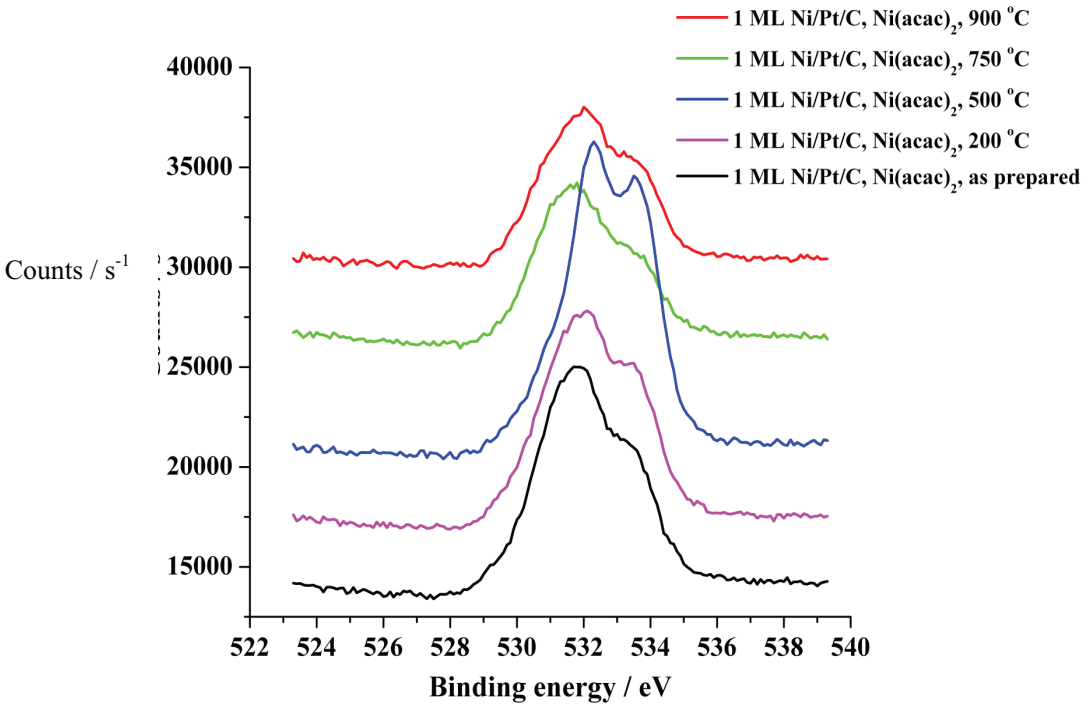

Figure 3- 10 XPS of O(1s) core level region of 1 ML Ni/Pt/C electrocatalysts prepared via the $Ni(acac)_2$ route.

Figure 3-10 shows the XPS spectra of the O(1s) core level region for the 1 ML Ni/Pt/C prepared via the $Ni(acac)_2$ route. It can be seen that all the catalysts but the 500 °C follow a similar trend over the same region of binding energy. The 500 °C catalyst exhibits a shift to higher binding energy. This deviation arises from the greater carbon-oxygen ratio exhibited by this sample in comparison to the others (not shown). This increases the carbon-oxygen work function of this sample thus, resulting in the shift of binding energy observed in the spectrum of the 500 °C.

Table 3-5 **Binding energies of 0.5 ML Ni/Pt/C electrocatalysts prepared via the $Ni(acac)_2$ route at different heat-treatment temperature as observed from their respective $Pt(4f_{7/2})$, Ni $(2p_{3/2})$ and O(1s) X-ray photoelectron spectra along with their respective atomic percentage and the atomic ratio of the metal components.**

Sample	O (1s) / eV	O / At%	Pt ($4f_{7/2}$) / eV	Pt / At %	Ni ($2p_{3/2}$) / eV	Ni / At %	Ni At % / Pt At %
0.5 ML Ni/Pt/C as prepared	532.3	12.4	71.4	1.3	855.9	0.5	0.4
0.5 ML Ni/Pt/C 200 °C	532.3	10.8	71.5	1.4	855.8	0.5	0.4
0.5 ML Ni/Pt/C 500 °C	532.4	10.5	71.5	1.4	855.8	0.4	0.3
0.5 ML Ni/Pt/C 750 °C	532.4	12.0	71.4	1.0	855.8	0.3	0.3
0.5 ML Ni/Pt/C 900 °C	532.4	9.9	71.4	1.0	855.8	0.2	0.2

Table 3-6 **Binding energies of 1 ML Ni/Pt/C electrocatalysts prepared via the $Ni(acac)_2$ route at different heat-treatment temperature as observed from their respective $Pt(4f_{7/2})$, Ni $(2p_{3/2})$ and O(1s) X-ray photoelectron spectra along with their respective atomic percentage and the atomic ratio of the metal components.**

Sample	O (1s) / eV	O / At%	Pt ($4f_{7/2}$) / eV	Pt / At %	Ni ($2p_{3/2}$) / eV	Ni / At %	Ni At % / Pt At %
1 ML Ni/Pt/C as prepared	531.8	7.7	71. 5	1.9	855.7	1.2	0.6
1 ML Ni/Pt/C 200 °C	532.0	7.9	71.5	1.8	855.8	1.1	0.6
1 ML Ni/Pt/C 500 °C	532.3	10.0	71.5	1.3	855.6	0.7	0.6
1 ML Ni/Pt/C 750 °C	531.7	5.0	71.5	1.6	855.8	0.8	0.5
1 ML Ni/Pt/C 900 °C	532.0	5.0	71.5	1.4	855.9	0.7	0.5

Table 3-7 **Binding energies of 2 ML Ni/Pt/C electrocatalysts prepared via the $Ni(acac)_2$ route at different heat-treatment temperature as observed from their respective $Pt(4f_{7/2})$, Ni $(2p_{3/2})$ and O(1s) X-ray photoelectron spectra along with their respective atomic percentage and the atomic ratio of the metal components.**

Sample	O (1s) / eV	O / At%	Pt $(4f_{7/2})$ / eV	Pt / At %	Ni $(2p_{3/2})$ / eV	Ni / At %	Ni At % / Pt At %
2 ML Ni/Pt/C as prepared	531.2	8.1	71.4	1.9	855.9	2.1	1.1
2 ML Ni/Pt/C 200 °C	531.5	7.5	71.4	1.7	855.8	1.7	1,0
2 ML Ni/Pt/C 500 °C	531.8	7.1	71.5	1.5	855.8	1.5	1,0
2 ML Ni/Pt/C 750 °C	531.6	5.8	71.5	1.4	855.8	1.2	0.9
2 ML Ni/Pt/C 900 °C	532.0	6.0	71.5	1.2	856.0	1.2	1.0

Table 3-8 **Binding energies of 1 ML Ni/Pt/C electrocatalysts prepared via the $Ni(Cp)_2$ route at different heat-treatment temperature as observed from their respective $Pt(4f_{7/2})$, Ni $(2p_{3/2})$ and O(1s) X-ray photoelectron spectra along with their respective atomic percentage and the atomic ratio of the metal components.**

Sample	O (1s) / eV	O / At%	Pt $(4f_{7/2})$ / eV	Pt / At %	Ni $(2p_{3/2})$ / eV	Ni / At %	Ni At % / Pt At %
1 ML Ni/Pt/C as prepared	532.3	13.8	71.5	1.4	856.0	1.4	1.0
1 ML Ni/Pt/C 200 °C	532.3	12.7	71.4	1.1	856.0	1.3	1.1
1 ML Ni/Pt/C 500 °C	532.3	6.8	71.6	1.4	856.3	1.3	0.9
1 ML Ni/Pt/C 750 °C	532.0	7.1	71.5	1.6	856.1	1.1	0.7
1 ML Ni/Pt/C 900 °C	532.4	8.1	71.6	1.2	856.2	1.2	1.0

Table 3-9 **Binding energies of 2 ML Ni/Pt/C electrocatalysts prepared via the $Ni(Cp)_2$ at different heat-treatment temperature as observed from their respective $Pt(4f_{7/2})$, $Ni\ (2p_{3/2})$ and O(1s) X-ray photoelectron spectra along with their respective atomic percentage and the atomic ratio of the metal components.**

Sample	O (1s) / eV	O / At%	Pt ($4f_{7/2}$) / eV	Pt / At %	Ni ($2p_{3/2}$) / eV	Ni / At %	Ni At % / Pt At %
2 ML Ni/Pt/C as prepared	532.2	16.2	71.4	0.8	855.8	1.7	2.1
2 ML Ni/Pt/C 200 °C	532.1	9.2	71.6	1.1	856.1	1.8	1.6
2 ML Ni/Pt/C 500 °C	532.1	9.9	71.6	1.0	856.1	1.9	1.9
2 ML Ni/Pt/C 750 °C	532.3	11.2	71.6	1.0	856.1	1.3	1.2
2 ML Ni/Pt/C 900 °C	532.3	12.0	71.5	0.8	856.2	1.2	1.5

The Pt(4f) XPS signal shown in **Figure 3- 8** is a doublet for all samples. The peak at low binding energy corresponds to the $4f_{7/2}$ electronic transition which exhibits a maximum at *ca.* 71.5 eV for all the electrocatalysts. The peak at higher binding energy corresponds to the $4f_{5/2}$ electronic transition which exhibits a maximum at *ca.* 74.7 eV. The peak at ~71.5 eV is the peak of interest as it corresponds to the published value for zero-valent Pt metal (71.3 eV).[31] Comparing the values of Pt($4f_{7/2}$) summarised in **Table 3-5** to **Table 3-9**, it can be noted that a positive shift is observed as opposed to the expected negative effect. A lower value is expected as Pt is more electronegative than Ni, 2.28 and 1.91 (Pauling electronegativity scale), respectively. As a consequence, Pt should have an electron withdrawing effect, hence lowering the binding energies of the Pt(4f) bands. The controversial effect of Ni on the Pt(4f) bands can be explained by studying the d-electron screening (filling of the *d*-shell) in the initial and final-states. Shirley *et al.*[32] concluded that adding Ni to Pt dramatically reduces the *d*-electron screening of the final-state which leads to an increase in the core-level binding energy as observed in the Pt(4f) X-ray photoelectron spectrum of all the Ni/Pt/C catalysts. Similar results can be found in the literature.[29]

The data recorded for the Ni($2p_{3/2}$) core level show a lower binding energy than that of the zero-valent Ni metal (859.4 eV).[31] A difference of 4 eV is observed and can be assigned to the electron pulling effect of Ni on Pt as previously discussed. The peak at *ca.* 862 eV (**Figure 3- 9**) is a known satellite peak, which is a result of multi-electron excitation.[33] In addition, peaks at 872 eV and 852 eV are observed on the XPS data of the 500, 750 and 900 °C catalysts. These peaks are attributed to the $2p_{1/2}$ and $2p_{3/2}$ of NiO and NiO_2, respectively. The emergence of these peaks is due to the oxidation of Ni after heat-treatment. These peaks are not observed for the non heat-treated and the 200 °C samples which may be due to the presence other adsorbed species on the Ni surfaces, however these species seem to be removed thermally at temperatures greater than 500 °C.

The binding energy corresponding to the O(1s) core level transition is typical for a metal-OH or metal-OH_2 species.[34] The O(1s) peak (**Figure 3- 10**) occurs as a

multiplet because of the interaction of the photoelectron with the unpaired electron of the oxygen.[35]

Table 3-5 to **Table 3-9** also summarise the atomic ratio of the metal components for all the Ni/Pt/C catalysts (**Chapter 2 section 6**) for the determination of the atomic percentage of the elements present). The relative amount of each individual element was given relative to the others. As a consequence, these values have only a small relevance by themselves. However, the ratio between elements of interest is more useful. In our case, Ni:Pt atomic ratios will be studied. It can be noted that the Ni:Pt atomic ratio decreases in both 0.5 and 1 ML Ni/Pt/C electrocatalysts prepared via the $Ni(acac)_2$ route and 1 and 2 ML Ni/Pt/C catalysts prepared via the $Ni(Cp)_2$ route as temperature increases. This decrease suggests that as the heat-treatment temperature increases, a surface enrichment in Pt metal takes place. This may be due to the formation of a surface alloy phase as suggested by the XRD data. The atomic ratio for the 2 ML Ni/Pt/C electrocatalysts prepared via the $Ni(acac)_2$ route remains fairly constant, *ca.* 1, as the heat-treatment temperature increases.

As both catalysts were heat-treated in a similar way, another interesting feature is the difference between the values of Ni:Pt atomic ratio obtained for the catalysts prepared via the $Ni(acac)_2$ route and those prepared via the $Ni(Cp)_2$ route. It can be clearly seen that the catalysts prepared via the $Ni(acac)_2$ route have a lower Ni:Pt atomic ratio which suggests that they have a higher concentration of Pt atoms at the surface than the catalysts prepared via the $Ni(Cp)_2$ route. The data suggest that the preparation of Ni/Pt/C catalysts via the $Ni(Cp)_2$ route leads to a more localised deposition of Ni on the Pt surface (clustering of Ni atoms). These data could also be used to argue that the rate of diffusion of the Ni atoms into the Pt bulk depends on the precursor used to prepare the catalysts. As the XPS is a surface sensitive method (10 atomic layers), it can be concluded that less Ni atoms are at the surface when using $Ni(acac)_2$ than when using $Ni(Cp)_2$. This is in accordance with the formation of larger Ni clusters when using $Ni(Cp)_2$ as precursor. This clustering effect was also observed in the XRD data shown in **Figure 3- 3** through **Figure 3- 7.**

3.1.4 TEM-EDX analysis

TEM-EDX analysis was performed on the 1 ML Ni/Pt/C *as prepared*, 500 and 900 ^{o}C electrocatalysts prepared via the $Ni(acac)_2$ and $Ni(Cp)_2$ route. TEM analysis was performed on the 0.5 and 2 ML Ni/Pt/C *as prepared*, 500 and 900 ^{o}C electrocatalysts prepared via the $Ni(acac)_2$ and $Ni(Cp)_2$ route. TEM micrographs at various magnifications with the scale bar corresponding to 100, 50, 10 and 5 nm for the 1 ML Ni/Pt/C 500 ^{o}C prepared via the $Ni(acac)_2$ route and 200 and 100 nm for that of the 1 ML Ni/Pt/C 500 ^{o}C prepared via the $Ni(Cp)_2$ route are shown in **Figure 3- 11** and **Figure 3- 12**, respectively, as examples of the data collected. For the other electrocatalysts, the data are included in **Appendix 2** and **Appendix 3** for the catalysts prepared via the $Ni(acac)_2$ and $Ni(Cp)_2$ routes, respectively.

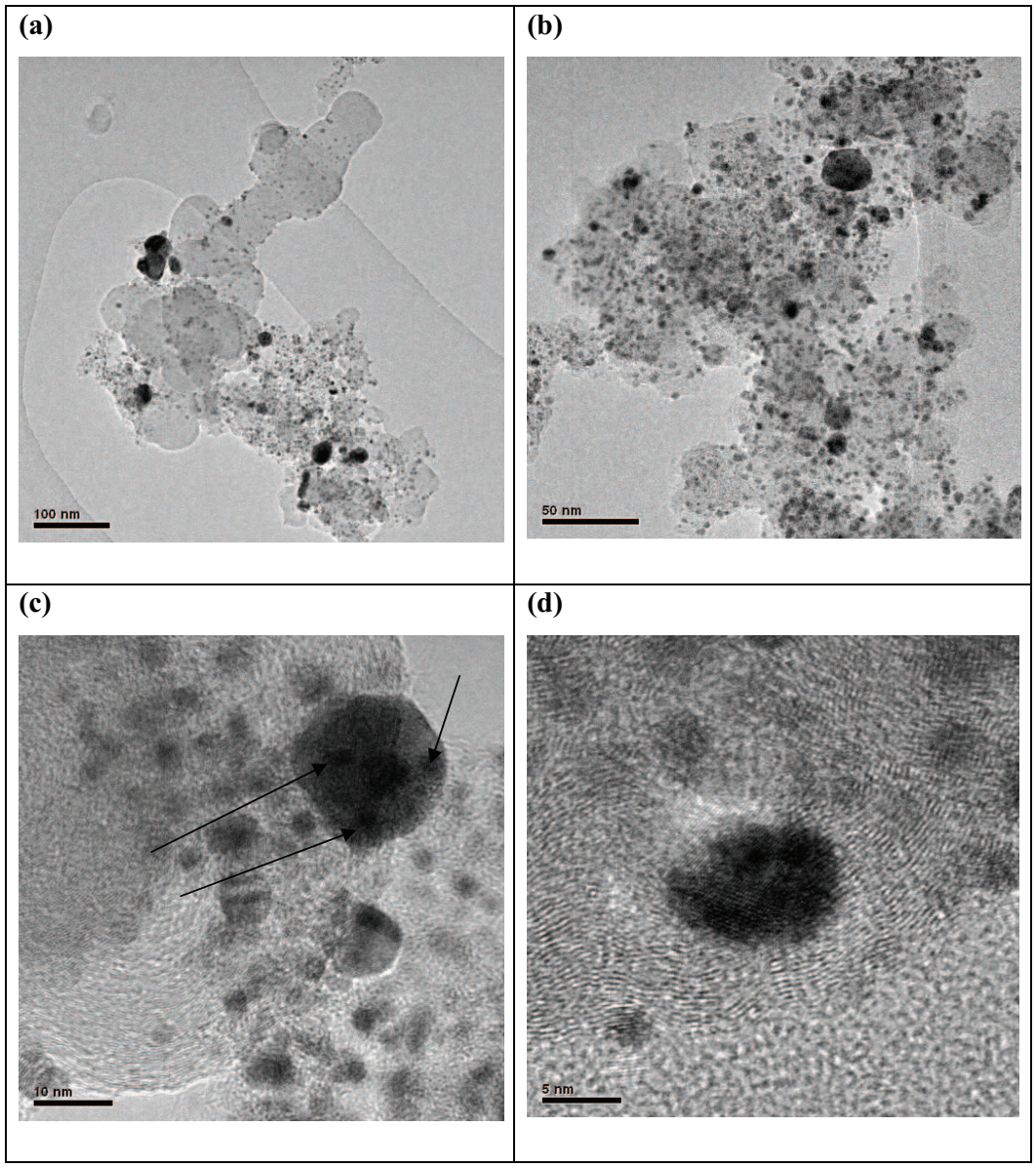

Figure 3- 11 TEM micrographs of 1 ML Ni/Pt/C 500 ºC via $Ni(acac)_2$ at different magnification 100 (a), 50 (b), 10 (c) and 5 nm (d). The arrows in (c) denote the particles that are not seen by the software when calculating the particle size distribution as it cannot differentiate them.

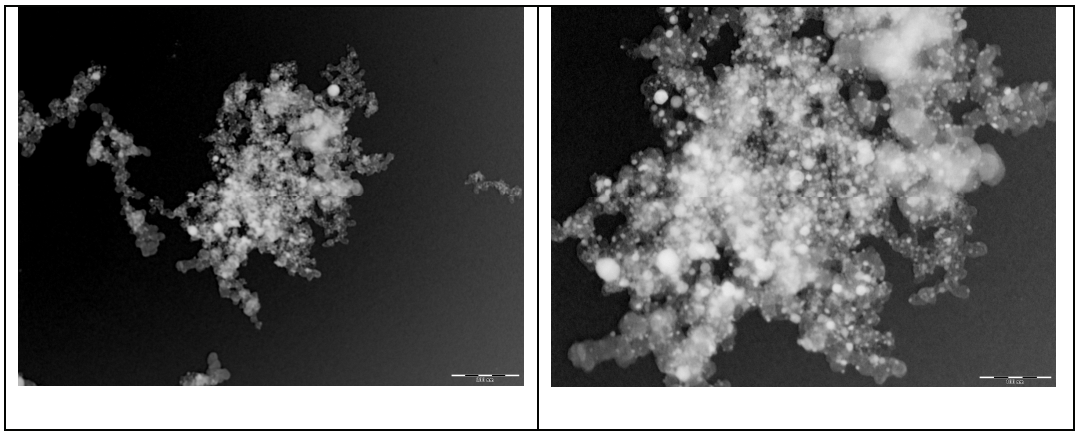

Figure 3- 12 TEM micrographs of 1 ML Ni/Pt/C 500 ºC via $Ni(Cp)_2$ at different magnification 200 (left) and 100 nm (right).

In this work, the main application of the TEM is to assess the particle size distribution of the different catalysts. From **Figure 3- 11** and **Figure 3- 12**, it can be observed that, the catalyst particles are well dispersed over the carbon support. It can also be noted that the deposition of Ni is not uniform as some areas are darker than others on the TEM pictures. Furthermore, as expected the average particle size increases as the heat treatment temperature increases (**Table 3-10**).

Figure 3- 13 shows the particle size distribution of 1 ML Ni/Pt/C *as prepared* prepared by via the $Ni(acac)_2$ route as an example of the data recorded. The particle size distribution follows a log normal-like shape exhibiting one maximum at *ca.* 1.50 nm. Similar particle size distributions were obtained for all the other electrocatalysts.

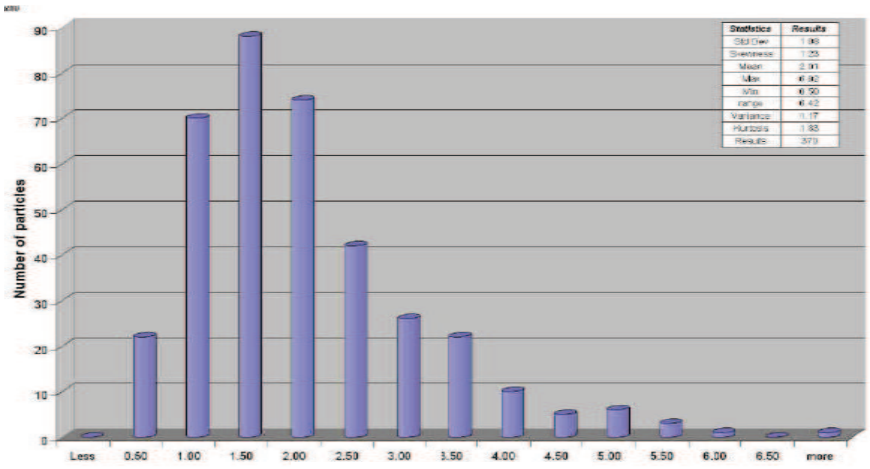

Figure 3- 13 Particle size distribution of 1 ML Ni/Pt/C *as prepared* prepared via the $Ni(acac)_2$ route.

Table 3-10 Summary of the mean particle size (nm) along with the associated error for all Ni/Pt/C electrocatalysts prepared via $Ni(acac)_2$ and $Ni(Cp)_2$ routes obtained by analysis of the TEM images.

Precursor / Annealing temperature	$Ni(acac)_2$			$Ni(Cp)_2$	
	0.5 ML*	**1 ML**	**2 ML***	**1 ML***	**2 ML***
As prepared	4.5 ± 1.7	2.0 ± 1.1	6.3 ± 2.3	6.1 ± 5.4	5.9 ± 1.8
200 °C		2.2 ± 1.5			
500 °C	9.4 ± 4.0	4.0 ± 4.1	7.3 ± 2.9	11.5 ± 8.5	14.0 ± 4.6
750 °C		6.1 ± 5.0			
900 °C	10.4 ± 9.6	6.1 ± 4.8	9.0 ± 5.3	11.3 ± 3.9	12.2 ± 4.8

* The average particle size and the error were estimated using 45 particles chosen at random.

** The average particle size and the error was estimated using 250 particles chosen at random

In most cases, the error associated with the mean particle size distribution is as big as the mean itself. This is due to the large particles being taken into account in the calculation of the standard deviation (**Equation 3-1**).

$$\sigma = \sqrt{\frac{\sum (x - \bar{x})^2}{n-1}} \qquad \textbf{Equation 3-1}$$

The main reasons for the large values obtained for the standard deviations are as follows. Firstly, the software used to determine the particle size regards each particle as being spherical, in other words, it determines the area of the particles and then calculates what the diameter would be for a spherical particle of the same area. In addition, the software does not differentiate between the different contrasts. So, if particles were to be agglomerated, it would assume that they are all just one particle see **Figure 3- 11c**. Secondly, the value obtained for the error associated with the average particle size can also be directly correlated to an inhomogeneous deposition of Ni onto the Pt/C. It can also be observed that the error associated with the *as prepared* samples is higher for the $Ni(Cp)_2$ samples than for the $Ni(acac)_2$ samples suggesting that the $Ni(acac)_2$ leads to a lower level of Ni clustering as was shown by the XPS and XRD data. (**Figure 3- 3** to **Figure 3- 10** and **Table 3-5** to **Table 3-9**).

The main use of the EDX function is to confirm the preparation of bimetallic particles. The EDX data of the 1 ML Ni/Pt/C 500 ^{o}C prepared via the $Ni(acac)_2$ route are shown in **Figure 3- 14** as an example of the data collected. The line profiles show that the Ni and Pt are present in the same area across a range of particles and that there are no isolated Ni particles and that no Ni had deposited onto the carbon support. This is good confirmation that the Ni specifically targets the Pt sites in the deposition process. The line profile for Ni/Pt/C prepared via the $Ni(Cp)_2$ was not performed as it has already been demonstrated that Ni specifically targets Pt/C. [28]

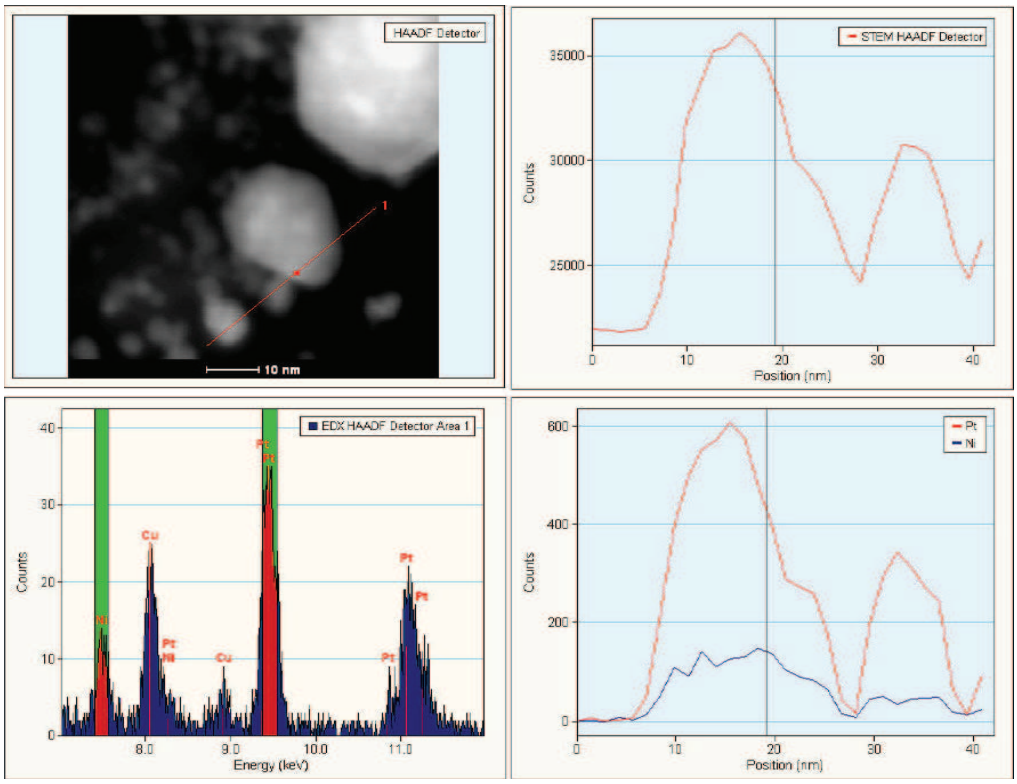

Figure 3- 14 TEM EDX line profile analysis for 1 ML Ni/Pt/C 500 ^{o}C via $Ni(acac)_2$. The upper left box shows the TEM image of the area under investigation. The EDX response for the red box is shown below the TEM image. The EDX responses across the red line labelled one are shown on the right hand side and in descending order show total counts, counts from Pt (red) and Ni (blue) respectively.

3.1.5 XANES and EXAFS analysis

XANES and EXAFS data were collected as boron nitrate pellets in atmospheres of air and hydrogen at the Pt L_3 edge. **Figure 3- 15** and **Figure 3- 16** show the XANES results for the Ni/Pt/C electrocatalysts prepared via $Ni(Cp)_2$ and $Ni(acac)_2$ routes, respectively.

(a)

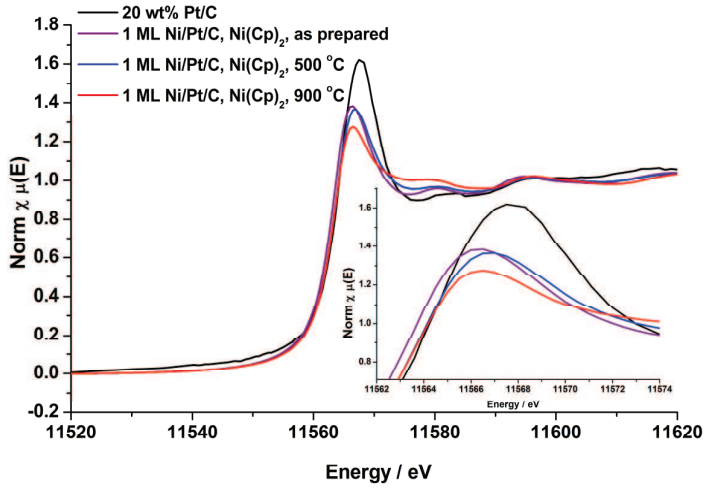

(b)

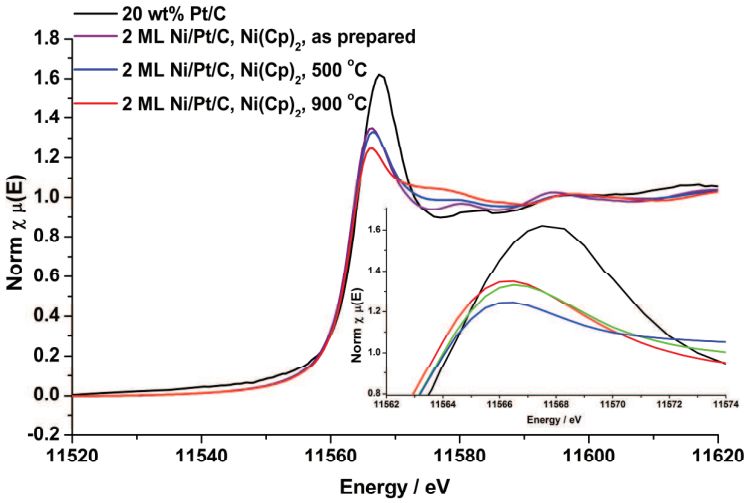

Figure 3- 15 Pt L_3 XANES of 1 and 2 ML Ni/Pt/C electrocatalysts prepared via $Ni(Cp)_2$ in air.

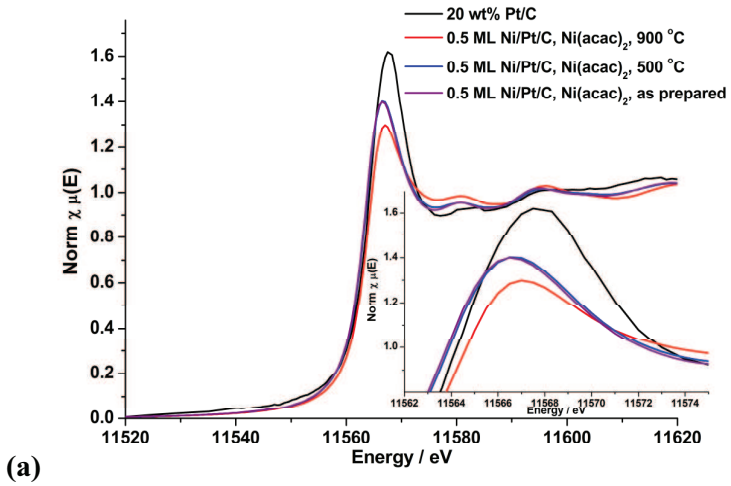

(a)

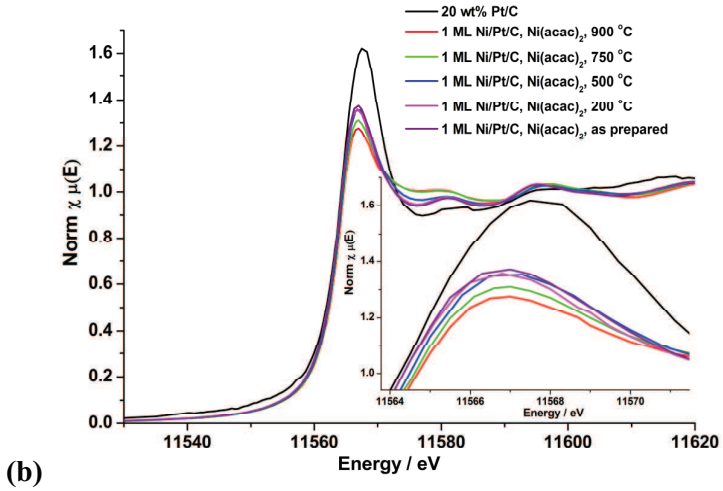

(b)

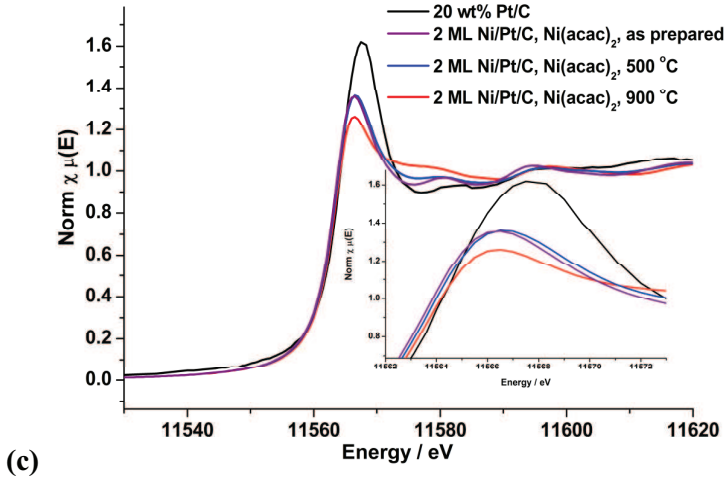

(c)

Figure 3- 16 Pt L_3 XANES of 0.5, 1 and 2 ML Ni/Pt/C electrocatalysts prepared via $Ni(acac)_2$ in air

The k-space EXAFS data along with the associated Fourier transforms collected in air for the Ni/Pt/C prepared the $Ni(acac)_2$ route and Ni/Pt/C prepared via the $Ni(Cp)_2$ route and 20 wt% Pt/C are presented in **Figure 3- 17** to **Figure 3- 19, Figure 3- 20** and **Figure 3- 21,** and **Figure 3- 22,** respectively**.** Similarly, the fitting parameters the Ni/Pt/C prepared the $Ni(acac)_2$ route and Ni/Pt/C prepared via the $Ni(Cp)_2$ route and 20 wt% Pt/C are presented in **Table 3-11** to **Table 3-14**, **Table 3-15** to **Table 3-16** and **Table 3-17**, respectively.

The k weighting of the k-space plot was set to two as it allows a good compromise between the contribution of the low Z atoms and the high Z atoms to the EXAFS data. Performing a Fourier transform on the k-space EXAFS data results in a plot that is related to the radial distribution of the scattering atoms (or neighbouring atoms). The data were fitted shell-by-shell and each shell was evaluated by its associated Debye-Waller factor (σ^2), coordination number (N) and the R_{EXAFS}. The fit was deemed acceptable when the R_{EXAFS} reached a value below 30 and that the σ^2, N for each shell and the R_{EXAFS} did not significantly changed.

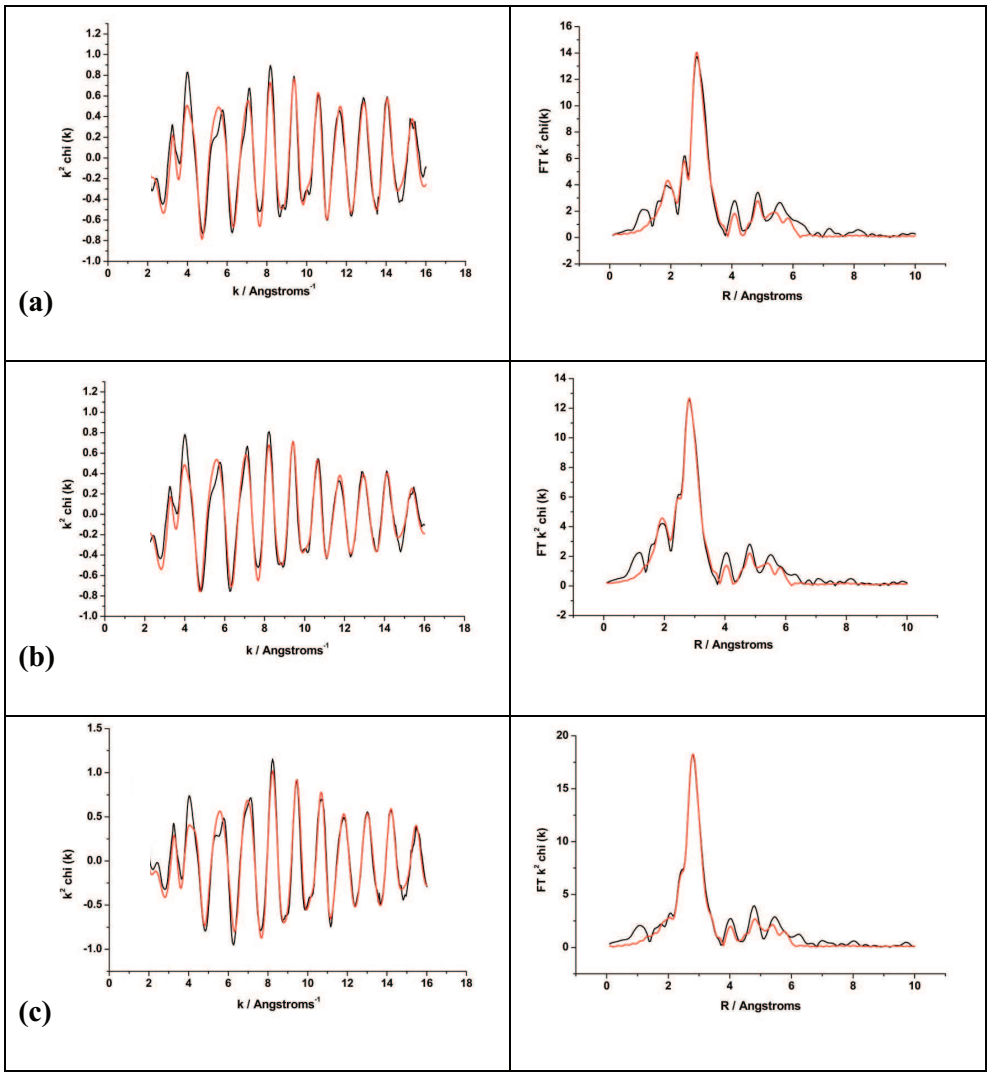

Figure 3- 17 (left) k^2 weighted experimental data and fit along with (right) the Fourier transform for 0.5 ML Ni/Pt/C (prepared via $Ni(acac)_2$ route) (a) as prepared, (b) 500 (c) 900 °C acquired in air at Pt L_3 edge. Data (black line) and fit (red line). (y-axis for k^2 plot for a, b and c has units of $Å^{-2}$).

Table 3-11 Structural parameters for 0.5 monolayer Ni/Pt/C (prepared via $Ni(acac)_2$ route) as prepared, 500 and 900 °C acquired in air by fitting the Pt L_3 edge EXAFS data. Un1 refers to multi-scattering process occurring in the same shell.

Condition	Ni/Pt/C 0.5 monolayer (via $Ni(acac)_2$ route) Calculated parameters (Pt L_3)					
	Shell	**N**	**R / Å**	**$2\sigma^2$ / $Å^2$**	**Ef / eV**	**R_{exafs} / %**
As prepared in air	Pt-O	1.1 ± 0.1	2.040 ± 0.012	0.013 ± 0.006	-9.7 ± 0.2	25.0
	Pt-Pt (Un1)	6.6 ± 0.4	2.756 ± 0.002	0.011 ± 0.001		
	Pt-Pt	0.9 ± 0.7	3.904 ± 0.019	0.008 ± 0.005		
	Pt-Pt	8.6 ± 1.7	4.800 ± 0.011	0.017 ± 0.003		
	Pt-Pt (Un1)	6.6 ± 0.4	5.428 ± 0.015	0.014 ± 0.003		
500 °C in air	Pt-O	1.2 ± 0.1	2.040 ± 0.010	0.013 ± 0.005	-9.8 ± 0.2	23.8
	Pt-Ni	0.3 ± 0.3	2.652 ± 0.018	0.016 ± 0.003		
	Pt-Pt(Un1)	5.9 ± 0.5	2.743 ± 0.002	0.012 ± 0.001		
	Pt-Pt	0.6 ± 0.6	3.879 ± 0.026	0.009 ± 0.008		
	Pt-Pt	7.9 ± 1.6	4.780 ± 0.013	0.019 ± 0.004		
	Pt-Pt (Un1)	5.9 ± 0.5	5.407 ± 0.016	0.006 ± 0.009		
900 °C in air	Pt-O	0.5 ± 0.1	2.049 ± 0.026	0.011 ± 0.011	-10.4 ± 0.3	22.1
	Pt-Ni	1.2 ± 0.4	2.677 ± 0.009	0.011 ± 0.005		
	Pt-Pt(Un1)	6.0 ± 0.5	2.732 ± 0.003	0.010 ± 0001		
	Pt-Pt	1.6 ± 0.8	3.868 ± 0.018	0.012 ± 0.005		
	Pt-Pt	8.0 ± 1.6	4.752 ± 0.010	0.016 ± 0.003		
	Pt-Pt (Un1)	6.0 ± 0.5	5.380 ± 0.014	0.014 ± 0.002		

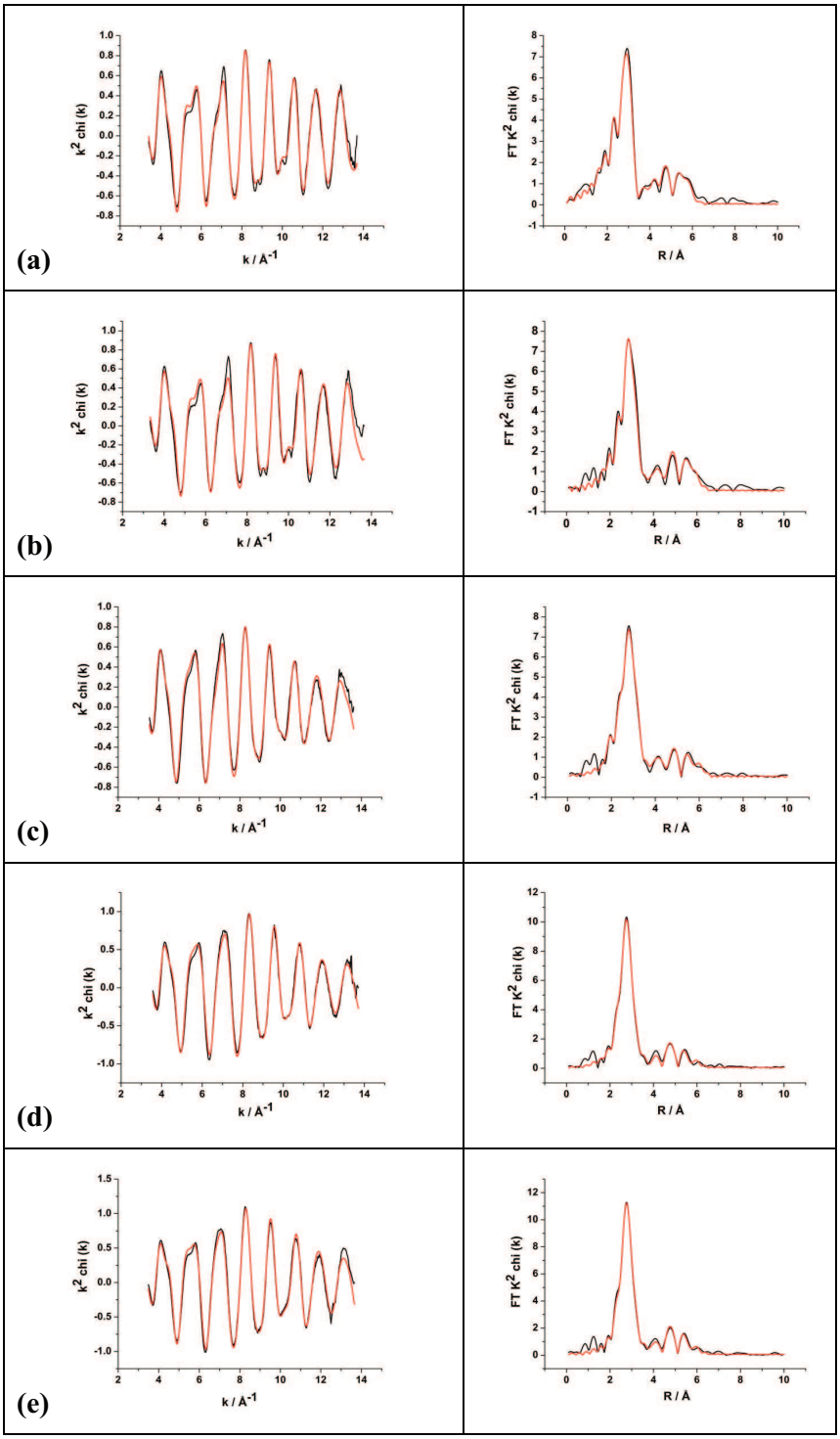

Figure 3- 18 (left) k^2 weighted experimental data and fit along with (right) the Fourier transform for 1 ML Ni/Pt/C (prepared via $Ni(acac)_2$ route) (a) as prepared, (b)200, (c) 500, (d) 750 and (e) 900 ^oC acquired in air at Pt L_3 edge. Data (black line) and fit (red line). (y-axis for k^2 plot a, b, c, d and e has units of $Å^{-2}$).

Table 3-12 Structural parameters for 1 monolayer Ni/Pt/C (prepared via $Ni(acac)_2$ route) at different annealing temperatures acquired in air by fitting the Pt L_3 edge EXAFS data. Un1 refers to multi-scattering process occurring in the same shell.

Condition	Ni/Pt/C 1 monolayer via $Ni(acac)_2$ route Calculated parameters (Pt L_3)					
	Shell	**N**	**R / Å**	**$2\sigma^2$ / $Å^2$**	**Ef / eV**	**R_{exafs} / %**
As prepared in air	Pt-O	0.8 ± 0.1	2.012 ± 0.008	0.018 ± 0.003	-12.4 ± 0.3	12.6
	Pt-Ni	0.3 ± 0.1	2.653 ± 0.028	0.019 ± 0.006		
	Pt-Pt (Un1)	6.6 ± 0.1	2.758 ± 0.001	0.012 ± 0.001		
	Pt-Pt	1.4 ± 0.3	3.872 ± 0.009	0.010 ± 0.001		
	Pt-Ni	2.1 ± 0.5	4.270 ± 0.017	0.023 ± 0.003		
	Pt-Pt	3.4 ± 0.5	4.756 ± 0.008	0.007 ± 0.001		
	Pt-Ni	3.3 ± 0.9	5.153 ± 0.012	0.007 ± 0.001		
	Pt-Ni	2.1 ± 0.5	5.364 ± 0.015	0.006 ± 0.001		
	Pt-Pt (Un1)	6.6 ± 0.1	5.552 ± 0.011	0.024 ± 0.002		

	Shell	**N**	**R / Å**	**$2\sigma^2$ / $Å^2$**	**Ef / eV**	**R_{exafs} / %**
200 °C in air	Pt-O	1.1 ± 0.1	2.023 ± 0.012	0.028 ± 0.005	-13.2 ± 0.3	17.7
	Pt-Ni	0.3 ± 0.1	2.677 ± 0.016	0.010 ± 0.003		
	Pt-Pt (Un1)	6.0 ± 0.1	2.757 ± 0.002	0.012 ± 0.001		
	Pt-Pt	2.2 ± 0.6	3.875 ± 0.015	0.015 ± 0.003		
	Pt-Ni	3.0 ± 1.0	4.281 ± 0.025	0.030 ± 0.006		
	Pt-Pt	4.4 ± 1.1	4.769 ± 0.013	0.009 ± 0.001		
	Pt-Ni	3.2 ± 1.8	5.160 ± 0.036	0.011 ± 0.003		
	Pt-Ni	2.5 ± 1.5	5.384 ± 0.028	0.009 ± 0.002		
	Pt-Pt (Un1)	6.0 ± 0.1	5.545 ± 0.016	0.021 ± 0.002		

	Shell	**N**	**R / Å**	**$2\sigma^2$ / $Å^2$**	**Ef / eV**	**R_{exafs} / %**
500 °C in air	Pt-O	0.6 ± 0.1	2.004 ± 0.009	0.011 ± 0.002	-10.9 ± 0.2	13.8
	Pt-Ni	0.7 ± 0.1	2.634 ± 0.006	0.013 ± 0.001		
	Pt-Pt (Un1)	6.5 ± 0.2	2.727 ± 0.001	0.014 ± 0.001		
	Pt-Pt	1.4 ± 0.3	3.837 ± 0.011	0.009 ± 0.002		
	Pt-Ni	0.9 ± 0.3	4.241 ± 0.018	0.010 ± 0.003		
	Pt-Pt	1.8 ± 0.5	4.720 ± 0.015	0.007 ± 0.001		
	Pt-Ni	2.4 ± 1.0	5.083 ± 0.017	0.011 ± 0.002		
	Pt-Ni	1.4 ± 1.0	5.316 ± 0.063	0.019 ± 0.008		
	Pt-Pt (Un1)	6.5 ± 0.2	5.500 ± 0.014	0.027 ± 0.001		

Table 3-13 (Sequel) Structural parameters for 1 monolayer Ni/Pt/C (prepared via $Ni(acac)_2$ route) at different annealing temperatures acquired in air by fitting the Pt L_3 edge EXAFS data. Un1 refers to multi-scattering process occurring in the same shell.

	Shell	N	R / Å	$2\sigma^2$ / $Å^2$	Ef / eV	R_{exafs} / %
750 ºC in air	Pt-O	0.6 ± 0.1	1.997 ± 0.019	0.033 ± 0.006	-10.4 ± 0.3	11.8
	Pt-Ni	2.1 ± 0.1	2.646 ± 0.003	0.015 ± 0.001		
	Pt-Pt (Un1)	5.8 ± 0.2	2.706 ± 0.001	0.013 ± 0.001		
	Pt-Pt	1.2 ± 0.2	3.827 ± 0.009	0.009 ± 0.002		
	Pt-Pt	2.1 ± 0.5	4.705 ± 0.010	0.009 ± 0.001		
	Pt-Ni	1.3 ± 0.3	4.626 ± 0.012	0.011 ± 0.003		
	Pt-Ni	1.5 ± 0.7	5.322 ± 0.019	0.013 ± 0.004		
	Pt-Pt (Un1)	5.8 ± 0.2	5.431 ± 0.013	0.027 ± 0.002		

	Shell	N	R / Å	$2\sigma^2$ / $Å^2$	Ef / eV	R_{exafs} / %
900 ºC in air	Pt-O	0.7 ± 0.1	2.044 ± 0.026	0.046 ± 0.010	-10.4 ± 0.2	12.5
	Pt-Ni	2.1 ± 0.1	2.662 ± 0.003	0.014 ± 0.001		
	Pt-Pt (Un1)	6.0 ± 0.1	2.711 ± 0.001	0.012 ± 0.001		
	Pt-Pt	1.4 ± 0.2	3.829 ± 0.008	0.009 ± 0.001		
	Pt-Ni	2.1 ± 0.4	4.643 ± 0.012	0.014 ± 0.002		
	Pt-Pt	2.5 ± 0.4	4.719 ± 0.009	0.008 ± 0.001		
	Pt-Ni	1.6 ± 0.7	5.321 ± 0.020	0.013 ± 0.004		
	Pt-Pt (Un1)	6.0 ± 0.2	5.456 ± 0.013	0.028 ± 0.002		

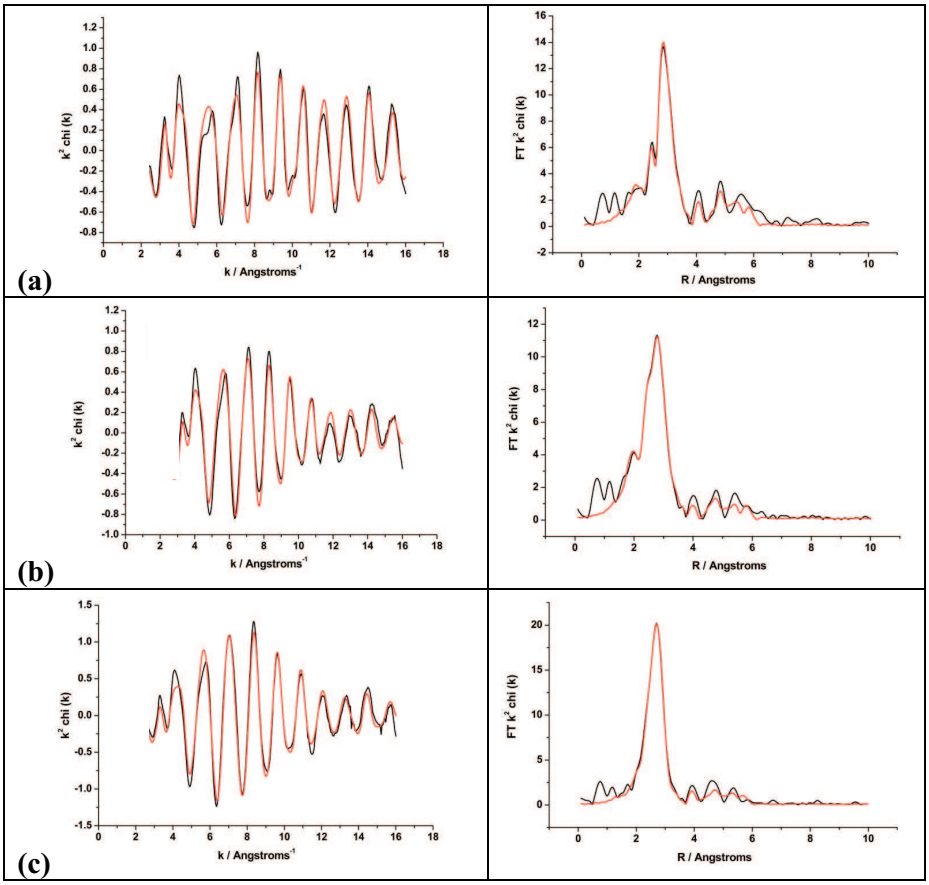

Figure 3- 19 (left) k^2 weighted experimental data and fit along with (right) the Fourier transform for 2 ML Ni/Pt/C (prepared via $Ni(acac)_2$ route) (a) as prepared, (b) 500 (c) 900 °C acquired in air at Pt L_3 edge. Data (black line) and fit (red line). (y-axis for k^2 plot a, b, and c has units of $Å^{-2}$).

Table 3-14 Structural parameters for 2 monolayer Ni/Pt/C (prepared via $Ni(acac)_2$ route) as prepared, 500 and 900 °C acquired in air by fitting the Pt L_3 edge EXAFS data. Un1 refers to multi-scattering process occurring in the same shell.

Condition	Ni/Pt/C 2 monolayer (via $Ni(acac)_2$ route) Calculated parameters (Pt L_3)					
	Shell	**N**	**R / Å**	**$2\sigma^2$ / $Å^2$**	**Ef / eV**	**R_{exafs} / %**
As prepared in air	Pt-O	0.8 ± 0.1	2.043 ± 0.016	0.017 ± 0.009	-10.1 ± 0.2	23.7
	Pt-Pt (Un1)	6.7 ± 0.4	2.756 ± 0.002	0.011 ± 0.001		
	Pt-Pt	1.1 ± 0.7	3.908 ± 0.018	0.009 ± 0.005		
	Pt-Pt	8.6 ± 1.6	4.798 ± 0.011	0.017 ±0.003		
	Pt-Pt (Un1)	6.7 ± 0.4	5.428 ± 0.014	0.015 ± 0.003		
500 °C in air	Pt-O	1.0 ± 0.1	2.043 ± 0.012	0.013 ± 0.005	-9.9 ± 0.3	26.6
	Pt-Ni	1.3 ± 0.4	2.618 ± 0.007	0.012 ± 0.003		
	Pt-Pt(Un1)	5.0 ± 0.5	2.726 ± 0.003	0.014 ±0.001		
	Pt-Pt	0.5 ± 0.7	3.842 ± 0.054	0.013 ± 0.015		
	Pt-Pt	5.8 ± 1.6	4.748 ± 0.020	0.022 ± 0.006		
	Pt-Pt (Un1)	5.0 ± 0.5	5.368 ± 0.025	0.019 ± 0.005		
900 °C in air	Pt-O	0.5 ± 0.1	2.087 ± 0.029	0.013 ± 0.012	-10.1 ± 0.4	23.5
	Pt-Ni	3.9 ± 0.5	2.627 ± 0.004	0.014 ± 0.002		
	Pt-Pt(Un1)	3.8 ± 0.5	2.690 ± 0.004	0.011 ± 0.001		
	Pt-Pt	1.2 ± 0.8	3.791 ± 0.026	0.012 ± 0.007		
	Pt-Pt	5.9 ± 1.8	4.681 ± 0.018	0.019 ± 0.005		
	Pt-Pt (Un1)	3.8 ± 0.5	5.306 ± 0.022	0.013 ± 0.004		

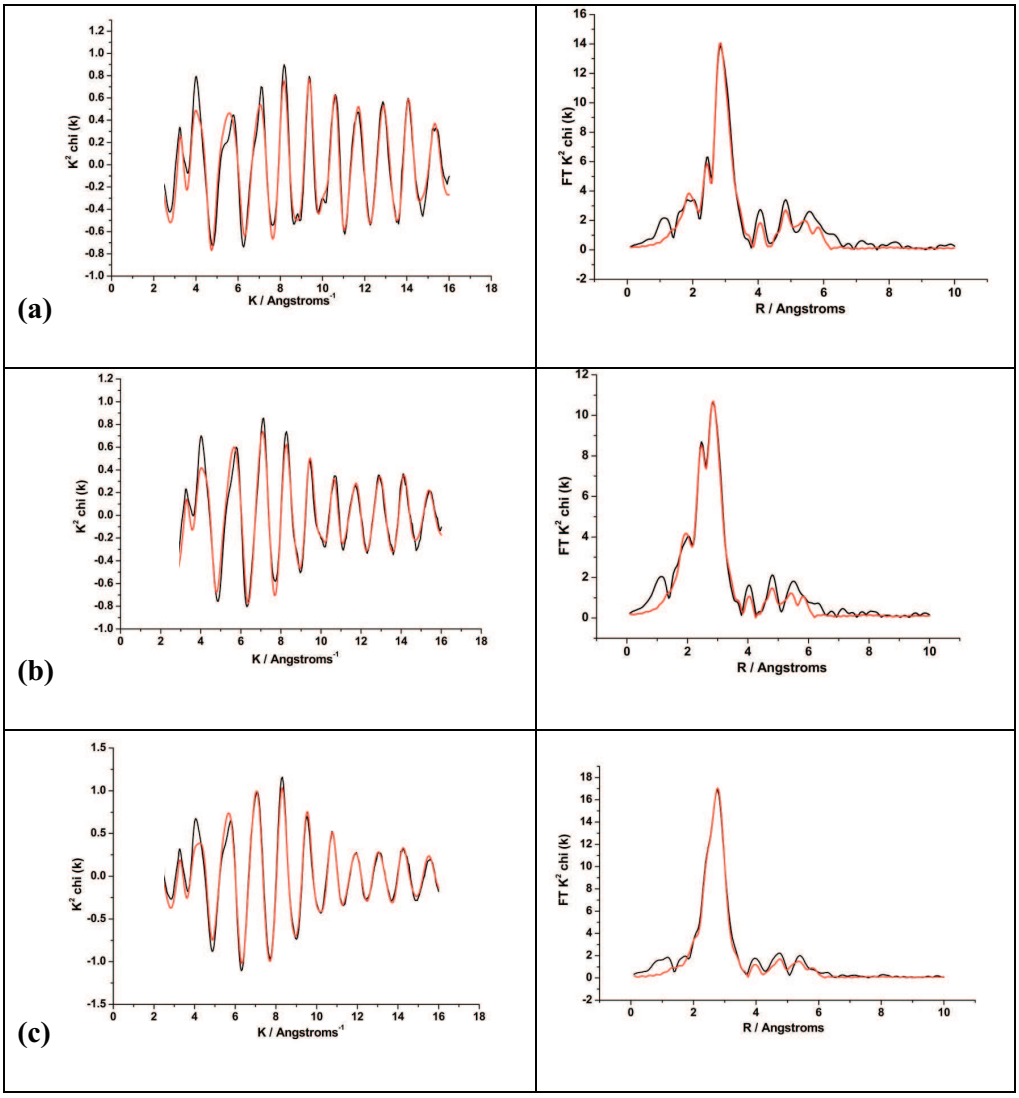

Figure 3- 20 (left) k^2 weighted experimental data and fit along with (right) the Fourier transform for 1ML Ni/Pt/C (prepared via $Ni(Cp)_2$ route) (a) as prepared, (b) 500 (c) 900 °C acquired in air at Pt L_3 edge. Data (black line) and fit (red line). (y-axis for k^2 plot a, band c has units of $Å^{-2}$).

Table 3-15 Structural parameters for 1 monolayer Ni/Pt/C (prepared via $Ni(Cp)_2$ route) as prepared, 500 and 900 °C acquired in air by fitting the Pt L_3 edge EXAFS data. Un1 refers to multi-scattering process occurring in the same shell.

Condition	Ni/Pt/C 1 monolayer (via $Ni(Cp)_2$ route) Calculated parameters (Pt L_3)					
	Shell	**N**	**R / Å**	**$2\sigma^2$ / $Å^2$**	**Ef / eV**	**R_{exafs} / %**
As prepared in air	Pt-O	0.9 ± 0.1	2.033 ± 0.013	0.014 ± 0.006	-10.0 ± 0.2	24.0
	Pt-Pt (Un1)	6.6 ± 0.4	2.753 ± 0.002	0.011 ± 0.001		
	Pt-Pt	0.9 ± 0.6	3.892 ± 0.017	0.008 ± 0.005		
	Pt-Pt	8.6 ± 1.5	4.796 ± 0.011	0.017 ± 0.003		
	Pt-Pt (Un1)	6.6 ± 0.4	5.428 ± 0.014	0.017 ± 0.003		
500 °C in air	**Shell**	**N**	**R / Å**	**$2\sigma^2$ / $Å^2$**	**Ef / eV**	**R_{exafs} / %**
	Pt-O	0.9 ± 0.1	2.037 ± 0.012	0.012 ± 0.005	-10.1 ± 0.3	24.5
	Pt-Ni	1.2 ± 0.4	2.596 ± 0.008	0.012 ± 0.004		
	Pt-Pt (Un1)	5.1 ± 0.5	2.739 ± 0.003	0.012 ± 0.001		
	Pt-Pt	0.4 ± 0.5	3.873 ± 0.031	0.007 ± 0.009		
	Pt-Pt	6.1 ± 1.5	4.782 ± 0.018	0.016 ± 0.004		
	Pt-Pt (Un1)	5.1 ± 0.5	5.405 ± 0.018	0.021 ± 0.005		
900 °C in air	**Shell**	**N**	**R / Å**	**$2\sigma^2$ / $Å^2$**	**Ef / eV**	**R_{exafs} / %**
	Pt-O	0.3 ± 0.1	2.072 ± 0.025	0.005 ± 0.008	-10.2 ± 0.3	21.5
	Pt-Ni (Un1)	3.1 ± 0.4	2.632 ± 0.005	0.015 ± 0.002		
	Pt-Pt (Un1)	4.5 ± 0.4	2.717 ± 0.003	0.011 ± 0.001		
	Pt-Pt	1.4 ± 0.9	3.841 ± 0.035	0.017 ± 0.010		
	Pt-Pt	6.9 ± 1.6	4.737 ± 0.018	0.020 ± 0.005		
	Pt-Ni (Un1)	3.1 ± 0.4	5.253 ± 0.040	0.020 ± 0.009		
	Pt-Pt (Un1)	4.5 ± 0.4	5.373 ± 0.034	0.019 ± 0.006		

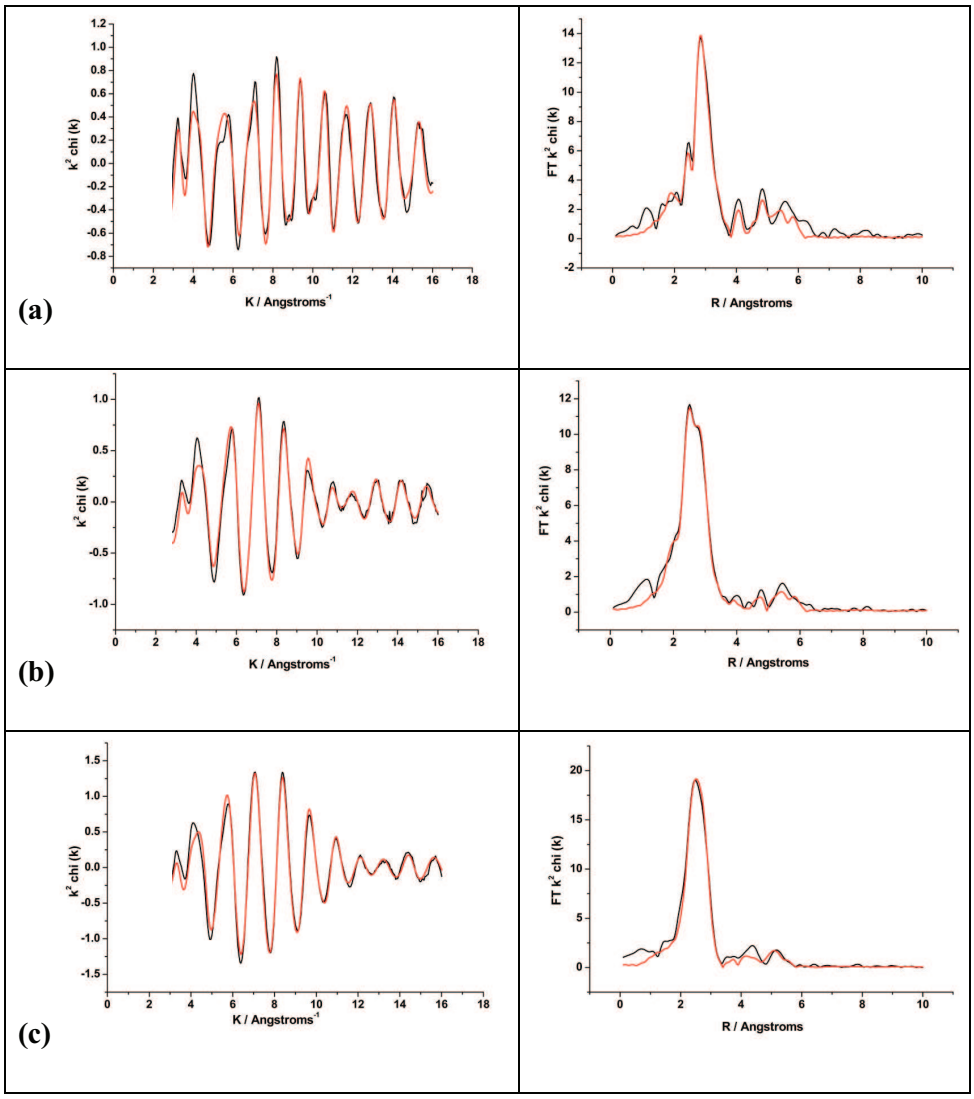

Figure 3- 21 (left) k^2 weighted experimental data and fit along with (right) the Fourier transform for 2 ML Ni/Pt/C (prepared via $Ni(Cp)_2$ route) (a) as prepared, (b) 500 (c) 900 °C acquired in air at Pt L_3 edge. Data (black line) and fit (red line). (y-axis for k^2 plot a, b and c has units of $Å^{-2}$).

Table 3-16 Structural parameters for 2 monolayer Ni/Pt/C (prepared via $Ni(Cp)_2$ route) as prepared, 500 and 900 °C acquired in air by fitting the Pt L_3 edge EXAFS data. Un1 refers to multi-scattering process occurring in the same shell.

Condition	Ni/Pt/C 2 monolayer (via $Ni(Cp)_2$ route) Calculated parameters (Pt L_3)					
	Shell	**N**	**R / Å**	**$2\sigma^2$ / $Å^2$**	**Ef / eV**	**R_{exafs} / %**
As prepared in air	Pt-O	0.7 ± 0.1	2.038 ± 0.018	0.014 ± 0.008	-10.1 ± 0.3	24.6
	Pt-Pt (Un1)	6.7 ± 0.4	2.754 ± 0.002	0.012 ± 0.001		
	Pt-Pt	1.3 ± 0.8	3.900 ± 0.018	0.011 ± 0.005		
	Pt-Pt	8.4 ± 1.6	4.796 ± 0.011	0.017 ± 0.003		
	Pt-Pt (Un1)	6.7 ± 0.4	5.425 ± 0.014	0.015 ± 0.003		
	Shell	**N**	**R / Å**	**$2\sigma^2$ / $Å^2$**	**Ef / eV**	**R_{exafs} / %**
500 °C in air	Pt-O	0.7 ± 0.1	2.048 ± 0.015	0.012 ± 0.006	-10.2 ± 0.3	25.0
	Pt-Ni (Un1)	2.5 ± 0.4	2.594 ± 0.004	0.014 ± 0.002		
	Pt-Pt (Un1)	3.9 ± 0.4	2.726 ± 0.004	0.013 ± 0.001		
	Pt-Pt	0.5 ± 0.9	3.792 ± 0.112	0.023 ± 0.038		
	Pt-Pt	5.3 ± 1.6	4.771 ± 0.034	0.027 ± 0.010		
	Pt-Ni (Un1)	2.5 ± 0.4	5.296 ± 0.032	0.016 ± 0.007		
	Pt-Pt (Un1)	3.9 ± 0.4	5.411 ± 0.029	0.017 ± 0.006		
	Shell	**N**	**R / Å**	**$2\sigma^2$ / $Å^2$**	**Ef / eV**	**R_{exafs} / %**
900 °C in air	Pt-Ni (Un1)	5.0 ± 0.5	2.606 ± 0.004	0.015 ± 0.001	-10.7 ± 0.4	24.4
	Pt-Pt (Un1)	2.9 ± 0.5	2.694 ± 0.005	0.011 ± 0.001		
	Pt-Pt	1.0 ± 1.0	3.782 ±0.044	0.016 ± 0.012		
	Pt-Pt	5.7 ± 2.1	4.662 ± 0.030	0.024 ± 0.009		
	Pt-Ni (Un1)	5.0 ± 0.5	5.274 ± 0.063	0.019 ± 0.015		
	Pt-Pt (Un1)	2.9 ± 0.5	5.309 ± 0.094	0.024 ± 0.018		

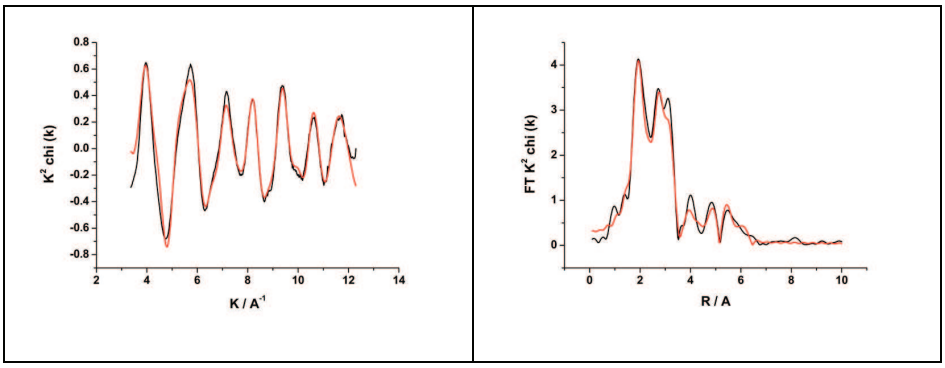

Figure 3- 22 (left) k^2 weighted experimental data and fit along with (right) the Fourier transform for 20 wt% Pt/C acquired in air at Pt L_3 edge. Data (black line) and fit (red line). (y-axis for k^2 plot has units of $Å^{-2}$).

Table 3-17 Structural parameters for 20 wt% Pt/C catalysts acquired in air by fitting the Pt L_3 edge EXAFS data.

Shell	*N*	*R* / Å	$2\sigma^2$ / $Å^2$	E_f / eV	R_{exafs} / %
Pt-O	1.7 ± 0.1	2.008 ± 0.004	0.010 ± 0.001	-11.3690 ± 0.2842	20.6
Pt-Pt (Un1)	3.6 ± 0.2	2.748 ± 0.003	0.012 ± 0.001		
Pt-Pt	1.8 ± 0.4	3.900 ± 0.013	0.014 ± 0.003		
Pt-Pt	2.8 ± 0.6	4.789 ± 0.012	0.012 ± 0.003		
Pt-Pt (Un1)	3.6 ± 0.2	5.546 ± 0.014	0.021 ± 0.003		

The absorption at the Pt L_3 edge (11564 eV) corresponds to the $2p_{3/2}$ to 5*d* electronic transition and the magnitude of the peak at the edge is directly related to the Pt 5*d* electronic density of states. The greater the area under this peak, the lower the occupancy. It can be seen that the magnitude of the white line decreases as the annealing temperature increases. This phenomenon can be attributed to a decrease in the number of the oxygen neighbours as temperature increases (**Table 3-18**) and is related to a decrease in the electron withdrawing effect on Pt, lowering the magnitude of the white line. From **Table 3-18**, the number of Pt-O neighbours for 20 wt% Pt/C is 1.7 ± 0.1 and ranges from 1.1 ± 0.1 to 0.7 ± 0.1 for the *as prepared* Ni/Pt/C catalysts. The decrease in Pt-O neighbours was expected as Ni was deposited on the Pt surface. The deposition of Ni on the Pt surface lowers the amount of surface Pt available and as a consequence a lower amount of Pt oxide is observed when the catalyst is in air. A similar difference is observed between the *as prepared* and the *900 °C* catalysts. This decrease in the magnitude of the white line can be attributed to the formation of a PtNi alloy phase as suggested by the

XRD data. The formation of a PtNi phase reduces the amount of "free" Pt sites and inevitably lowers the number of Pt-O neighbours.

Table 3-18 Summary of the Pt-O neighbours for all Ni/Pt/C electrocatalysts and 20 wt% Pt/C obtained from the Pt L_3 EXAFS data collected in air (Table 3-11 to Table 3-16).

Precursor / Annealing temperature	$Ni(acac)_2$			$Ni(Cp)_2$	
	0.5 ML	**1 ML**	**2 ML**	**1 ML**	**2 ML**
As prepared	1.1 ± 0.1	0.8 ± 0.1	0.8 ± 0.1	0.9 ± 0.1	0.7 ± 0.1
200 °C		1.1 ± 0.1			
500 °C	1.2 ± 0.1	0.6 ± 0.1	1.0 ± 0.1	0.9 ± 0.1	0.7 ± 0.1
750 °C		0.6 ± 0.1			
900 °C	0.5 ± 0.1	0.7 ± 0.1	0.5 ± 0.1	0.3 ± 0.1	0
20 wt% Pt/C	1.7 ± 0.1				

If we were to assume that the Ni is evenly distributed on the Pt surface, as the fraction of Ni increases, the number of Pt-O neighbour should decrease, reaching zero as the fraction of Ni reaches 1 monolayer. However, from **Table 3-18** it can be clearly seen that Pt-O neighbours are observed for all Ni/Pt/C catalysts. The presence of oxygen neighbours suggests the formation of Ni clusters on the Pt surface instead of a smooth Ni layer as depicted by **Figure 3- 23**. The idea of cluster formation is further supported by the data for the 2 ML Ni/Pt/C catalysts. From the ICP-OES data, it was shown that the entire Ni precursor had been deposited onto the Pt/C and the EDX data proved that the Ni was specifically targeting the Pt sites. From the EXAFS data, the number of Pt-O neighbour for the 1 ML and 2 ML Ni/Pt/C electrocatalysts prepared via both routes are within the error estimates of each other, 0.8 ± 0.1 for $Ni(acac)_2$ and 0.7 ± 0.1 and 0.9 ± 0.1 for $Ni(Cp)_2$. In other words, despite depositing more Ni, a similar amount of Pt-O neighbours is observed which strongly suggests a clustering of Ni atoms. The particle size also affects the number of Pt-O neighbours, however, all particle sizes were within error of each other (**Figure 3-10**) therefore it is impossible to conclude of any particle size effect.

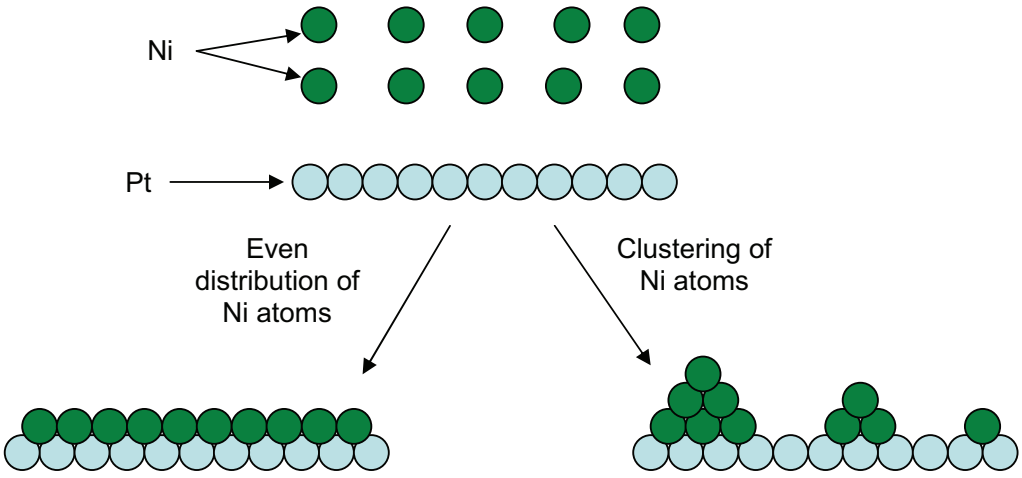

Figure 3- 23 Schematic diagram to illustrate how Ni can form clusters or form an evenly distributed layer on the Pt surface

The k-space EXAFS data along with the associated Fourier transform collected in air for the Ni/Pt/C prepared the $Ni(acac)_2$ route and Ni/Pt/C prepared via the $Ni(Cp)_2$ route and 20 wt% Pt/C are presented in **Figure 3- 24** to **Figure 3- 26, Figure 3- 27** and **Figure 3- 28,** and **Figure 3- 29,** respectively**.** Similarly, the fitting parameters the Ni/Pt/C prepared the $Ni(acac)_2$ route and Ni/Pt/C prepared via the $Ni(Cp)_2$ route and 20 wt% Pt/C are presented in **Table 3-19** to **Table 3-24**, **Table 3-25** to **Table 3-28**, and **Table 3-29**, respectively.

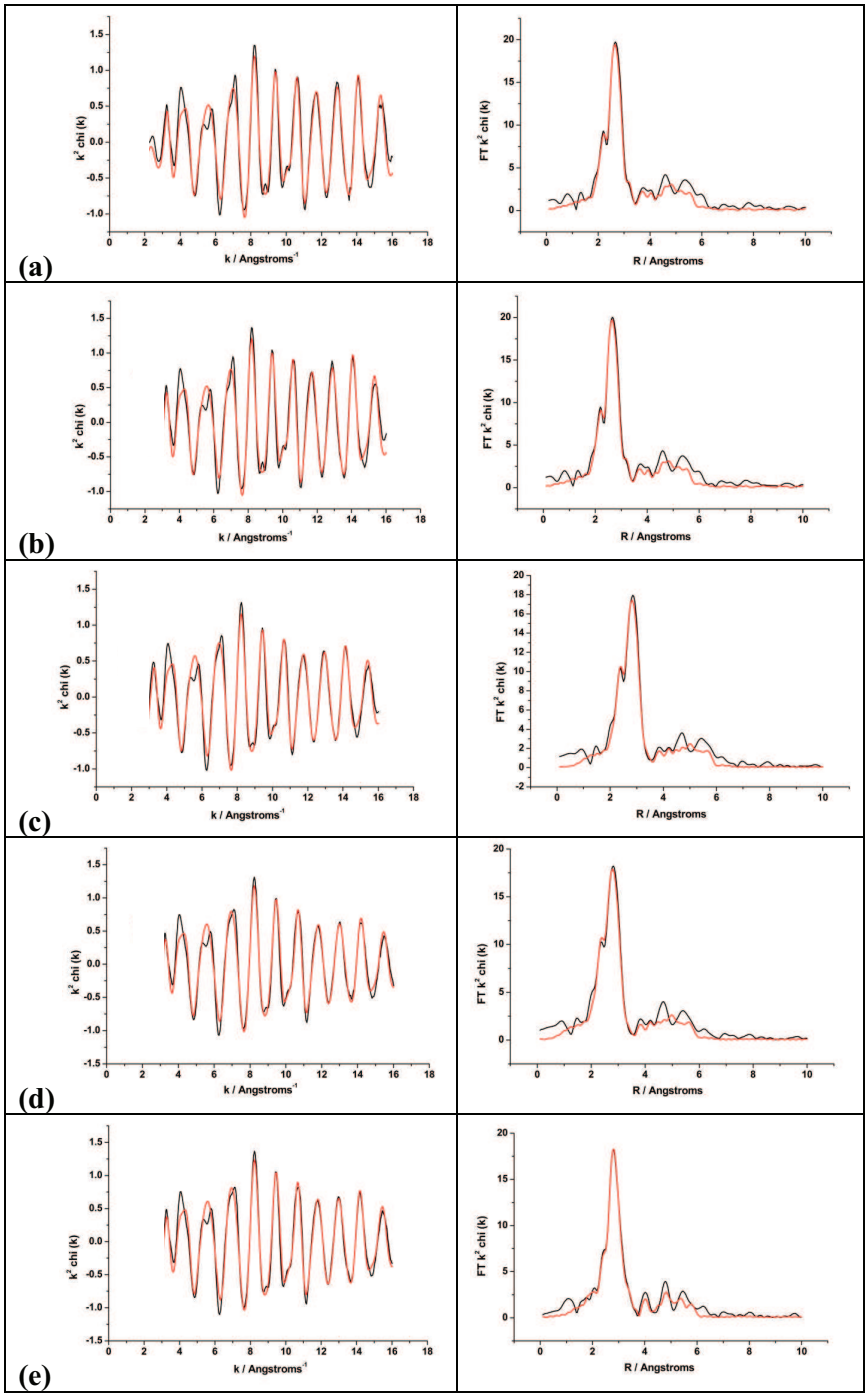

Figure 3- 24 (left) k^2 weighted experimental data and fit along with (right) the Fourier transform for 0.5 ML Ni/Pt/C (prepared via $Ni(acac)_2$ route) as prepared (a), 200 (b), 500 (c), 750 (d) and 900 °C (e) acquired in H_2 at Pt L_3 edge. Data (black line) and fit (red line). (y-axis for k^2 plot a, b, c, d and e has units of $Å^{-2}$).

Table 3-19 Structural parameters for 0.5 monolayer Ni/Pt/C (prepared via $Ni(acac)_2$ route) as prepared, 200, 500, 750 and 900 °C acquired in H_2 by fitting the Pt L_3 edge EXAFS data. Un1 refers to multi-scattering process occurring in the same shell.

Condition	Ni/Pt/C 0.5 monolayer via $Ni(acac)_2$ route Calculated parameters (Pt L_3)					
	Shell	**N**	**R / Å**	**$2\sigma^2$ / $Å^2$**	**Ef / eV**	**R_{exafs} / %**
As prepared in H_2	Pt-Ni	1.3 ± 0.8	2.673 ± 0.020	0.021 ± 0.011	-13.0 ± 0.3	25.5
	Pt-Pt(Un1)	7.3 ± 0.6	2.754 ± 0.002	0.010 ± 0.004		
	Pt-Pt	2.2 ± 1.0	3.900 ± 0.015	0.010 ± 0.004		
	Pt-Pt	8.6 ± 2.0	4.790 ± 0.010	0.014 ± 0.003		
	Pt-Pt (Un1)	7.3 ± 0.6	5.426 ± 0.013	0.012 ± 0.002		
200 °C in H_2	Pt-Ni	1.4 ± 0.9	2.672 ± 0.020	0.023 ± 0.011	-12.7 ± 0.3	25.4
	Pt-Pt (Un1)	7.4 ± 0.6	2.755 ± 0.002	0.010 ± 0.001		
	Pt-Pt	2.1 ± 1.0	3.896 ± 0.014	0.010 ± 0.004		
	Pt-Pt	8.6 ± 2.0	4.791 ± 0.010	0.014 ± 0.003		
	Pt-Pt (Un1)	7.4 ± 0.6	5.428 ± 0.012	0.023 ± 0.002		
500 °C in H_2	Pt-Ni	1.9 ± 0.7	2.678 ± 0.011	0.018 ± 0.006	-12.6 ± 0.3	24.2
	Pt-Pt (Un1)	6.6 ± 0.6	2.745 ± 0.002	0.010 ± 0.001		
	Pt-Pt	2.3 ± 1.1	3.886 ± 0.018	0.013 ± 0.005		
	Pt-Pt	8.1 ± 1.9	4.773 ± 0.012	0.016 ± 0.003		
	Pt-Pt (Un1)	6.6 ± 0.6	5.402 ± 0.016	0.014 ± 0.003		
750 °C in H_2	Pt-Ni	2.3 ± 0.6	2.681 ± 0.009	0.017 ± 0.004	-12.6 ± 0.3	23.3
	Pt-Pt (Un1)	6.4 ± 0.5	2.734 ± 0.002	0.100 ± 0.001		
	Pt-Pt	1.9 ± 1.0	3.869 ± 0.019	0.012 ± 0.005		
	Pt-Pt	8.3 ± 1.8	4.753 ± 0.012	0.015 ± 0.003		
	Pt-Pt (Un1)	6.4 ± 0.5	5.383 ± 0.014	0.013 ± 0.002		

Table 3-20 (Sequel) Structural parameters for 0.5 monolayer Ni/Pt/C (prepared via $Ni(acac)_2$ route) as prepared, 200, 500, 750 and 900 °C acquired in H_2 by fitting the Pt L_3 edge EXAFS data. Un1 refers to multi-scattering process occurring in the same shell.

	Shell	N	R / Å	$2\sigma^2$ / $Å^2$	Ef / eV	R_{exafs} / %
900 °C in H_2	Pt-Ni	2.2 ± 0.6	2.686 ± 0.009	0.016 ± 0.004	-12.9 ± 0.3	22.8
	Pt-Pt(Un1)	6.6 ± 0.5	2.735 ± 0.002	0.010 ± 0.001		
	Pt-Pt	1.8 ± 0.9	3.870 ± 0.016	0.011 ± 0.005		
	Pt-Pt	8.6 ± 1.8	4.754 ± 0.010	0.014 ± 0.003		
	Pt-Pt (Un1)	6.6 ± 0.5	5.386 ± 0.014	0.013 ± 0.003		

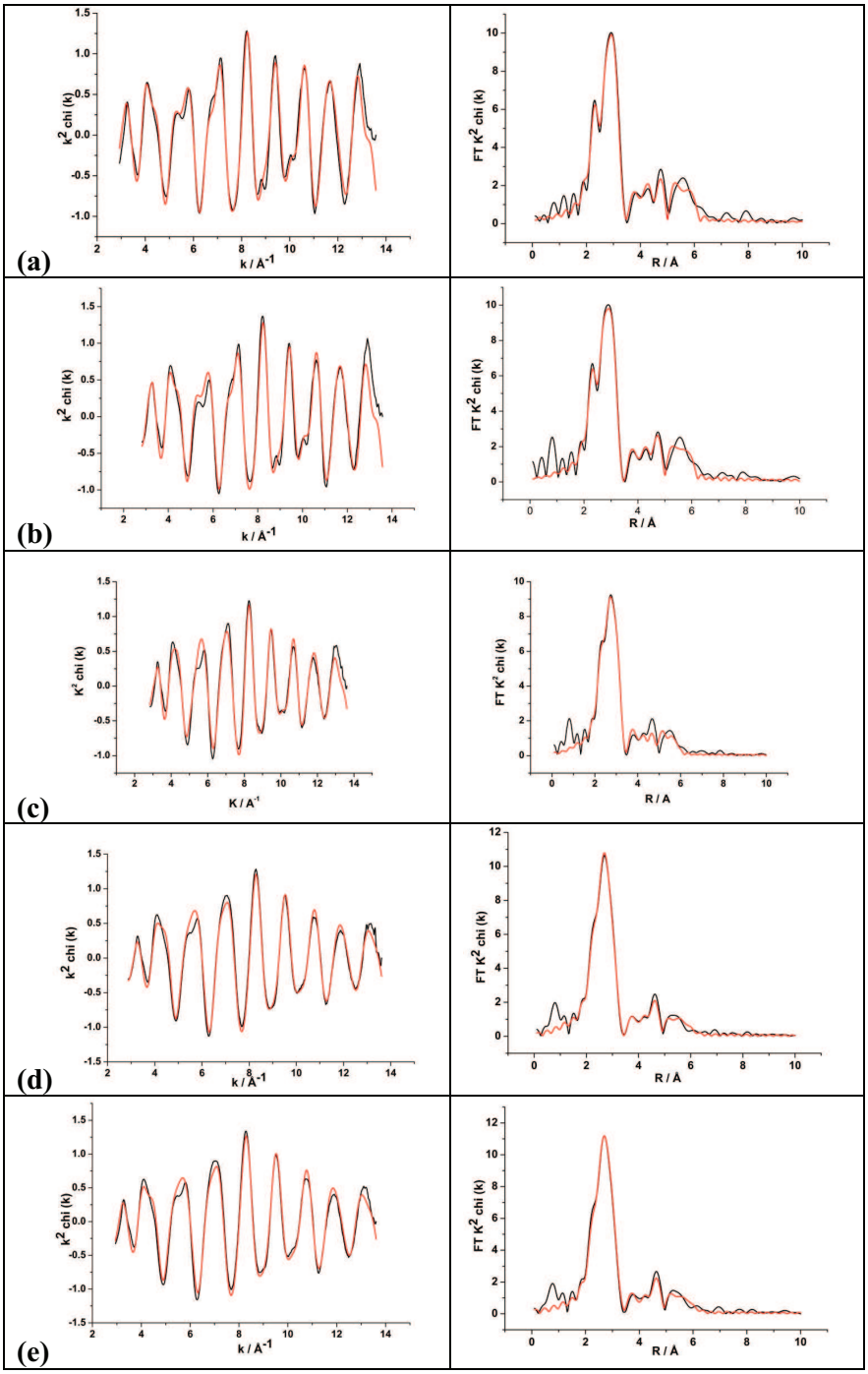

Figure 3- 25 (left) k^2 weighted experimental data and fit along with (right) the Fourier transform for 1 ML Ni/Pt/C (prepared via $Ni(acac)_2$ route) (a) as prepared, (b) 200, (c) 500, (d)750 and (e) 900 °C acquired in H_2 at Pt L_3 edge. Data (black line) and fit (red line). (y-axis for k^2 plot a, b, c, d and e has units of $Å^{-2}$).

Table 3-21 Structural parameters for 1 monolayer Ni/Pt/C (prepared via $Ni(acac)_2$ route) as prepared, 200, 500, 750 and 900 °C acquired in H_2 by fitting the Pt L_3 edge EXAFS data. Un1 refers to multi-scattering process occurring in the same shell.

Condition	Ni/Pt/C 1 monolayer via $Ni(acac)_2$ route Calculated parameters (Pt L_3)					
	Shell	**N**	**R / Å**	**$2\sigma^2$ / $Å^2$**	**Ef / eV**	**R_{exafs} / %**
As prepared in H_2	Pt-Ni	1.0 ± 0.4	2.619 ± 0.029	0.033 ± 0.008	-11.4 ± 0.3	18.5
	Pt-Pt (Un1)	9.0 ± 0.1	2.752 ± 0.002	0.012 ± 0.001		
	Pt-Pt	2.2 ± 0.5	3.862 ± 0.012	0.008 ± 0.002		
	Pt-Ni	1.4 ± 0.5	4.239 ± 0.023	0.009 ± 0.003		
	Pt-Pt	3.7 ± 0.4	4.774 ± 0.005	0.005 ± 0.001		
	Pt-Pt (Un1)	9.0 ± 0.1	5.522 ± 0.007	0.019 ± 0.002		
200 °C in H_2	Pt-Ni	1.3 ± 0.5	2.637 ± 0.029	0.032 ± 0.007	-10.7 ± 0.2	21.9
	Pt-Pt (Un1)	8.9 ± 0.3	2.751 ± 0.002	0.011 ± 0.001		
	Pt-Pt	1.9 ± 0.5	3.858 ± 0.012	0.006 ± 0.001		
	Pt-Ni	1.8 ± 0.6	4.240 ± 0.026	0.011 ± 0.004		
	Pt-Pt	5.6 ± 0.8	4.775 ± 0.007	0.008 ± 0.001		
	Pt-Pt (Un1)	8.9 ± 0.3	5.524 ± 0.009	0.018 ± 0.002		
500 °C in H_2	Pt- Ni	2.2 ± 0.2	2.658 ± 0.007	0.020 ± 0.002	-10.8 ± 0.4	19.5
	Pt-Pt (Un1)	7.3 ± 0.3	2.730 ± 0.002	0.013 ± 0.001		
	Pt-Pt	2.7 ± 0.5	3.844 ± 0.012	0.011 ± 0.002		
	Pt-Ni	1.3 ± 0.5	4.253 ± 0.025	0.012 ± 0.005		
	Pt-Pt	3.0 ± 0.5	4.746 ± 0.009	0.007 ± 0.002		
	Pt-Pt (Un1)	7.3 ± 0.3	5.392 ± 0.011	0.014 ± 0.002		
750 °C in H_2	Pt-Ni	3.3 ± 0.2	2.660 ± 0.003	0.018 ± 0.001	-10.8 ± 0.3	14.9
	Pt-Pt (Un1)	5.7 ± 0.2	2.713 ± 0.002	0.011 ± 0.001		
	Pt-Pt	1.3 ± 0.2	3.829 ± 0.009	0.006 ± 0.002		
	Pt-Ni	1.9 ± 0.5	4.245 ± 0.019	0.018 ± 0.004		
	Pt-Pt	6.2 ± 0.7	4.714 ± 0.007	0.014 ± 0.001		
	Pt-Pt (Un1)	5.7 ± 0.2	5.465 ± 0.009	0.022 ± 0.002		

Table 3-22 (Sequel) Structural parameters for 1 monolayer Ni/Pt/C (prepared via $Ni(acac)_2$ route) as prepared, 200, 500, 750 and 900 °C acquired in H_2 by fitting the Pt L_3 edge EXAFS data. Un1 refers to multi-scattering process occurring in the same shell.

	Shell	N	R / Å	$2\sigma^2$ / $Å^2$	Ef / eV	R_{exafs} / %
900 °C in H_2	Pt-Ni	2.5 ± 0.1	2.659 ± 0.003	0.014 ± 0.001	-11.2 ± 0.2	15.9
	Pt-Pt (Un1)	6.2 ± 0.2	2.715 ± 0.002	0.011 ± 0.001		
	Pt-Pt	2.1 ± 0.3	3.834 ± 0.009	0.008 ± 0.001		
	Pt-Ni	1.1 ± 0.3	4.268 ± 0.019	0.010 ± 0.004		
	Pt-Pt	5.7 ± 0.6	4.713 ± 0.006	0.012 ± 0.001		
	Pt-Pt (Un1)	6.2 ± 0.2	5.465 ± 0.009	0.023 ± 0.002		

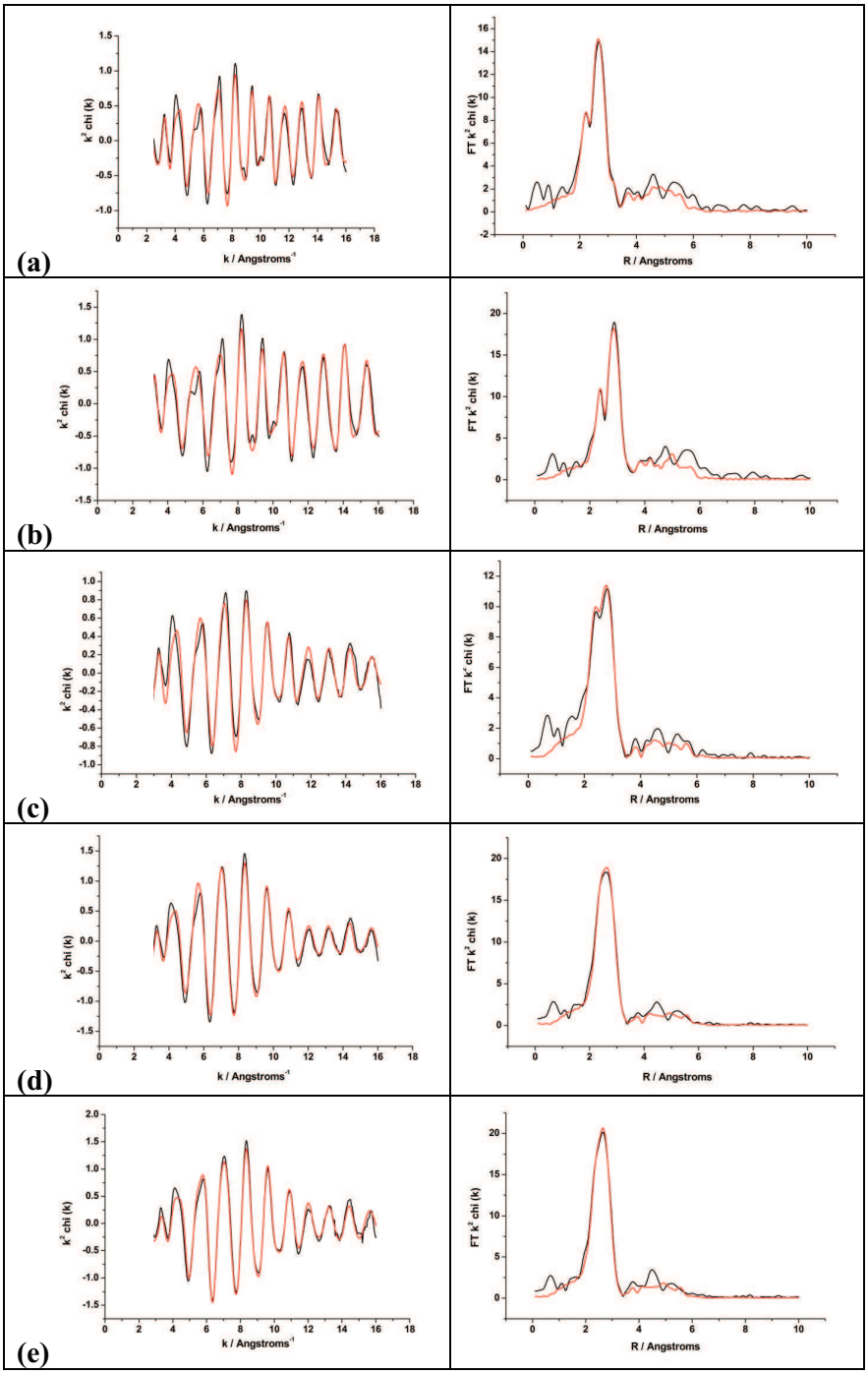

Figure 3- 26 (left) k^2 weighted experimental data and fit along with (right) the Fourier transform for 2 ML Ni/Pt/C (prepared via $Ni(acac)_2$ route) as prepared (a), 200 (b), 500 (c), 750 (d) and 900 °C (e) acquired in H_2 at Pt L_3 edge. Data (black line) and fit (red line). (y-axis for k^2 plot a, b, c, d and e has units of $Å^{-2}$).

Table 3-23 Structural parameters for 2 monolayer Ni/Pt/C (prepared via $Ni(acac)_2$ route) as prepared, 200, 500, 750 and 900 °C acquired in H_2 by fitting the Pt L_3 edge EXAFS data. Un1 refers to multi-scattering process occurring in the same shell.

Condition	Ni/Pt/C 2 monolayer via $Ni(acac)_2$ route Calculated parameters (Pt L_3)					
	Shell	**N**	**R / Å**	**$2\sigma^2$ / $Å^2$**	**Ef / eV**	**R_{exafs} / %**
As prepared in H_2	Pt-Ni	2.2 ± 0.8	2.633 ± 0.013	0.026 ± 0.007	-13.1 ± 0.3	25.6
	Pt-Pt (Un1)	6.1 ± 0.5	2.751 ± 0.002	0.010 ± 0.001		
	Pt-Pt	1.7 ± 0.9	3.902 ± 0.018	0.012 ± 0.005		
	Pt-Pt	7.2 ± 1.6	4.790 ± 0.009	0.015 ± 0.003		
	Pt-Pt (Un1)	6.1 ± 0.5	5.422 ± 0.016	0.013 ± 0.003		
	Shell	**N**	**R / Å**	**$2\sigma^2$ / $Å^2$**	**Ef / eV**	**R_{exafs} / %**
200 °C in H_2	Pt-Ni	2.0 ± 0.9	2.645 ± 0.016	0.025 ± 0.008	-12.9 ± 0.3	24.6
	Pt-Pt	6.9 ± 0.6	2.754 ± 0.002	0.009 ± 0.001		
	Pt-Pt	3.3 ± 1.0	3.903 ± 0.014	0.014 ± 0.003		
	Pt-Pt	6.0 ± 1.6	4.783 ± 0.010	0.012 ± 0.003		
	Pt-Pt	6.9 ± 0.6	5.432 ± 0.028	0.009 ± 0.003		
	Shell	**N**	**R / Å**	**$2\sigma^2$ / $Å^2$**	**Ef / eV**	**R_{exafs} / %**
500 °C in H_2	Pt-Ni	3.1 ± 0.7	2.637 ± 0.008	0.023 ± 0.004	-13.4 ± 0.4	28.7
	Pt-Pt	5.1 ± 0.6	2.726 ± 0.004	0.013 ± 0.001		
	Pt-Pt	0.6 ± 0.9	3.861 ± 0.056	0.013 ± 0.015		
	Pt-Pt	5.8 ± 1.9	4.754 ± 0.022	0.020 ± 0.006		
	Pt-Pt	5.1 ± 0.6	5.367 ± 0.031	0.018 ± 0.006		
	Shell	**N**	**R / Å**	**$2\sigma^2$ / $Å^2$**	**Ef / eV**	**R_{exafs} / %**
750 °C in H_2	Pt-Ni	4.9 ± 0.5	2.624 ± 0.004	0.015 ± 0.001	-13.6 ± 0.4	24.0
	Pt-Pt(Un1)	3.8 ± 0.5	2.703 ± 0.004	0.011 ± 0.001		
	Pt-Pt	1.7 ± 1.1	3.813 ± 0.039	0.019 ± 0.012		
	Pt-Pt	5.2 ± 1.7	4.683 ± 0.018	0.017 ± 0.005		
	Pt-Pt (Un1)	3.8 ± 0.5	5.324 ± 0.024	0.014 ± 0.005		

Table 3-24 (Sequel) Structural parameters for 2 monolayer Ni/Pt/C (prepared via $Ni(acac)_2$ route) as prepared, 200, 500, 750 and 900 °C acquired in H_2 by fitting the Pt L_3 edge EXAFS data. Un1 refers to multi-scattering process occurring in the same shell.

	Shell	N	R / Å	$2\sigma^2$ / $Å^2$	Ef / eV	R_{exafs} / %
900 °C in H_2	Pt-Ni	5.1 ± 0.6	2.629 ± 0.004	0.015 ± 0.002	-13.2 ± 0.4	24.2
	Pt-Pt(Un1)	3.8 ± 0.5	2.697 ± 0.004	0.010 ± 0.001		
	Pt-Pt	1.5 ± 1.0	3.901 ± 0.029	0.014 ± 0.008		
	Pt-Pt	5.6 ± 1.8	4.682 ± 0.016	0.015 ± 0.004		
	Pt-Pt (Un1)	3.8 ± 0.5	5.314 ±0.024	0.013 ± 0.004		

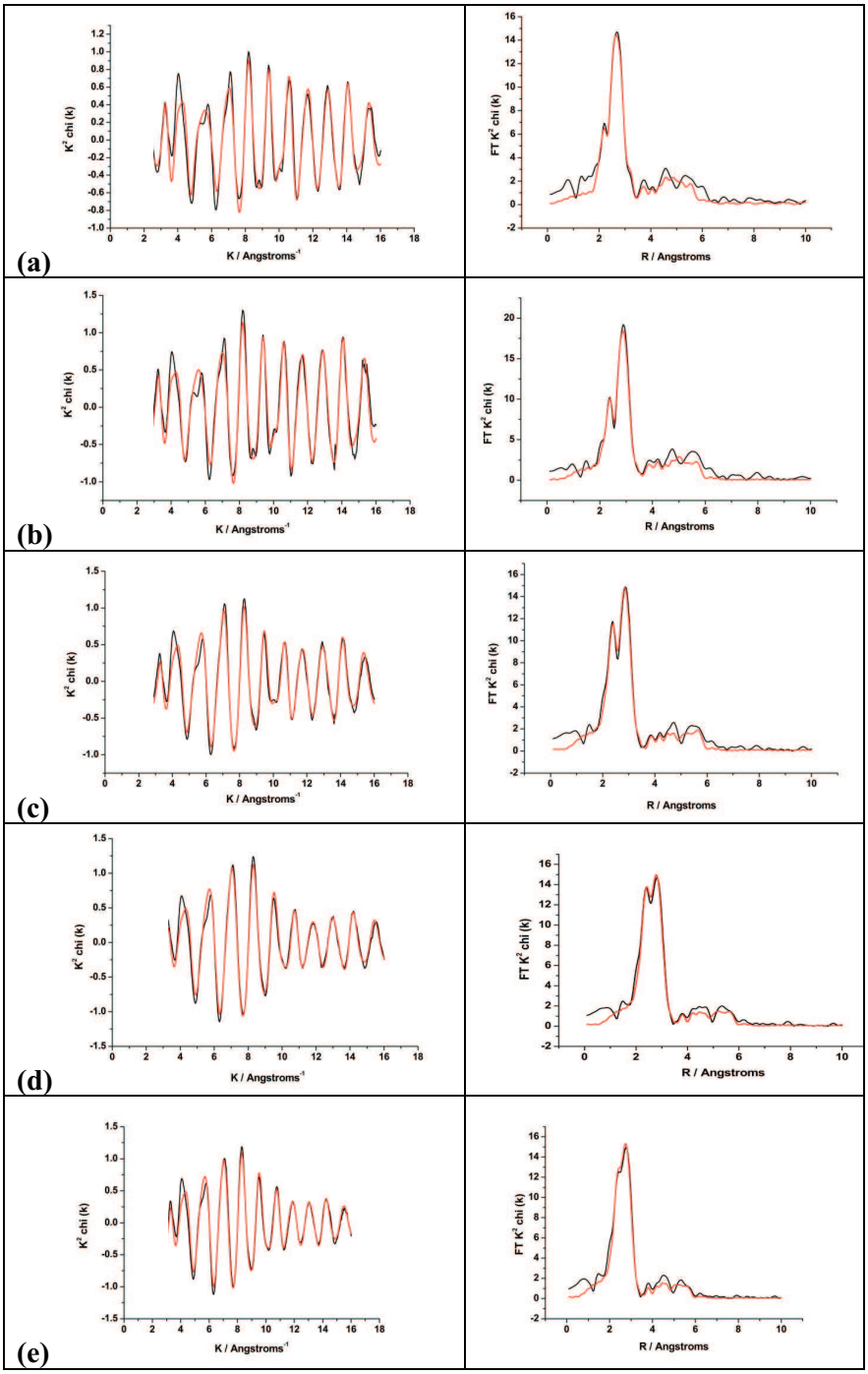

Figure 3- 27 (left) k^2 weighted experimental data and fit along with (right) the Fourier transform for 1 ML Ni/Pt/C (prepared via $Ni(Cp)_2$ route) as prepared (a), 200 (b), 500 (c), 750 (d) and 900 °C (e) acquired in H_2 at Pt L_3 edge. Data (black line) and fit (red line). (y-axis for k^2 plot a, b, c, d and e has units of $Å^{-2}$).

Table 3-25 Structural parameters for 1 monolayer Ni/Pt/C (prepared via $Ni(Cp)_2$ route) as prepared, 200, 500, 750 and 900 °C acquired in H_2 by fitting the Pt L_3 edge EXAFS data. Un1 refers to multi-scattering process occurring in the same shell.

Condition	Ni/Pt/C 1 monolayer via $Ni(Cp)_2$ route Calculated parameters (Pt L_3)					
	Shell	**N**	**R / Å**	**$2\sigma^2$ / $Å^2$**	**Ef / eV**	**R_{exafs} / %**
As prepared in H_2	Pt-Pt(Un1)	7.5 ± 0.5	2.756 ± 0.002	0.011 ± 0.001	-12.9 ± 0.3	26.4
	Pt-Pt	1.4 ± 0.9	3.900 ± 0.020	0.010 ± 0.006		
	Pt-Pt	8.7 ± 2.0	4.800 ± 0.010	0.016 ± 0.003		
	Pt-Pt (Un1)	7.5 ± 0.5	5.430 ± 0.017	0.014 ± 0.003		
200 °C in H_2	Pt-Ni	1.4 ± 0.9	2.662 ± 0.024	0.025 ± 0.014	-12.8 ± 0.3	25.1
	Pt-Pt (Un1)	7.3 ± 0.6	2.756 ± 0.002	0.010 ± 0.001		
	Pt-Pt	2.2 ± 1.0	3.900 ± 0.015	0.010 ± 0.004		
	Pt-Pt	8.3 ± 1.9	4.795 ± 0.010	0.014 ± 0.003		
	Pt-Pt (Un1)	7.3 ± 0.6	5.428 ± 0.012	0.012 ± 0.002		
500 °C in H_2	Pt-Ni	2.8 ± 0.6	2.627 ± 0.008	0.021 ± 0.004	-13.1 ± 0.3	23.2
	Pt-Pt (Un1)	5.6 ± 0.5	2.743 ± 0.002	0.010 ± 0.001		
	Pt-Pt	1.3 ± 0.8	3.880 ±0.017	0.010 ± 0.005		
	Pt-Pt	5.5 ± 1.7	4.788 ± 0.015	0.014 ± 0.003		
	Pt-Ni (Un1)	2.8 ± 0.6	5.274 ± 0.020	0.012 ± 0.005		
	Pt-Pt (Un1)	5.6 ± 0.5	5.419 ± 0.016	0.014 ± 0.003		
750 °C in H_2	Pt-Ni	3.8 ± 0.6	2.628 ± 0.005	0.018 ± 0.002	-13.4 ± 0.3	22.9
	Pt-Pt (Un1)	4.7 ± 0.5	2.730 ± 0.003	0.010 ± 0.001		
	Pt-Pt	1.4 ± 1.0	3.863 ± 0.030	0.015 ± 0.008		
	Pt-Pt	6.4 ± 1.8	4.759 ± 0.019	0.018 ± 0.005		
	Pt-Ni (Un1)	3.8 ± 0.6	5.253 ± 0.042	0.015 ± 0.006		
	Pt-Pt (Un1)	4.7 ± 0.5	5.403 ± 0.032	0.015 ± 0.006		

Table 3-26 (sequel) Structural parameters for 1 monolayer Ni/Pt/C (prepared via $Ni(Cp)_2$ route) as prepared, 200, 500, 750 and 900 ºC acquired in H_2 by fitting the Pt L_3 edge EXAFS data. Un1 refers to multi-scattering process occurring in the same shell.

	Shell	N	R / Å	$2\sigma^2$ / $Å^2$	Ef / eV	R_{exafs} / %
900 ºC in H_2	Pt-Ni	3.6 ± 0.5	2.640 ± 0.005	0.018 ± 0.002	-13.0 ± 0.3	22.6
	Pt-Pt (Un1)	4.8 ± 0.5	2.722 ± 0.003	0.011 ± 0.001		
	Pt-Pt	1.1 ± 0.8	3.844 ± 0.029	0.013 ± 0.008		
	Pt-Pt	7.5 ± 1.8	4.746 ± 0.018	0.019 ± 0.004		
	Pt-Ni (Un1)	3.6 ± 0.5	5.250 ± 0.037	0.020 ± 0.009		
	Pt-Pt (Un1)	4.8 ± 0.5	5.382 ± 0.032	0.018 ± 0.006		

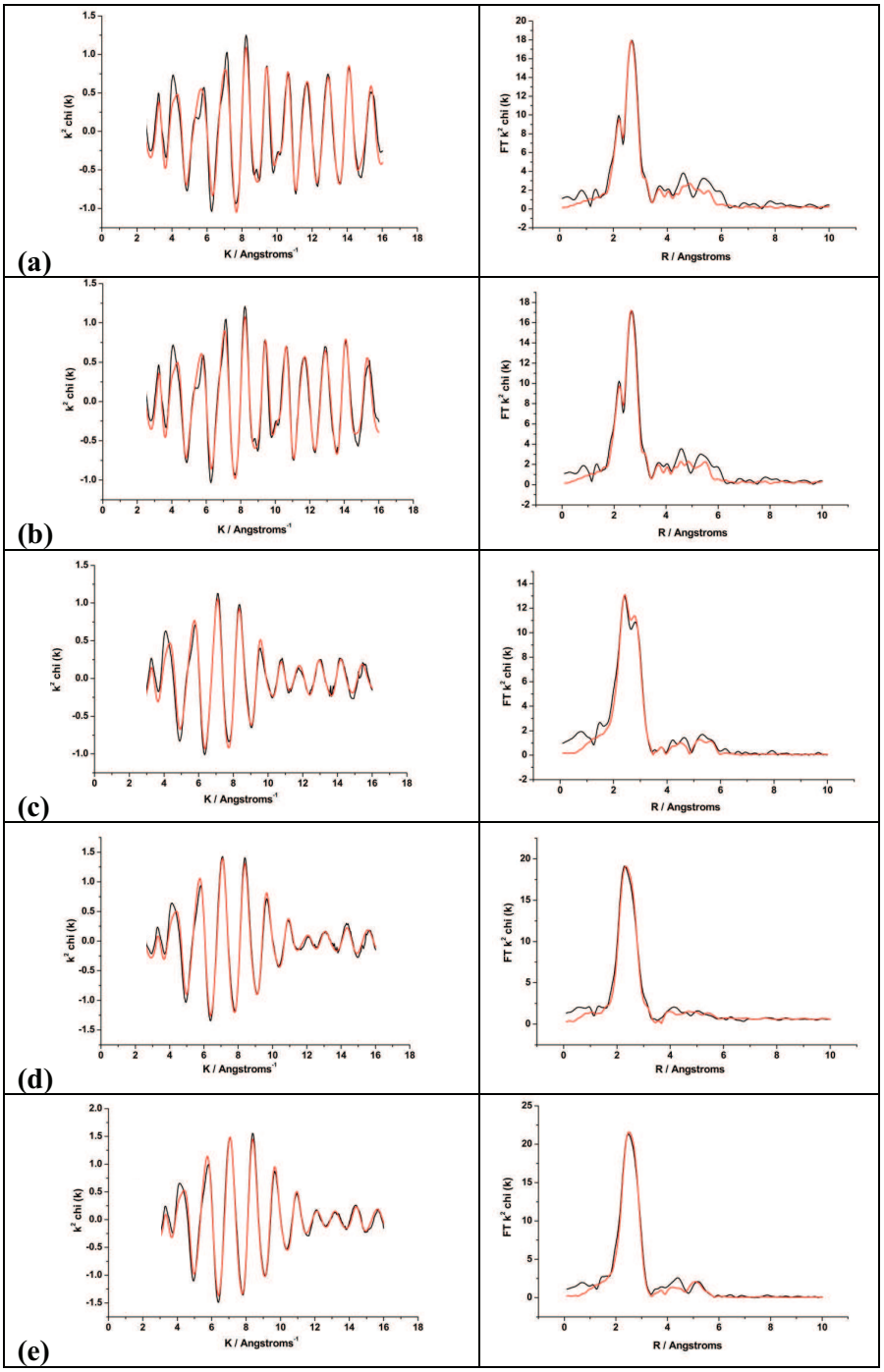

Figure 3- 28 (left) k^2 weighted experimental data and fit along with (right) the Fourier transform for 2 ML Ni/Pt/C (prepared via $Ni(Cp)_2$ route) as prepared (a), 200 (b), 500 (c), 750 (d) and 900 °C (e) acquired in H_2 at Pt L_3 edge. Data (black line) and fit (red line). (y-axis for k^2 plot a, b, c, d and e has units of $Å^{-2}$).

Table 3-27 Structural parameters for 2 monolayer Ni/Pt/C (prepared via $Ni(Cp)_2$ route) as prepared, 200, 500, 750 and 900 °C acquired in H_2 by fitting the Pt L_3 edge EXAFS data. Un1 refers to multi-scattering process occurring in the same shell.

Condition	Ni/Pt/C 2 monolayer via $Ni(Cp)_2$ route Calculated parameters (Pt L_3)					
	Shell	**N**	**R / Å**	**$2\sigma^2$ / $Å^2$**	**Ef / eV**	**R_{exafs} / %**
As prepared in H_2	Pt-Ni (Un1)	1.7 ± 0.8	2.618 ± 0.016	0.022 ± 0.008	-12.9 ± 0.3	25.1
	Pt-Pt (Un1)	7.0 ± 0.6	2.752 ± 0.002	0.010 ± 0.001		
	Pt-Pt	2.0 ± 1.0	3.892 ± 0.015	0.015 ± 0.003		
	Pt-Pt	8.1 ± 1.9	4.786 ± 0.011	0.013 ± 0.002		
	Pt-Pt (Un1)	7.0 ± 0.6	5.417 ± 0.012	0.013 ± 0.002		
	Shell	**N**	**R / Å**	**$2\sigma^2$ / $Å^2$**	**Ef / eV**	**R_{exafs} / %**
200 °C in H_2	Pt-Ni (Un1)	2.4 ± 0.8	2.619 ± 0.012	0.010 ± 0.001	-12.9 ± 0.3	23.9
	Pt-Pt (Un1)	6.5 ± 0.5	2.750 ± 0.002	0.010 ± 0.004		
	Pt-Pt	1.8 ± 0.9	3.896 ± 0.015	0.016 ± 0.003		
	Pt-Pt	9.5 ± 2.0	4.795 ± 0.012	0.012 ± 0.002		
	Pt-Ni (Un1)	2.4 ± 0.8	5.283 ± 0.022	0.025 ± 0.006		
	Pt-Pt (Un1)	6.5 ± 0.5	5.422 ± 0.013	0.009 ± 0.005		
	Shell	**N**	**R / Å**	**$2\sigma^2$ / $Å^2$**	**Ef / eV**	**R_{exafs} / %**
500 °C in H_2	Pt-Ni (Un1)	3.7 ± 0.5	2.607 ± 0.005	0.018 ± 0.002	-13.2 ± 0.4	26.6
	Pt-Pt (Un1)	4.1 ± 0.5	2.729 ± 0.004	0.012 ± 0.001		
	Pt-Pt	0.7 ± 0.9	3.831 ± 0.079	0.018 ± 0.024		
	Pt-Pt	5.3 ± 1.9	4.762 ± 0.034	0.023 ± 0.009		
	Pt-Ni (Un1)	3.7 ± 0.5	5.258 ± 0.032	0.018 ± 0.007		
	Pt-Pt (Un1)	4.1 ± 0.5	5.408 ± 0.034	0.017 ± 0.007		
	Shell	**N**	**R / Å**	**$2\sigma^2$ / $Å^2$**	**Ef / eV**	**R_{exafs} / %**
750 °C in H_2	Pt-Ni (Un1)	5.4 ± 0.5	2.605 ± 0.004	0.015 ± 0.001	-13.6 ± 0.4	23.7
	Pt-Pt (Un1)	3.0 ± 0.5	2.706 ± 0.004	0.010 ± 0.001		
	Pt-Pt	1.1 ± 0.9	3.779 ± 0.044	0.017 ± 0.012		
	Pt-Pt	5.6 ± 1.9	4.679 ± 0.026	0.021 ± 0.008		
	Pt-Ni (Un1)	5.4 ± 0.5	5.256 ± 0.034	0.022 ± 0.008		
	Pt-Pt (Un1)	3.0 ± 0.5	5.348 ± 0.090	0.022 ± 0.018		

Table 3-28 (Sequel) Structural parameters for 2 monolayer Ni/Pt/C (prepared via $Ni(Cp)_2$ route) as prepared, 200, 500, 750 and 900 °C acquired in H_2 by fitting the Pt L_3 edge EXAFS data. Un1 refers to multi-scattering process occurring in the same shell.

	Shell	N	R / Å	$2\sigma^2$ / Å^2	Ef / eV	R_{exafs} / %
900 °C in H_2	Pt-Ni (Un1)	5.8 ± 0.5	2.609 ± 0.003	0.015 ± 0.001	-13.2 ± 0.4	22.3
	Pt-Pt (Un1)	3.0 ± 0.5	2.698 ± 0.004	0.010 ± 0.001		
	Pt-Pt	1.4 ± 1.0	3.786 ± 0.039	0.017 ± 0.011		
	Pt-Pt	6.4 ± 2.0	4.665 ± 0.026	0.020 ± 0.007		
	Pt-Ni (Un1)	5.8 ± 0.5	5.270 ± 0.037	0.027 ± 0.010		
	Pt-Pt (Un1)	3.0 ± 0.5	5.304 ± 0.068	0.019 ± 0.014		

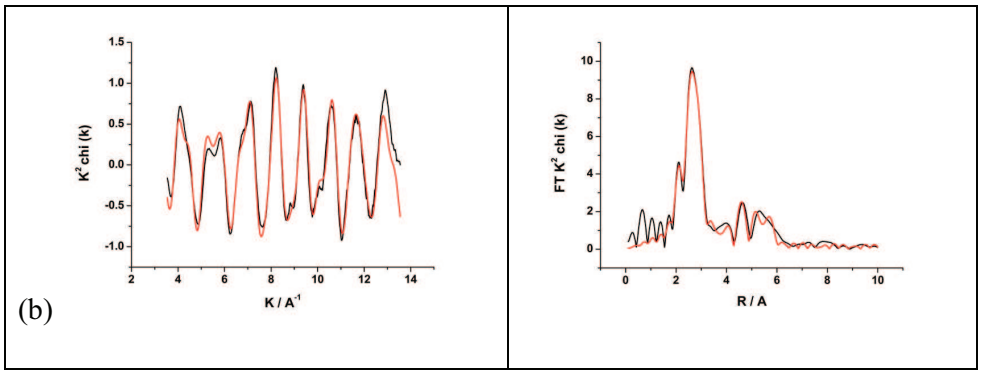

Figure 3- 29 (left) k^2 weighted experimental data and fit along with (right) the Fourier transform for 20 wt% Pt/C acquired in H_2. Data (black line) and fit (red line). (y-axis for k^2 plot has units of Å^{-2}).

Table 3-29 Structural parameters for 20 wt% Pt/C catalysts acquired in H_2 by fitting the Pt L_3 edge EXAFS data.

Shell	*N*	*R* / Å	$2\sigma^2$ / Å^2	E_f / eV	R_{exafs} / %
Pt-Pt (Un1)	8.7 ± 0.3	2.753 ± 0.002	0.012 ± 0.001	-9.2 ± 0.3	23.6
Pt-Pt	1.4 ± 0.3	3.877 ± 0.010	0.005 ± 0.002		
Pt-Pt	6.2 ± 0.8	4.779 ± 0.007	0.009 ± 0.001		
Pt-Pt (Un1)	8.7 ± 0.3	5.522 ± 0.009	0.020 ± 0.002		

One of the suggested reasons for the improved catalytic activity of the Pt-alloys towards the ORR is the shortening of the Pt-Pt first coordination shell distance. From **Table 3-30**, it can be seen that as the heat treatment temperature increases, the Pt-Pt bond distance decreases. Significant differences between the Ni/Pt/C catalysts and 20 wt% Pt/C are seen at heat treatment temperature greater than 500 °C. The shortening of the Pt-Pt bond distance was expected as the XRD data (**Table 3-3** and **Table 3-4**) showed a decrease in lattice parameter as the heat treatment temperature increases. The reduction in lattice parameter results from the incorporation of smaller Ni atoms into the Pt lattice. As a consequence, the distance between the Pt neighbours decreases which is consistent with the presence of bimetallic bond.[36, 37]

Table 3-30 Pt-Pt first shell coordination distances (Å) obtained from fitting of the Pt L_3 edge EXAFS data in H_2 for all the prepared Ni/Pt/C catalysts.

Precursor / Annealing temperature	$Ni(acac)_2$			$Ni(Cp)_2$	
	0.5 ML	**1 ML**	**2 ML**	**1 ML**	**2 ML**
As prepared	2.754 ± 0.002	2.752 ± 0.002	2.751 ± 0.002	2.756 ± 0.002	2.752 ± 0.002
200 °C	2.755 ± 0.002	2.751 ± 0.002	2.754 ± 0.002	2.756 ± 0.002	2.750 ± 0.002
500 °C	2.745 ± 0.002	2.730 ± 0.002	2.726 ± 0.004	2.743 ± 0.004	2.729 ± 0.002
750 °C	2.734 ± 0.002	2.713 ± 0.002	2.703 ± 0.004	2.730 ± 0.004	2.706 ± 0.002
900 °C	2.735 ± 0.002	2.715 ± 0.002	2.696 ± 0.003	2.722 ± 0.004	2.698 ± 0.002
20 wt% Pt/C	2.753 ± 0.002				

The following discussion of the metal neighbours' contribution was assessed by examining the data in H_2 as this ensures the maximum number of metal neighbours (because the surface oxides have been reduced). From **Figure 3- 30**, it can be seen that as the metal fraction of Ni increases, the number of Pt-Ni neighbours increases. No Pt-Ni shell could be fitted for the *as prepared* 1 ML Ni/Pt/C prepared via the $Ni(Cp)_2$ as the associated Debye-Waller factor and the coordination number were both negative. Within the error estimate, the Ni/Pt/C catalysts prepared via the $Ni(acac)_2$ route have a similar number of Pt-Ni neighbours which would be consistent with Ni evenly distributed on the Pt surface. However, the number of Pt-Ni neighbours of the Ni/Pt/C prepared via the $Ni(Cp)_2$ route would rather support the theory of clustering seeing the significant difference in Pt-Ni coordination number for the 1 and 2 ML catalysts.

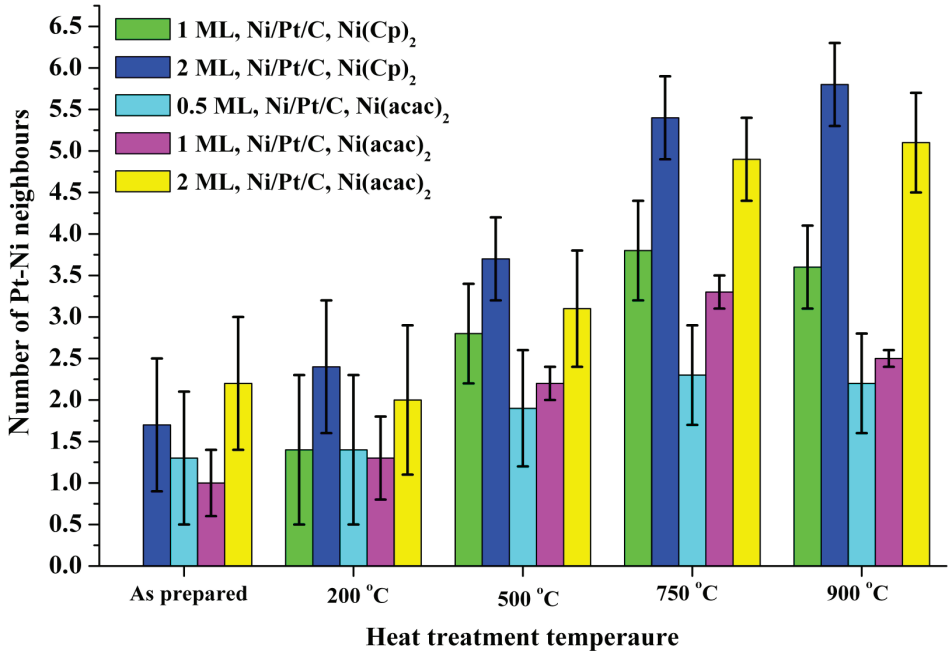

Figure 3- 30 Histograms showing the number of Pt-Ni nearest neighbours for all Ni/Pt/C catalysts. Obtained from the EXAFS data collected in H_2. (Error bars are those derived from the EXAFS data analysis)

As the heat-treatment temperature increases, the number of Pt-Ni neighbours increases which supports the formation of a PtNi alloy phase, as more Ni atoms are incorporated into the Pt lattice. From **Figure 3- 30**, it can also be observed that as the fraction of Ni increases and the heat-treatment temperature increases, a larger

number of Pt-Ni neighbours are recorded. This was expected because as the fraction of Ni deposited increases, more Ni atoms are deposited on the Pt surface and as a consequence, more Ni atoms are able to diffuse through the Pt atoms, increasing the number of Pt-Ni neighbours. The diffusion of Ni atoms into the Pt bulk is also supported by the XPS data as the ratio Ni At% to Pt At% decreases as the heat-treatment temperature increases (**Table 3-5** and **Table 3-9**). The formation of an alloy phase is also supported by the shift of the Pt and Ni XRD peaks observed in **Figure 3- 3** to **Figure 3- 7**. Finally, the number of first shell Pt-Pt nearest neighbours decreases (and the number of first shell Pt-Ni nearest neighbours increases) as the heat-treatment temperature increases, which is also what would be expected for alloy formation.

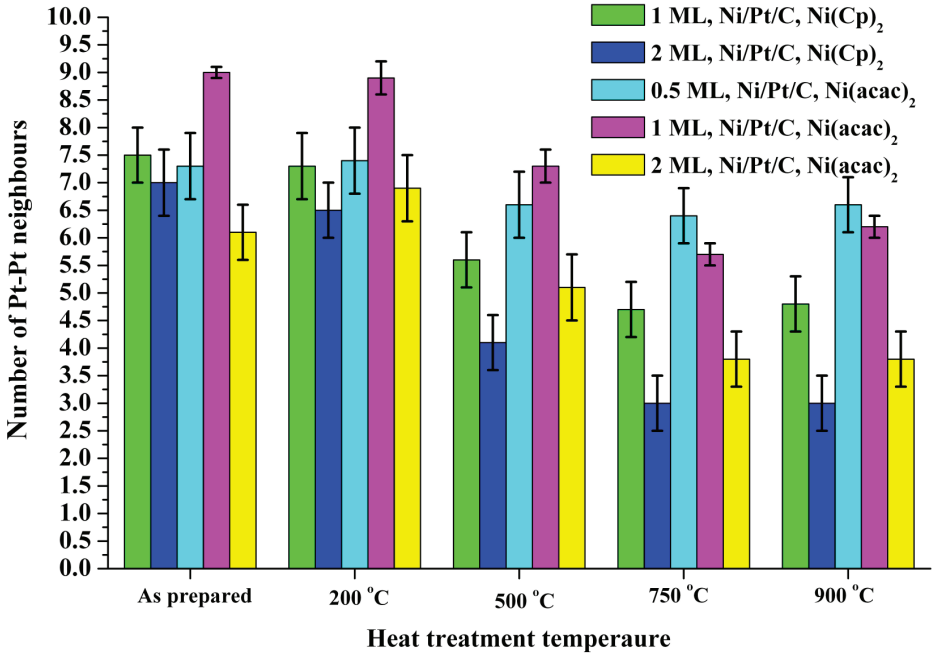

Figure 3- 31 Histograms showing the number of Pt-Pt nearest neighbours for all Ni/Pt/C catalysts. Obtained from the EXAFS data collected in H_2. (Error bars are those derived from the EXAFS data analysis)

Within the error estimates, the number of neighbours around the scattering Pt atoms remains the same throughout the samples. This suggests that the average particle size of each different sample is rather similar as was suggested by the TEM analysis.

3.1.6 Summary of the structural analysis

The shift of the XRD peaks for the Pt fcc and Ni fcc in the XRD data, as the heat treatment temperature increases, is showing an increase in the degree of alloying. The broadness of the peaks also increased as the amount of Ni is increased and as the heat treatment temperature increases, indicating the formation of larger clusters.

The TEM results demonstrated an inhomogeneous deposition of Ni on the Pt/C surface. This was supported by the large error associated with the average particle size as well as the TEM micrographs. However, all the particle size distributions were log normal like.

The XPS data showed a synergistic effect of Ni on Pt as the peak position for the $Pt(4f_{7/2})$ shifts to lower binding energy. It was also shown that a surface enrichment of Pt occurred as the heat treatment temperature increased.

The EXAFS analysis supported the non-uniformity of the deposition of Ni on Pt/C as Pt-O shells were fitted in all the Ni/Pt/C catalysts). It was found that the preparation of Ni/Pt/C via the $Ni(acac)_2$ route resulted in a lower degree of clustering than those prepared via the $Ni(Cp)_2$ route. Also, the Pt-Pt bond distance was found to decrease as the heat treatment temperature increased which is consistent with an alloy phase formation. In addition, the number of Pt-Ni and Pt-Pt nearest neighbours was also found to increase and decrease, respectively, as the heat treatment temperature increased, which also confirms the formation of a PtNi alloy phase.

3.2 Electrochemistry and catalytic activity

3.2.1 Cyclic voltammetry – Half cell studies

The cyclic voltammograms (CV) of 0.5, 1 and 2 ML Ni/Pt/C electrocatalysts prepared via the $Ni(acac)_2$ route are presented in **Figure 3- 32**, **Figure 3- 33** and **Figure 3- 34**, respectively. The CV of 1 and 2 ML Ni/Pt/C electrocatalysts prepared via the $Ni(Cp)_2$ route are presented in **Figure 3- 35** and **Figure 3- 36**, respectively. The CV have been normalised to the available Pt surface area calculated from the area underneath the hydrogen adsorption peak. The mass normalised Pt area in $m_{Pt}^{2}\ g_{Pt}^{-1}$ for each catalyst has been summarised in **Table 3-31**.

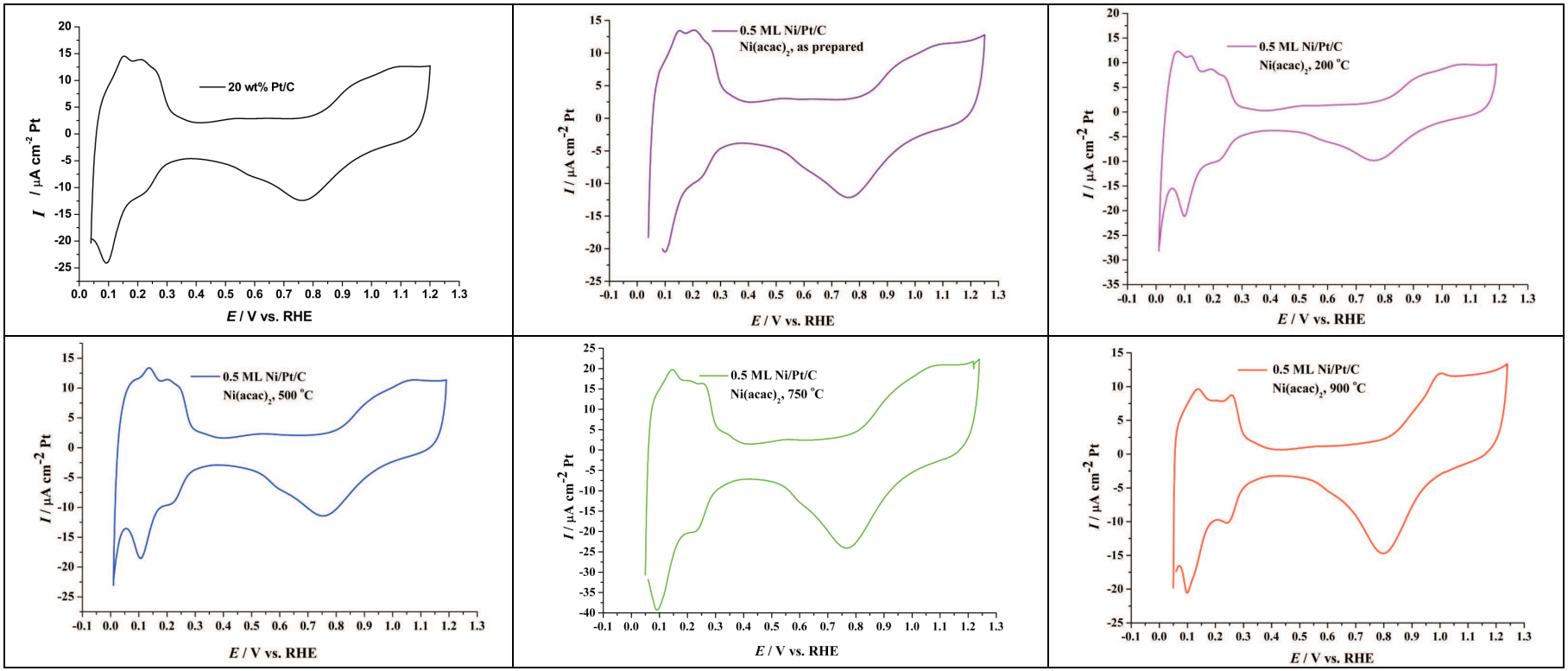

Figure 3- 32 Cyclic voltammograms of 0.5 ML Ni/Pt/C electrocatalysts (via $Ni(acac)_2$ route) (a) as prepared, (b) 200, (c) 500, (d) 750 and (e) 900 °C. Cyclic voltammogram of 20 wt% Pt/C is also shown for comparison purposes. The Cyclic voltammograms were recorded in 1M H_2SO_4 at 10 mV s^{-1}.

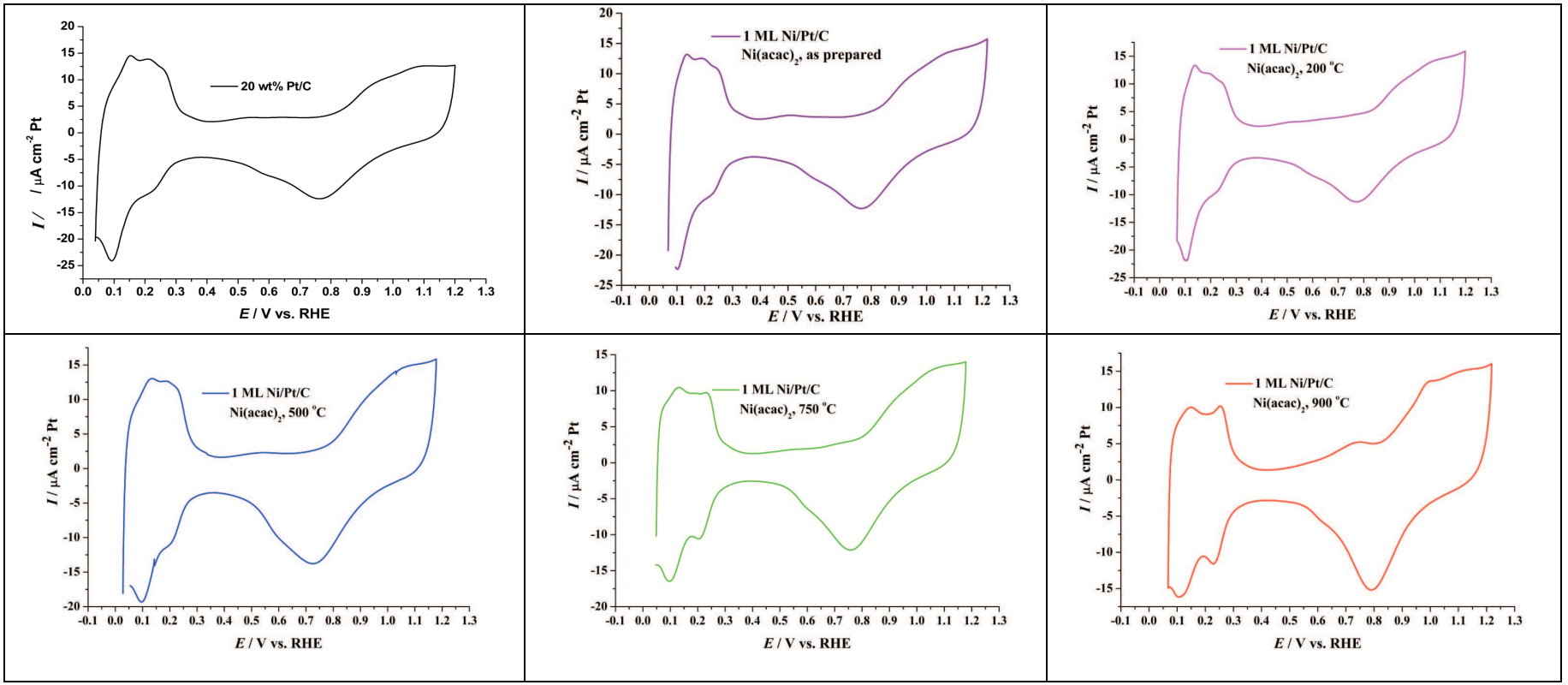

Figure 3- 33 Cyclic voltammograms of 1 ML Ni/Pt/C electrocatalysts (via $Ni(acac)_2$ route) (a) as prepared, (b) 200, (c) 500, (d) 750 and (e) 900 °C. Cyclic voltammogram of 20 wt% Pt/C is also shown for comparison purposes. The Cyclic voltammograms were recorded in 1M H_2SO_4 at 10 mV s^{-1}.

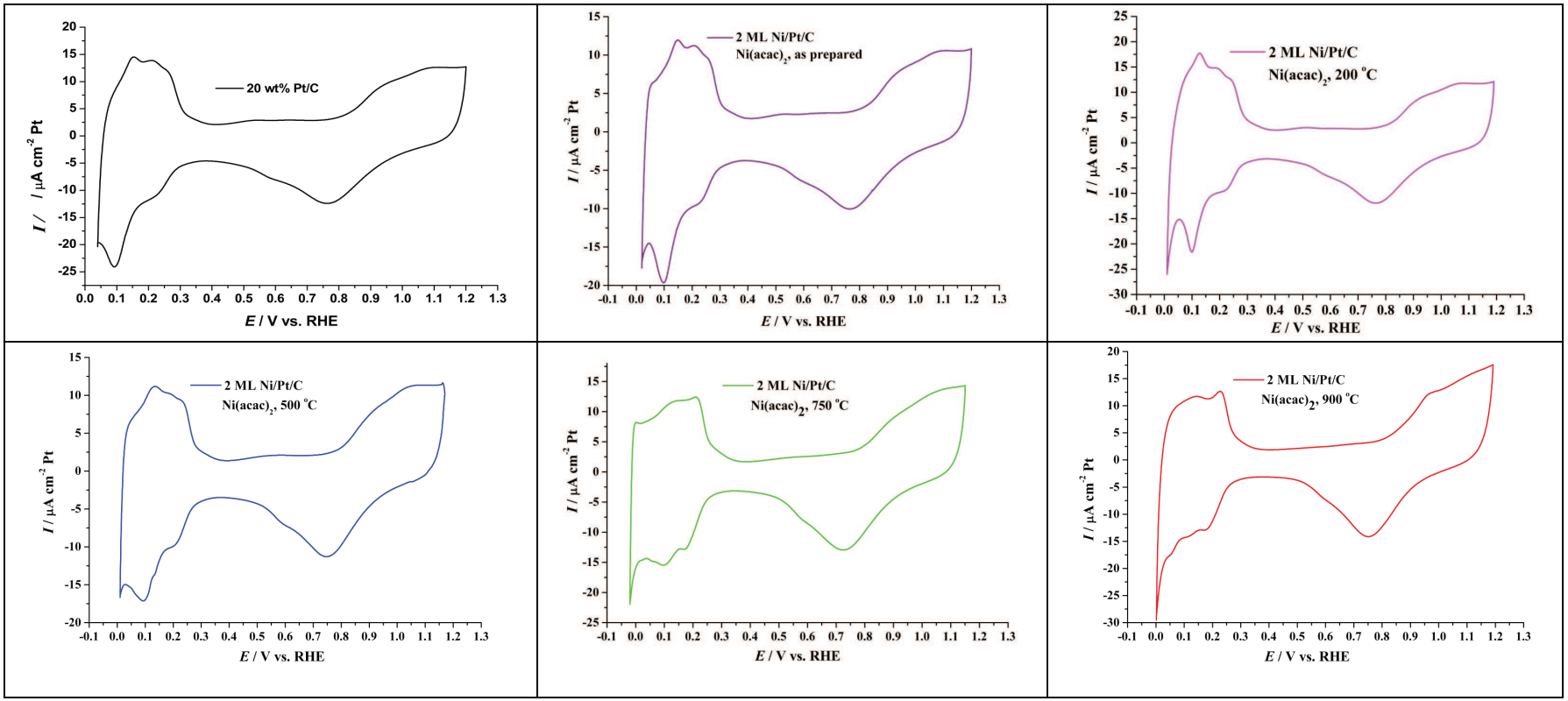

Figure 3- 34 Cyclic voltammograms of 2 ML Ni/Pt/C electrocatalysts (via $Ni(acac)_2$ route) (a) as prepared, (b) 200, (c) 500, (d) 750 and (e) 900 ºC. Cyclic voltammograms of 20 wt% Pt/C is also shown for comparison purposes. The Cyclic voltammograms were recorded in 1M H_2SO_4 at 10 mV s^{-1}.

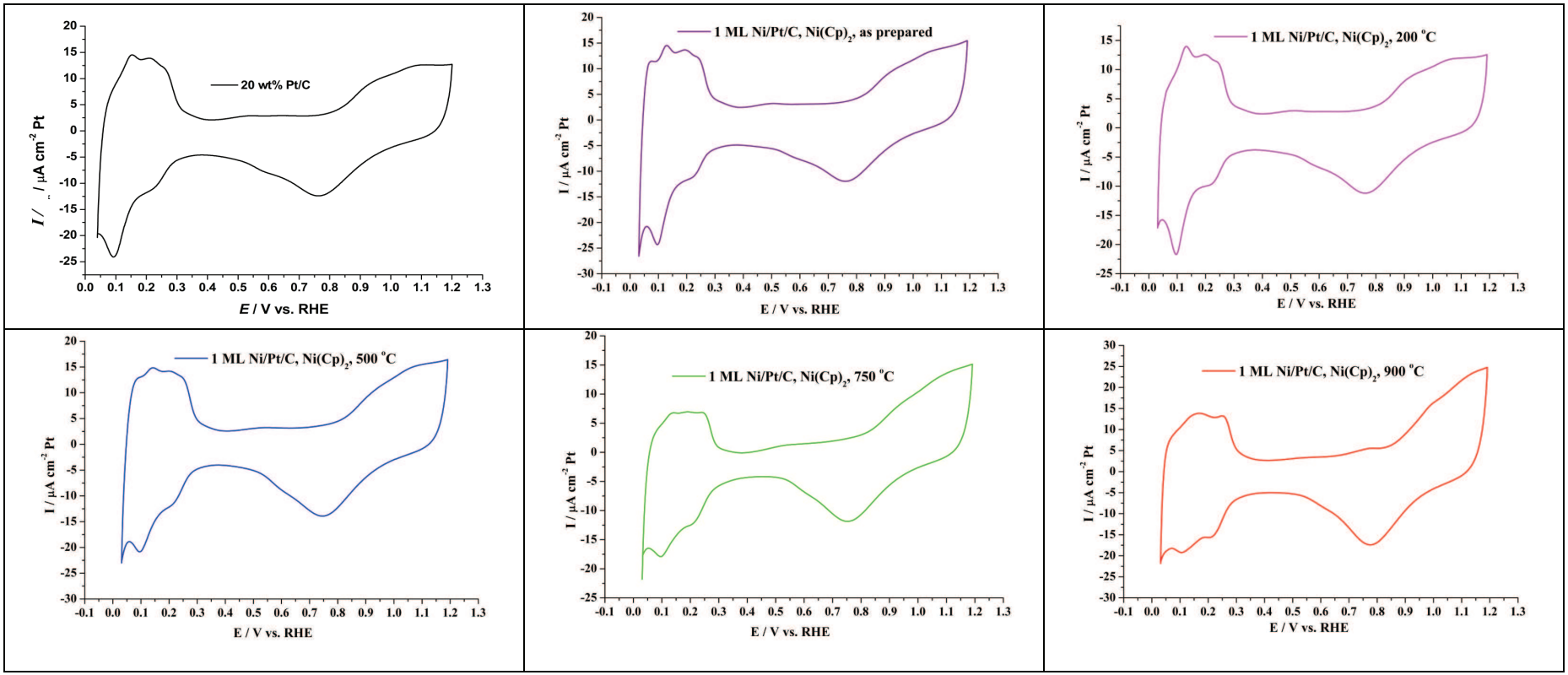

Figure 3- 35 Cyclic voltammograms of 1 ML Ni/Pt/C electrocatalysts (via $Ni(Cp)_2$ route) (a) as prepared, (b) 200, (c) 500, (d) 750 and (e) 900 °C. Cyclic voltammogram of 20 wt% Pt/C is also shown for comparison purposes. The Cyclic voltammograms were recorded in 1M H_2SO_4 at 10 mV s^{-1}.

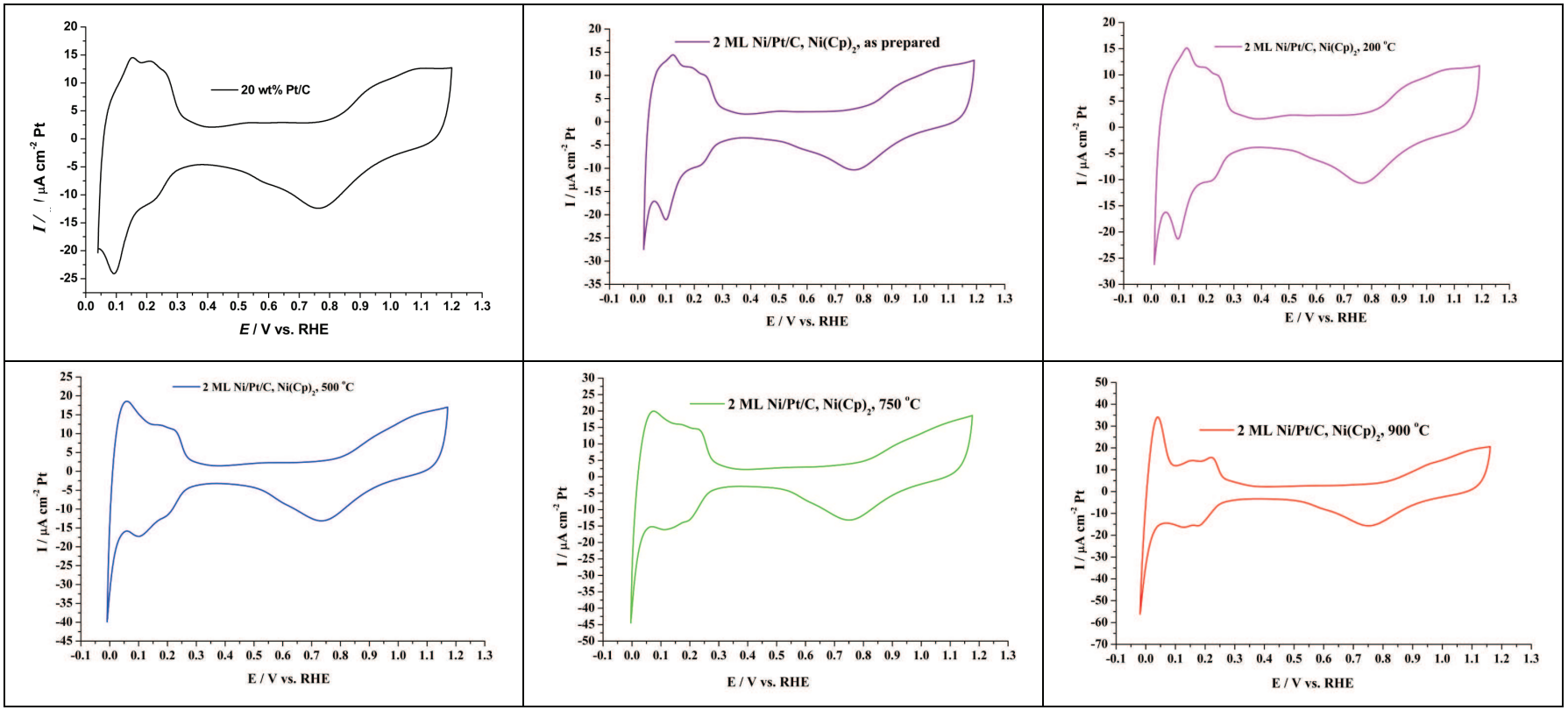

Figure 3- 36 Cyclic voltammograms of 2 ML Ni/Pt/C electrocatalysts (via $Ni(Cp)_2$ route) (a) as prepared, (b) 200, (c) 500, (d) 750 and (e) 900 ºC. Cyclic voltammograms of 20 wt% Pt/C is also shown for comparison purposes. The Cyclic voltammograms were recorded in 1M H_2SO_4 at 10 mV s^{-1}.

Assessing the cyclic voltammograms of the Ni/Pt/C catalysts prepared via the $Ni(acac)_2$ and the $Ni(Cp)_2$ routes, several observations can be made. All cyclic voltammograms have a Pt-like shape as they all exhibit a hydrogen region, a double layer region and an oxide region. The hydrogen region undergoes few modifications as the heat-treatment temperature increases and the oxide reduction peak remains at *ca.* 0.8 V vs. RHE.

The peaks observed in the hydrogen adsorption/desorption region have been attributed to the different Pt crystal planes.[38, 39] Based on this analysis, it can be observed that as the heat-treatment temperature increases, the two hydrogen desorption peaks at 0.1 V and 0.25 V vs. RHE, corresponding to the Pt(100) and Pt(111) crystal planes respectively, become more well defined and/or that a third hydrogen adsorption peak situated at *ca.* 0.15 V vs. RHE can be detected. This additional peak is attributed to the Pt(110) crystal plane (2 ML Ni/Pt/C, $Ni(acac)_2$, 900 ^{o}C). The EXAFS, TEM and XRD data have illustrated that Ni is not uniformly deposited across the Pt surface. In other words, some of the Pt sites are not covered by Ni and those sites will be able to produce the features observed in the CVs. In addition, as depicted by the XPS data, the higher the heat-treatment temperature, the higher the surface concentration of Pt atoms. In other words, the higher the temperature, the more Pt atoms diffuse to the surface of the particle. The diffusion of Pt atoms towards the surface of the particles results in the formation of larger and more well-defined Pt crystal planes. This in turn is reflected in the CV analysis as more well-defined peaks in the hydrogen region.

At small particle sizes, Pt will mainly be in an amorphous state with only small areas of well defined Pt crystalline facets at the surface, giving rise to a lack of distinctive adsorption/desorption hydrogen sites as shown by the cyclic voltammogram of 20 wt% Pt/C and that of the *as prepared* catalysts. On increasing the heat-treatment temperature, the TEM showed sintering (**Table 3-10**) of the particles whilst the XPS data showed a surface enrichment of Pt atoms takes place (**Table 3-5** to **Table 3-9**). As more and more Pt atoms are reaching the surface, more extended Pt crystal planes are being formed on the outer part of the particles[40], which results in more distinctive hydrogen adsorption/desorption peaks. Despite the surface enrichment of Pt, a significant decrease in mass normalised Pt area (**Table 3-31**) can be observed.

This decrease can be due to an increase in particle size or clustering of the particles. However, it can only be suspected as the errors on the TEM results are quite significant. The decrease in Pt area could also be due to alloy formation as the heat treatment temperature increases which decreases the number of Pt site available for H_{ads} to occur. Nonetheless, the values for these mass normalised areas should be treated with a certain degree of caution as there are several areas where errors can be introduced e.g. the compression of the catalyst layer, the amount of catalyst in electrical contact, and loss of catalyst in the pressing procedure However, it does not mean that the measurement of the mass normalised Pt is totally irrelevant. It can still be used to identify trends and obtain approximate values. As a result, it was more appropriate to normalise the current recorded in the cyclic voltammogram to the available Pt surface area.

Table 3-31 Pt electrochemical surface area for 20 wt% Pt/C and all the Ni/Pt/C electrocatalysts. All the results have a unit of $m_{Pt}^2\ g_{Pt}^{-1}$.

Precursor / Annealing temperature	$Ni(acac)_2$			$Ni(Cp)_2$	
	0.5 ML	**1 ML**	**2 ML**	**1 ML**	**2 ML**
As prepared	52.5	55.6	67.7	54.3	50.0
200 °C	54.9	55.4	60.9	54.1	51.4
500 °C	54.6	52.4	63.1	49.1	45.3
750 °C	40.2	50.3	48.8	40.5	36.8
900 °C	27.6	33.9	37.1	24.7	31.1
20 wt% Pt/C	58.9				

The TEM results (**Table 3-10**), the XRD data (**Figure 3- 3** through **Figure 3- 7**) and the above discussion suggested an increase in crystallite size. Kinoshita[40] proposed that as the Pt particle size increases, the fraction of surface atoms on Pt(100) and Pt(111) facets increases compared to those at the edge or corner sites. Ross[41] compared the cyclic voltammetry of Pt(111) and Pt(100) single crystal in 0.5 M H_2SO_4. He observed that Pt(100) facets exhibited a lower overpotential for the oxide reduction peak than that of Pt(111). This indicates that the Pt(100) phase should be more catalytically active towards the ORR than that of the Pt(111) The oxygen adsorbs via a dual site adsorption mode[42] and therefore edge and corner sites

are less favourable for this reaction because of their geometrical arrangement. However, Pt(100) and Pt(111) terraces are suitable for the dual adsorption mode. As a consequence, more favourable sites for oxygen adsorption are being formed which in turns indicate that a greater specific activity may be exhibited by the catalysts. Thus, for the Ni/Pt/C catalysts in this thesis, one would predict that as the heat treatment temperature increases, more appropriate sites for the adsorption of oxygen will be formed (e.g. Pt(100) crystal planes) and that the ORR activity should be greater.

Table 3-32 Potential of the oxide reduction peak for 20 wt% Pt/C and all the Ni/Pt/C electrocatalysts. All the results have a unit of V vs. RHE.

Precursor / Annealing temperature	$Ni(acac)_2$			$Ni(Cp)_2$	
	0.5 ML	**1 ML**	**2 ML**	**1 ML**	**2 ML**
As prepared	0.758	0.765	0.766	0.762	0.768
200 °C	0.760	0.771	0.760	0.761	0.766
500 °C	0.756	0.731	0.751	0.747	0.746
750 °C	0.772	0.758	0.748	0.752	0.764
900 °C	0.799	0.794	0.754	0.772	0.772
20 wt% Pt/C	0.753				

Table 3-32 summarises the potential of the oxide reduction peak for 20 wt% Pt/C and all the Ni/Pt/C electrocatalysts. It can be seen that the potential of the oxide stripping peak for all the *as prepared* electrocatalysts is greater than that of 20 wt% Pt/C by *ca.* 10 mV. In addition, it also increases as the heat treatment temperature increases. In other words, a lower overpotential is needed to reduce the oxide present at the Pt surface. This suggests a weaker binding of the OH_{ads} on the Pt surfaces. This is consistent with the XANES results (**section 3.1.5**) as it was observed that the magnitude of the white line decreased as the annealing temperature increased. The decrease in the magnitude of the white line was attributed to the formation of a PtNi alloy phase which reduces the amount of "free" Pt sites and inevitably lowers the number of Pt-OH.

3.2.2 RDE measurements

RDE measurements allow the determination of the catalytic activity (specific activity and mass activity if coupled with the results obtained with the CV measurements) of each catalysts as described by **Equation 3-2**.

$$Mass\ activity\ \left(A\ g^{-1}Pt\right) = \frac{Specific\ activity\ \left(\mu A\ cm^{-2}Pt\right)\ \times\ Pt_{area}\left(m^2 g^{-1}Pt\right)}{100}$$

Equation 3-2

Three different rotation rates were used to study the ORR (900, 1600 and 2500 rpm) and a Levich plot (limiting current vs. square root of rotation rate) was plotted to confirm that the RDE experiment was running under a good mass-transport regime as illustrated in **Figure 3- 37a**.

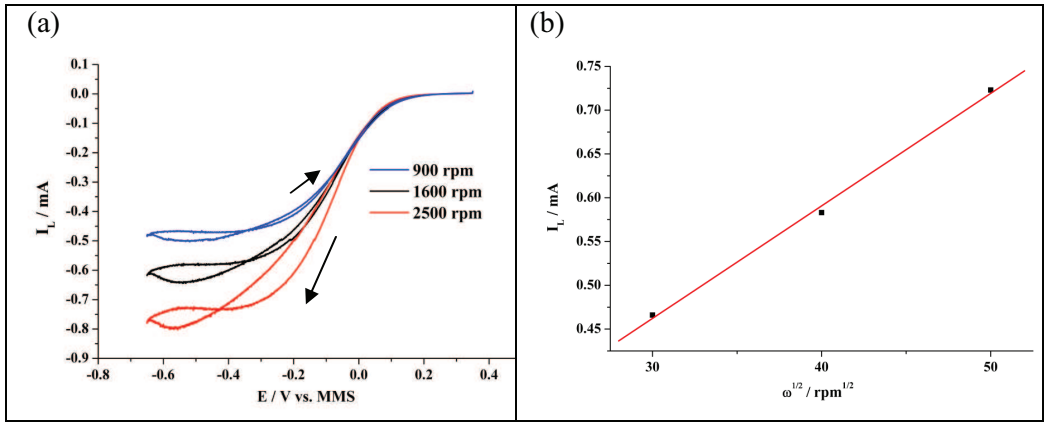

Figure 3- 37 (a) Typical polarisation curve obtained during a RDE measurement and (b) its associated Levich plot (the limiting currents were read at -0.55 V vs. RHE). Data were obtained for the 1 ML Ni/Pt/C prepared via the $Ni(acac)_2$ route in O_2 saturated 1 M H_2SO_4 at 10 mV s^{-1}.

To analyse the data, only the forward scan (negative going) of the polarisation curve was used to prevent the undesired effect (increase in current) due to the adsorption of other species whilst the Pt surface is being freed of oxygenated species. For the Levich plot, the limiting currents were determined at -0.55 V vs. MMS and were plotted against the square root of the electrode rotation rate. A straight line not passing through the origin (intercept = 0.15 mA) was obtained with the slope that woud be expected for a 4-electron reduction reaction. As a result, according to the Levich plot, a 4 electron transfer is taking place during the ORR.

To assess the performance of the catalysts, the forward scan (negative going) of the polarisation curve was used and the kinetic current was extracted from the recorded current by rearranging **Equation 1-14**. The kinetic current was then normalised to the Pt active area (determined by CO adsorption) and the log of the normalised kinetic current was plotted against the potential (Tafel plot). The value of the the normalised kinetic current at 0.9 V vs. RHE was used to assess the specific activity of the catalysts. The specific activity is by definition the kinetic current per area of active material.

All the RDE measurements were performed in O_2 saturated 1M H_2SO_4 with a scan rate of 10 mV s^{-1} and the data presented is the mean of 3 replicates. For the specific activities, the value recorded is the mean of 3 replicates and its associated error is the highest error between the mean and the data recorded by each measurement.

The Tafel plots for the 0.5, 1 and 2 ML catalysts prepared via the $Ni(acac)_2$ route are shown in **Figure 3- 38**, **Figure 3- 39** and **Figure 3- 40**. Similarly, the Tafel plots for the 1 and 2 ML Ni/Pt/C electrocatalysts prepared via the $Ni(Cp)_2$ route are shown in **Figure 3- 41** and **Figure 3- 42**. For each set of catalysts, the Tafel plot of the 20 wt% Pt/C was included for comparison purposes.

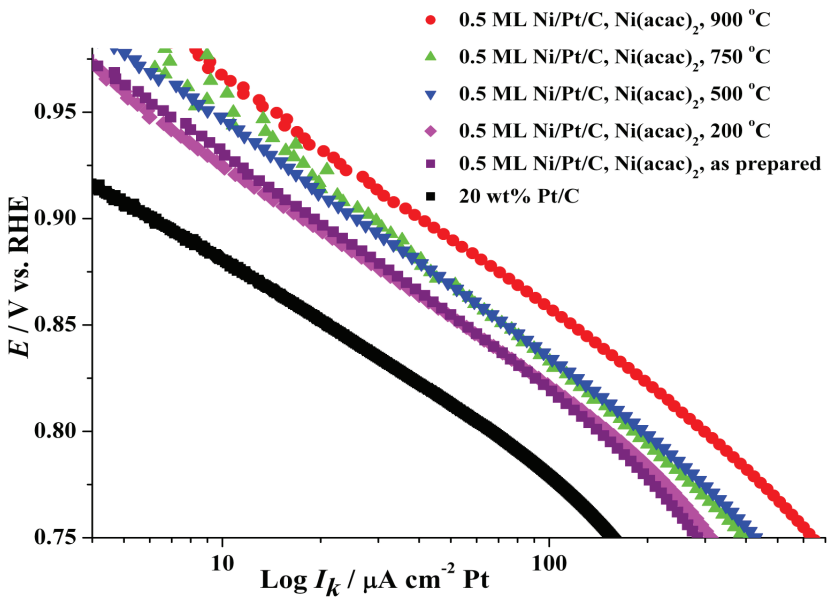

Figure 3- 38 Oxygen reduction Tafel plots for 0.5 ML Ni/Pt/C ($Ni(acac)_2$) as prepared, 200, 500, 750 and 900 °C in O_2 saturated 1 M H_2SO_4 at 2500 rpm and 10 mV s^{-1}. Tafel plot for 20 wt% Pt/C is shown for comparison purposes.

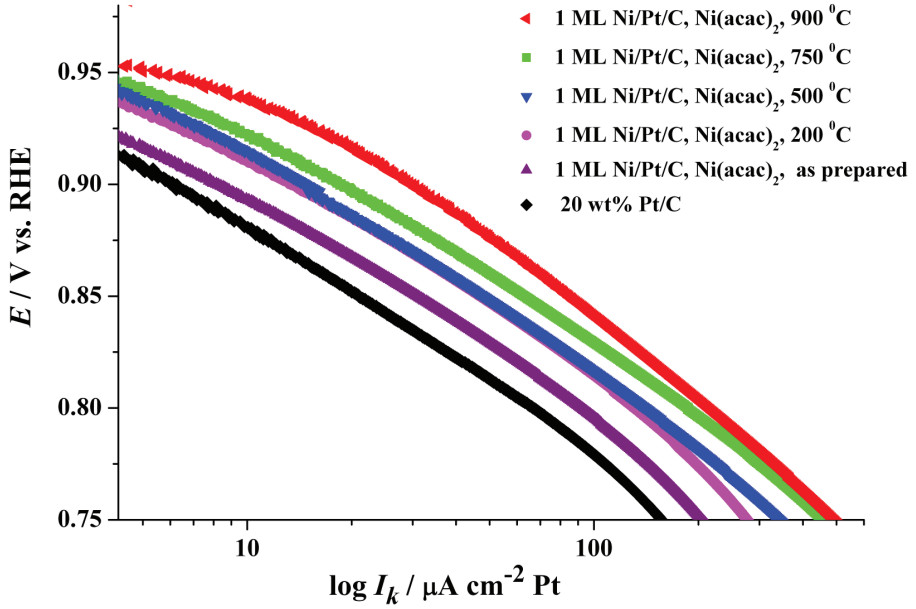

Figure 3- 39 Oxygen reduction Tafel plots for 1 ML Ni/Pt/C ($Ni(acac)_2$) as prepared, 200, 500, 750 and 900 °C in O_2 saturated 1 M H_2SO_4 at 2500 rpm and 10 mV s^{-1}. Tafel plot for 20 wt% Pt/C is shown for comparison purposes.

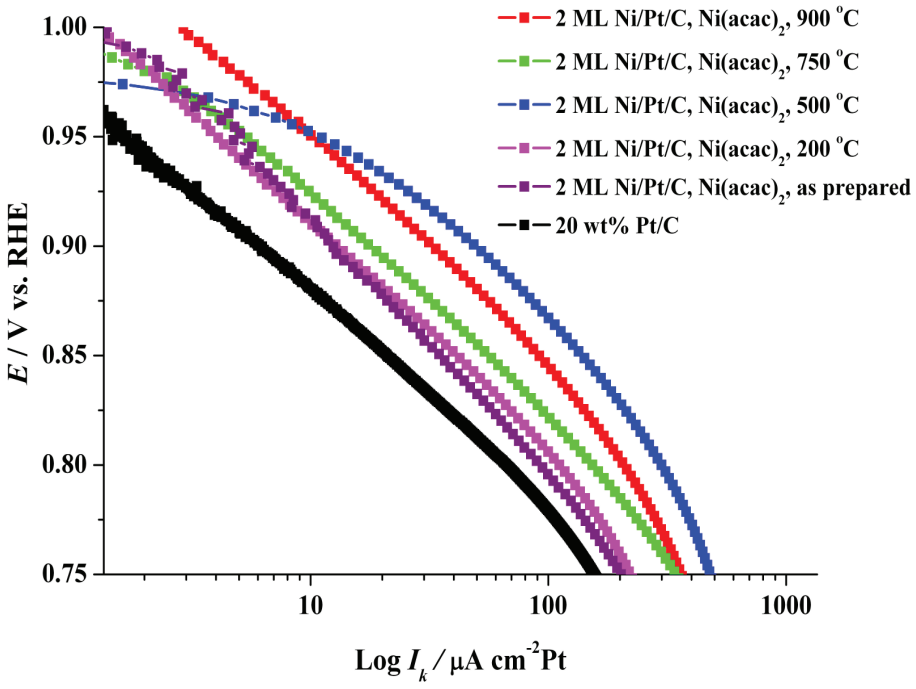

Figure 3- 40 Oxygen reduction Tafel plots for 2 ML Ni/Pt/C ($Ni(acac)_2$) as prepared, 200, 500, 750 and 900 °C in O_2 saturated 1 M H_2SO_4 at 2500 rpm and 10 mV s^{-1}. Tafel plot for 20 wt% Pt/C is shown for comparison purposes.

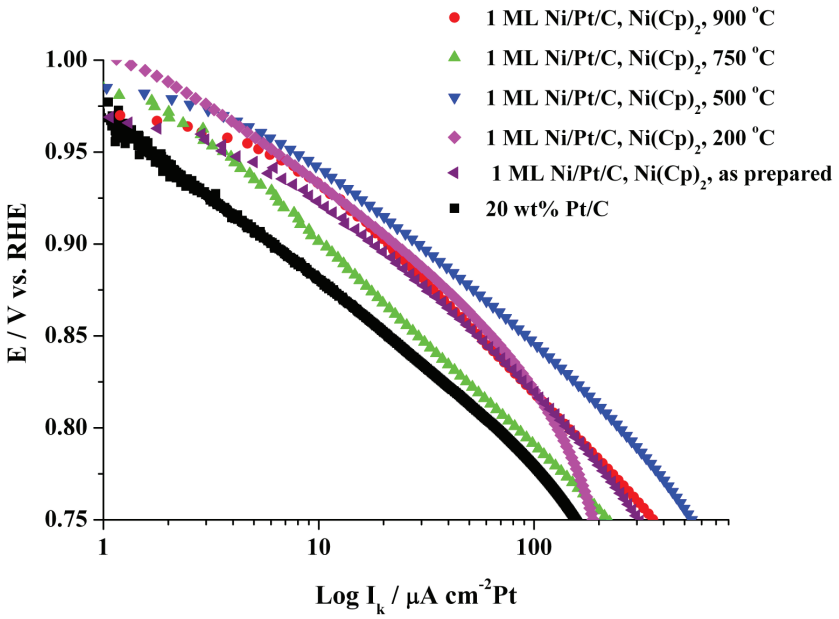

Figure 3- 41 Oxygen reduction Tafel plots for 1 ML Ni/Pt/C ($Ni(Cp)_2$) as prepared, 200, 500, 750 and 900 °C in O_2 saturated 1 M H_2SO_4 at 2500 rpm and 10 mV s^{-1}. Tafel plot for 20 wt% Pt/C is shown for comparison purposes.

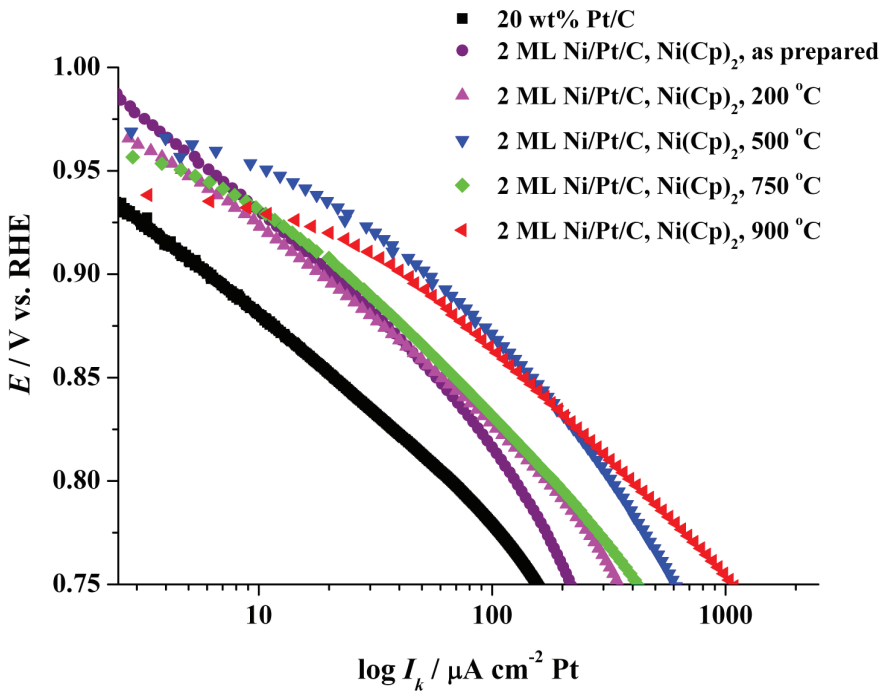

Figure 3- 42 Oxygen reduction Tafel plots for 2 ML Ni/Pt/C ($Ni(Cp)_2$) as prepared, 200, 500, 750 and 900 °C in O_2 saturated 1 M H_2SO_4 at 2500 rpm and 10 mV s^{-1}. Tafel plot for 20 wt% Pt/C is shown for comparison purposes.

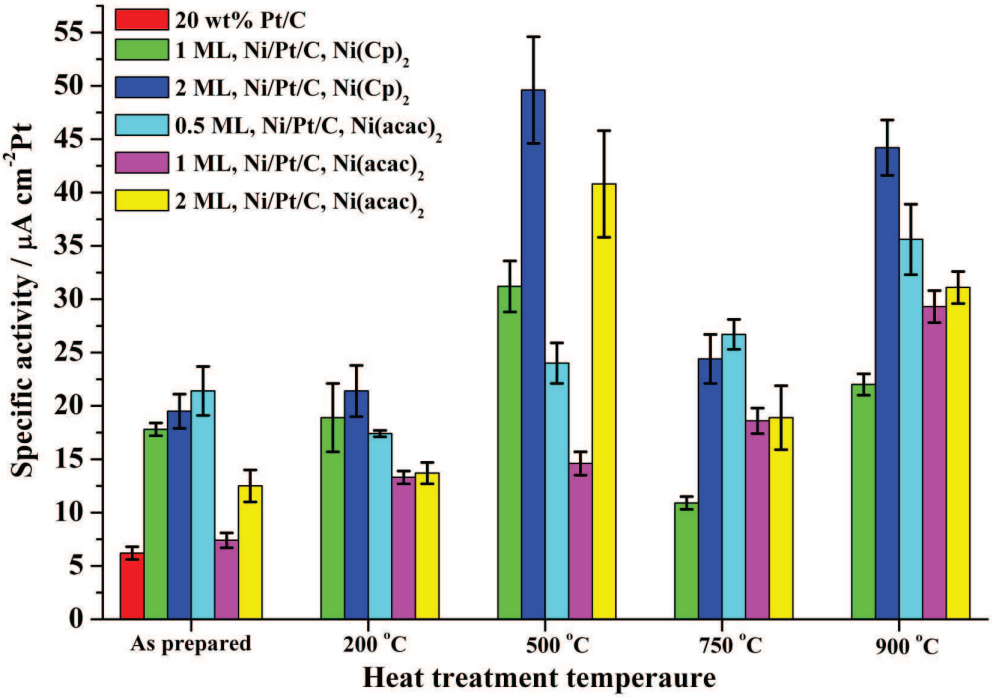

Figure 3- 43 Histograms of the specific activity of all the Ni/Pt/C electrocatalysts and 20 wt% Pt/C was added for comparison purposes. The values of the specific activity were taken at 0.9 V vs. RHE. Graph shows the mean of 3 replicates along with the larger error calculated between the mean and the values used to calculate it.

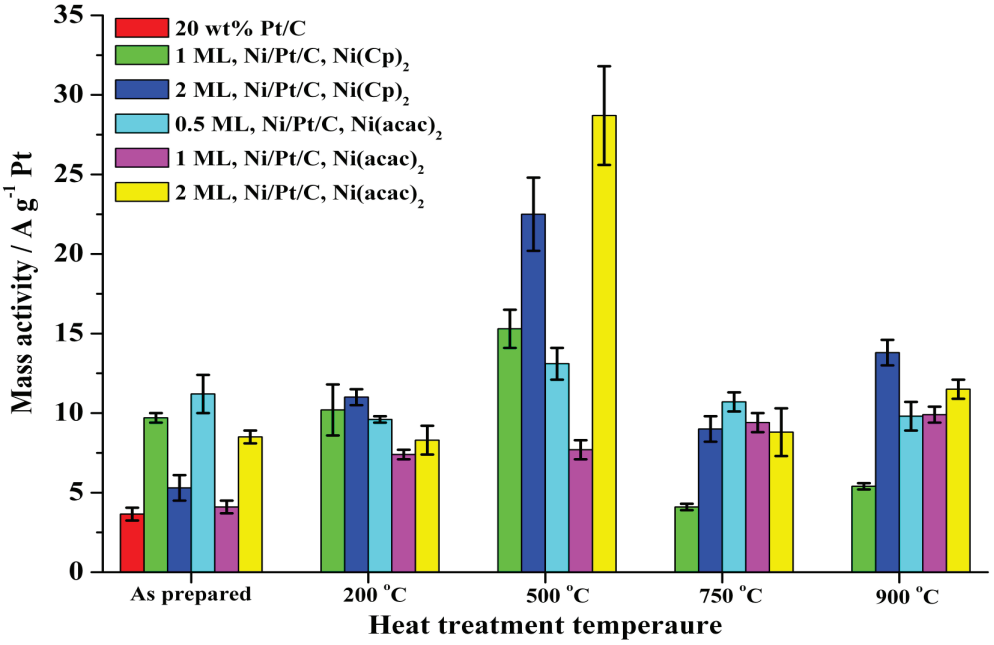

Figure 3- 44 Histograms of the mass activity of all the Ni/Pt/C electrocatalysts and 20 wt% Pt/C was added for comparison purposes. The values of mass activity weretaken at 0.9 V vs. RHE. Graph shows the mean of 3 replicates along with the larger error calculated between the mean and the values used to calculate it.

The trend in specific activity (**Figure 3-43**) and mass activity (**Figure 3-44**) are similar. Thus, the discussion below will only refer to the specific activities. It can be observed from that the general trend for the specific activity (SA) is that it increases as the heat-treatment temperature increases. There is up to a 6-fold increase in SA for the Ni/Pt/C prepared via the $Ni(acac)_2$ route and up to a 8-fold increase for the Ni/Pt/C prepared via the $Ni(Cp)_2$ route. However, a discrepancy is observed for the 2 ML Ni/Pt/C prepared via the $Ni(acac)_2$ route and the 1 and 2 ML Ni/Pt/C prepared via the $Ni(Cp)_2$ route. The discrepancy is that the SA obtained for the sample heat-treated at 500 °C is higher than that of the sample heat-treated at 750 and 900 °C. The activity observed for the $Ni(acac)_2$ and $Ni(Cp)_2$ series can be explained by referring to the structural data described in **section 3.1**.

Both $Ni(acac)_2$ and $Ni(Cp)_2$ series have been shown to consist of a PtNi alloy after heat treatment at temperatures greater than 500 °C and the degree of alloying was shown to increase as the heat treatment temperature increased (**Figure 3- 3** to **Figure 3- 7**). Wells[43] found that heat-treating Pt/C to 900 °C slightly increased the Pt particle size to around 5 nm and that a similar particle size was observed for the prepared catalysts (not heat treated). He concluded that the increase in particle size attributed to the heat treated catalysts must have been caused by the heat treatment conditions and not by the deposition of the secondary metal. In addition, the increase in SA exhibited by the prepared catalysts was mainly assigned to alloy formation because when the secondary metal was present at the surface of the catalysts (but not part of an alloy phase), no catalytic improvement was observed. In this work, it is very difficult to draw any conclusions from the particle size data because of the large errors associated with the values. However, it can still be observed that the presence of the secondary metal enhances the catalytic activity of the catalysts even though it is not part of an alloy phase. In addition, the catalytic improvement was even greater when the secondary metal was part of an alloy phase. Thus, it is possible to deduce that the degree of alloying has a direct impact on the SA of the catalysts. This trend is especially observed for the sets of catalysts 0.5 ML and 1 ML Ni/Pt/C prepared via the $Ni(acac)_2$ route. However, as mentioned previously, a discrepancy for the SA is exhibited by the sets of catalysts, 2 ML Ni/Pt/C prepared via the $Ni(acac)_2$ route and 1 ML and 2 ML Ni/Pt/C prepared via the $Ni(Cp)_2$ route (shift in the XRD peaks, **Figure 3- 3** to **Figure 3- 7** and the TEM analysis). This

supports an alloying phase effect on the SA of the Ni/Pt/C catalysts. From our data, it can be noted that if large particle sizes are present (at high Ni monolayer coverage or low dispersion of Ni on the Pt surface), a disordered PtNi transition phase occurs at 500°C which is more active than a well-ordered PtNi alloy phase (obtained for the 900 °C catalysts). This effect has been previously observed.[27, 28] As a result, the presence of a specific alloy phase(s) could be the cause of the catalytic activity exhibited by the prepared catalysts.

The CV data showed a more well-defined surface structure and a lower Pt surface active area as the heat treatment temperature increased. The formation of a more well-defined structure was attributed to an increase in particle size (decrease in Pt surface area). As discussed in **section 3.2.1**, the increase in particle size leads to the formation of more Pt(111) and Pt(100) terraces which are suitable adsorption sites for the dual adsorption mode of the oxygen molecules thus providing more active sites towards the ORR resulting in a higher SA. In addition the CV data demonstrated a shift in the potential of the oxide stripping peak (10-50 mV), which indicates a weaker binding between the OH_{ads} and the Pt surfaces. As a result, the SA exhibited by the catalyst increased as the heat treatment temperature increased because more Pt sites were "oxide" free at lower overpotential.

The increase in SA (in comparison to Pt/C (900 °C) of a similar particle size[43] (~6.5 nm) was found to be 7.8 μA cm^{-2} Pt.) despite a decrease in Pt surface area, can be attributed to a PtNi alloy formation. The synergistic effect of Ni on Pt induces a change in the electronic properties of the Pt at the surface of the catalyst particle, which is apparent in the XANES data (**Figure 3- 15** and **Figure 3- 16**) as a decrease in the white line intensity. Such a decrease is attributed to a lower *d*-band vacancy. This electronic effect of Ni on Pt was also observed in the XPS data as a shift in the Pt($4f_{7/2}$) peak and that of the Ni($2p_{3/2}$) (**Table 3-5** to **Table 3-9**).

The other outcome of the PtNi alloy formation is also shown by the decrease of the Pt-Pt nearest neighbour bond distance as the degree of alloying increases (or as the heat treatment temperature increases) (**Table 3-30**) in the EXAFS analysis. The results obtained in this work do support the theory that the SA increases as the Pt-Pt nearest neighbour bond distance decreases (shorter than that of 20 wt% Pt/C). It was found previously that the reduction of the Pt-Pt nearest neighbour bond distance

favours the adsorption of oxygen[30], leading to an increase in the SA. [14, 30] In this work, a similar conclusion can be reached for the 0.5 and 1 ML Ni/Pt/C prepared via the $Ni(acac)_2$ route (though the increase is not linear). However, the same conclusion cannot be reached for the other sets of catalysts (**Table 3-30, Figure 3.43 and Figure 3-44**). This is because for some sets of catalysts, the intermediate heat-treated catalysts (500 °C) exhibited a higher catalytic activity than those heat-treated at 900 °C. As a result, no optimum Pt-Pt nearest neighbour bond distance could be determined for the Ni/Pt/C catalysts. The increase in activity could be explained by the rearrangement of the Ni and Pt atoms occurring with increasing temperature. As the temperature increases, more Ni atoms enter the Pt bulk and more Pt atoms diffuse to the surface of the particle resulting in a rearrangement of the Ni and Pt atoms. The rearrangement of the Pt and Ni atoms seem to create more suitable adsorption sites for the ORR, thus increasing the activity of the catalysts. This may be due to a bifunctional mechanism (similar to that of PtRu as explained in **Chapter 1 section 3.3**) whereby Ni adsorbs the oxygenated species which then diffuse onto the Pt to react or the oxygenated species adsorb on the bridge site between Ni and Pt and dissociate and then react. In-situ IR combined with electrochemistry could provide more information regarding the mechanism occurring at the electrode surface.

4 Conclusions

In this chapter, the effective preparation of several Ni/Pt/C electrocatalysts using two precursors, $Ni(acac)_2$ and $Ni(Cp)_2$ has been demonstrated. It was also shown that the preparation of Ni/Pt/C via the $Ni(acac)_2$ and $Ni(Cp)_2$ routes resulted in a complete deposition of the precursor onto the Pt/C in contrast to the previous work of Qian *et al*.[28]

It was also demonstrated that the deposition of Ni on Pt/C was accompanied with a certain extent of clustering of the Ni atoms. The extent of clustering was found to be dependant upon both the amount of Ni deposited and the precursor employed during the preparation of the catalyst, with $Ni(Cp)_2$ leading to a larger extent of clustering than $Ni(acac)_2$. This clustering effect was observed by both the TEM which showed a large standard deviation and by the EXAFS which showed the presence of Pt-O neighbours in all the *as prepared* catalysts.

The RDE data showed up to a 6-fold and 8-fold increase in SAs for the Ni/Pt/C prepared via the $Ni(acac)_2$ and $Ni(Cp)_2$ routes, respectively. Similarly, up to a 9-fold and 7-fold increase in MAs were observed for the Ni/Pt/C prepared via the $Ni(acac)_2$ and $Ni(Cp)_2$ routes, respectively. However, according to the Levich plot, only 2 electrons were involved in the ORR but RRDE should be performed to confirm the formation of H_2O_2.

The increased SA and MA were attributed to PtNi alloy phase formation as shown by the XRD data. As more Ni entered the fcc crystal structure of Pt, a shrinking of the lattice parameter and a shift in the *d*-band centre of Pt occurred. Both of these were confirmed by the EXAFS and XANES data as a decrease in Pt-Pt nearest neighbour bond distance was observed along with a decrease in the normalised white line intensity. The modification of the electronic property was also thought to result in a lowering of the binding energy of the oxide species. Also, the increase in particle size as the heat treatment temperature increases resulted in the formation of more Pt(100) and Pt(111) crystal planes which are more favourable sites for the oxygen adsorption as described by the CV data. The increase in SA also results from a weaker bond between the OH_{ads} and the Pt surfaces as demonstrated by the shift of

the potential of the oxide stripping peak to lower overpotentials and the XANES results.

All in all, the observed catalytic enhancement of the prepared Ni/Pt/C electrocatalysts was thought to be due to several factors working together such as alloy phase formation, increase of the particle size, decrease in *d*-band vacancy, shorter Pt-Pt nearest neighbour bond distance and geometrical changes.

5 References

1. E. Yeager, *Electrochimica Acta*, **29**, 1527 (1984).
2. T. Jacob, *Fuel Cells*, **6**, 159 (2006).
3. X. Yu and S. Ye, *Journal of Power Sources*, **172**, 145 (2007).
4. E. Antolini, J. R. C. Salgado and E. R. Gonzalez, *Journal of Power Sources*, **160**, 957 (2006).
5. M. P. Hogarth and T. R. Ralph, *Platinum Metals Review*, **46**, 3 (2002).
6. T. Ioroi and K. Yasuda, *Journal of The Electrochemical Society*, **152**, A1917 (2005).
7. H. I. Takako Toda, Hiroyuki Uchida, and Masahiro Watanabe, *Journal of The Electrochemical Society*, **146**, 3750 (1999).
8. V. R. Stamenkovic, B. Fowler, B. S. Mun, G. F. Wang, P. N. Ross, C. A. Lucas and N. M. Markovic, *Science*, **315**, 493 (2007).
9. S. Mukerjee and S. Srinivasan, *Journal of Electroanalytical Chemistry*, **357**, 201 (1993).
10. D. Thompsett, *Handbook of Fuel Cells: Fundamentals, Technology and Applications. Volume 3, Chapter 37: Pt-Alloys as Oxygen Reduction Catalysts.*, John Wiley & Sons ltd, New york (2003).
11. J. R. Kitchin, J. K. Norskov, M. A. Barteau and J. G. Chen, *The Journal of Chemical Physics*, **120**, 10240 (2004).
12. J. K. Nørskov, T. Bligaard, A. Logadottir, S. Bahn, L. B. Hansen, M. Bollinger, H. Bengaard, B. Hammer, Z. Sljivancanin, M. Mavrikakis, Y. Xu, S. Dahl and C. J. H. Jacobsen, *Journal of Catalysis*, **209**, 275 (2002).
13. L. Santos, C. H. F. Oliveira, I. R. Moraes and E. A. Ticianelli, *Journal of Electroanalytical Chemistry*, **596**, 141 (2006).
14. V. Jalan and E. J. Taylor, *Journal of The Electrochemical Society*, **130**, 2299 (1983).
15. F. H. B. Lima, J. R. C. Salgado, E. R. Gonzalez and E. A. Ticianelli, *Journal of The Electrochemical Society*, **154**, A369 (2007).
16. E. Antolini, J. R. C. Salgado, M. J. Giz and E. R. Gonzalez, *International Journal of Hydrogen Energy*, **30**, 1213 (2005).
17. H. R. Colon-Mercado and B. N. Popov, *Journal of Power Sources*, **155**, 253 (2006).

18. M. Götz and H. Wendt, *Electrochimica Acta*, **43**, 3637 (1998).
19. Y. Chen, F. Yang, Y. Dai, W. Wang and S. Chen, *The Journal of Physical Chemistry C*, **112**, 1645 (2008).
20. M. Shao, K. Sasaki, N. S. Marinkovic, L. Zhang and R. R. Adzic, *Electrochemistry Communications*, **9**, 2848 (2007).
21. A. Henglein, *The Journal of Physical Chemistry B*, **104**, 2201 (2000).
22. S. U. Son, Y. Jang, J. Park, H. B. Na, H. M. Park, H. J. Yun, J. Lee and T. Hyeon, *Journal of the American Chemical Society*, **126**, 5026 (2004).
23. E. M. Crabb and M. K. Ravikumar, *Electrochimica Acta*, **46**, 1033 (2001).
24. C. Travers, J. P. Bournonville and G. Martino, in *Proceedings of the 8th International Congress on Catalysis*, p. 891, Berlin (1984).
25. J. Margitfalvi, M. Hegedus, S. Gobolos, E. Kern-Talas, P. Szedlacsek, S. Szabo and F. Nagy, in *Proceedings of the 8th International Congress on Catalysis*, p. 903, Berlin (1984).
26. P. P. Wells, Y. D. Qian, C. R. King, R. J. K. Wiltshire, E. M. Crabb, L. E. Smart, D. Thompsett and A. E. Russell, *Faraday Discuss.*, **138**, 273 (2008).
27. W. V. Hui Yang, Claude Lamy, and Nicolás Alonso-Vante, *The Journal of Physical Chemistry B (Materials)*, **108**, 11024 (2004).
28. Y. Qian, 2004, *Preparation of Pt-based Bimetallic Catalysts for the Oxygen Reduction Reaction in PEM Fuel Cells*, Thesis (PhD in Chemistry), The Open University.
29. A. K. Shukla, M. Neergat, P. Bera, V. Jayaram and M. S. Hegde, *Journal of Electroanalytical Chemistry*, **504**, 111 (2001).
30. M.-k. Min, J. Cho, K. Cho and H. Kim, *Electrochimica Acta*, **45**, 4211 (2000).
31. S. Hüfner and G. K. Wertheim, *Physical Review B*, **11**, 678 (1975).
32. D. A. Shirley, R. L. Martin, S. P. Kowalczyk, F. R. McFeely and L. Ley, *Physical Review B*, **15**, 544 (1977).
33. N. H. H. Abu Bakar, M. M. Bettahar, M. Abu Bakar, S. Monteverdi, J. Ismail and M. Alnot, *Journal of Catalysis*, **265**, 63 (2009).
34. L. A. da Silva, V. A. Alves, S. C. de Castro and J. F. C. Boodts, *Colloids and Surfaces A: Physicochemical and Engineering Aspects*, **170**, 119 (2000).

35. J. W. Niemantsverdriet, *Spectroscopy in Catalysis: An Introduction, Chapter 3: Photoemmission and Auger Spectroscopy*, p. 37, Wiley-VCH, Weinheim (2000).

36. S. Mukerjee, S. Srinivasan and M. P. Soriaga, *Journal of The Electrochemical Society*, **142**, 1409 (1995).

37. S. Lu, W. W. Lonergan, J. P. Bosco, S. Wang, Y. Zhu, Y. Xie and J. G. Chen, *Journal of Catalysis*, **259**, 260 (2008).

38. G. A. Attard, J. E. Gillies, C. A. Harris, D. J. Jenkins, P. Johnston, M. A. Price, D. J. Watson and P. B. Wells, *Applied Catalysis A: General*, **222**, 393 (2001).

39. B. E. Conway and S. Gottesfeld, *Journal of the Chemical Society, Faraday Transactions 1: Physical Chemistry in Condensed Phases* **69**, 1090 (1973).

40. K. Kinoshita, *Journal of The Electrochemical Society*, **137**, 845 (1990).

41. P. N. Ross Jr, *Surface Science*, **102**, 463 (1981).

42. E. Yeager, *Journal of Molecular Catalysis*, **38**, 5 (1986).

43. P. Wells, 2007, *Controlled surface modification of supported platinum group metal catalysts*, Thesis (PhD in Chemistry), University of Southampton.

CHAPTER FOUR: Pt MODIFIED Ni/C ELECTROCATALYSTS FOR THE ORR FOR USE IN PEMFC

1 Introduction

Over the past few decades, the Pt loading of PEMFC has been decreased to 0.6-0.8 $mg_{Pt}\,cm^{-2}$ whilst the power density, at *ca.* 0.65 V vs. RHE, has increased to 0.7 $W\,cm^{-2}$ which corresponded to 0.85-1.1 $g_{Pt}\,kW^{-1}$. However, to ensure the commercialisation of PEMFC, a further decrease of the Pt-specific power density to 0.2 $g_{Pt}\,kW^{-1}$ is required to ensure cost effectiveness and suitable use of the Pt resources.[1]

We are therefore confronted with a fundamental problem which is decreasing the cost of the catalyst (by decreasing the amount of Pt used) whilst simultaneously increasing its catalytic activity. As a result, research groups have followed several alternative routes to tackle this issue. Some have tried to find a catalyst based on non-noble metals whilst others tried to focus on reducing the amount of Pt by depositing Pt onto other metal surfaces and form core-shell catalysts. Both routes are described below with a particular emphasis on the latter.

Despite Pt being the most active metal towards the ORR, its high cost and scarcity led to research projects focusing on non-noble metal electrocatalysts. Liu *et al.*[2] studied the ORR activity of several Ru-based bimetallic catalysts. The electrocatalysts were prepared using a chelation approach. They found that the transition metal used in combination with Ru greatly influenced the catalytic enhancement, with Fe having the greatest effect. The PtFe alloy catalyst exhibited a maximum power density of 0.18 $W\,cm^{-2}$ and no performance degradation for 150 h. The enhanced activity was attributed to a synergistic effect between the two metals used.

Kim *et al.*[3] also considered Ru-based catalysts for the ORR but focused on the effect of nitrogen content in the catalyst. The catalysts were prepared by adding propylene diammine to Ru/C. They reported that Ru-N/C complexes showed activity towards the ORR. They also demonstrated that as the molar ratio Ru:N increased, the activity

and selectivity of the catalyst towards the ORR also increased. In addition, they modified the Ru-N/C catalyst with urea to increase the activity of the catalyst further. The urea modified catalyst exhibited both a higher catalytic activity and selectivity towards the ORR than any of the prepared Ru-N/C catalysts. Its activity was similar to that of commercial Pt/C catalyst and it generated less than 2% H_2O_2 indicating a 4-electron reduction process. The activity exhibited by such catalysts was believed to be due to the presence of nitrogen and oxygen functional groups which contribute to the formation of more active sites.

Wang *et al*.[4] prepared a range of Pd-Co bimetallic alloys via the modified polyol reduction method. The catalysts were also subjected to several heat treatment temperatures. They reported that the catalytic activity of the catalysts exhibited a volcano-type shape as a function of temperature, with a maximum catalytic activity exhibited by the catalyst heat-treated at 500 ºC. It was also demonstrated that the latter had a high selectivity and did not lead to any H_2O_2 production. The increase in catalytic activity observed for the prepared catalysts as the temperature increased was explained by the increase in the degree of alloying between Pd and Co. The odd, but high, catalytic enhancement displayed by the catalyst heat treated at 500 ºC was explained by its similarities to the most active Pd-based bimetallic catalyst, Pd-Fe/C. The Pd-Pd bond distance of the heat treated catalyst matched that of the Pd-Fe/C and thus, it was thought to provide an adequate site for the O_2 molecule to adsorb and undergo reduction.

Zhong *et al*.[5] studied the ORR on tungsten nitride supported on carbon (W_2N/C). The catalysts were prepared by the incipient wetness method and temperature-programmed reaction (TPR). Briefly, ammonium metal carbide was dissolved in water and a dispersing agent and was impregnated on carbon for 12 h. After drying, the resulting powder was nitrified under an ammonia atmosphere using a TPR process. The catalyst was tested in a 5 cm^2 MEA. The H_2 and O_2 were humidified and supplied at 90 and 85 ^oC at the anode and cathode, respectively. The gas pressure was kept at 0.2 MPa and the loading was 0.30 and 0.64 mg cm^{-2} for the anode and cathode, respectively. The catalyst used at the anode was 46 wt% Pt/C. The TEM analysis showed highly dispersed particles with a narrow particle size peaking at 4 nm. The catalyst demonstrated a catalytic activity that increased as the cell temperature increased with a maximum power density of 0.039 W cm^{-2}

observed at 80 ^{o}C. The activity of the W_2N/C catalyst was attributed to the synergistic effect between the two compounds (W and N) and the nanostructure which provided a large surface area.

Despite being less expensive, non-noble catalysts still struggle to match the activity exhibited by the standard Pt/C catalyst and therefore cannot be seen as a viable option for the near future. As a consequence, several research projects concentrated on lowering the amount of Pt used in the preparation of the catalysts.

Stamenkovic *et al.*[6] studied the ORR on well-defined Pt_3Ni and Pt_3Co alloy surfaces prepared under ultrahigh vacuum. The catalysts were then cleared of any carbon and oxygen residue by repeating sputtering and annealing cycles with Ar^+ and oxygen, respectively, until a clean surface was produced. To modify the surface composition, the samples were either annealed at 1000 K or mildly sputtered with a 0.5 keV beam of Ar^+. The LEIS confirmed a surface composition of 75% Pt and 25% Ni or Co. The annealing step led to catalysts having a first atomic layer composed of Pt atoms only, whilst the sputtering step led to Ni or Co and Pt being present on the outermost layer. A 4-fold increase in specific activity (SA) was reported for the annealed PtCo and a 2-fold and 3-fold increase in SA was reported for the sputtered Pt_3Ni and Pt_3Co, respectively. They concluded that the kinetics of the ORR were dependant upon the nature of the alloy and the arrangement of the alloying elements in the surface region. The ORR was found to follow a 4-electron reaction and that the catalytic enhancement was attributed to the inhibition of Pt-OH_{ads} on Pt sites surrounded by nickel oxide or cobalt oxide atoms beyond 0.8 V vs. RHE. It was also suggested that an electronic effect due to the secondary-metal-enriched layer situated underneath the Pt-skin may also be responsible for some of the enhancement.

Toda *et al.*[7] investigated the ORR on PtFe, PtNi and PtCo alloys catalysts. The catalysts were prepared with a radio frequency magnetron sputtering apparatus on a clean Pyrex glass disks. In all cases, Pt and the secondary metal were deposited simultaneously onto the surface at room temperature and at a controlled rate. Pt, Ni, Co and Fe electrodes were also prepared and used as references. The alloy formation was confirmed by energy-dispersive fluorescent X-ray analysis and crystallographic structures were determined by a grazing-angle XRD. They successfully prepared

catalysts with a range of metal:Pt ratios. From their RDE analysis, they reported a 10, 15 and 20-fold increase in SA towards the ORR for the most active PtNi, PtCo and PtFe alloys, respectively. The enhancement was attributed to the addition of the transition metal which increased the 5 *d*-band vacancy of Pt. This, in turn, led to an increase in 2π donation from the oxygen resulting in the increase in O_2 adsorption and a weakening of the oxygen bond thus, rendering the scission of the oxygen molecule easier.

Zhang *et al.*[8] reported catalysts consisting of a Pt monolayer on either Pd(111) or Pd nanoparticles as catalysts for the ORR. The catalysts were prepared by underpotential deposition of a copper (Cu) monolayer on the Pd(111) (or Pd nanoparticles) followed by a galvanic displacement of the Cu layer by Pt. The reaction scheme can be found elsewhere.[9] RDE data showed 5 to 8-fold catalytic enhancement (compared to Pt/C) for the Pt monolayer catalysts. In addition, only a very small amount of H_2O_2 was produced by the prepared catalysts indicating a 4-electron reduction reaction. The catalytic enhancement was attributed to a mismatch of the lattice constant between Pd and Pt and the shift in the *d*-band centre of Pt. This shift was reported to be caused by the interaction between Pd and Pt, which in turn, resulted in the charge redistribution through hybridisation of the states of each atom. The change in *d*-band centre caused a decrease in Pt-OH adsorption and a corresponding increase in the catalytic activity of the catalysts.

Lee *et al.*[10] studied the activity of a Pt monolayer on Co/C towards the ORR. The catalysts were prepared by adding a mixture of carbon and the Co precursor for 30 min at 142 °C resulting in the formation of Co/C. Then, $Pt(acac)_2$ and surfactants were added and the temperature was increased to 205 °C for 1 h. The XRD data showed that under the conditions used to prepare the catalyst a low degree of alloying was achieved (< 15%) but that the absence of Co diffraction peak indicated that the structure was that of rich Co core covered by a Pt rich shell. The prepared catalyst also exhibited a narrow particle size distribution with an average particle size of 3 nm. The core-shell catalysts exhibited a 1.5 and 1.8-fold enhancement in mass activity (MA) and SA, respectively. The catalytic improvement was explained by a reduction in the mean Pt-Pt bond distance as well as an electronic effect caused by the presence of Co. Another piece of their research consisted of studying the

effect of the thermal annealing on the catalytic activity of the $Co_{rich\ core}/Pt_{rich\ shell}/C$.[11] The catalysts were subjected to two annealing conditions: (a) 400 °C in N_2 for 0, 5, 10 and 15 h and (2) annealed at 250 °C in air for 10 min followed by 400 °C under 6% H_2/N_2 for 2 h. The catalysts annealed in N_2 showed an increase in SA from 8.22 to 12.02 μA cm^{-2} Pt as the annealing time increased. The catalyst annealed under H_2 exhibited a 2.5 and 1.9-fold enhancement in MA and SA (in comparison to Pt/C) respectively. The increase in activity was attributed to an increase in the extent of alloying and a concordant decrease in lattice parameter as the annealing time increased.

Yang *et al*.[12] explored the activity of Pd-Pt core-shell catalysts towards the ORR. The catalysts were prepared by dropwise addition of a solution of K_2PtCl_4 dissolved in water to a Pd/C water suspension. The mixture was left to react for 5 h. The amount of Pt added was equivalent to Pt:Pd atomic ratios of 20:80, 30:70 and 40:60. The particle size of the different catalysts was determined by XRD and was found to be similar to that of the Pd/C precursor (4.8 nm). The XRD data also showed a shift in the diffraction peak and an expansion of the lattice parameter indicating that some Pt atoms are displacing the Pd atoms. The CV data showed a lower overpotential to strip off the oxide layer (20 mV) suggesting a weaker binding of the OH_{ads} on the surface of the particles. The RDE data also showed a 2 to 8-fold catalytic improvement over Pt/C indicating a more efficient use of the noble metal.

Successful preparation methods were developed for the deposition of Pt on several metals (commonly used in combination with Pt) however, no preparation methods could be found involving the preparation of $Ni_{core}/Pt_{shell}/C$ catalysts (deposition of Pt on Ni nanoparticles). As a consequence, this is believed to be the first successful attempt to deposit Pt on a cheap metal core such as Ni. In this chapter, the preparation of Pt on Ni/C electrocatalysts (Pt/Ni/C) using the SOMC methodology is reported. The Pt/Ni/C electrocatalysts were prepared by depositing Pt on reduced Ni/C using platinum acetonylacetonate in toluene. The catalysts were characterised using X-ray Diffraction, Transmission Electron Microscopy, Cyclic Voltammetry and Rotating Disk Electrode measurements.

2 Experimental

2.1 Catalyst preparation

5 g of Ni/C was introduced into a 2 neck round-bottomed flask fitted with a dropping funnel, a condenser and a thermocouple. N_2 was then flowed through (75 ml min^{-1}) the flask for 20 min to remove any traces of O_2. Next, to reduce the Ni surface, the temperature was increased to 575 °C for 3 h using a high temperature heating mantle (or a tube furnace) and 4% H_2/N_2 (or pure H_2) was flowed (75 ml min^{-1}) through the flask. Subsequently, the Ni/C was allowed to cool down to room temperature before adding 100 ml of toluene (or water) previously deaerated with N_2 for 15 min. The solution was stirred and heated at 90 °C whilst bubbling H_2 through the solution. A solution containing the required amount of Pt precursor (platinum acetonylacetonate ($Pt(acac)_2$) or potassium tetrachloroplatinate (K_2PtCl_4)) corresponding to 1 monolayer in 50 ml of toluene (or water), previously deaerated with N_2 for 15 min, was added dropwise to keep the temperature constant at 90 °C. Once the addition was completed, the slurry was left under constant stirring and heating for 5.5 h at 90 °C whilst bubbling 4% H_2/N_2 (or H_2) through the solution. The solution was then allowed to cool to room temperature and the gas was switched to N_2 for another 15 min to remove any traces of H_2. The solution was filtered off and the precipitate was thoroughly washed with toluene and then with water (or with water only).

In the above procedure, when the tube furnace was used to reduce Ni/C, a water bath was used to maintain the reaction temperature at 90 °C.

Two different methods were used to prepare the catalysts to determine the effectiveness of the reduction step. The reduction step involving the furnace was more likely to allow the re-oxidation of Ni as it involved the transfer of the reduced Ni/C support into the 2 neck round-bottomed flask in a glove box which was then brought to the laboratory and the dropping funnel, a condenser and a thermocouple were then fitted and the experiment continued.

To establish the specificity of the deposition of Pt onto the Ni particles, two Pt-deposition experiments were carried out on activated carbon using a similar procedure to that described above. 0.5 g of XC-72R activated carbon was introduced

into a 2 neck round-bottomed flask fitted with a dropping funnel, a condenser and a thermocouple. N_2 was then flowed through (75 ml min^{-1}) the flask for 20 min to remove any traces of O_2. Next, the temperature was increased to 90 °C for 30 min and H_2 was flowed (75 ml min^{-1}) through the flask before adding 100 ml of toluene (or water) previously deaerated with N_2 for 15 min. The solution was stirred and heated at 90 °C using a water bath whilst bubbling H_2 through the solution. A solution containing the required amount of Pt precursor ($Pt(acac)_2$ or K_2PtCl_4) corresponding to *ca.* 4 wt% Pt (previously deaerated with N_2 for 15 min) in 50 ml of toluene (or water) was added dropwise to keep the temperature constant at 90 °C. Once the addition was completed, the slurry was left under constant stirring and heating for 5.5 h at 90 °C whilst bubbling H_2 through the solution. The solution was then allowed to cool to room temperature and the flowed gas was switched to N_2 for another 15 min to remove any traces of H_2. The solution was filtered off and the precipitate was thoroughly washed with toluene and then with water (or water only).

2.2 ICP-OES

All samples were submitted to *Johnson Matthey Technology Centre* where the analyses were performed by one of their analytical scientists.

2.3 Electrochemical characterisation

2.3.1 Cyclic voltammetry

All samples were analysed using the procedure detailed in **Chapter 2 section 2.2**.

2.3.2 Oxygen reduction testing

All samples were analysed using the procedure detailed in **Chapter 2 section 2.3**.

2.4 XRD

All samples were submitted to *Johnson Matthey Technology centre* where the analyses were performed by one of their analytical scientists. See **Chapter 2 section 3** for more information on the experimental procedure followed.

2.5 TEM-EDX

All samples were submitted to *Johnson Matthey Technology centre* where the analyses were performed by one of their analytical scientists. See **Chapter 2 section 4** for more information on the experimental procedure followed.

3 Results

3.1 Metal assay analysis

Elemental analysis of the as-prepared 1 monolayer (ML) Pt/Ni/C catalysts were carried out at *Johnson Matthey Technology Centre* by one of their analytical scientists. The experimental and theoretical values based on the amount of Pt and Ni/C introduced, are shown in **Table 4-1**.

Table 4-1 Elemental analysis for all the prepared 1 ML Pt/Ni/C (duplicate analysis).

Sample	Wt% Pt theoretical	Wt% Pt experimental	Wt% Ni theoretical	Wt% Ni experimental
Pt/Ni/C, furnace, K_2PtCl_4, H_2	6.7	5.8 ± 0.3	8.8	8.0 ± 0.3
Pt/Ni/C, furnace, $Pt(acac)_2$, H_2	6.7	4.8 ± 0.3	9.7	8.8 ± 0.3
Pt/Ni/C, furnace $Pt(acac)_2$, 4% H_2/N_2	9.0	3.3 ± 0.3	8.7	7.1 ± 0.3
Pt/Ni/C, heating mantle $Pt(acac)_2$, H_2	9.1	3.8 ± 0.3	8.7	8.3 ± 0.3
Pt/Ni/C, heating mantle $Pt(acac)_2$, 4% H_2/N_2	6.7	1.7 ± 0.3	9.8	9.3 ± 0.3

The assays of the prepared electrocatalysts show that the experimental values are not in good agreement with the theoretical values, indicating that the reaction between the Pt precursors and the Ni/C is incomplete. Several reasons could be attributed to the incomplete deposition. Firstly, these results indicate that the conditions used to prepare the catalysts are not optimum. Secondly, the difference between the theoretical and experimental values could be attributed to the re-oxidation of Ni to NiO after its exposure to a source of oxygen thus, preventing the SOMC reaction from taking place. For the K_2PtCl_4 route, the source of oxygen is the solvent itself, whilst the source of oxygen for the $Pt(acac)_2$ route could be from the presence of water in the toluene. And thirdly, **Table 4-1** also shows that the catalysts prepared

using H_2 (instead of 4% H_2/N_2) led to more complete Pt deposition which, also indicates that the reducing gas has an effect.

3.2 Which precursor?

To determine the specific deposition of Pt on the Ni particles, two blank syntheses were performed and the results of these analyses are presented in **Table 4-2**.

Table 4-2 Elemental analysis for the blank syntheses.

Precursor	Wt% Pt theoretical	Wt% Pt experimental
K_2PtCl_4	4.4	3.5 ± 0.3
$Pt(acac)_2$	3.3	0.1 ± 0.3

From the results in **Table 4-2**, it can be seen that a significant amount of Pt deposited on the carbon support during the K_2PtCl_4 blank experiment whilst a very low amount of Pt was detected on the carbon support during the $Pt(acac)_2$ blank experiment. These results indicate that the K_2PtCl_4 route leads to Pt depositing on both the Ni surface and the carbon support during the reaction (mainly the carbon support). As a consequence, the results in this chapter will only focus on the catalysts that were prepared via the $Pt(acac)_2$ route as this synthesis involves the specific deposition of Pt on the Ni particles.

3.3 XRD analysis

XRD patterns of 1 ML Pt/Ni/C catalysts prepared via the $Pt(acac)_2$ route are presented in Error! Reference source not found.. The blue vertical dotted lines correspond to the peak position of face-centred cubic (fcc) Pt. The orange vertical dotted lines correspond to the peak position of fcc Ni (all the Bragg angles for both Pt and Ni can be calculated theoretically using **Equation 2-17**, in our case the Bragg angles were part of a database Bruker AXS Diffrac Plus, Eva 2005 (V13)).

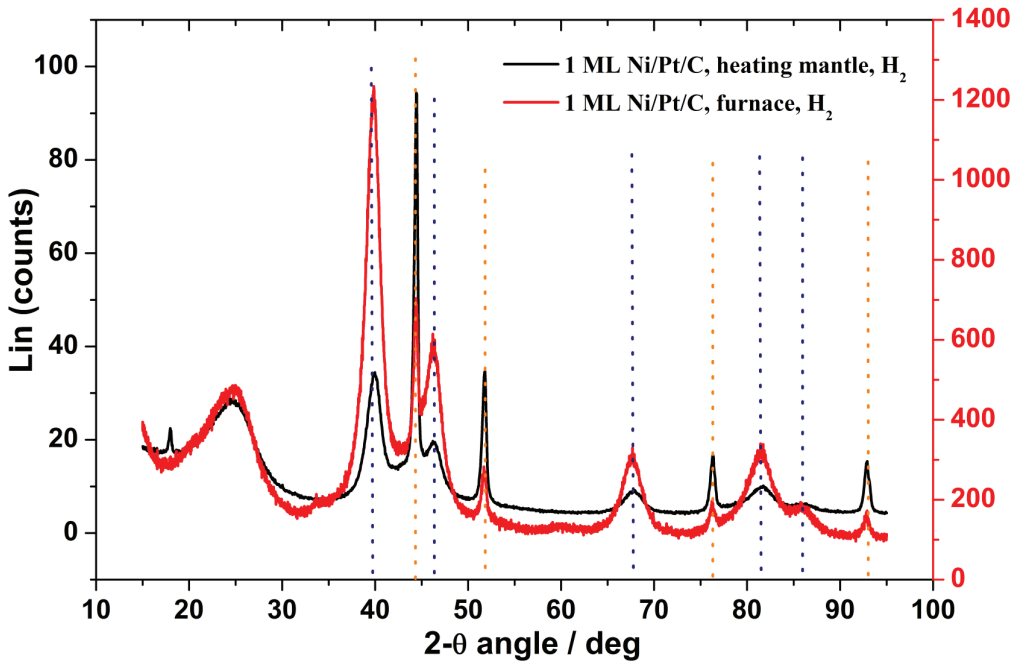

Figure 4- 1 XRD patterns of the 1 ML Pt/Ni/C catalysts prepared by reduction of Ni/C using a furnace (red) and heating mantle (black) and $Pt(acac)_2$. Peak position of fcc Pt is shown by the blue vertical dotted lines. Peak position of fcc Ni is shown by the orange vertical dotted lines.

The diffraction peak at 2θ ~ 25 ^{o} observed in all the XRD patterns is due to the (002) plane of the hexagonal structure of Vulcan XC-72 carbon.[13] All XRD patterns show the main characteristics of the fcc crystalline Ni (shown by the orange vertical dotted lines). In order of increasing the diffraction angle, the Ni crystal planes are (111), (200), (220) and (311). Also, peaks corresponding to the fcc crystalline Pt are present (shown by the blue vertical dotted lines); this includes the (111), (200), (220), (311) and (220) Pt crystal planes, in increasing diffraction angle. The presence of the Ni XRD peaks indicate that some of the Ni cores have not been modified by the Pt deposition, which is consistent with the metal assay analysis. The presence of Pt XRD peaks indicates that the Pt present in the catalysts is not amorphous and suggests the formation of Pt crystallites on the surface of the Ni particles.

Table 4-3 summarises the Ni and Pt lattice parameters along with their respective particle sizes. The large particle size recorded for the Ni nanoparticles suggests the sintering of the latter during the reduction process (initial Ni particle size was *ca.* 10 nm). The particle size obtained for the Pt/Ni/C catalysts is close to that of the Pt/C used as reference (2.7 nm) and therefore any increase in catalytic activity will not be due to a particle size effect.

In addition, the Pt lattice parameter decreases from the 3.92 Å for the Pt/C reference catalyst to 3.91 Å and 3.90 Å for the 1 ML Pt/Ni/C catalysts as shown by **Table 4-3**. This decrease in lattice parameter can be attributed to the incorporation of smaller Ni atoms in the Pt lattice. The decrease in lattice parameter suggests two things: a shortening of Pt-Pt nearest neighbour bond distance and a synergistic effect of Ni on Pt as is observed in Pt_3Ni alloys.[14, 15] Similarly, the Ni lattice parameter increases from 3.52 Å for the reference Ni/C to 3.53 and 3.52 Å for the 1 ML Pt/Ni/C catalysts. This indicates the incorporation of larger Pt atoms in the Ni lattice.

Table 4-3 Lattice parameter and particle size for the 1 ML Pt/Ni/C catalysts prepared by reduction of Ni/C with a furnace and heating mantle under H_2.

Samples	Ni lattice parameter[a] / Å	Ni particle size / nm	Pt lattice parameter[b] / Å	Pt particle size / nm
Pt/Ni/C, furnace, H_2	3.53	19.9	3.91	4.0
Pt/Ni/C, heating mantle, H_2	3.52	16.6	3.90	3.3

[a] Ni/C lattice parameter 3.52 Å for particles of 9.7 nm.
[b] Pt/C lattice parameter of 3.91 Å for particles of 2.7 nm.

3.4 TEM analysis

TEM-EDX analysis was performed on the 1 ML Pt/Ni/C catalysts. TEM micrographs at various magnifications with the scale bar corresponding to 200, 50 and 20 nm for the 1 ML Ni/Pt/C prepared by reduction of Ni/C using a furnace are presented in **Figure 4- 2**. TEM micrographs at various magnifications with the scale bar corresponding to 50, 20 nm for the 1 ML Pt/Ni/C prepared by reduction of Ni/C using a heating mantle furnace are presented in **Figure 4- 3**.

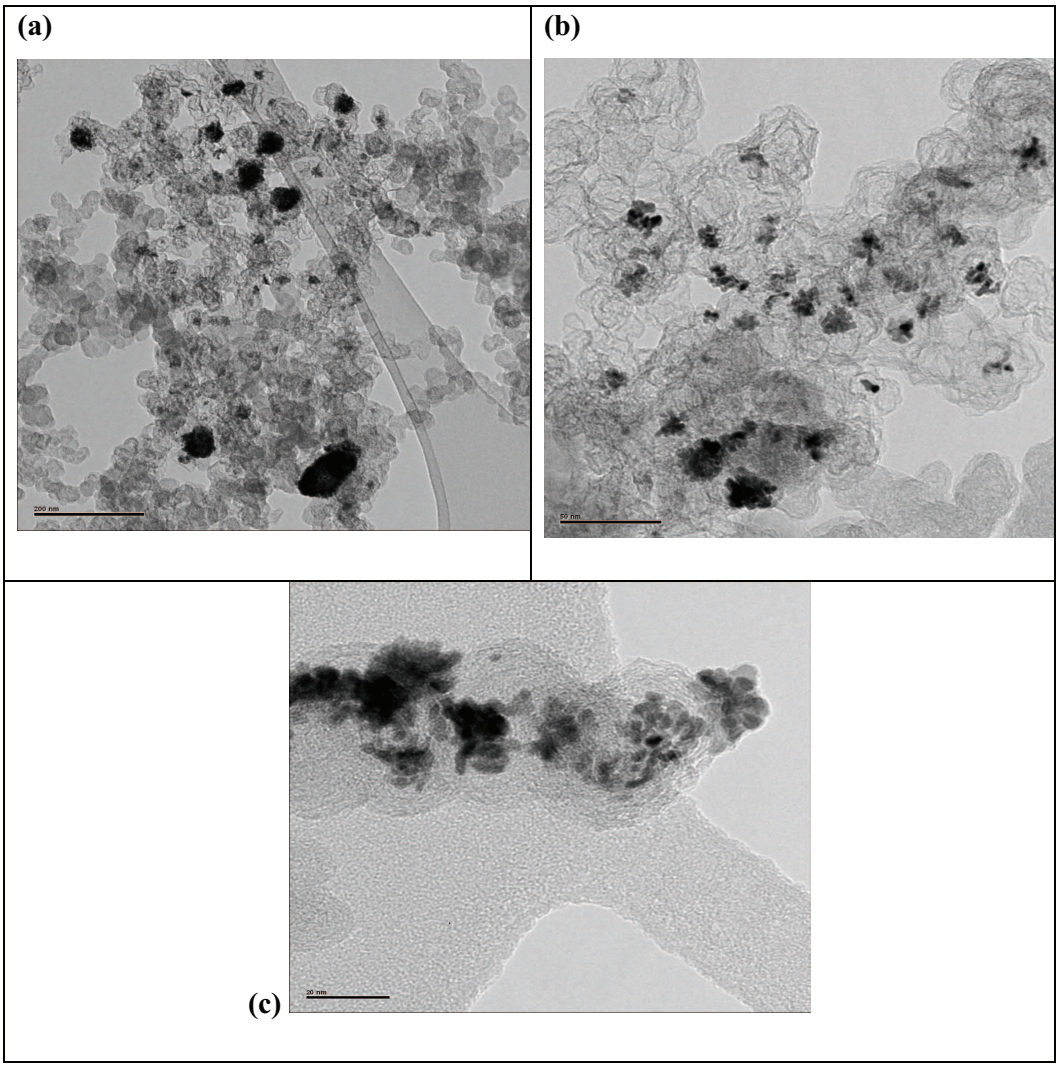

Figure 4- 2 TEM micrographs of 1 ML Pt/Ni/C catalysts prepared by reduction of Ni/C using a furnace at different magnifications 200 (a), 50 (b), and 20 nm (c).

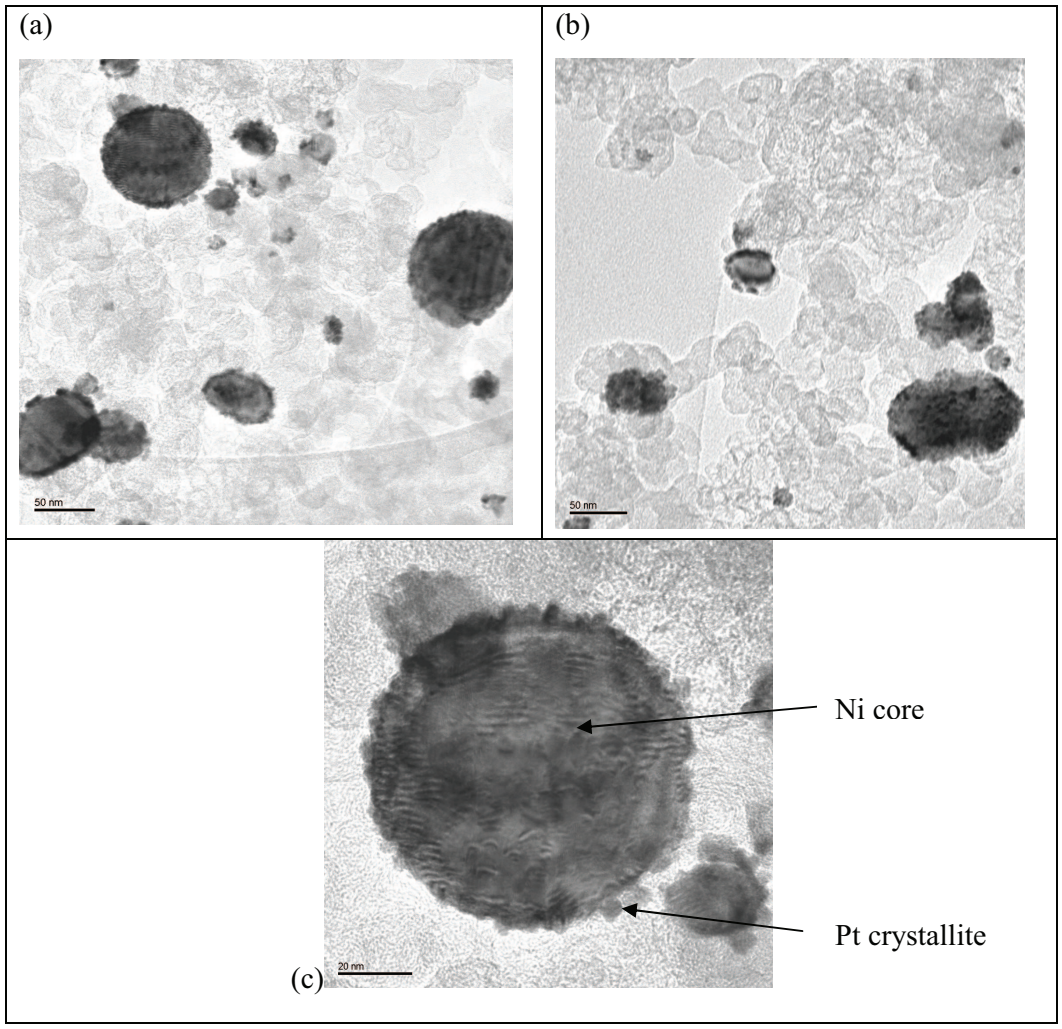

Figure 4- 3 TEM micrographs of 1 ML Pt/Ni/C catalysts prepared by reduction of Ni/C using a heating mantle under H_2. Scale bar of (a) 50 nm, (b) 50 nm and 20 nm (b).

In this work, the main application of the TEM is to assess the dispersion of the particles on the carbon support. From **Figure 4- 2** and **Figure 4- 3**, it can be observed that the catalyst particles are not well dispersed over the carbon support but form rather large agglomerates. The presence of large agglomerates indicates that the preparation of the Ni/C could be further optimised to achieve a better dispersion of the Ni nanoparticles over the carbon support, which in turn may improve the Pt deposition thereafter. Achieving this may result in a greater catalytic activity being exhibited by the 1 ML Pt/Ni/C catalysts. From the TEM data in **Figure 4-3**, it can also be seen that the Pt deposited as crystallites on the surface of the Ni particles as supported by the EDX analysis in **Figure 4- 4**.

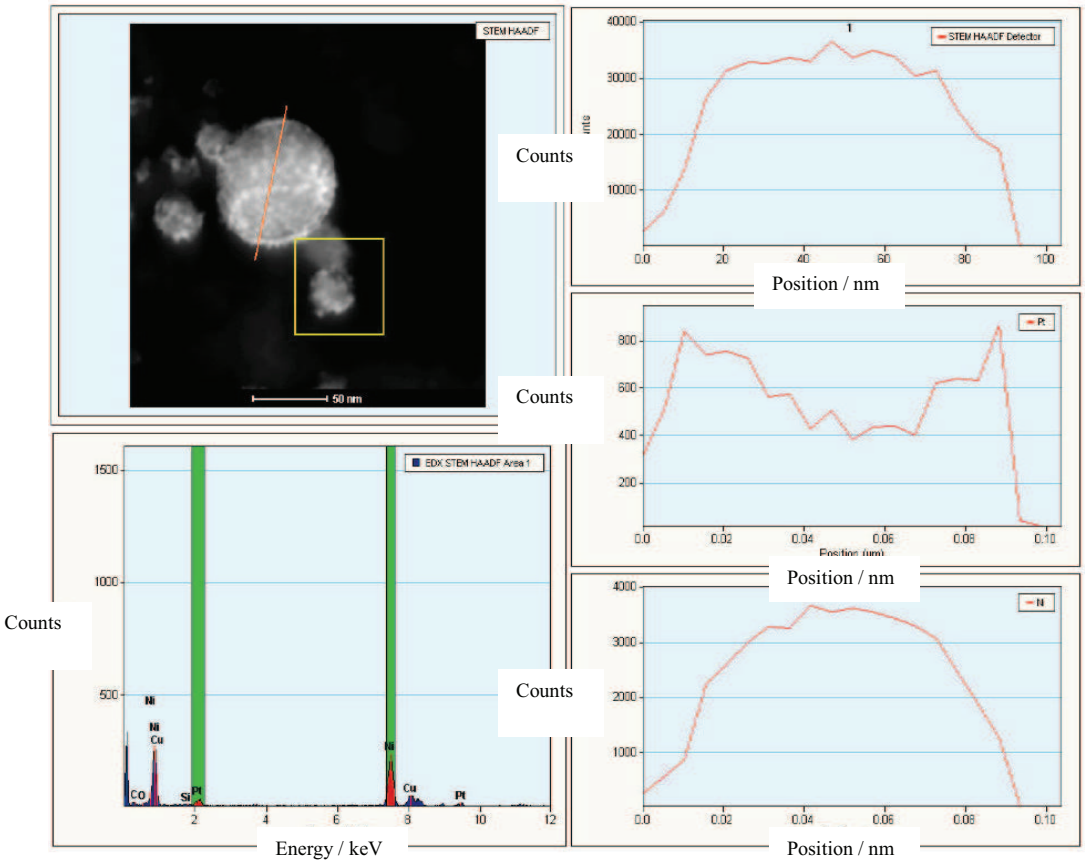

Figure 4- 4 TEM EDX line profile analysis for 1 ML Pt/Ni/C catalysts prepared by reduction of Ni/C using a heating mantle under H_2. The upper left box shows the TEM image of the area under investigation. The EDX response for the red square is shown below the TEM image. The EDX responses across the red line labelled one are shown on the right hand side and in descending order show total counts, counts from Pt and Ni, respectively.

3.5 Cyclic voltammetry – Half cell studies

The cyclic voltammograms (CV) of all the 1 ML Pt/Ni/C electrocatalysts prepared via the $Pt(acac)_2$ route are presented in **Figure 4- 5**. The CVs have been normalised to the available Pt surface area calculated from the area underneath the hydrogen adsorption peak. The mass normalised Pt areas in $m_{Pt}^{2}\ g_{Pt}^{-1}$ along with the potential of the oxide reduction peak are summarised in **Table 4-4**. The corresponding data for the 20 wt% Pt/C are shown for comparison purposes.

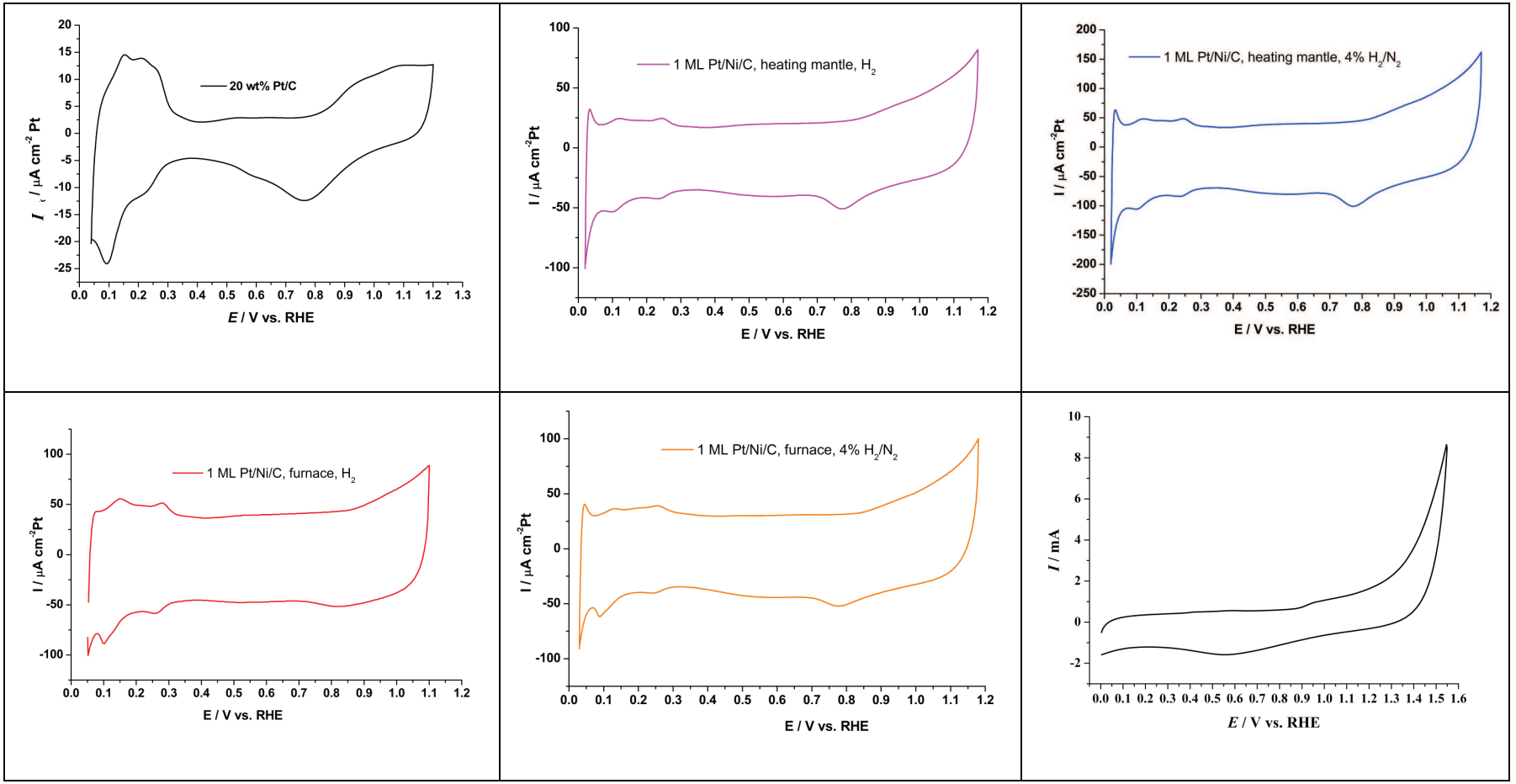

Figure 4- 5 Cyclic voltammograms of all 1 ML Pt/Ni/C electrocatalysts and Ni/C recorded in 1M H_2SO_4 at 10 mV s^{-1}. Cyclic voltammogram of 20 wt% Pt/C is shown for comparison purposes.

Table 4-4 Electrochemical parameters for the 20 wt% Pt/C and all the 1 ML Pt/Ni/C electrocatalysts.

Sample	Pt area / (m_{Pt}^2 g_{Pt}^{-1})	Potential of oxide reduction peak / V vs. RHE
20 wt% Pt/C	58.9	0.761
Pt/Ni/C, furnace, H_2	171.7	0.819*
Pt/Ni/C, furnace, 4% H_2/N_2	191.3	0.776
Pt/Ni/C, heating mantle, H_2	156.3	0.772
Pt/Ni/C, heating mantle, 4% H_2/N_2	249.0	0.773

*This CV was recorded within the potential range 0.0 to 1.1 V vs. RHE which may explain the discrepancy observed. If the potential range would have been extended to 1.2 V vs. RHE, the potential of the oxide stripping peak would have been shifted towards a higher reduction potential (closer to 0).

Assessing the cyclic voltammograms of the Pt/Ni/C catalysts, several observations can be made. All cyclic voltammograms have a Pt-like shape as they all exhibit a hydrogen region, a double layer region and an oxide region.

The hydrogen adsorption/desorption peak is different for the different sets of catalyst (heating mantle and furnace). The catalysts prepared using the furnace exhibit a more well-defined hydrogen region than those prepare using the heating mantle. One of the possible reasons is that the increase in particle size led to an increase in the number of Pt(100) and Pt(111) planes as described by Kinoshita.[16] The development of larger Pt(100) and Pt(111) planes will be observed by a more well-defined hydrogen adsorption/desorption peaks in the CV. The other assumption that could be made is that the deposition of Pt when using a furnace is not as homogeneous as the deposition obtained when using a heating mantle. The agglomeration of the Pt particles would lead to larger particles which would exhibit larger Pt crystal planes, thus exhibiting more well-defined hydrogen adsorption/desorption peaks.

The higher double layer capacitance exhibited by the Pt/Ni/C catalysts (in comparison to that of the Ni/Pt/C catalysts see page 127-131) can be explained by the lower Pt metal content of the Pt/Ni/C catalysts. As the Pt loadings for the Pt/Ni/C electrode buttons were similar to that of the Ni/Pt/C electrode buttons, a greater number of layers had to be painted onto the electrode buttons for the Pt/Ni/C

to achieve the required Pt loading, which in turn resulted in a thicker catalyst layer. The thicker catalyst layer led to more carbon being painted on the electrode buttons for the Pt/Ni/C catalysts. As a result, a higher charge capacitance attributed to the presence of more carbon, is exhibited by the Pt/Ni/C catalysts.

A similar discussion as the one in **Chapter 3 section 3.2.1** could be made regarding the hydrogen region and will not be repeated here.

Table 4-4 summarises the potential of the oxide reduction peak for all the 1 ML Pt/Ni/C catalysts. It can be seen that a lower overpotential (10 mV) is needed to strip off the oxide layer from the Pt surfaces of the prepared catalysts than from the Pt surfaces of the 20 wt% Pt/C catalyst. This enhancement can be due to the incorporation of Ni into the Pt lattice as shown by the decrease in Pt lattice parameter (**Table 4-3**). The incorporation of Ni atoms in the Pt lattice induces a synergistic effect between these two metals. This synergistic effect results in a weaker binding strength between the OH_{ads} and the Pt surfaces. As a result, a lower overpotential is needed to reduce the oxide peak. In addition, it also suggests that the SA exhibited by the catalysts should be higher increased because more Pt sites will be "oxide" free at lower overpotential.[9, 12]

The mass normalised area showed a 3 to 5-fold increase in comparison to that of the 20 wt% Pt/C. The increase mass normalised area suggests a higher utilisation of the noble metal. Nonetheless, the values for these mass normalised area should be treated with a certain degree of caution as there are several areas where errors can be introduced e.g. the compression of the catalyst layer, the amount of catalyst in electrical contact, and loss of catalyst in the pressing procedure However, it does not mean that the measurement of the mass normalised Pt is totally irrelevant. It can still be used to identify trends and obtain approximate values. As a result, it was more appropriate to normalise the current recording in the cyclic voltammogram by the available Pt surface area.

3.6 RDE measurements

RDE measurements allow the determination of the catalytic activity, SA and MA (if coupled with the results obtained with the CV measurements), of each catalysts. Three different rotation rates were used to study the ORR (900, 1600 and 2500 rpm)

and a Levich plot (limiting current vs. square root of rotation rate) was plotted to confirm that the RDE experiment was running under a good mass-transport regime.

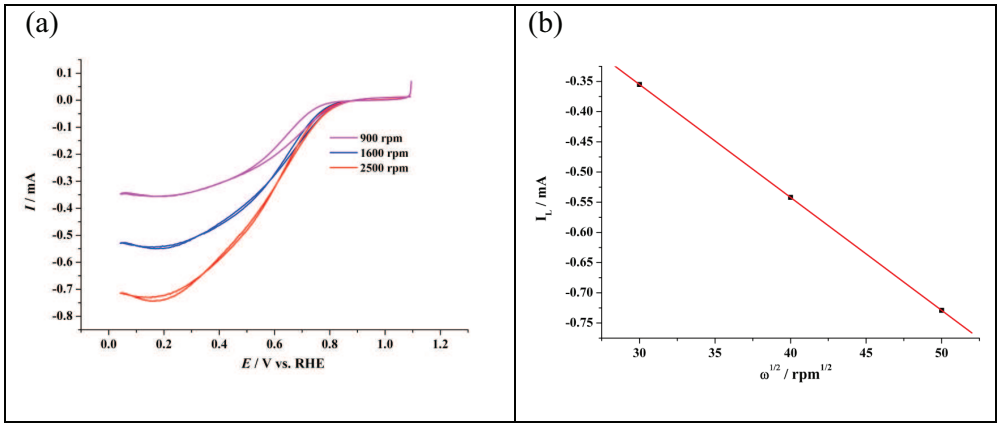

Figure 4- 6 (a) Typical polarisation curve obtained during a RDE measurement and (b) its associated Levich plot. Data were obtained for the 1 ML Pt/Ni/C (prepared by reduction of Ni/C using a heating mantle and 4% H_2/N_2) in O_2 saturated 1 M H_2SO_4 at 10 mV s^{-1}.

To analyse the data, only the forward scan (negative going) of the polarisation curve was used to prevent the undesired effect due to the adsorption of other species. For the Levich plot, the limiting currents were determined at -0.55 V vs. RHE and plotted against the square root of the electrode rotation rate. A straight line passing close (intercept = 0.0002 mA) to the origin was obtained with the slope that woud be expected for a 4-electron reduction reaction. As a result, according to the Levich plot, a 4 electron transfer is taking place during the ORR.

To assess the performance of the catalysts, the forward scan (negative going) of the polarisation curve was used and the kinetic current was extracted from the recorded current by rearranging **Equation 1-14**. The kinetic current was then normalised to the Pt active area (determined by CO adsorption) and the log of the normalised kinetic current (J_k) was plotted against the potential (Tafel plot). The value of the log of the normalised kinetic current at 0.9 V vs. RHE was used to assess the specific activity of the catalysts. The specific activity is the kinetic current per area of active material.

All the RDE measurements were performed in O_2 saturated 1M H_2SO_4 with a scan rate of 10 mV s^{-1} and the data presented is the mean of 3 replicates. For the specific

activities, the value recorded is the mean of 2 replicates and its associated error is the difference between the mean and the data recorded by each measurement.

The Tafel plots for the 1 ML Pt/Ni/C catalysts are shown in **Figure 4- 7**. Data for the 20 wt% Pt/C was included for comparison purposes. All the data were repeated at least 2 or 3 times to ensure the reproducibility of the results.

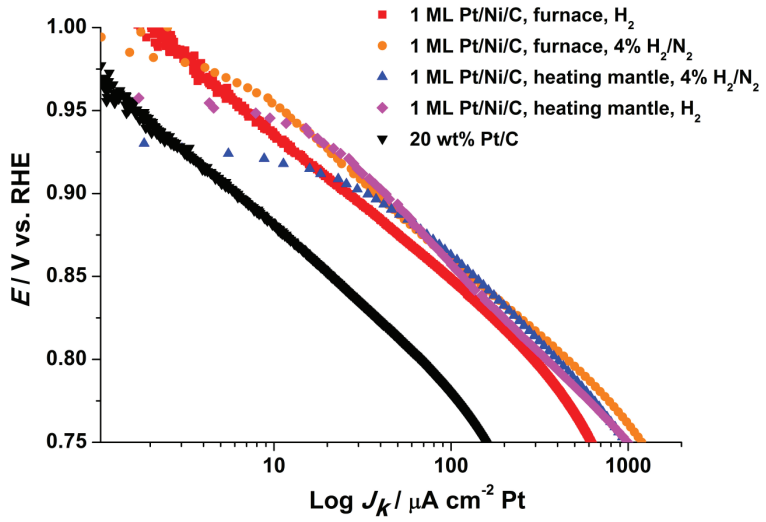

Figure 4- 7 Oxygen reduction Tafel plots for all the 1 ML Ni/Pt/C catalysts and for 20 wt% Pt/C in O_2 saturated 1 M H_2SO_4, 10 mV s^{-1} and 2500 rpm.

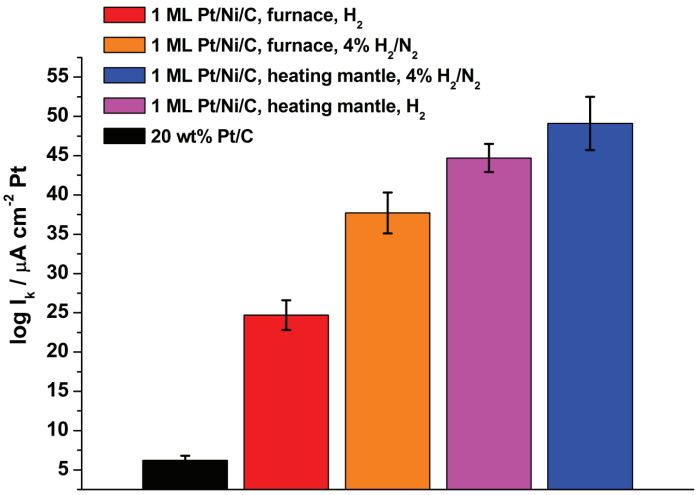

Figure 4- 8 Histograms of the specific activity of the electrocatalysts prepared via the $Ni(Cp)_2$ route. The 20 wt% Pt/C catalyst was added for comparison purposes. SA obtained at 0.9 V vs. RHE. Mean of 2 replicates its associated error.

From **Figure 4- 7** and **Figure 4- 8**, it can be seen that all the 1 ML Pt/Ni/C catalysts exhibit higher SA and MA than 20 wt% Pt/C. The increase in catalytic activity can be explained by referencing to the XRD, TEM and CV data gathered in the previous sections.

Any particle size effect on the SA exhibited by the Pt/Ni/C catalysts can be ruled out as all the catalysts exhibited similar particle size as shown by the XRD data in **Table 4-3**.

The XRD data (**Table 4-3**) also showed a decrease in Pt lattice parameter, suggesting that smaller Ni atoms enter the Pt lattice. The decrease in lattice parameter suggests a shortening in the Pt-Pt nearest bond distance. If the Pt-Pt nearest neighbour bond distance was to be calculated for the theoretical Pt fcc and those found for the different Pt/Ni/C catalysts, it would results in 2.774 Å for the theoretical Pt fcc and *ca.* 2.760 Å for the Pt/Ni/C. This decrease in Pt-Pt bond distance is not as significant as that found in the literature[17, 18] but it seems to be enough to provide a more suitable adsorption sites for the O_2 molecules[17, 19] thus, increasing the SA of the catalyst.

The CVs (**Figure 4- 5**) showed well defined H_{ads} and H_{des} peaks, indicating that well-defined Pt(100) and Pt(111) crystal planes were present in all the Pt/Ni/C catalysts. It was demonstrated that Pt(100) and Pt(111) terraces are more suitable adsorption sites for the dual adsorption mode of the oxygen molecules thus providing more active sites towards the ORR resulting in a higher SA.[16, 20] In addition, the CV data (**Table 4-4**) demonstrated a shift in the potential of the oxide stripping peak (10 mV), which indicates a weaker binding strength between the OH_{ads} and the Pt surfaces. As the Pt surface is "oxide" free at lower overpotential, it results in more Pt sites being available for the ORR to take place, thus increasing the SA.[18, 21] The weakening of the bond between OH and the Pt surface also suggests a synergistic effect of Ni on Pt as Ni atoms incorporate the Pt lattice. [6, 9, 12]

Due to the low amount of Pt in the prepared catalysts and because of the incomplete formation of a Pt monolayer on the Ni nanoparticles, it was important to check the activity of Ni/C towards the ORR. **Figure 4-** 9 shows that a very low current can be

attributed to the Ni/C (*ca.* 5%) and as a consequence does not affect the determination of the catalytic activity of the prepared 1 ML Pt/Ni/C.

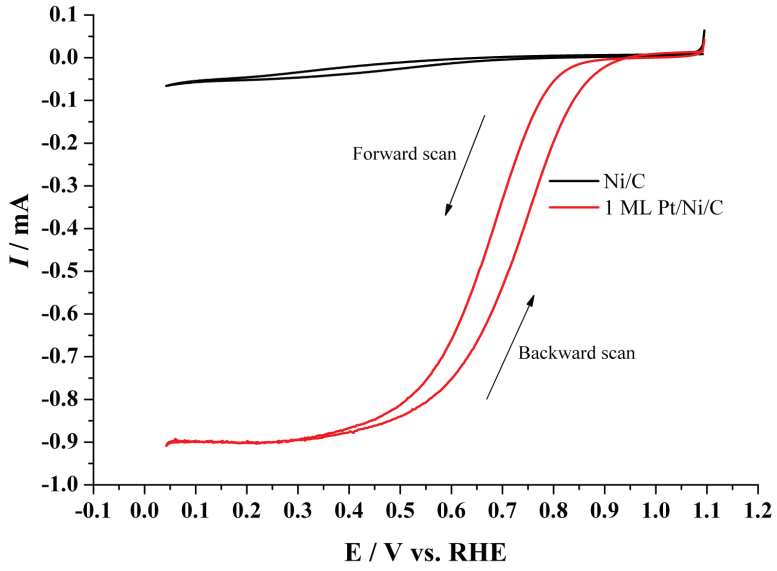

Figure 4- 9 Polarisation curves obtained for Ni/C (black) and 1 ML Pt/Ni/C in 1 M H_2SO_4 at 10 mV s^{-1}. Rotation speed of 2500 rpm.

4 Conclusions

In this chapter, we reported the preparation of several 1 ML Pt/Ni/C catalysts using the SOMC methodology to study the ORR. Pt was deposited on thermally reduced Ni/C using $Pt(acac)_2$ dissolved in toluene. Despite having a low Pt content (<5 wt%), the prepared catalysts exhibited 4 to 8-fold enhancement in catalytic activity with respect to that of the 20 wt% Pt/C. The increase in activity was attributed to a decrease in Pt lattice parameter due to the incorporation of Ni atoms in the Pt lattice. The geometric modification suggested a shortening of the Pt-Pt nearest neighbour bond distance which was found to be a cause of the catalytic enhancement of Pt-alloys.[17, 18] A synergistic effect between the Ni and Pt was also proposed as Ni atoms enter the Pt lattice. This was demonstrated by the decrease in the potential of the oxide reduction peak in the CV experiments. As a lower overpotential is needed to reduce the oxide form the Pt surfaces, it indicates the formation of a weaker bond between the oxide species and the Pt surfaces. In addition, the Levich plot demonstrated a 4 electron reduction reaction.

The enhancement in catalytic activity was also shown to be due independent of the particle size as all the catalysts exhibited a similar average particle size. Also, the Ni/C support was ruled out as a possible source for the catalytic improvement as the limiting current recorded in the RDE experiment was less than 5% of the total limiting current recorded for the catalysts.

It was shown that the deposition of Pt on the Ni nanoparticles was incomplete. This was thought to be due to the poor dispersion of the Ni nanoparticles on the carbon support and due to the presence of water in the solvent. As a consequence, it was suggested that improving the dispersion of Ni on the carbon support and working under anhydrous conditions could increase the amount of Pt deposited. As a result, a higher SA could be achieved for these catalysts.

5 References

1. H. A. Gasteiger, S. S. Kocha, B. Sompalli and F. T. Wagner, *Applied Catalysis B-Environmental*, **56**, 9 (2005).
2. L. Liu, J.-W. Lee and B. N. Popov, *Journal of Power Sources*, **162**, 1099 (2006).
3. L. Liu, H. Kim, J.-W. Lee and B. N. Popov, *Journal of The Electrochemical Society*, **154**, A123 (2007).
4. W. Wang, D. Zheng, C. Du, Z. Zou, X. Zhang, B. Xia, H. Yang and D. L. Akins, *Journal of Power Sources*, **167**, 243 (2007).
5. H. Zhong, H. Zhang, Y. Liang, J. Zhang, M. Wang and X. Wang, *Journal of Power Sources*, **164**, 572 (2007).
6. V. Stamenkovic, T. J. Schmidt, P. N. Ross and N. M. Markovic, *The Journal of Physical Chemistry B*, **106**, 11970 (2002).
7. H. I. Takako Toda, Hiroyuki Uchida, and Masahiro Watanabe, *Journal of The Electrochemical Society*, **146**, 3750 (1999).
8. J. Zhang, Y. Mo, M. B. Vukmirovic, R. Klie, K. Sasaki and R. R. Adzic, *Journal of Physical Chemistry B*, **108**, 10955 (2004).
9. J. Zhang, F. H. B. Lima, M. H. Shao, K. Sasaki, J. X. Wang, J. Hanson and R. R. Adzic, *Journal of Physical Chemistry B*, **109**, 22701 (2005).
10. M. H. Lee and J. S. Do, *Journal of Power Sources*, **188**, 353 (2009).
11. J.-S. Doa, Y.-T. Chena and M.-H. Lee, *Journal of Power Sources*, **176**, 623 (2007).
12. J. H. Yang, J. Y. Lee, Q. B. Zhang, W. J. Zhou and Z. L. Liu, *Journal of the Electrochemical Society*, **155**, B776 (2008).
13. A. K. Shukla, M. Neergat, P. Bera, V. Jayaram and M. S. Hegde, *Journal of Electroanalytical Chemistry*, **504**, 111 (2001).
14. J. R. Kitchin, J. K. Norskov, M. A. Barteau and J. G. Chen, *The Journal of Chemical Physics*, **120**, 10240 (2004).
15. W. V. Hui Yang, Claude Lamy, and Nicolás Alonso-Vante, *The Journal of Physical Chemistry B (Materials)*, **108**, 11024 (2004).
16. K. Kinoshita, *Journal of The Electrochemical Society*, **137**, 845 (1990).
17. V. Jalan and E. J. Taylor, *Journal of the Electrochemical Society*, **130**, 2299 (1983).

18. F. H. B. Lima, J. R. C. Salgado, E. R. Gonzalez and E. A. Ticianelli, *Journal of the Electrochemical Society*, **154**, A369 (2007).
19. E. Yeager, *Journal of Molecular Catalysis*, **38**, 5 (1986).
20. E. Yeager, *Electrochimica Acta*, **29**, 1527 (1984).
21. P. N. Ross Jr, *Surface Science*, **102**, 463 (1981).

CHAPTER FIVE: CONCLUSIONS AND FUTURE WORKS

1 Conclusions and future works

The aim of this work was to prepare Pt/Ni/C and Ni/Pt/C core-shell electrocatalysts using the control surface modification of Pt/C or Ni/C support by Ni and Pt, respectively. The catalytic activity of these catalysts were evaluated they were shown to demonstrate an improved performance towards the oxygen reduction reaction (ORR) when compared to 20 wt% Pt/C.

The study of Ni deposition on Pt cores, in **Chapter 3**, showed complete reaction of both Ni precursors. The EDX data showed that Ni preferentially deposited on the Pt nanoparticles with no Ni found separately on the carbon support. Despite the complete reaction between Ni and Pt, an inhomogeneous Ni deposition occurred as revealed by the TEM and EXAFS results. Despite the clustering of the nickel particles on the Pt/C support, a 6 and 8-fold increase in specific activities (SA) for the Ni/Pt/C prepared via the $Ni(acac)_2$ and $Ni(Cp)_2$ routes, respectively, was recorded. Similarly, 9 and 7-fold increase in mass activities (MA) were observed for the Ni/Pt/C prepared via the $Ni(acac)_2$ and $Ni(Cp)_2$ routes, respectively. The catalytic enhancement was attributed to PtNi alloy formation which resulted in decrease in *d*-band centre, a decrease in the Pt lattice parameter, and a shortening of the Pt-Pt nearest neighbour bond distance. All of these were confirmed by XRD, XPS, CV and EXAFS analysis. Further analysis such as LEIS should be performed on the catalysts to determine the composition more precisely. Being able to tune the structure of the outermost layer could lead to the prepared catalyst being able to exhibit its full potential towards the ORR.

The deposition of Pt on thermally reduced Ni surface, Pt/Ni/C, was also studied in **Chapter 4**. It was shown that an incomplete reaction occurred between the Pt precursor and the Ni/C support. The incomplete deposition was attributed to the presence of water in the solvent which re-oxidised the Ni to nickel oxide, thus, reducing the number of available site for the Pt deposition. Despite all the catalysts containing less than 5 wt% Pt, they exhibited between 4 and 8-fold enhancements in catalytic activity with respect to that of the 20 wt% Pt/C. The catalytic improvement

was attributed to geometric modification of the catalysts (shortening of the Pt-Pt nearest neighbour bond distance) and to a synergistic effect between the Ni and Pt. The particle size and the Ni/C support were both ruled out as possible sources of the enhancement. The catalytic activity of the catalysts could be further increased should the poor dispersion of the Ni nanoparticles, shown by the TEM micrographs, be improved. Improving the dispersion of the Ni nanoparticles would provide more sites for the Pt to deposit on and thus, provide more sites for the oxygen reduction reaction to occur.

Depositing Pt or Pd on Pd/C or Pt/C support, respectively, by control surface modification (CSR) led to the preparation of core-shell catalysts with full monolayer coverage of the deposited metal.[1, 2] However, such deposition was not obtained for the Pt/Ni/C catalysts prepared in this work. The ability that both metals, Pt and Pd, have to adsorb hydrogen could be responsible for the successful deposition using CSR. Hydrogen adsorption (or reduction of the metal surface) is a key step in the preparation of catalysts by SOMC because the Pd-H or Pt-H sites are what triggers the reduction of the acetonylacetonate metal precursor. Winkler[3] showed that the surface coverage of atomic hydrogen on Ni(110) and Ni(111) reaches 1, however, the surface coverage of molecular hydrogen only reaches a maximum of 0.4. In this work, according to the metal assay results for the Pt/Ni/C, it can only be assumed that on the Ni/C support, the hydrogen adsorbs as molecular hydrogen and that would explain the low Pt deposition. Also, nickel can be easily oxidised so should there be any air in the system at any time, competitive reaction between hydrogen adsorption and oxide adsorption would occur, thus resulting in a lower Pt deposition.

Gasteiger and Markovic[4] summarised the different strategies employed to date to increase the catalytic activity of the cathode catalysts. The strategies were as follows: (1) the most common approach involved the alloying of Pt with another transition metal, (2) the "de-alloying" of the Pt alloy particles with a Pt alloy core and a Pt shell, (3) 10 monolayer-thick Pt films on a nanostructured supports and (4) large particles of Pt alloy with a specific Pt crystal planes on the outer surface. The turnover frequency increased from 60 to 2800 s^{-1} from (1) to (4), yielding to 10 times increased in mass activity in comparison to that of Pt/C. From the TEM results, it was shown that the catalysts particles consisted of a metal core with crystallite particles of the second metal surrounding it. After heat treatment, the

crystallite layer turned into an alloy phase with different degree of alloying as suggested by the XRD and XPS data. The CV results also showed that Pt(100) and Pt(111) crystal planes were present even for the heat treated catalysts. It could be assumed that as the heat treatment temperature increases, we are going from 2-layer particles to 3-layer particles; the first layer consisting of the metal core, the second consisting of an alloy phase and the third being a Pt-rich layer, as depicted by **Figure 1**.

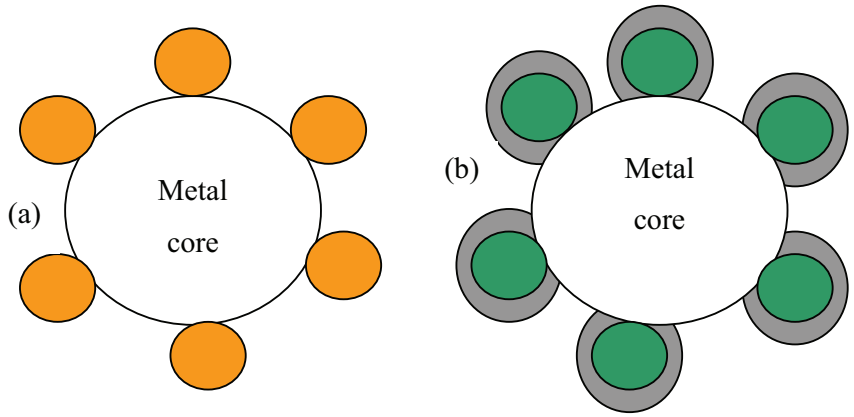

Figure 1 **Schematic of the prepared particles showing (a) the as prepared catalysts exhibiting 2 layer particles consisting of a metal core and crystallite particles of the secondary metal surrounding it and (b) the heat treated catalysts exhibiting 3-layer particles consisting of a metal core, an alloy phase surrounding the metal core and a Pt-rich shell surrounding the alloy phase.**

This work managed to combine 2 of the 4 strategies described, namely strategies (2) and (4). Combining the two strategies allowed the preparation of more catalytically active metal particles. The RDE data showed up to 8-fold and up to 9-fold increase in specific activity and mass activity, respectively. Also, the different Tafel slopes to that of Pt/C exhibited by the catalysts indicate that different ORR mechanisms are occurring at the electrode surface. However, these new ORR mechanism seem to result in a better utilisation of the potential of the catalysts. In conclusion, if 2 or more strategies could be merged, as in this work, it would be possible to further increase the catalytic activity of the cathode catalysts, thus bringing us closer to the commercial availability of fuel cell technology.

The preparation of Ni/Pt/C could also be performed via electrochemical routes. El-Shafei[5] studied the Ni underpotential deposition (UPD) on polycrystalline Pt in acidic and nearly neutral conditions. The Ni UPD was performed in 0.1 M $HClO_4$ and 0.1 M KH_2PO_4 in phosphate buffer (pH 6.85) with $Ni(ClO_4)$. It was found that

in 0.1 M $HClO_4$, the Ni UPD occurred in the hydrogen adsorption-desorption region. However, raising the pH allowed the separation of both Ni UPD and the hydrogen adsorption-desorption processes. This enabled quantification of the amount of Ni underpotentially deposited on the Pt surface. The maximum Ni UPD coverage that could be achieved was 60%. Preparing Ni/Pt/C catalysts using a similar procedure (also performing several heat treatments) and determining their structural parameters as well as their catalytic activities would provide both another preparation method and useful information to further understand the complexity of the ORR.

Electrochemical reduction of Ni/C could also be used prior to depositing Pt as the standard reduction potentials of Ni^{2+}/Ni and Pt^{2+}/Pt are -0.25 V and +1.18 V, respectively. This would prevent the clustering of the Ni nanoparticles as demonstrated by the XRD results in **Chapter 4**. A higher Pt coverage may also be achieved as the Ni would be constantly reduced which would provide suitable adsorption sites for the Pt deposition to occur.

In addition, performing heat treatments on these catalysts, Pt/Ni/C prepared in **Chapter 4** and Pt/Ni/C prepared using electrochemical methods only, would modify the geometric and electronic structure of the catalysts and maybe increase their catalytic performance. Performing EXAFS, XPS and LEIS analysis would result in a strong structural characterisation of the catalysts which could provide insight into how the catalysts should be tuned to exhibit higher catalytic enhancement.

From a commercial point of view, the catalyst stability is as important as its catalytic activity. Cyclic voltammetry can be used to study the durability of the catalysts. Cycling a painted electrode between 0.6 and 1.0 V vs. RHE for 1000 cycles at 20 mV s^{-1} and 80 °C and comparing the electrochemical areas before and after cycling should give an indication of the stability of the catalysts. In addition, a stability testing could be performed in a membrane electrode assembly in a PEMFC environment to provide information on the electrocatalytic activity of the catalysts as well as the effect of the dissolution of the non-precious metal on the electrocatalytic activity.[6, 7]

Finally, performing MEA testing on selected catalysts under H_2/O_2 at 75 °C at 300 kPa would allow the collection of data under real PEMFC conditions. This will enable the true evaluation of the catalysts and will allow the study of the effect of Ni

dissolution and the Pt sintering on the cell performance as well as allow direct comparison with the other cathode catalysts such as Pt-alloys.[8]

The key finding in this work is that the presence of nickel greatly influences the reactivity of Pt towards the ORR in comparison to other first row transition metals such as Co[2] and Cr[2]. For the Co and Cr modified Pt/C, the improved catalytic activity was assigned to the increase in the degree of alloying and to the decrease of the Pt-Pt nearest neighbour bond distance. However, in this work, all *as prepared* Ni/Pt/C catalysts and most of the as prepared Pt/Ni/C catalysts exhibited a higher specific activity than the Cr and Co modified Pt/C. The origin of the synergistic effect between Ni and Pt is not yet quite clear however, it appears that the atomic arrangement plays a crucial part. This was confirmed by the XRD and XAS data but also by Stamenkovic *et al.*.[9] Additional studies into the structure characterisation would prove crucial to improve the understanding of the synergistic effect occurring between Pt and Ni.

2 References

1. B. Tessier, Preparation, Characterisation and Evaluation of Core-Shell Electrocatalyst for PEMFCs, Thesis (PhD in *Chemistry*), University of Southampton, Southampton (2009).
2. P. Wells, Controlled surface modification of supported platinum group metal catalysts, Thesis (PhD in *Chemistry*), University of Southampton, Southampton (2007).
3. A. Winkler, *Applied Physics A*, **67**, 637.
4. H. A. Gasteiger and N. M. Markovic, *Science*, **324**, 48 (2009).
5. A. A. El-Shafei, *Journal of Electroanalytical Chemistry*, **447**, 81 (1998).
6. E. Antolini, J. R. C. Salgado and E. R. Gonzalez, *Journal of Power Sources*, **160**, 957 (2006).
7. H. R. Colon-Mercado and B. N. Popov, *Journal of Power Sources*, **155**, 253 (2006).
8. D. Thompsett, *Handbook of Fuel Cells: Fundamentals, Technology and Applications. Volume 3, Chapter 37: Pt Alloys as Oxygen Reduction Catalysts.*, John Wiley & Sons ltd, New york (2003).
9. V. R. Stamenkovic, B. Fowler, B. S. Mun, G. F. Wang, P. N. Ross, C. A. Lucas and N. M. Markovic, *Science*, **315**, 493 (2007).

APPENDIX 1 A

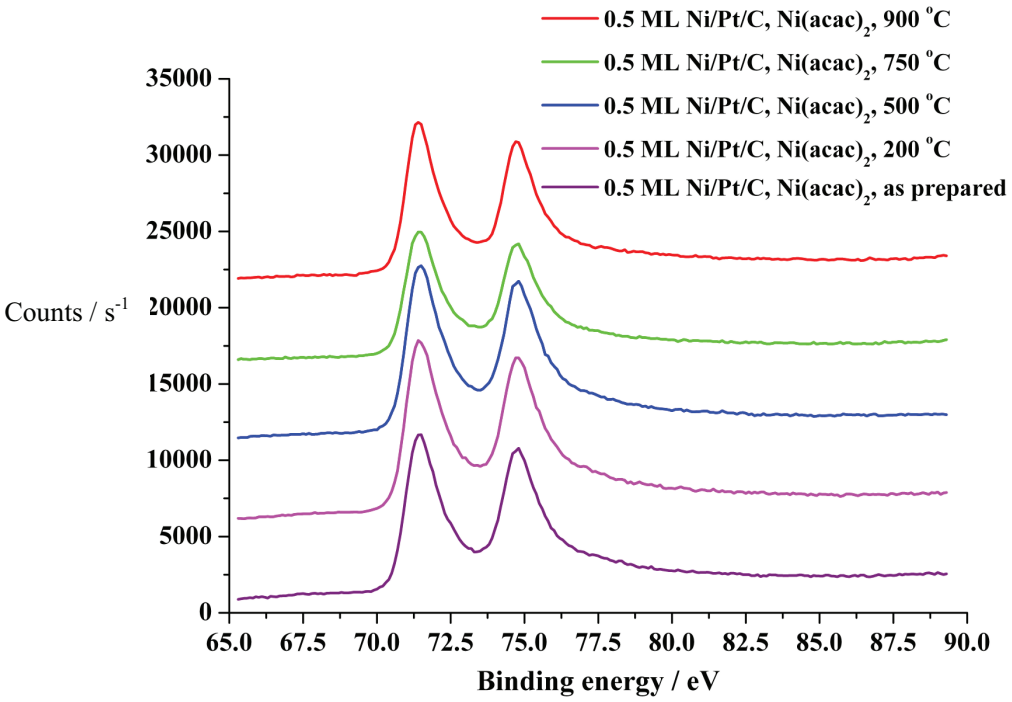

Figure 1 **XPS of Pt(4f) core level region of 0.5 ML Ni/Pt/C electrocatalysts prepared via the $Ni(acac)_2$ route.**

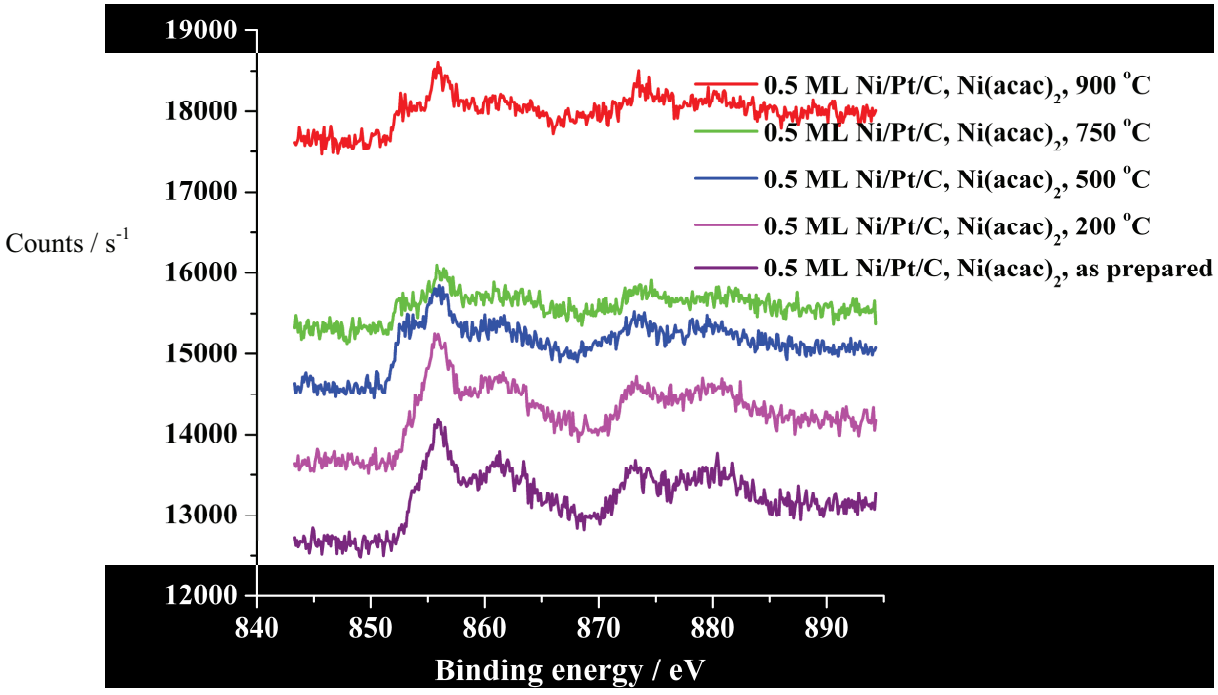

Figure 2 **XPS of Ni(2p) core level region of 0.5 ML Ni/Pt/C electrocatalysts prepared via the $Ni(acac)_2$ route.**

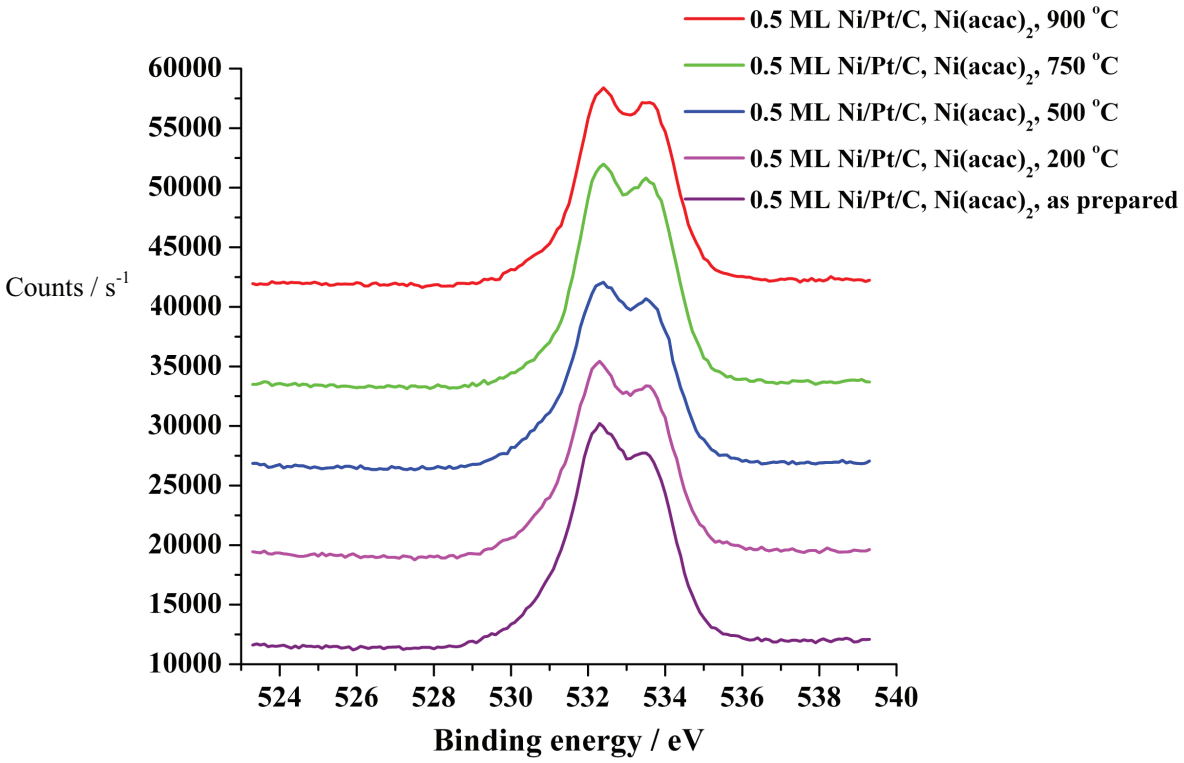

Figure 3 **XPS of O(1s) core level region of 0.5 ML Ni/Pt/C electrocatalysts prepared via the $Ni(acac)_2$ route.**

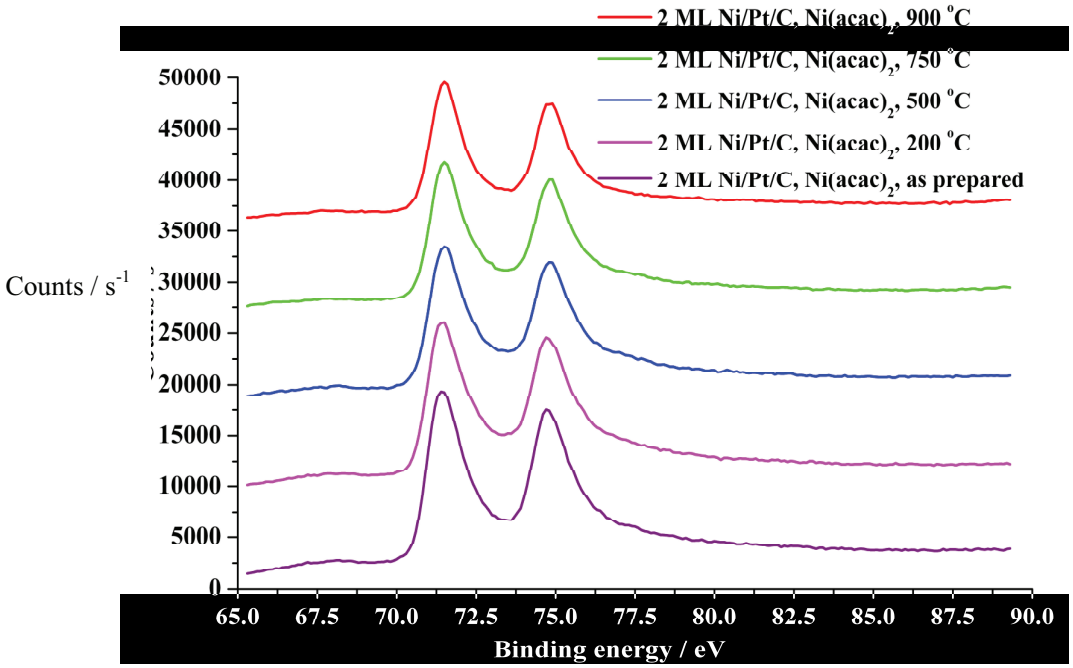

Figure 4 **XPS of Pt(4f) core level region of 2 ML Ni/Pt/C electrocatalysts prepared via the $Ni(acac)_2$ route.**

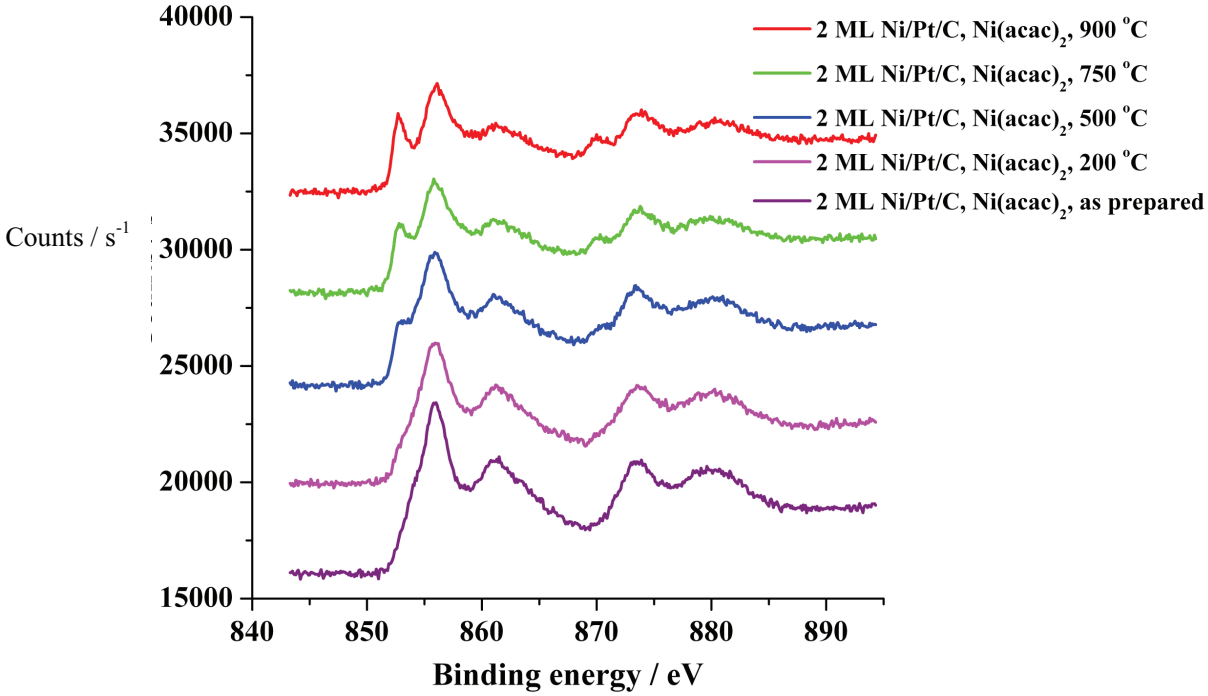

Figure 5 **XPS of Ni(2p) core level region of 2 ML Ni/Pt/C electrocatalysts prepared via the $Ni(acac)_2$ route.**

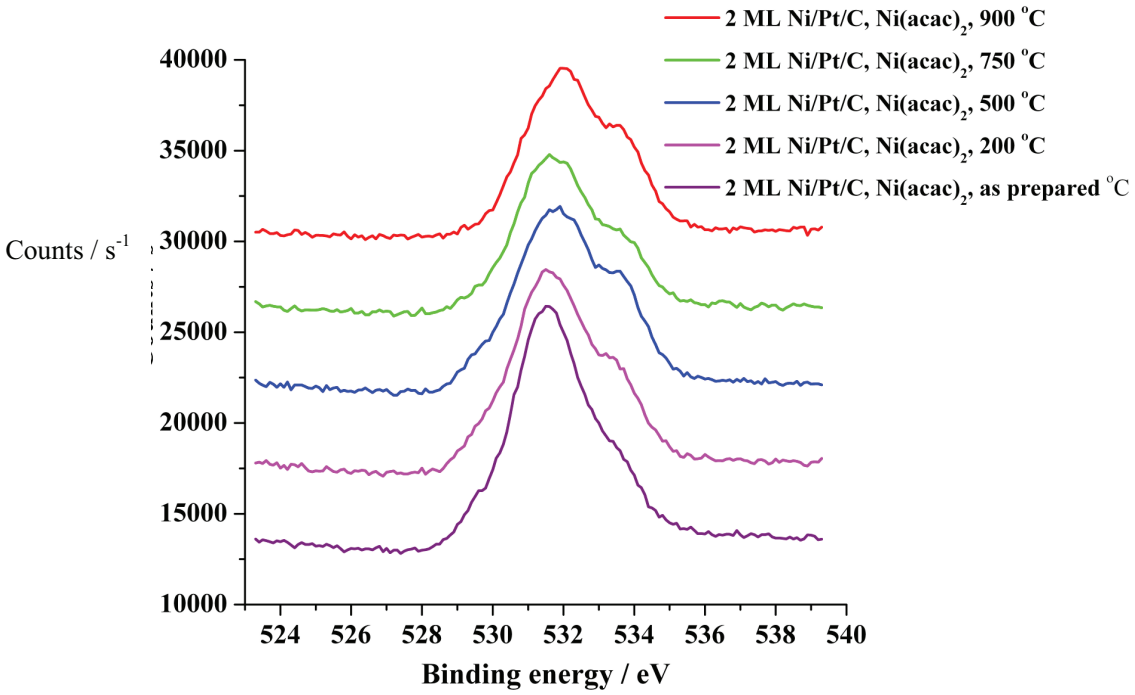

Figure 6 **XPS of O(1s) core level region of 2 ML Ni/Pt/C electrocatalysts prepared via the $Ni(acac)_2$ route.**

APPENDIX 1 B

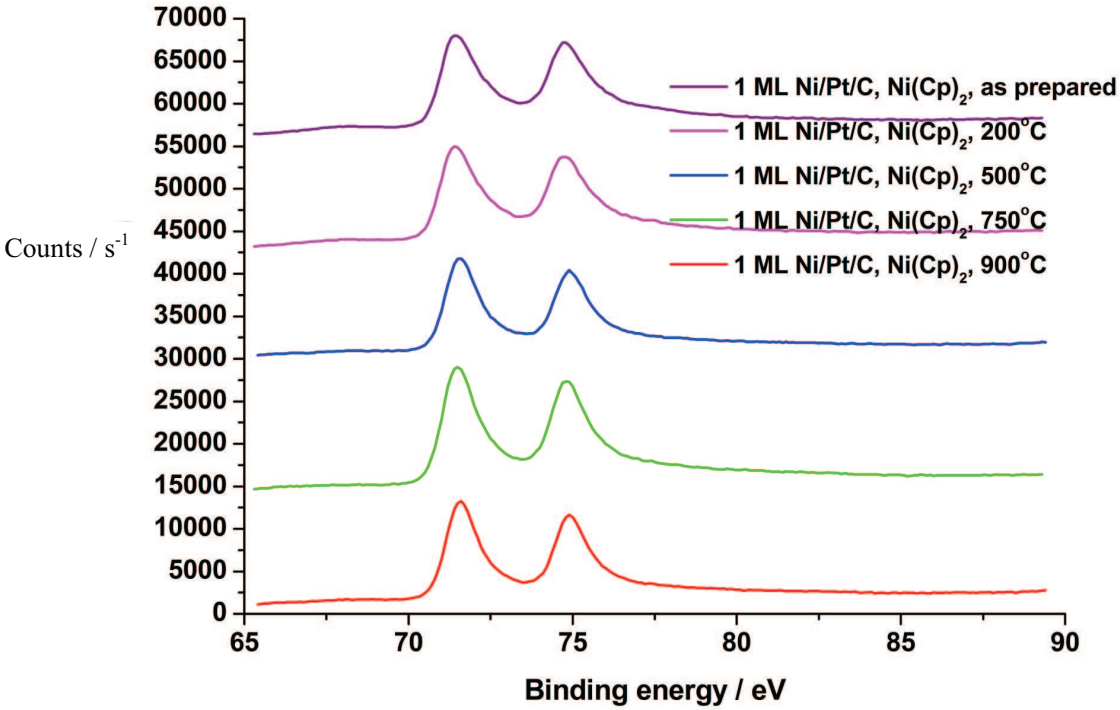

Figure 1 **XPS of Pt(4f) core level region of 1 ML Ni/Pt/C electrocatalysts prepared via the $Ni(Cp)_2$ route**

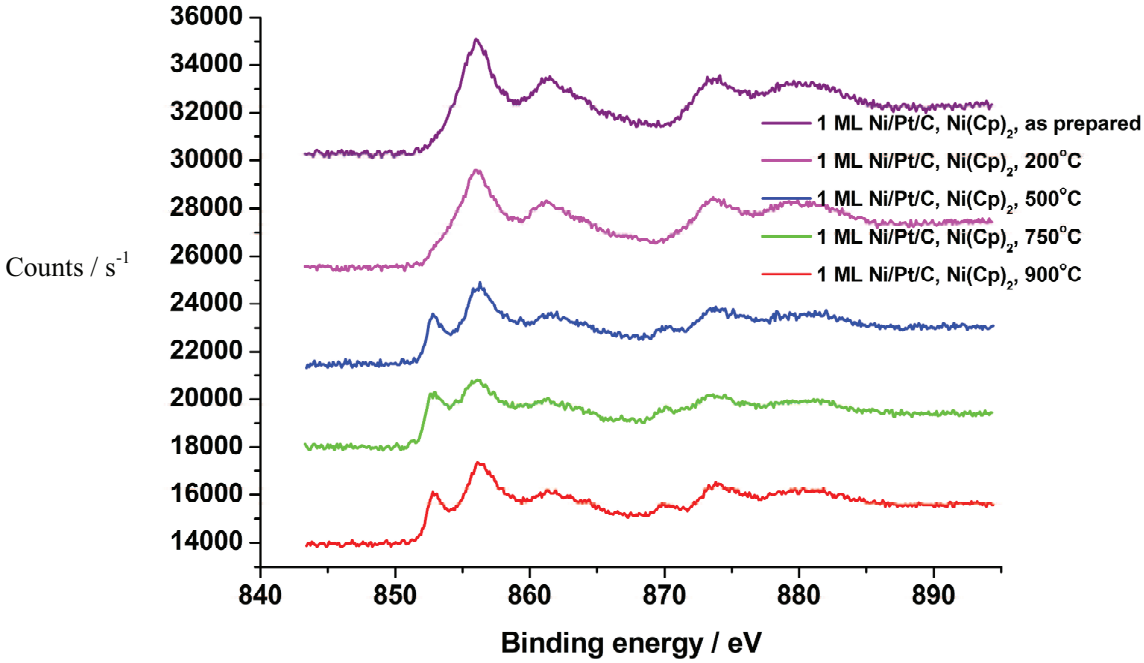

Figure 2 **XPS of Ni(2p) core level region of 1 ML Ni/Pt/C electrocatalysts prepared via the $Ni(Cp)_2$ route**

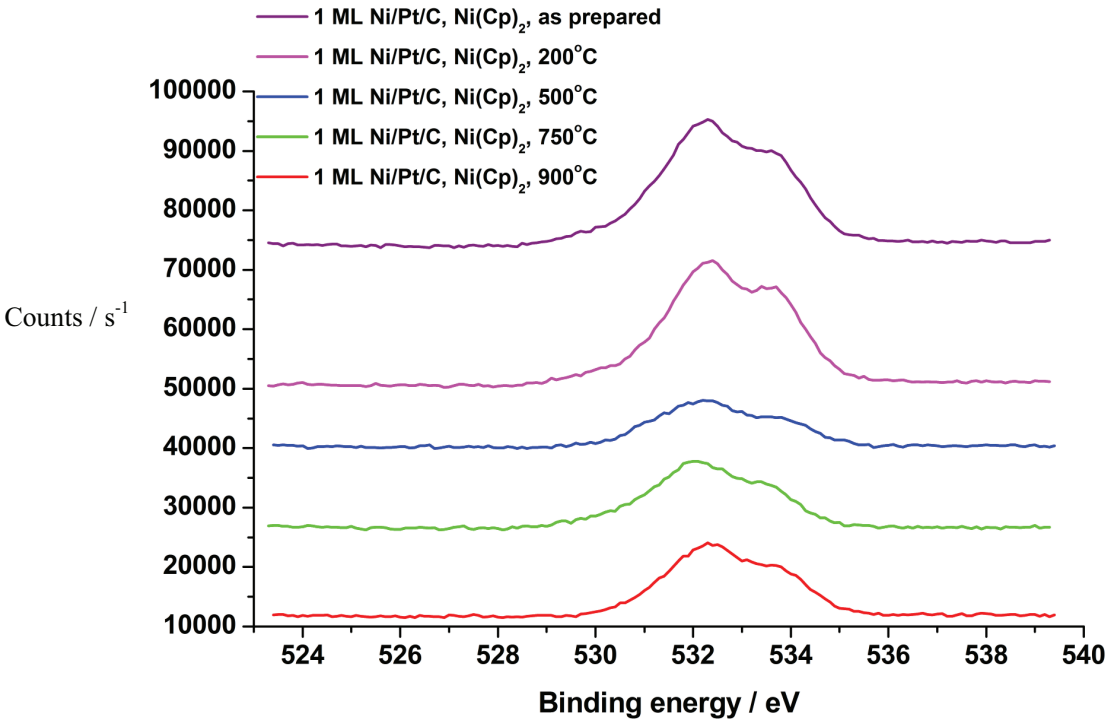

Figure 3 **XPS of O(1s) core level region of 1 ML Ni/Pt/C electrocatalysts prepared via the $Ni(Cp)_2$ route.**

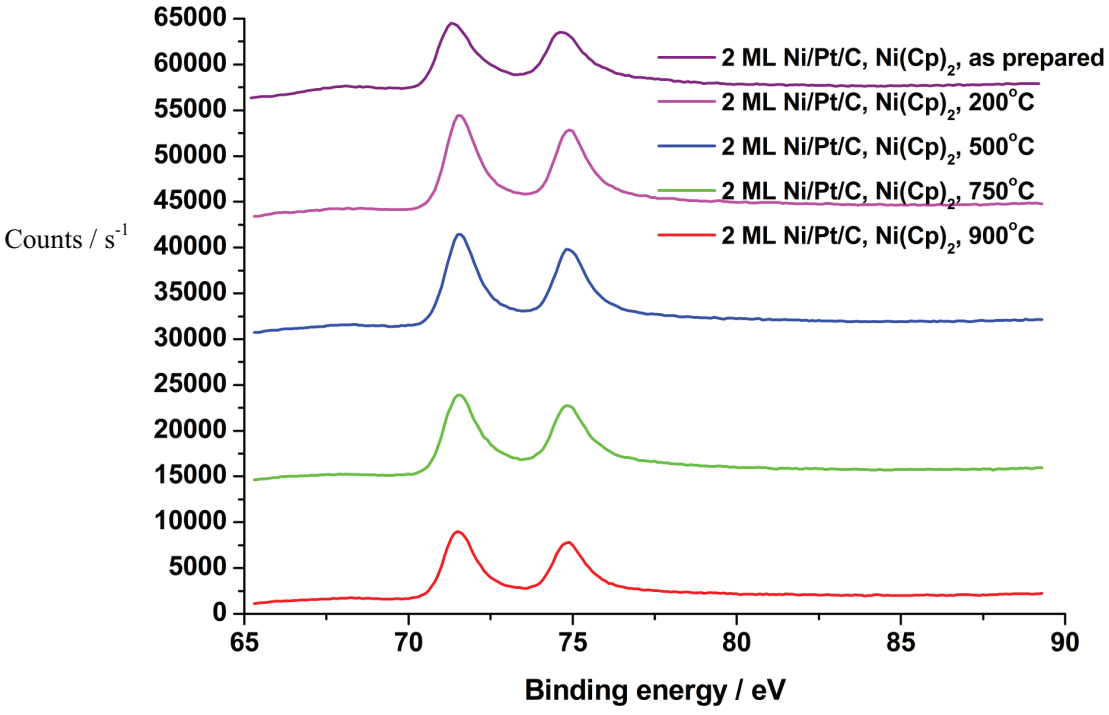

Figure 4 **XPS of Pt(4f) core level region of 1 ML Ni/Pt/C electrocatalysts prepared via the $Ni(Cp)_2$ route**

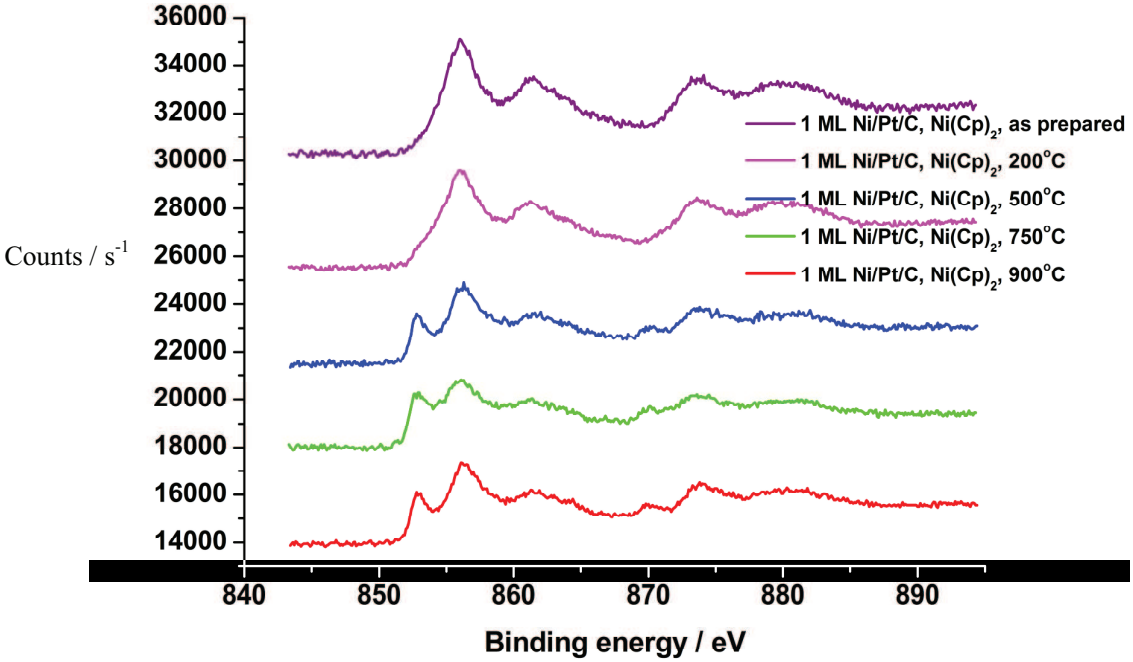

Figure 5 **XPS of Ni(2p) core level region of 1 ML Ni/Pt/C electrocatalysts prepared via the $Ni(Cp)_2$ route**

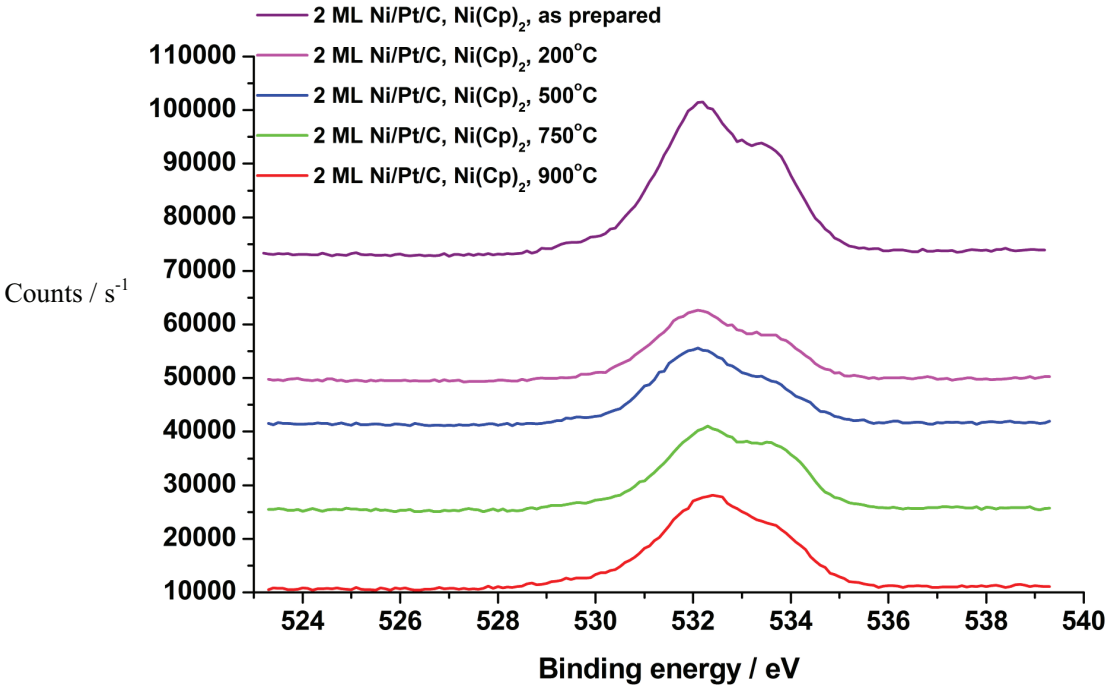

Figure 6 **XPS of O(1s) core level region of 1 ML Ni/Pt/C electrocatalysts prepared via the $Ni(Cp)_2$ route.**

APPENDIX 2

1 ML Ni/Pt/C as prepared via the $Ni(acac)_2$ route

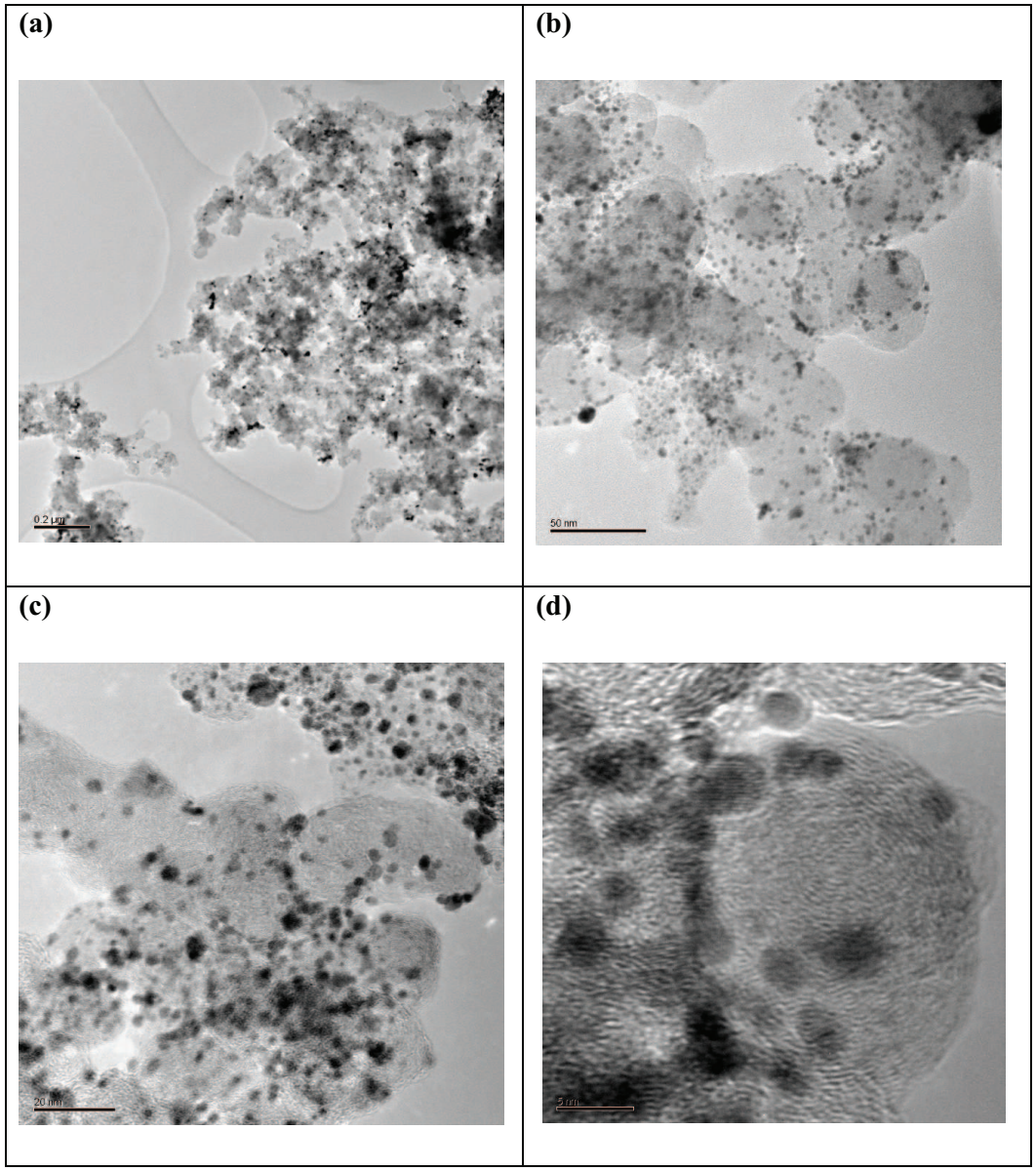

Figure 1 **TEM micrographs of 1 ML Ni/Pt/C as prepared via $Ni(acac)_2$ at different magnification 200 (a), 50 (b), 20 (c) and 5 nm (d).**

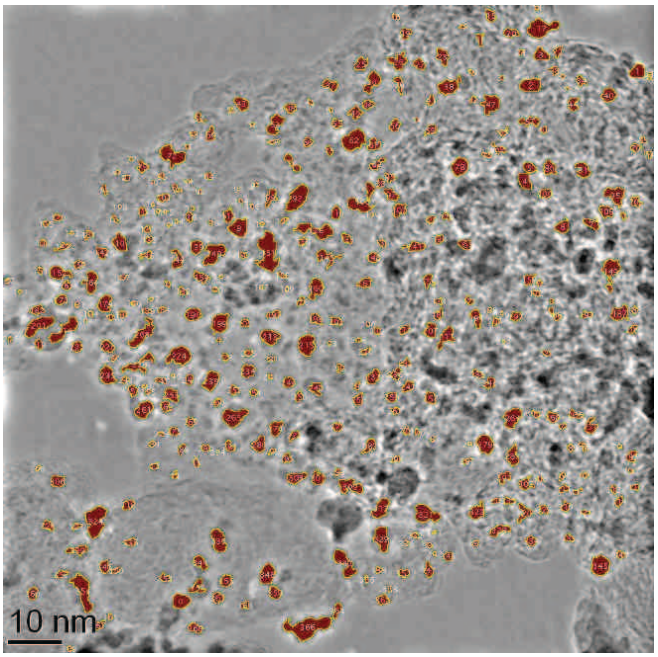

Figure 2 **TEM micrograph of 1 ML Ni/Pt/C as prepared via $Ni(acac)_2$ used to calculate particle size**

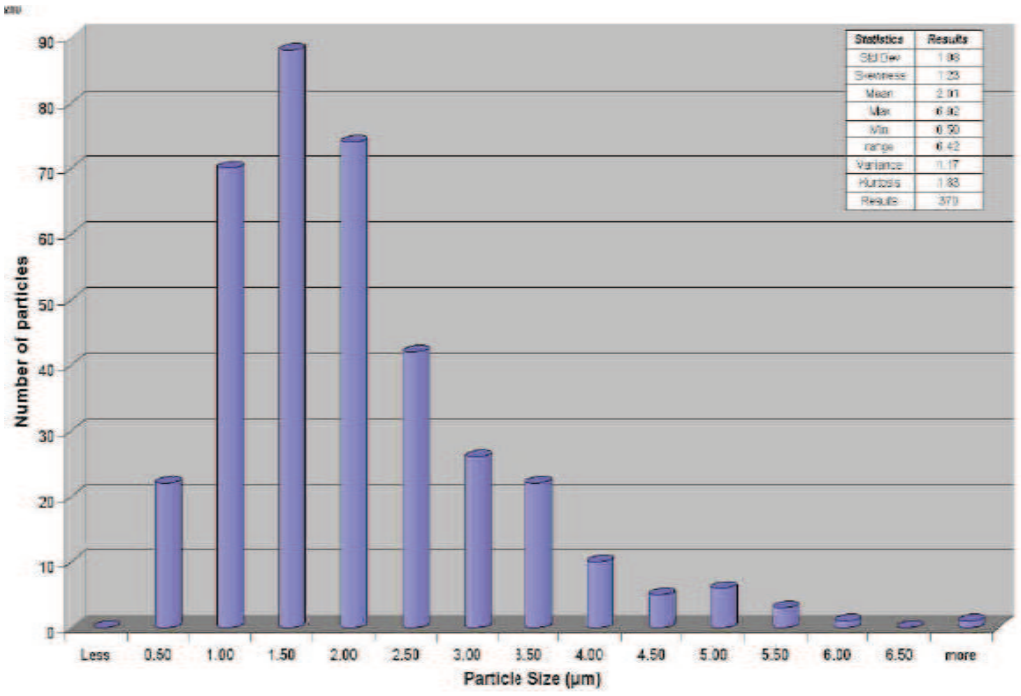

Figure 3 **Particle size distribution of 1 ML Ni/Pt/C as prepared via $Ni(acac)_2$**

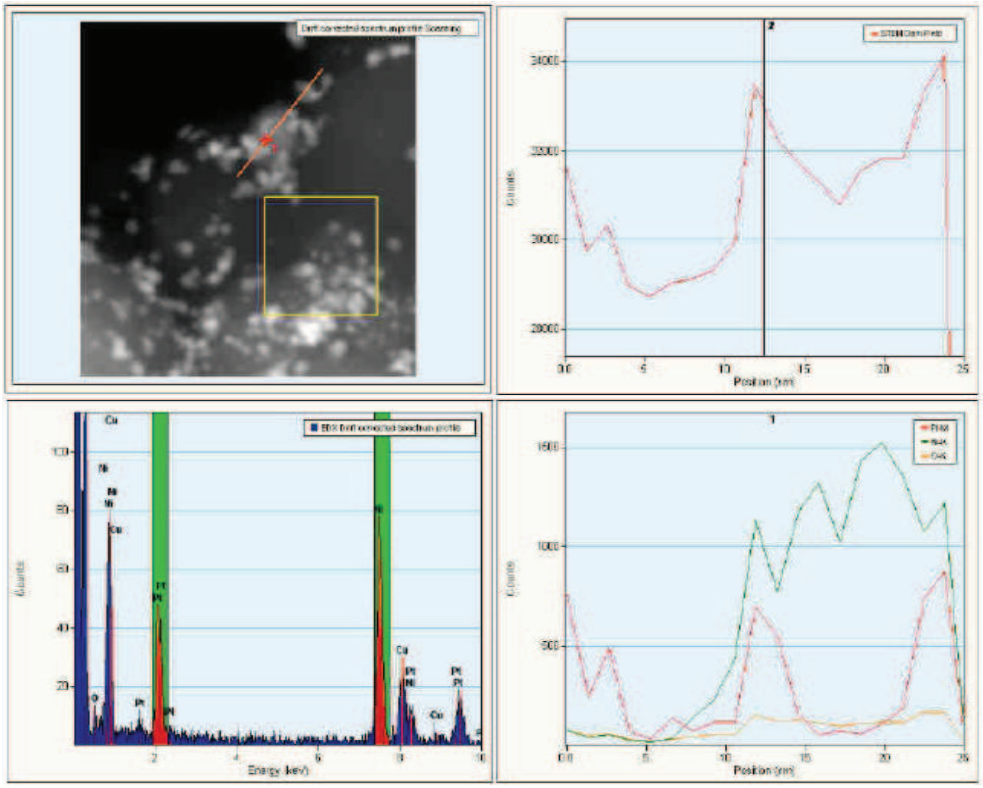

Figure 4 **TEM EDX line profile analysis for 1 ML Ni/Pt/C as prepared via $Ni(acac)_2$. The upper left box shows the TEM image of the area under investigation. The EDX response for the red box is shown below the TEM image. The EDX responses across the red line labelled one are shown on the right hand side and in descending order show total counts, counts from Pt (red) and Ni (blue) respectively.**

1 ML Ni/Pt/C 200 ºC prepared via the $Ni(acac)_2$ route

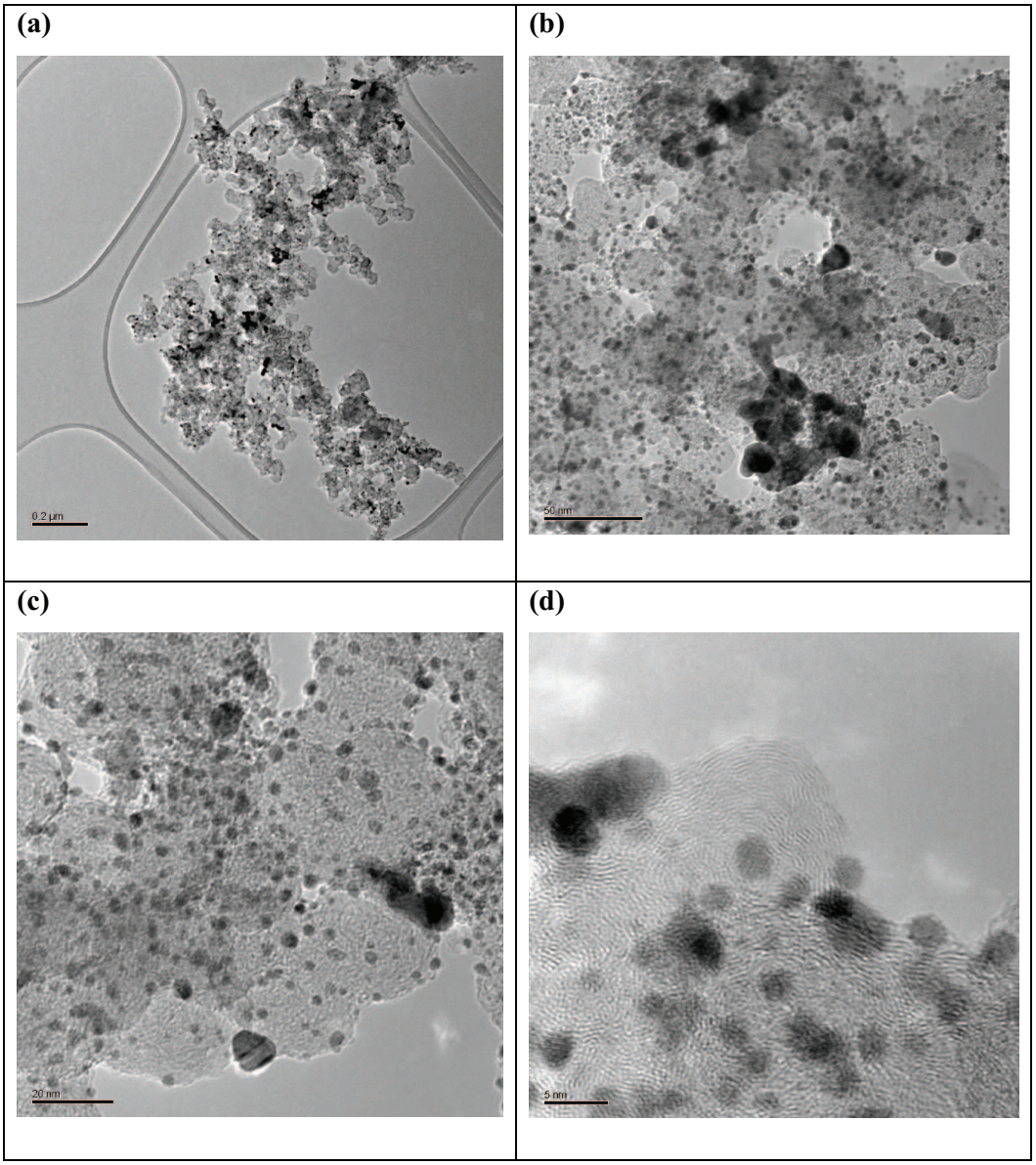

Figure 5 **TEM micrographs of 1 ML Ni/Pt/C 200 ºC via $Ni(acac)_2$ at different magnification 200 (a), 50 (b), 20 (c) and 5 nm (d).**

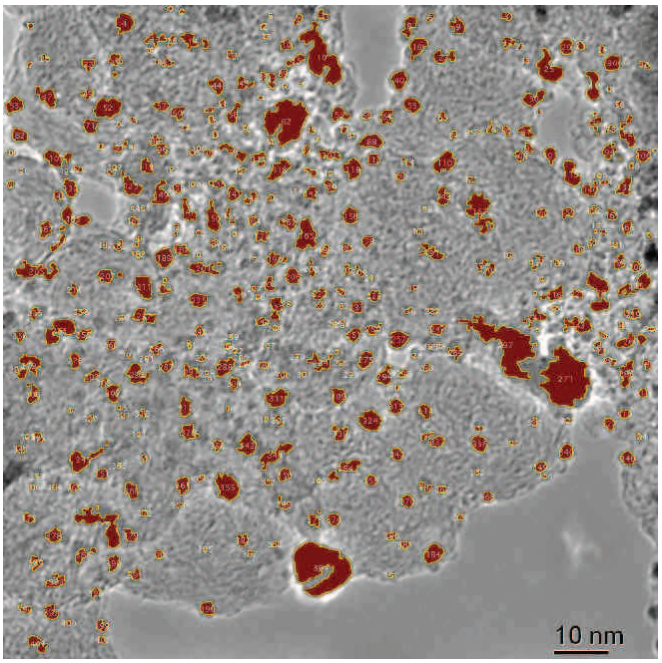

Figure 6 **TEM micrograph of 1 ML Ni/Pt/C 200 ºC prepared via the $Ni(acac)_2$ route used to calculate particle size**

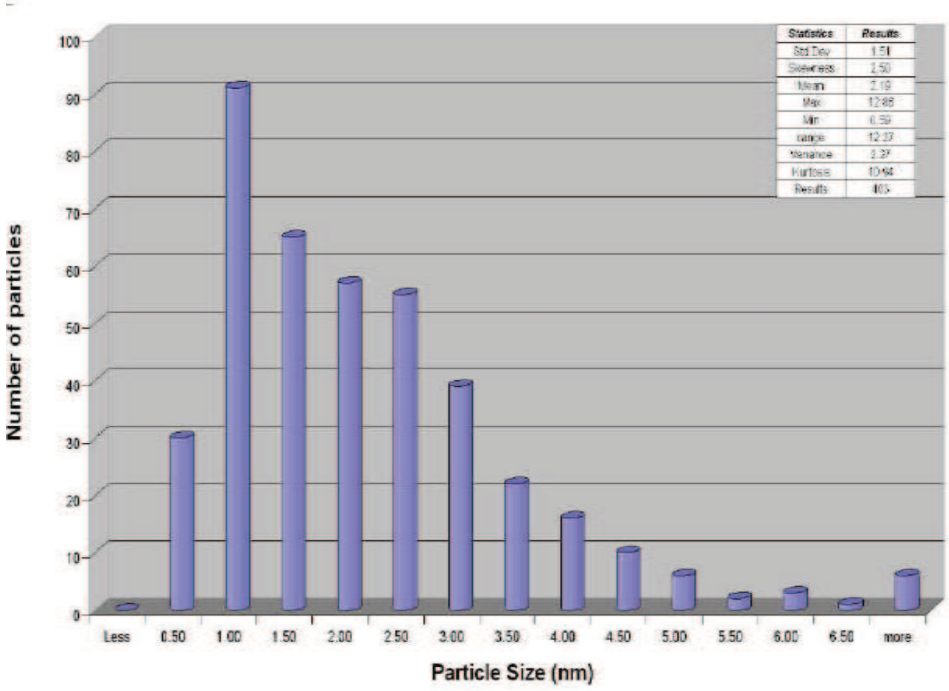

Figure 7 **Particle size distribution of 1 ML Ni/Pt/C 200 ºC prepared via the $Ni(acac)_2$ route.**

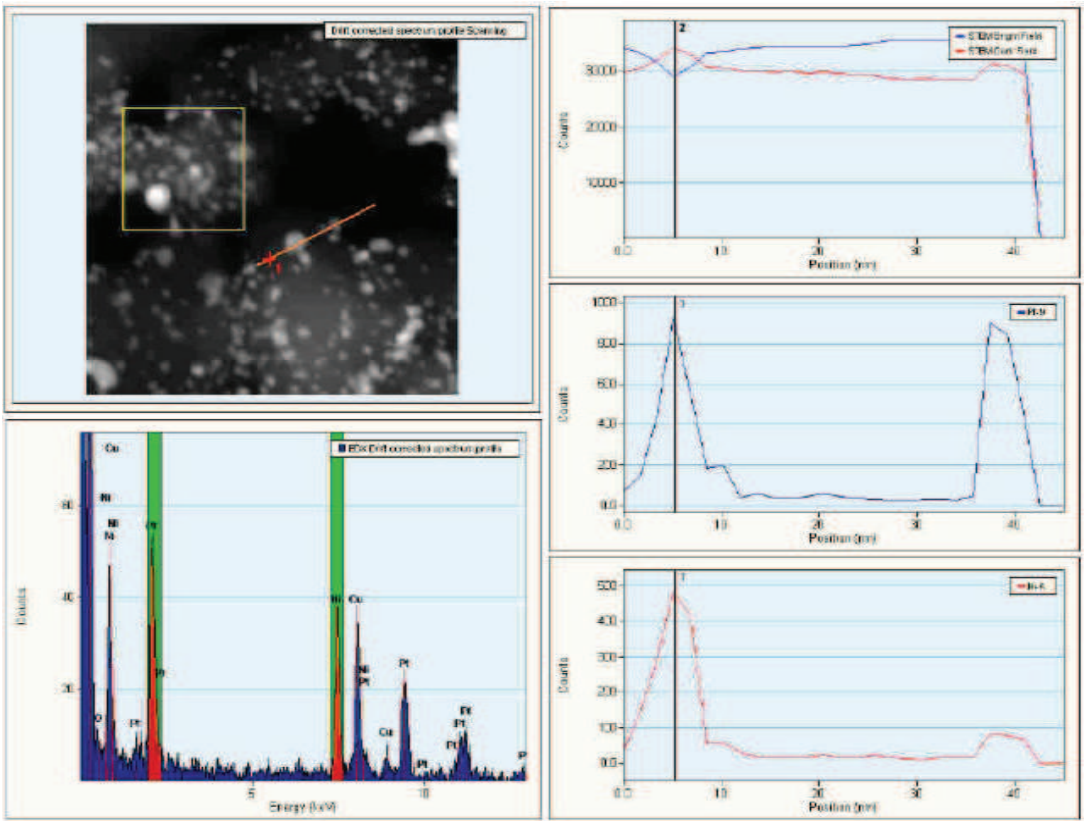

Figure 8 **TEM EDX line profile analysis for 1 ML Ni/Pt/C 200 ºC prepared via the $Ni(acac)_2$ route. The upper left box shows the TEM image of the area under investigation. The EDX response for the red box is shown below the TEM image. The EDX responses across the red line labelled one are shown on the right hand side and in descending order show total counts, counts from Pt (red) and Ni (blue) respectively.**

1 ML Ni/Pt/C 750 ºC prepared via the $Ni(acac)_2$ route

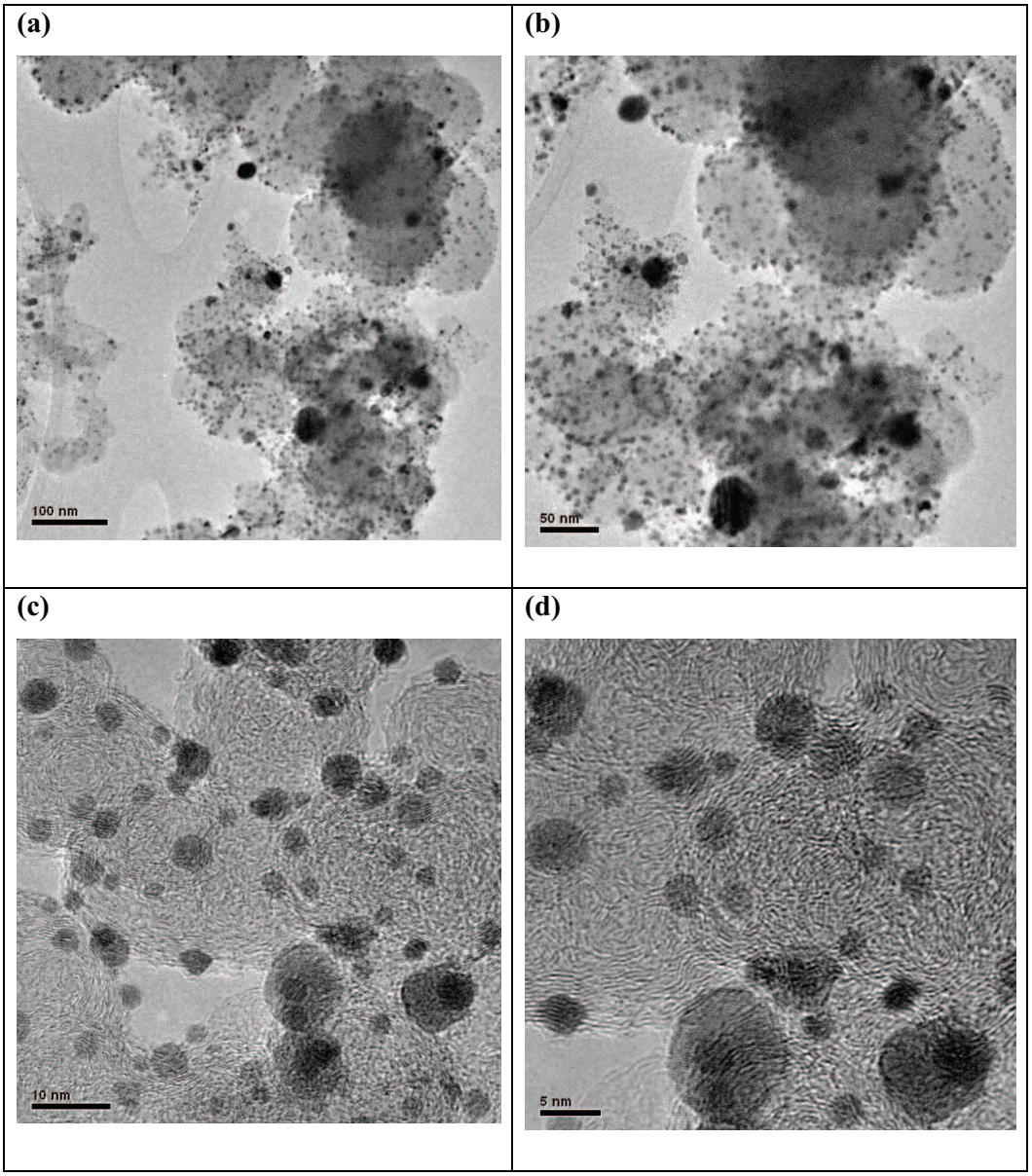

Figure 9 **TEM micrographs of 1 ML Ni/Pt/C 750 ºC prepared via the $Ni(acac)_2$ at different magnification 100 (a), 50 (b), 10 (c) and 5 nm (d).**

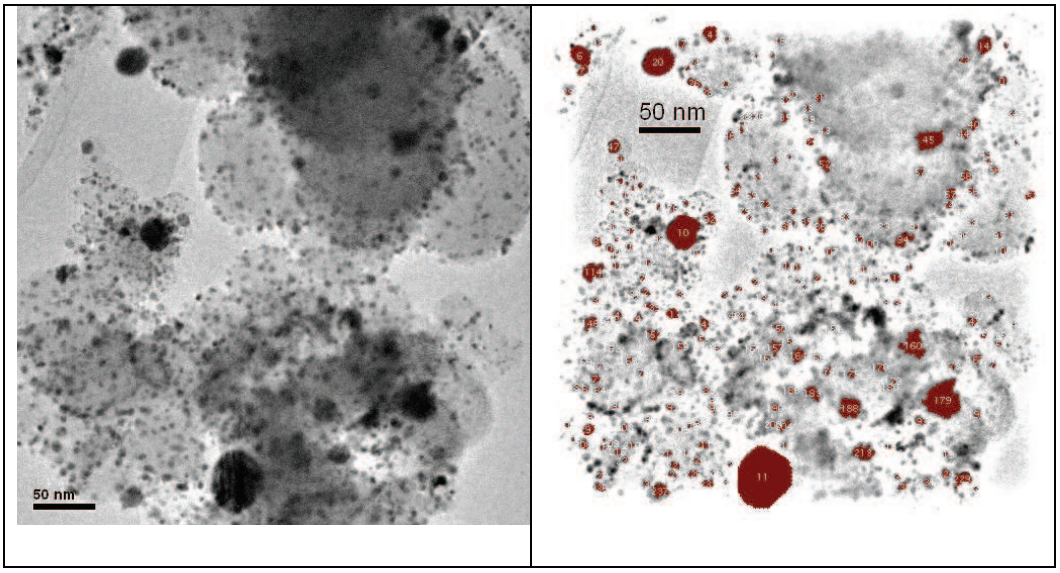

Figure 10 **TEM micrograph of 1 ML Ni/Pt/C 750 ºC prepared via the $Ni(acac)_2$ used to calculate particle size**

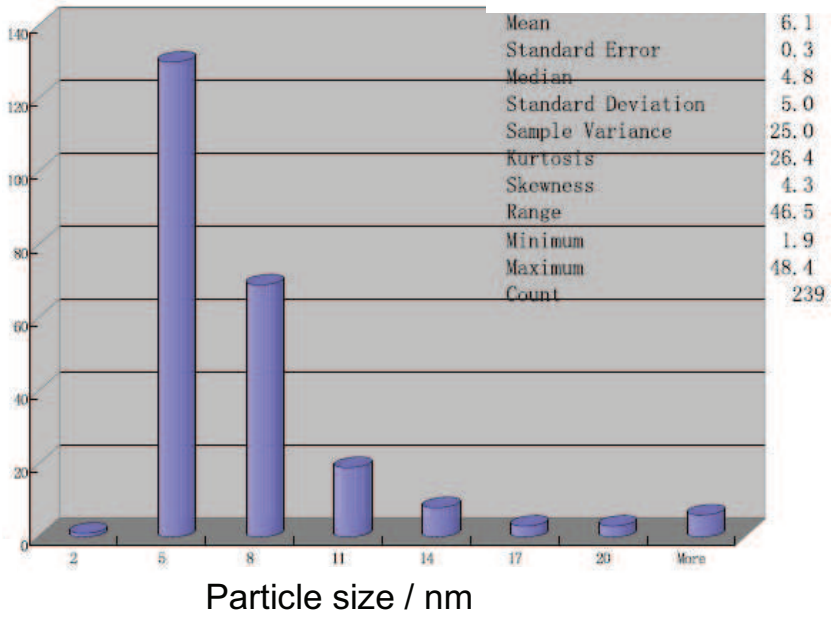

Figure 11 **Particle size distribution of 1 ML Ni/Pt/C 750 ºC prepared via the $Ni(acac)_2$ route**

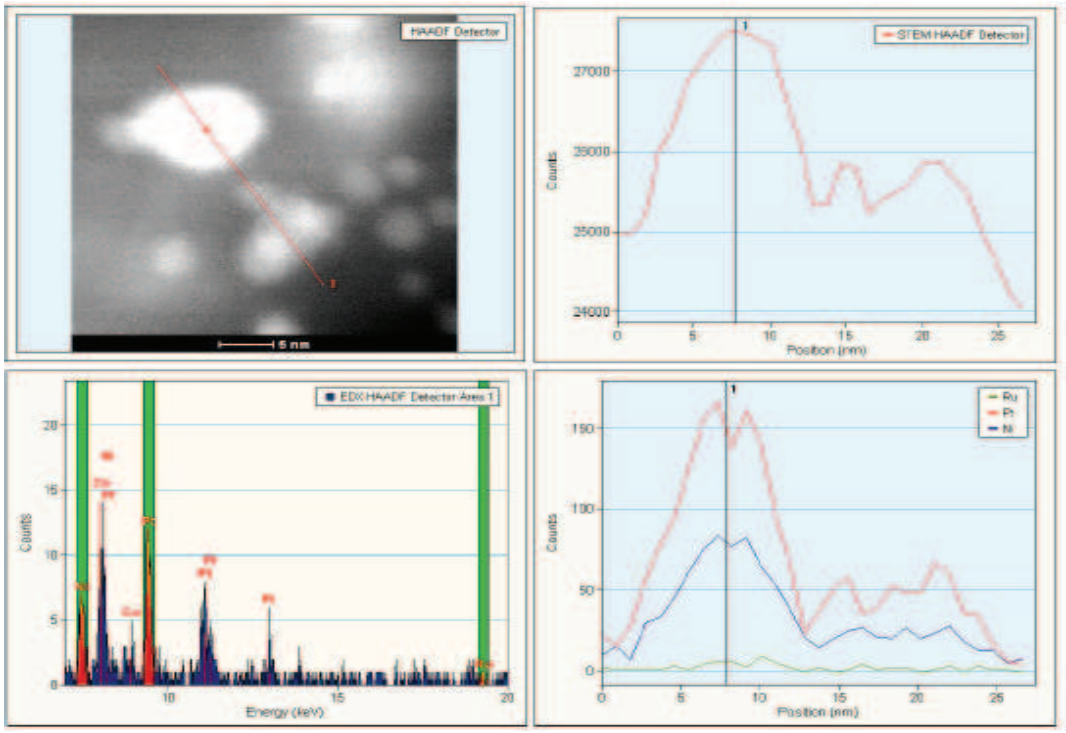

Figure 12 **TEM EDX line profile analysis for 1 ML Ni/Pt/C 750 ºC prepared via the $Ni(acac)_2$ route. The upper left box shows the TEM image of the area under investigation. The EDX response for the red box is shown below the TEM image. The EDX responses across the red line labelled one are shown on the right hand side and in descending order show total counts, counts from Pt (red) and Ni (blue) respectively.**

1 ML Ni/Pt/C 900 ºC prepared via the $Ni(acac)_2$ route

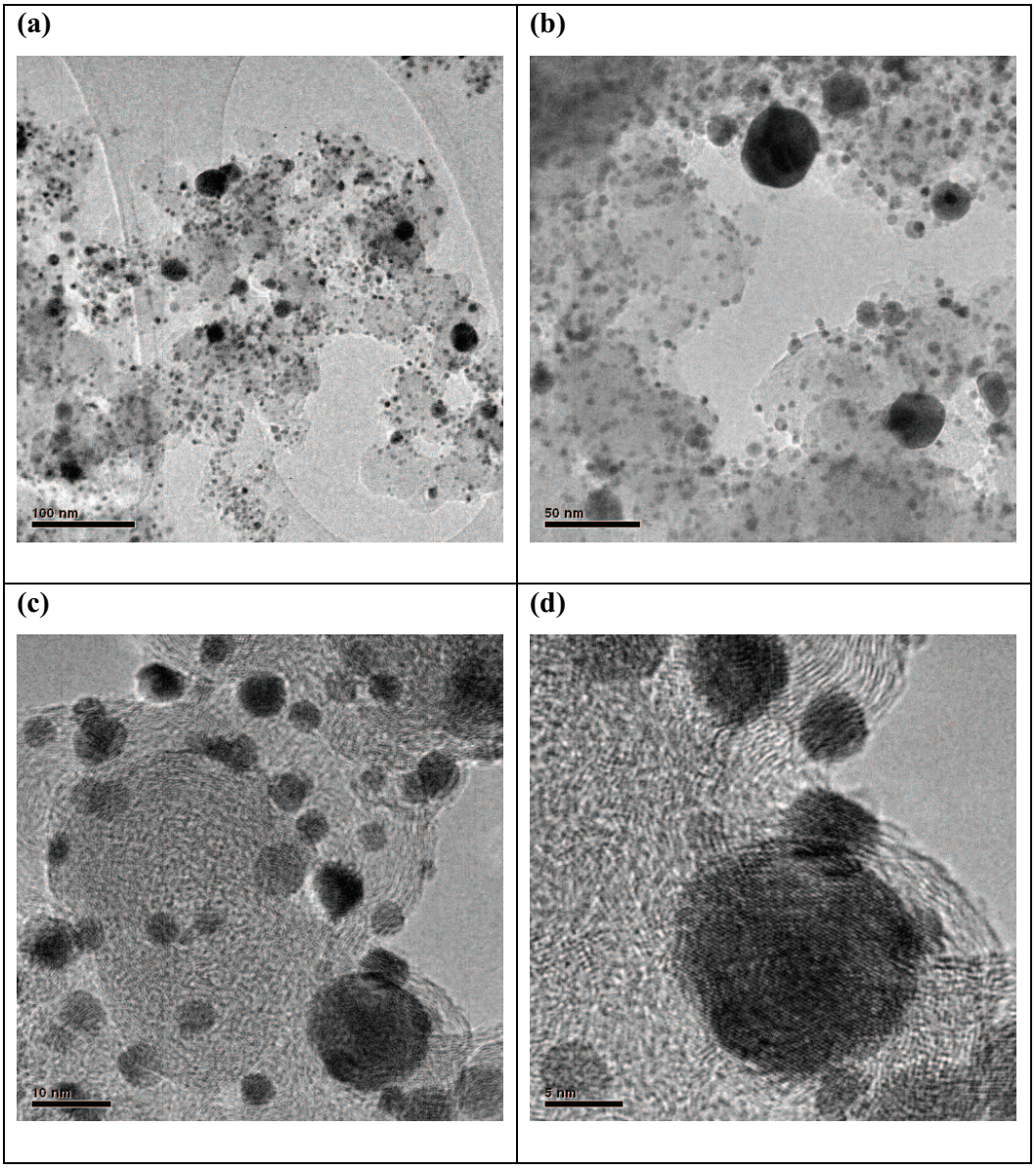

Figure 13 **TEM micrographs of 1 ML Ni/Pt/C 900 ºC prepared via the $Ni(acac)_2$ at different magnification 100 (a), 50 (b), 10 (c) and 5 nm (d).**

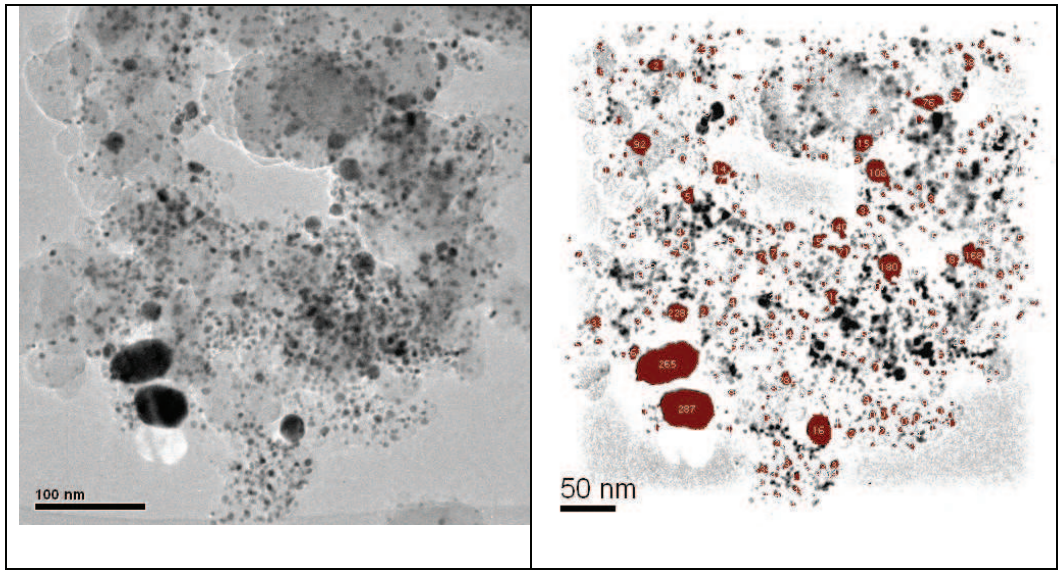

Figure 14 **TEM micrograph of 1 ML Ni/Pt/C 900 °C prepared via the $Ni(acac)_2$ used to calculate particle size**

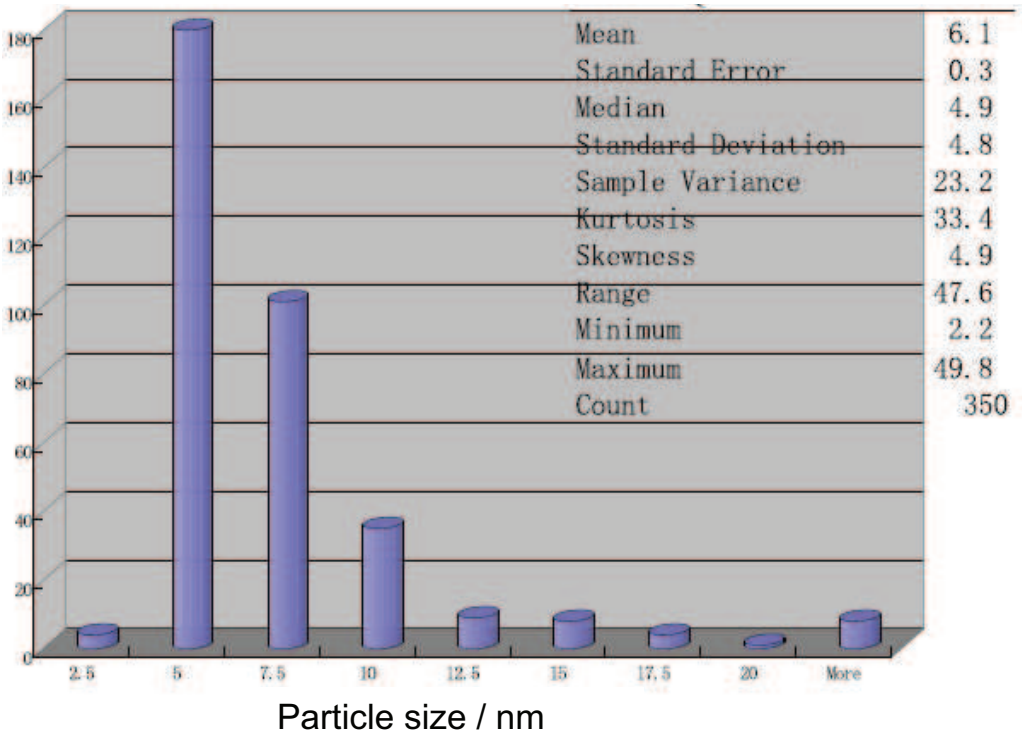

Figure 15 **Particle size distribution of 1 ML Ni/Pt/C 900 °C prepared via the $Ni(acac)_2$.**

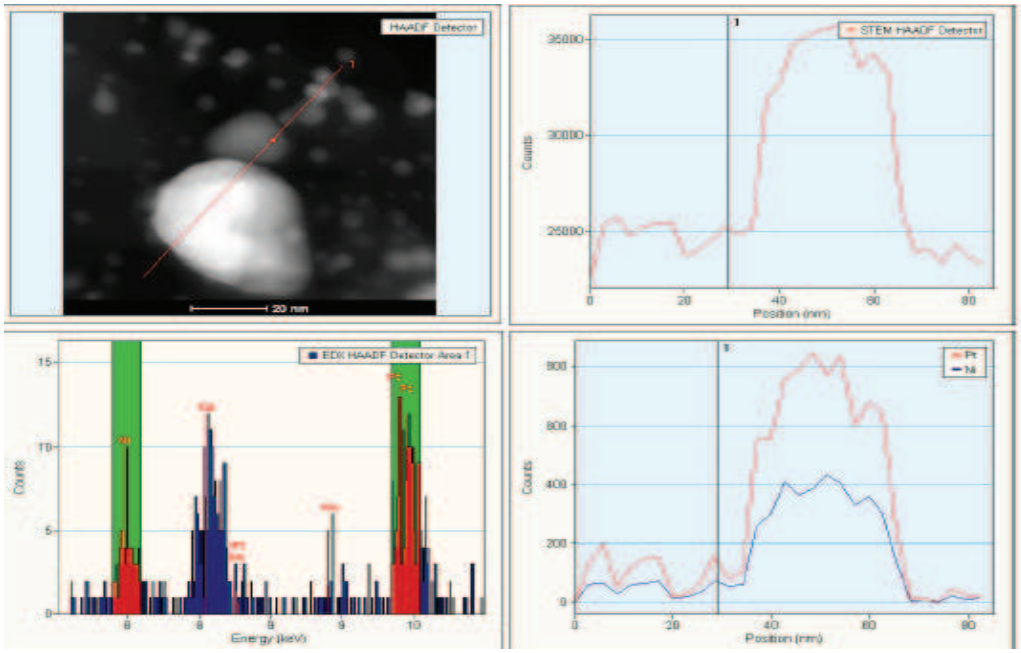

Figure 16 **TEM EDX line profile analysis for 1 ML Ni/Pt/C 900 ^{o}C prepared via the Ni(acac)$_2$ route. The upper left box shows the TEM image of the area under investigation. The EDX response for the red box is shown below the TEM image. The EDX responses across the red line labelled one are shown on the right hand side and in descending order show total counts, counts from Pt (red) and Ni (blue) respectively.**

Particle size for the Ni/Pt/C prepared via the Ni(acac)2 route. All values are in nm

	0.5 ML				2 ML		
	as prepared	500	900		as prepared	500	900
	4.61	5.64	58.4		5.61	12.16	4.99
	3.46	13.83	42.08		13.4	8.42	19.01
	5.3	12.81	8.59		4.68	7.48	31.79
	5.07	7.17	12.02		4.36	4.36	28.05
	4.61	8.2	7.73		3.12	9.04	11.53
	3.92	7.69	8.16		3.12	4.36	10.29
	6.22	9.22	18.47		7.48	4.36	7.79
	3.69	9.73	5.58		4.99	9.04	6.55
	2.77	9.73	20.18		10.91	5.61	9.66
	6.22	7.62	9.02		4.68	15.9	8.42
	2.77	5.12	10.74		10.91	7.48	6.86
	4.38	8.71	6.01		9.66	4.36	6.86
	5.99	6.66	8.59		8.42	10.91	5.61
	2.77	6.15	12.88		11.53	5.61	7.48
	4.15	6.66	7.3		6.23	4.36	7.79
	3.69	7.69	7.73		5.3	4.99	10.91
	2.77	21.01	17.61		8.1	7.48	4.99
	3.69	5.12	6.01		6.55	5.3	7.79
	3.92	14.35	7.3		10.29	5.3	9.66
	8.76	18.96	6.87		6.55	15.27	7.76
	9.45	7.69	4.29		6.23	6.86	9.35
	2.77	5.12	7.73		6.55	5.61	9.66
	3.23	9.22	6.44		6.55	6.23	9.97
	3	17.69	6.01		5.61	10.91	6.23
	3.23	10.76	9.45		4.99	9.04	5.61
	4.15	6.15	6.01		4.36	10.6	5.81
	5.3	5.64	3.44		4.99	9.97	5.61
	4.38	9.22	6.01		7.79	3.12	7.17
	4.15	8.2	5.15		3.74	7.79	8.73
	3.92	8.71	9.45		3.74	5.3	5.61
	9.91	7.71	9.88		7.48	5.61	7.48
	5.3	6.15	7.3		4.99	6.86	3.74
	3.23	5.12	8.59		6.23	7.79	7.79
	7.14	9.22	8.16		6.23	9.66	9.66
	5.07	7.69	5.15		4.68	5.92	4.99
	3.69	7.17	6.01		3.74	4.68	7.17
	4.15	9.22	8.16		3.43	10.92	6.55
	4.15	7.69	6.87		6.23	6.23	8.1
	3.23	10.25	7.73		7.79	5.92	9.04
	5.76	9.22	5.58		4.68	4.36	5.61
	3.23	19.98	10.74		6.23	5.3	6.86
	3.69	10.25	15.46		6.23	4.68	9.04
	5.76	15.12	7.73		6.55	9.04	6.86
	2.77	7.17	6.01		4.36	7.17	8.73
		9.22	9.02		6.23	5.61	15.27
Mean	4.5	9.4	10.4		6.3	7.3	9.0
Standard Deviation	1.7	4.0	9.6		2.3	2.9	5.3

APPENDIX 3

Particle size of Ni/Pt/C catalysts prepared via the Ni(Cp)2 route.
All values are in nm.

1 ML				2 ML		
As prepared	500	900		AP	500	900
5.07	14.65	17.61		6.55	16.32	10.29
38.26	19.33	9.45		10.29	16.75	14.03
5.3	29.61	7.3		4.99	15.89	11.22
5.536	20.88	13.31		5.92	9.02	6.55
5.3	30.55	12.02		4.36	19.32	12.1
3.92	31.17	11.59		3.74	15.03	11.53
4.84	27.74	17.61		7.79	11.59	6.55
7.37	27.43	11.59		7.17	15.03	13.4
5.3	30.55	8.59		5.61	17.61	9.66
3.69	8.1	19.32		6.23	9.45	15.91
2.77	4.36	9.45		8.42	11.17	13.4
3.69	4.36	21.04		4.99	21.04	9.97
4.15	6.23	6.01		5.92	15.89	13.4
5.3	4.99	7.3		5.61	10.31	10.91
15.44	4.99	9.45		4.68	18.47	12.16
7.14	4.36	9.88		4.99	20.18	12.78
7.61	6.23	10.31		4.99	12.45	31.79
4.15	4.68	10.74		6.23	8.59	19.01
4.15	8.1	7.73		5.61	10.74	17.14
7.61	4.99	11.59		8.42	10.31	12.16
5.07	4.99	9.88		4.99	25.34	10.29
7.37	4.36	9.45		4.68	11.17	9.04
6.68	5.61	13.31		13.4	12.45	16.52
6.68	5.92	8.59		5.61	21.04	5.3
6.68	6.86	10.74		5.3	12.88	22.75
5.76	7.17	12.02		6.55	13.31	7.48
3.69	10.6	8.16		5.92	8.59	10.29
6.22	9.66	17.61		6.86	7.73	11.53
4.61	6.86	15.89		5.61	9.02	9.97
8.07	6.23	11.59		3.12	9.88	12.16
5.76	8.73	13.31		6.23	9.02	7.17
4.15	12.16	13.31		4.36	18.47	10.91
5.99	15.27	13.31		4.68	17.61	9.35
3.23	5.61	10.74		5.3		12.78
3.46	8.1	8.59		6.86		10.29
4.15	16.52	5.15		3.74		7.79
5.99	8.1	6.87		4.36		12.78
2.54	6.86	8.59		4.99		17.77
2.77	22.13	21.04		6.23		8.73
4.15	19.95	10.31		6.86		
4.15	4.68	7.3		4.36		
3.69	5.3	8.59		4.36		
5.76	8.73	8.59				
4.38	6.86	6.44				
	7.79	15.03				
Mean 6.2	11.8	11.5		6.0	14.4	12.5
Standard deviation 5.4	8.5	3.9		1.8	4.5	4.8